JOURNAL OF APPLIED PHYSICS

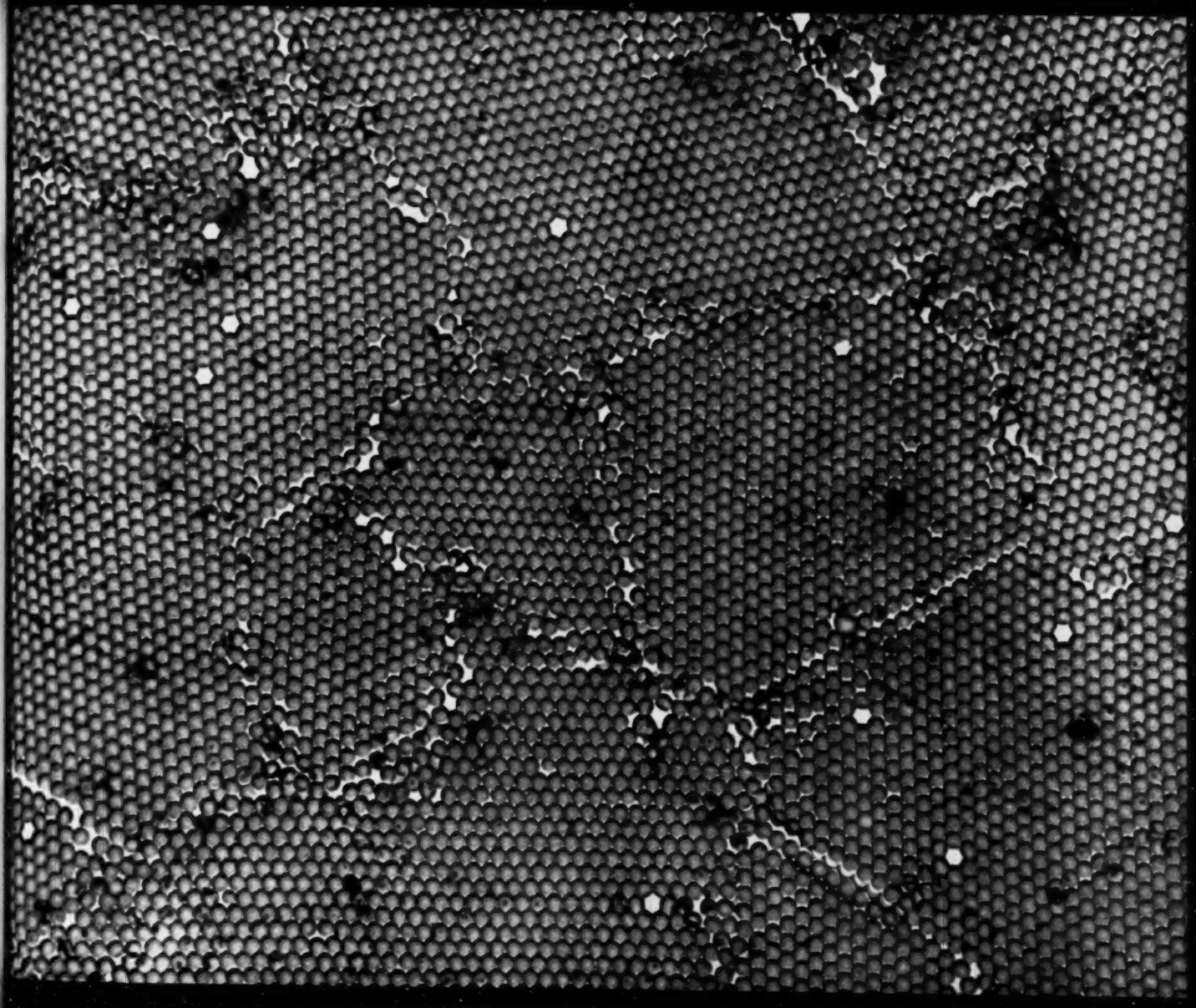

JOURNAL
OF
APPLIED PHYSICS

Vol. 23, No. 6 JUNE, 1952

In This Issue

Page

Electromagnetic Reflection and Transmission by Gratings of Resistive Wires Edward A. Lewis and Joseph P. Casey, Jr. 605

Electron Microscope Study of Plasticized Latices E. B. Bradford 609

Radiation Resistance of Resonant Transmission Lines R. A. Chipman, E. F. Carr, N. A. Hoy, and M. Yurko 613

Thermal Neutron Diffusion Length in a Heterogeneous Pile Gilbert N. Plass 621

Mathematical Analysis of Parallel-Connected Magnetic Amplifiers with Resistive Loads Louis A. Pipes 625

Study of the Annealing Kinetics in Cold Worked Copper Dwain Bowen, R. R. Eggleston, and R. H. Kropschot 639

Chemical Reactions in Barium Oxide on Tungsten Emitters R. C. Hughes, P. P. Coppola, and H. T. Evans 635

On the Kinetics of Ordering in Ni_2Mn Lewis R. Aronin 642

Characteristics of the High Current Tungsten Arc in Argon, Helium, and Their Mixtures Merrill Skolnik and T. B. Jones 643

Equivalences for the Analysis of Circuits with Small Nonlinearities W. J. Cunningham 653

Incandescent Lamp Bulbs in Voltage Stabilizers W. J. Cunningham 658

X-Ray Absorption Corrections for Single Crystals Howard T. Evans, Jr. 663

Physical Processes in the *L* Cathode D. L. Schaefer and John E. White 669

Electrical Noise from Instrument Cables Subjected to Shock and Vibration Thomas A. Perls 674

Determination of the Transverse Permeabilities of Large Core Samples from Petroleum Reservoirs R. E. Collins 681

Conical Surfaces of Fracture Produced by Asymmetrical Impulsive Loading John S. Rinehart and John Pearson 685

Radiation Characteristics of a Turnstile Antenna Shielded by a Section of a Metallic Tube Closed at One End Alfredo Baños, Jr., David S. Saxon, and Louis L. Bailin 688

Letters to the Editor:

Change of the Elastic Constants of β-Brass with Composition H. Jones 697

Receiver of High Effective Absorption for Penetrating Radiation Rudolf Frerichs 697

Intensity Calculation for Determining Weight Percentage in a Binary Alloy by X-Ray Fluorescent Analysis P. K. Koh, B. Caugherty, and R. E. Burket 698

Energy Transference between Wave Numbers in Isotropic Turbulence Hiroshi Sato 698

Dielectric Image Line D. D. King 699

New Booklets and Other Publications 700

Index to Advertisers xxxii

BOARD OF EDITORS
Elmer Hutchisson, *Editor*
Earle C. Gregg, *Assistant Editor*

Associate Editors
Howard H. Aiken
Ray E. Bolz
Lyle D. Borst
Robert D. Heidenreich
James Hillier
Leonard B. Loeb
W. James Lyons
Eric Reissner
Roman Smoluchowski

Publication of the American Institute of Physics

OFFICERS
George R. Harrison, *Chairman*
George B. Pegram, *Treasurer*

GOVERNING BOARD
Karl K. Darrow
G. J. Dienes
S. A. Goudsmit
G. P. Harnwell
George R. Harrison
F. V. Hunt
Rudolph Kingslake
Hugh S. Knowles
C. C. Lauritsen
F. W. Loomis
William F. Meggers
George B. Pegram
I. I. Rabi
Duane Roller
Frederick Seitz
Francis G. Slack
John C. Steinberg
Richard M. Sutton
Mark W. Zemansky

Consultant on Printing
Melvin Loos

ADMINISTRATIVE STAFF
Henry A. Barton, *Director*
Wallace Waterfall, *Executive Secretary*
Theodore Vorburger, *Advertising Manager*
Ruth F. Bryans, *Publication Manager*
Betty H. Goodfriend, *Assistant Secretary*
Eileen B. Neuberger, *Circulation Manager*
Kathryn Setze *Assistant Treasurer*

The Journal of Applied Physics, published monthly at Prince and Lemon Sts., Lancaster, Pa., is devoted to physics in its role as the science basic to other natural sciences and to the arts and industries. Previous to 1937 this publication was known as Physics. The Journal of Applied Physics publishes editorials and reviews, as well as technical papers of applied physics. Articles appearing in it are indexed regularly, according to their field, by Physics Abstracts, Chemical Abstracts, Engineering Index, Inc., Industrial Arts Index, etc.

Manuscripts should be submitted to Elmer Hutchisson, Editor, Case Institute of Technology, Cleveland 6, Ohio. Unless otherwise stated, submission of a manuscript is a representation that it has been neither copyrighted, published, nor submitted for publication elsewhere. The authors' institutions are requested to pay a **publication charge** of $8 per page which, if honored, entitles them to 100 reprints without further charge. Instructions will be sent with galley proofs.

Subscriptions, renewals, and orders for back numbers should be addressed to the American Institute of Physics, 57 East 55 Street, New York 22, New York.

Subscription Price	U.S. and Canada	Elsewhere
To members of the American Institute of Physics and Affiliated Societies	$10.00	$11.00
To all others	12.00	13.00

Back Number Prices

Yearly back number rate when complete year is available: $10.00. Single copies: $1.00 each.

Changes of address should be sent to the American Institute of Physics; **corrected proofs** should be sent to the Publication Manager, American Institute of Physics. **Advertising rates** supplied on request. Orders, advertising copy, and cuts should be sent to the American Institute of Physics.

Entered as second class matter January 22, 1937, at the Post Office at Lancaster, Pennsylvania, under the Act of March 3, 1879. Accepted for mailing at the special rate of postage provided for in paragraph (d-2), section 34.40, P. L. & R. of 1948, authorized May 2, 1932.

Journal
of
Applied Physics

Volume 23, Number 6 June, 1952

Electromagnetic Reflection and Transmission by Gratings of Resistive Wires

EDWARD A. LEWIS AND JOSEPH P. CASEY, JR.
Air Force Cambridge Research Center, Cambridge, Massachusetts
(Received November 28, 1951)

Calculations show that the effect of increasing the resistivity of the wires is to decrease the amplitude of the reflection coefficient and the phase of the transmission coefficient. The sign of the changes in the amplitude of the transmission coefficient and the phase of the reflection coefficient depends upon the amplitude of the reflection coefficient of a geometrically similar grating having no resistance. A numerical example for a typical grating is worked out and several charts are supplied for convenience in computing.

THE EFFECTS OF RESISTANCE IN WIRE GRATINGS

THE reflection and transmission of an electromagnetic wave by a plane grating of parallel wires is included in the very general considerations of Ignatowsky,[1,*] whereas other mostly subsequent papers[2–7,*] have given more direct and also more restricted treatments. Nevertheless, it seems that the theory for a wave falling with arbitrary angle of incidence on a grating of wires with finite conductivity has not hitherto been presented in a simple form convenient for numerical work.†

Wessel[3] remarked that, with wires made of ordinary good-conducting materials, the effects of resistance are small. While this may be true for a grid in free space, the resistance is by no means negligible when the grid is an element of a resonant structure. For example, between a pair of similar, parallel, highly reflecting gratings, there is an interference action[8] which is highly sensitive to losses and phase changes[9]; in fact, when tuned, the maximum transmission is determined almost entirely by resistive effects.

For use as reflecting surfaces in interference filters, interest is confined to grids in which the wire spacing (d) is less than a half-wave ($\lambda/2$) of the radiation being used, and the wire radius (a) is assumed much less than (d). With these restrictions, a plane wave of amplitude E_0, having its electric vector parallel to the wires, and incident at angle α from the normal, gives rise to just one reflected wave (coming off at reflection angle α), and just one transmitted wave (proceeding in the original direction).‡ The reflected wave is regarded as originating from the currents induced in the wires, while the transmitted wave is the superposition of the induced and incident fields.

The induced currents all have the same magnitude but differ in phase from wire to wire by the angle $kd\sin\alpha$, where $k\equiv 2\pi/\lambda$. If I_0 is the current in any particular wire chosen for reference, it can be shown[10] that the diffracted wave is

$$E_D=-60\pi I_0/d\cos\alpha, \quad \text{(MKS units)} \quad (1)$$

the phase being relative to the reference wire. By definition, the reflection coefficient is the ratio of the reflected wave to the incident wave:

$$r=E_D/E_0=-60\pi/Zd\cos\alpha, \quad (2)$$

[1] W. v. Ignatowsky, Ann. Physik **44**, 369 (1914).
* Translated by H. H. Kolm, M.I.T., Translation Service.
[2] R. Honerjäger, Ann. Physik (Folge 6), Vol. 4, 25 (1948).
[3] W. v. Wessel, Hochfrequenztechnik **54**, 62 (1939).
[4] G. G. MacFarlane, J. Inst. Elec. Engrs. (London), Pt. III A, **93**, 1523.
[5] R. Gans, Ann. Physik **61**, 447 (1920).
[6] C. Schaefer, Ann. Physik **74**, 275 (1924).
[7] C. Schaefer and M. Laugwitz, Ann. Physik **21**, 587 (1906); **23**, 951 (1907).
† Gans' explicit treatment (see reference 5) of the effect of the wire resistance is limited to the case of normal incidence and contains the restriction that the wavelength be much greater than the grating constant. It can be shown that the latter restriction is equivalent to ignoring the term F in Eq. (24) of the present paper.
[8] E. A. Lewis and J. P. Casey, J. Opt. Soc. Am. **41**, 360 (1951).
[9] E. A. Lewis, AFCRC Report, "Notes on Interference Filters," April, 1952.
‡ Actually side waves do not occur unless $(\lambda/d)<1+\sin\alpha$. (See reference 4.)
[10] Reference 2, Eq. (29).

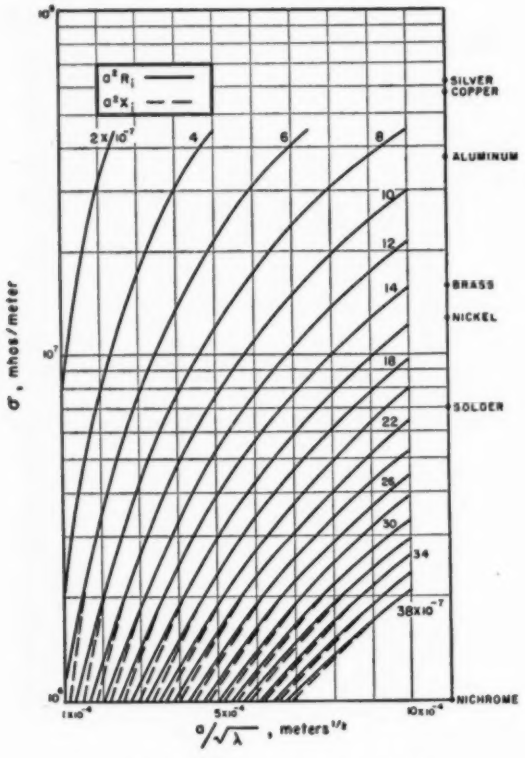

FIG. 1. Internal impedance of a wire.

where

$$Z=E_0/I_0. \tag{3}$$

The transmission coefficient is

$$t=(E_D+E_0)/E_0=1+r=\tau e^{i\phi}. \tag{4}$$

It is now seen that the properties of the grid are determined once the "grid impedance" Z is calculated. Honerjäger's[2] calculation can easily be extended to include losses in the following manner.

Let e_1 be the electric field at the surface of the reference wire caused by its own current, and the current in all the other wires, each having unit magnitude. The quantity e_1 is calculated in terms of λ, d, α, a. The total field at the wire is then

$$E_w=E_0+I_0e_1. \tag{5}$$

If the wire is perfectly conducting the boundary condition "tangential E continuous" requires $E_w=0$, so by Eqs. (3) and (5), the grid impedance for perfectly conducting wires is

$$Z_p=-e_1. \tag{6}$$

With lossy wires,

$$E_w=I_0Z_i, \tag{7}$$

where Z_i is the "internal impedance" of a single grid wire, a quantity expressible in terms of the *ber* and *bei* functions[11,12]:

$$Z_i=\frac{R_s}{\pi a\sqrt{2}}\times\left[\frac{BerqBei'q-BeiqBer'q+iBerqBer'q+iBeiqBei'q}{(Ber'q)^2+(Bei'q)^2}\right], \tag{8}$$

where $q=a(\omega\mu\sigma)^{\frac{1}{2}}$; $R_s=(\omega\mu/2\sigma)^{\frac{1}{2}}$; $\omega=2\pi$ times frequency; $\mu=$magnetic permeability$=4\pi\times10^{-7}$ for the metals to be considered here (MKS system); and $\sigma=$conductivity. For good conductors and high frequencies, and for wire radii not too small, q is large, in which case Eq. (8) reduces to

$$Z_i\simeq(R_s/2\pi a)(1+i). \tag{9}$$

(Approximate values of the real and imaginary parts of $Z_i=R_i+iX_i$ may be obtained by means of Fig. 1.) From Eqs. (5) and (7)

$$\begin{aligned} Z&=Z_i-e_1, \text{ and by Eq. (6)}\\ &=Z_i+Z_p. \end{aligned} \tag{10}$$

The effect of loss is to increase the grid impedance, as if the single wire impedance were added in series.

The loss introduced by the grid is simply the difference between the incident intensity and the combined intensities of the reflected and transmitted waves. The fractional loss is thus

$$l=(1-rr^*-tt^*). \tag{11}$$

By using Eq. (4),

$$l=2(Re(r)+rr^*). \tag{12}$$

Let R, R_i, R_p and X, X_i, X_p be, respectively, the real and imaginary parts of Z, Z_i, and Z_p (having units ohm/meter). These quantities multiplied by $d\cos\alpha/60\pi$ are denoted by primes. In terms of these dimensionless quantities, Eq. (2) becomes

$$r=\frac{-1}{(R_p'+R_i')+i(X_p'+X_i')}. \tag{13}$$

Substituting in Eq. (12)

$$l=-\frac{2(1-R_i'-R_p')}{(R_p'+R_i')^2+(X_p'+X_i')^2}. \tag{14}$$

Now for lossless wires, $R_i'=0$, and l must be zero. It follows from Eq. (14) that R_p' *is unity*, regardless of wire sizes and spacing, within the range of these variables previously defined. Thus the reflection coefficient

[11] S. Ramo and J. R. Whinnery, *Fields and Waves in Modern Radio* (John Wiley & Sons, Inc., New York, 1944), Art. 6.09.
[12] H. B. Dwight, *Tables of Integrals* (Macmillan Company, New York, 1945).

for the grid, lossless or not, is

$$r=\frac{-1}{(1+R_i')+i(X_p'+X_i')} \tag{15}$$

and

$$l=\frac{2R_i'}{(1+R_i')^2+(X_p'+X_i')^2}. \tag{16}$$

Writing

$$r=\rho e^{i\theta} \tag{17}$$

and comparing with Eq. (15),

$$\rho=+\frac{1}{[(1+R_i')^2+(X_p'+X_i')^2]^{\frac{1}{2}}} \tag{18}$$

and

$$\cos\theta=-\rho(1+R_i') \tag{19}$$

$$=-\left(\rho+\frac{l}{2\rho}\right) \text{ by Eq. (16).} \tag{20}$$

From Eq. (4) by means of Eqs. (15) and (19) it follows that

$$\tau=[1-\rho^2-2\rho^2R_i']^{\frac{1}{2}} \tag{21}$$

$$\phi=\tan^{-1}\frac{\rho[1-\rho^2(1+R_i')^2]^{\frac{1}{2}}}{1-\rho^2(1+R_i')}. \tag{22}$$

To complete the above formulas it is necessary to know

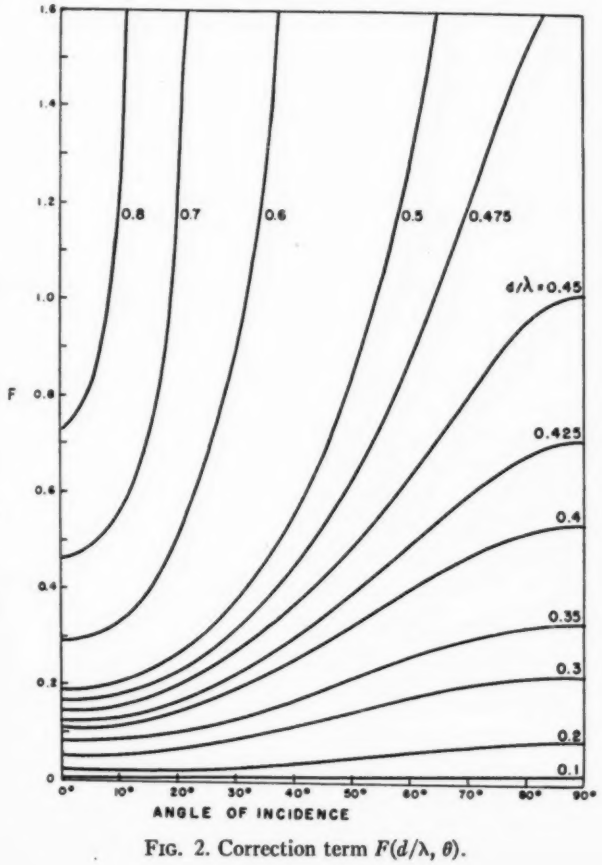

FIG. 2. Correction term $F(d/\lambda, \theta)$.

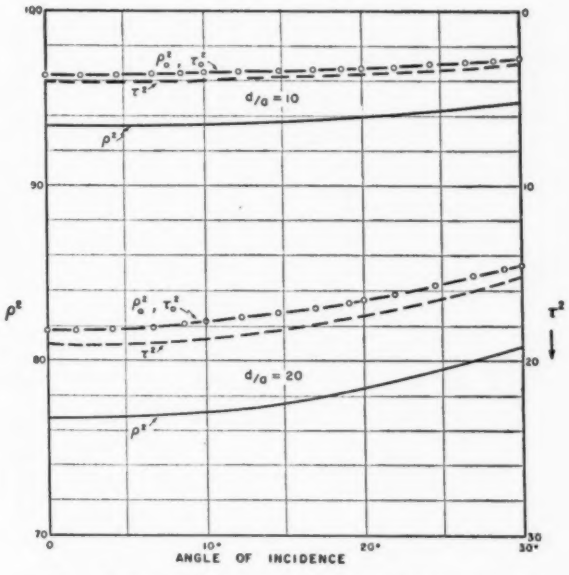

FIG. 3. Transmission, reflection, and loss properties of a wire grating.

the dimensionless quantity[13]

$$X_p'=-\frac{2\pi d\cos\alpha}{\lambda}\Big[\sum_{n=1}^{\infty}\cos(nkd\sin\alpha)N_0(nkd)+(1/\pi)\ln(0.890ka)\Big], \tag{23}$$

where $k=2\pi/\lambda$, and N_0 is the zero-order Bessel function of the second kind. For the range of parameters of interest here ($\lambda>2d$; $d\gg a$). Equation (23) can be written[14]

$$X_p'=\frac{2d\cos\alpha}{\lambda}\left[\ln\frac{d}{2\pi a}+F\right], \tag{24}$$

where

$$F=\tfrac{1}{2}\sum_{n=1}^{\infty}\left(\frac{1}{[(n+(d/\lambda)\sin\alpha)^2-d^2/\lambda^2]^{\frac{1}{2}}}+\frac{1}{[(n-(d/\lambda)\sin\alpha)^2-d^2/\lambda^2]^{\frac{1}{2}}}-\frac{2}{n}\right). \tag{25}$$

Honerjäger[15] has given curves of X_p' *versus* angle of incidence for certain values of the parameters, while a plot of the quantity F has been published by MacFarlane[16] and is reproduced for convenience in Fig. 2. In Fig. 3, the quantities ρ^2 and τ^2 which are the *intensity* coefficients for reflection and transmission are plotted against angle of incidence for the two cases $d/a=10$ and $d/a=20$, when $d/\lambda=0.2$ and $\sigma=0.1\times10^7$ mhos/

[13] Reference 2, Eqs. (11), (15), (18), (21), and (26). For the case $\alpha=0$ this expression reduces to Eq. (67) of Wessel (reference 3). Wessel gives a table for $\sum_1^{\infty}N_0(nX)$.

[14] Infeld, Smith, and Chien, J. Math. Phys. **26**, 22 (1947).
[15] Reference 2, Fig. 7.
[16] Reference 4, Fig. 6.

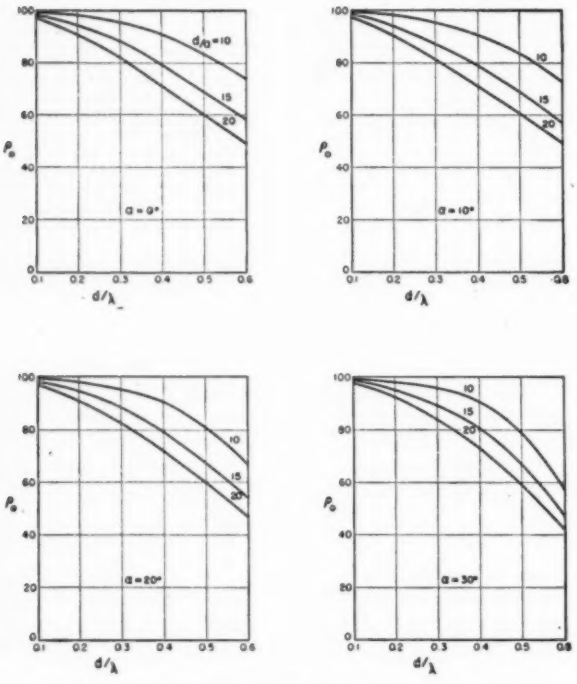

FIG. 4. Reflection coefficient of wire gratings.

meter (Nichrome). Curves are also given for perfectly conducting wires, denoted by the subscript zero.

Figure 4 includes a wider range of parameters but applies only to the lossless case. However, from these curves it is possible to estimate the increments $\Delta\rho$, $\Delta\theta$, $\Delta\tau$, and $\Delta\phi$ which occur when the wires become only slightly resistive. In this case $R_i' \ll 1$ and $X_i' \ll 1$ so that Eqs. (16) to (22) can be approximated with reasonable accuracy. Thus:

$$\Delta\rho \simeq -\rho_0^2 R_i' \left[\rho_0 + \frac{X_i'}{R_i'}(1-\rho_0^2)^{\frac{1}{2}}\right] \tag{26}$$

$$\Delta\theta \simeq \frac{\Delta\rho + \rho_0 R_i'}{1-\rho_0^2} = -\rho_0 R_i' \left[\frac{X_i'}{R_i'}\rho_0 - (1-\rho_0^2)^{\frac{1}{2}}\right] \tag{27}$$

$$\Delta\tau \simeq -\rho_0 \Delta\theta \simeq \rho_0^2 R_i' \left[\frac{X_i}{R_i'}\rho_0 - (1-\rho_0^2)^{\frac{1}{2}}\right] \tag{28}$$

TABLE I.

	Approximated formulas	Original formulas
$\Delta\rho$	-0.030	-0.0287
$\Delta\theta$	$-5.90°$	$-5.79°$
$\Delta\tau$	0.0093	0.0098
$\Delta\phi$	$-3.9°$	$-3.78°$

$$\Delta\phi \simeq \frac{\Delta\rho}{(1-\rho_0^2)^{\frac{1}{2}}} \simeq -\rho_0^2 R_i' \left[\frac{X_i'}{R_i'} + \frac{\rho_0}{(1-\rho_0^2)^{\frac{1}{2}}}\right] \tag{29}$$

$$l \approx 2\rho_0^2 R_i'. \tag{30}$$

Referring to Fig. 1, (X_i'/R_i') is a positive quantity (for high frequencies and good conductors $(X_i'/R_i') \approx 1$), $\Delta\rho$ and $\Delta\phi$ are always negative, whereas the signs of $\Delta\theta$ and $\Delta\tau$ depend on the magnitude of ρ_0.

NUMERICAL EXAMPLE

For $d/a=20$, $d/\lambda=0.2$, and normal incidence, the value $\rho_0=0.9046$ can be read approximately from Fig. 4. It follows from Eq. (18) that $X_p'=0.4712$. Suppose now the wavelength, λ, is 500 microns or 5×10^{-4} meter, whence it follows that $a(=d/20=0.2\lambda/20)=5\times10^{-6}$ meter, and $a^2=2.5\times10^{-11}$ meter.[2] If the wires are made of Nichrome, which is a rather poorly conducting metal $(\sigma=0.1\times10^7)$ it will be found from Fig. 1 that for an abscissa of $a/(\lambda)^{\frac{1}{2}}=5\times10^{-6}/(5)^{\frac{1}{2}}\times10^{-2}=2.24\times10^{-4}$, $a^2R_i \approx 13.1\times10^{-7}$ and $a^2X_i \approx 12.2\times10^{-7}$. As defined in connection with Eq. (13), $R_i'=(d/60\pi)R_i \approx 0.0278$ and similarly $X_i' \simeq 0.0259$. The changes in ρ, etc., due to the wire resistance may be calculated from the approximate formulas, Eqs. (26) to (30), or by working from the original expressions of Eqs. (16) to (22) (see Table I). For the metals which would ordinarily be used for such gratings, the effects would of course be much smaller than these.

ACKNOWLEDGMENT

The authors wish to thank Dr. MacFarlane for permission to use his curves of the function F. In addition we are indebted to Professor Eric Reissner of Massachusetts Institute of Technology for calling to our attention reference 14. We also wish to express our appreciation to Mrs. Virginia Gerdes for numerical computations in connection with this work.

JOURNAL OF APPLIED PHYSICS VOLUME 23, NUMBER 6 JUNE, 1952

Electron Microscope Study of Plasticized Latices*

E. B. BRADFORD
Physical Research Laboratory, The Dow Chemical Company, Midland, Michigan
(Received November 28, 1951)

Silicon monoxide replicas of the surfaces of air-dried films are shown which were cast from a Saran latex containing various amounts of plasticizer. It can be observed that the poor films are composed of discrete individual particles while in a continuous transparent film the particles have coalesced into a polymeric mass. Replicas of surfaces of films are shown which were produced from different types of synthetic latices before and after they had been plasticized.

INTRODUCTION

THE recent increase in the use of synthetic latices in the textile, paper, and paint industries has promoted extensive investigation of the complex problem of latex formulation. In many industrial applications of these latices it is necessary for the polymer particles to readily coalesce into a continuous and durable film. It is therefore desirable to know how these particles aggregate during the process of forming a film. In order to produce such a film, many latices must be modified by adding a plasticizer of one type or another. The purpose of this paper is to picture, by use of a replica technique, the individual particles as they actually appear in the surface of films cast from latices before and after they have been plasticized.

EXPERIMENTAL TECHNIQUE

In order to make replicas of surfaces of poor films cast from synthetic latices it was first necessary to form films which would withstand handling. It was found that by pouring a thin layer of the latex into a crystallizing dish and allowing the water to evaporate, a suitable film was obtained which was two to three mm in thickness. This relatively thick film was very brittle but could be handled with care. A section of the film was placed in an evaporating unit and, after an operating vacuum of at least 10^{-4} mm of mercury was obtained, a thin film of silicon monoxide was evaporated normally onto the surface of the film. After removing the specimen from the evaporating unit, the surface of the film was lightly scored into approximately $\frac{1}{8}$-inch squares. The specimen was then placed in a solvent which dissolved the polymer film leaving the silicon monoxide replicas. These replicas were then transferred to a clean bath of the solvent for rinsing before they were caught on a 200-mesh standard electron microscope specimen screen.

DISCUSSION

Many synthetic latices are not inherently film-forming and must be modified in order to produce useful films. One of the most convenient methods of obtaining a good film is to add a plasticizer to the latex so that a coherent and durable film is formed when the latex dries at room temperature. Since the plasticizers used vary widely in composition and consequently have somewhat different effects on the properties of the latex, the method of plasticizer addition must be varied in order to obtain the best latex compatibility and avoid coagulation. Sometimes a plasticizer can be easily stirred directly into the latex but often the plasticizer will separate from the latex to form an ineffective separate layer. Sometimes this stratifying can be avoided by adding the plasticizer in the form of a water emulsion to the latex. Another method of incorporating the plasticizer into the latex is known as "phase inversion." In this process the latex is slowly added to the plasticizer and thoroughly mixed forming a latex-in-oil emulsion; as more latex is added an inversion takes place and one obtains a plasticizer-in-latex emulsion which is very stable. Usually these plasticized latices must be aged to allow the plasticizer to diffuse into the individual polymer particles.

Saran Latices

A latex which is made by copolymerizing vinyl chloride and vinylidene chloride is a typical latex which will not produce a useful film without modification. Figure 1 is a picture of the individual particles of a Saran latex which has not been plasticized and which will not produce a continuous film when dried in air without heating. These particles were dispersed upon a collodion membrane from the diluted latex and then "shadowed"[1] with chromium. One can observe from the shape of the shadows that the particles are hard and spherical. In order to observe visually the type of film formed by these particles, a small amount of the concentrated latex was spread onto a microscope slide at room temperature and allowed to dry. This same procedure was followed after the latex had been modified by adding five, ten, and fifteen percent plasticizer (based on the polymer content of the latex).

In order to picture what happens to individual particles in such films as plasticizer is added to the latex, replicas of the films were made using the above-mentioned silicon monoxide one-step replica technique.

* Presented at the ninth meeting of the Electron Microscope Society of America in Philadelphia, Pennsylvania, November 8, 1951.

[1] R. C. Williams and R. W. G. Wyckoff, J. Appl. Phys. **17**, 23 (1946).

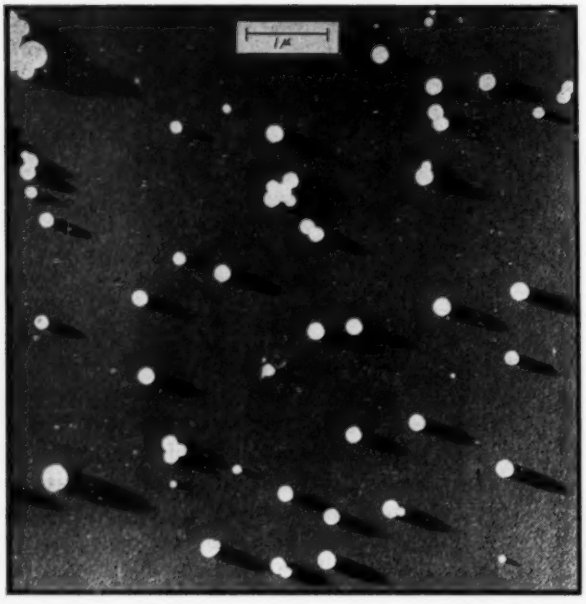

FIG. 1. Chromium shadowed particles from a Saran latex.

Figure 2 is a replica of the surface of a film cast from the latex shown in Fig. 1 to which no plasticizer had been added. This surface is composed of essentially discrete spherical particles which vary considerably in size. The dark spots are probably polymer particles or groups of particles that were not completely dissolved or washed from the replica film by the tetrahydrofuran which was used as the solvent. In Fig. 3 the effect of adding only 5 percent of plasticizer is plainly visible. In this replica the particles appear to have begun to coalesce, although some were not affected as much as others. There are some residual polymer particles visible in this replica also. A crack can be seen in this replica which extends under one of these particles. In Fig. 4 one sees the effect of 15 percent plasticizer. Practically all of the individual particles have now lost their identity, and only an uneven mass of polymer results which shows why this plasticized Saran latex produces a transparent and continuous film.

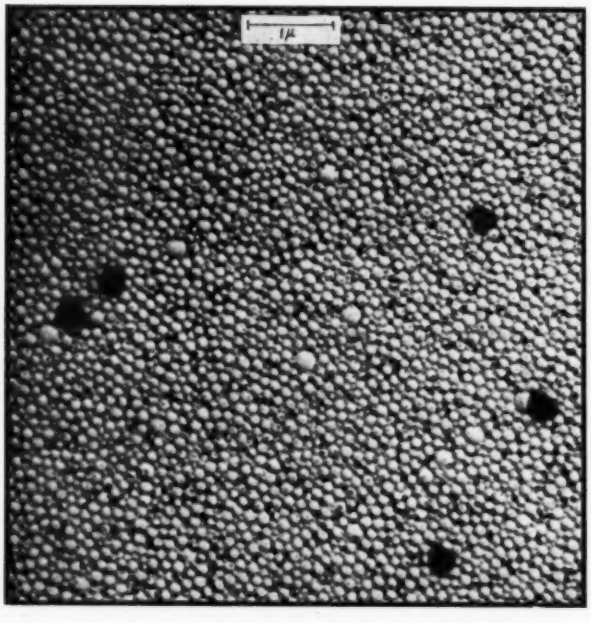

FIG. 2. SiO replica of a film cast from a Saran latex.

Polystyrene Latices

Figure 5 pictures the surface of an air-dried film cast from a production batch of polystyrene latex. Its surface is composed of spherical particles which are similar to the particles in the unplasticized Saran film. However, these particles appear a little larger and have a narrower distribution of particle sizes. There is no apparent order

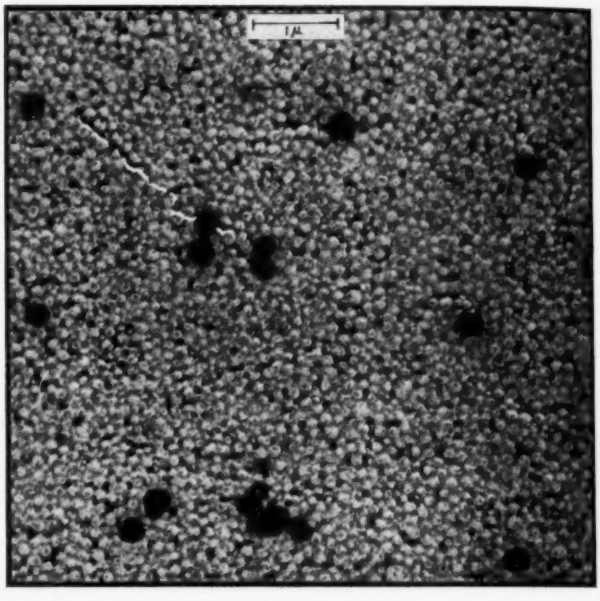

FIG. 3. SiO replica of a film cast from a Saran latex containing 5 percent plasticizer.

of packing of the spheres in this surface. Some of this same batch of polystyrene was then plasticized with a plasticizer that had a tendency (at least in the quantities used here) to separate from the dried film. After adding the plasticizer, the latex was agitated thoroughly and allowed to age four days before a film was cast. This air dried film was soft, tacky, and opaque. A replica of the surface of this film is shown in Fig. 6 which is at the same magnification as Fig. 5. A pattern of light and dark areas is evident here. In the lighter areas the particles are closely packed, while in the darker areas the particles are more widely separated as a result of localized concentrations of plasticizer. The dark regions in the photograph are apparently caused by the plasticizer adhering to the replica from these localized areas. In the lighter areas, one can also observe that the

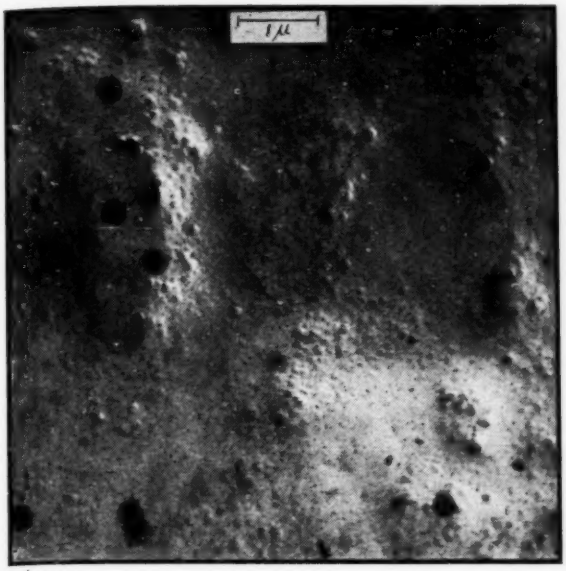

FIG. 4. SiO replica of a film cast from a Saran latex containing 15 percent plasticizer.

particles appear to form a more ordered arrangement than in the darker areas. This regularity of packing was absent in films made from this latex before it was plasticized. Possibly this plasticizer acted as a lubricant which allowed some of the particles to achieve an ordered arrangement more readily. The lack of complete absorption of the plasticizer by the latex particles in this film may be caused by poor compatability between the latex and plasticizer or by an extremely slow diffusion rate of the plasticizer into the particles so that the four-day aging period was not adequate for this plasticizer.

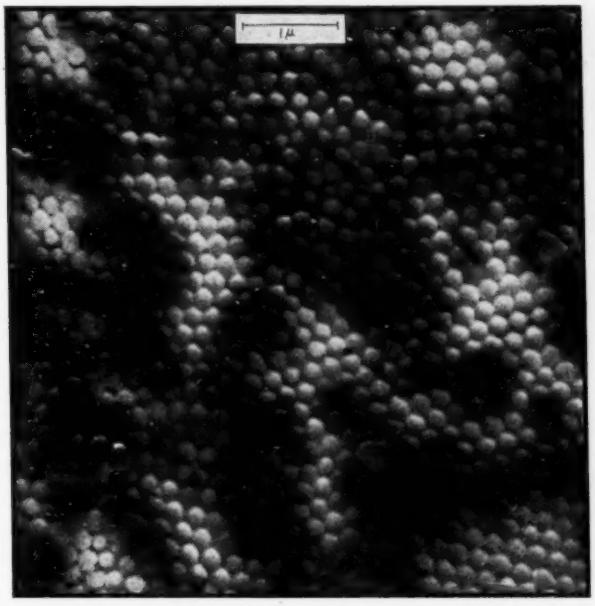

FIG. 6. SiO replica of a film cast from a plasticized polystyrene latex.

Polyvinyltoluene Latices

The properties of a polyvinyltoluene latex are very similar to those of a polystyrene latex. A replica of the surface of an air-dried polyvinyltoluene latex is shown in Fig. 7. The cast film from this latex was powdery and opaque, having very little strength because it was composed of hard uniform spheres, packed in a regular geometric lattice, which show no tendency to coalesce. The remarkable regularity of the particle array in the surface of the film is also indicated by the fact that the film and the replica exhibit diffraction colors when white

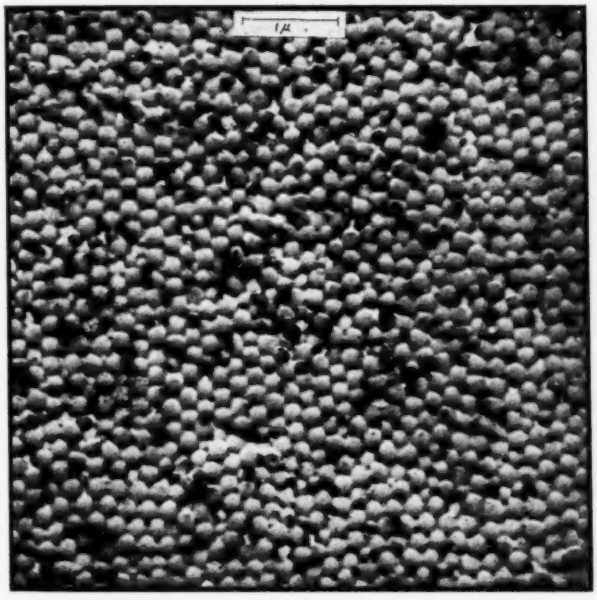

FIG. 5. SiO replica of a film cast from a polystyrene latex.

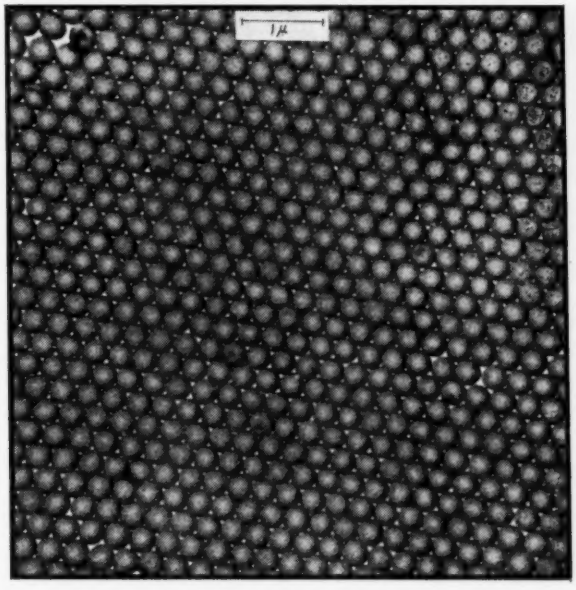

FIG. 7. SiO replica of a film cast from a polyvinyltoluene latex.

FIG. 8. Types of packing found in a film cast from a polyvinyltoluene latex.

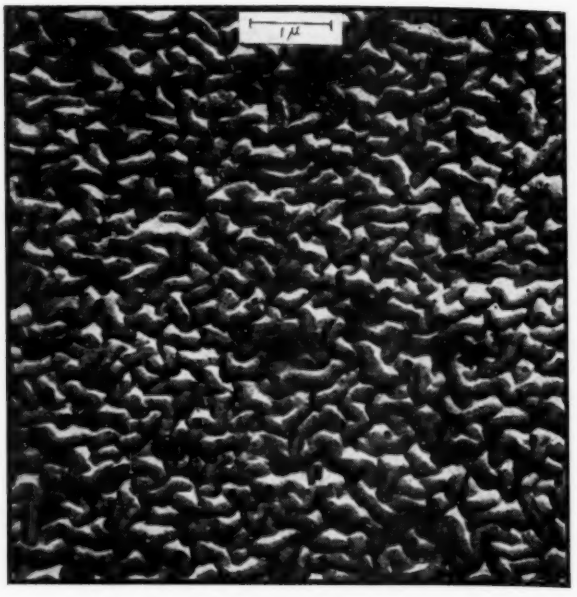

FIG. 9. SiO replica of a film cast from a preplasticized polyvinyltoluene latex.

light is reflected from their surfaces. This replica shows hexagonal close packing of uniform spheres. Figure 8 is a replica of the same polyvinyltoluene latex film taken at a lower magnification. In addition to regions of hexagonal close packing, one can observe a region of cubical packing. The small dark spots again appear to be polymer that was not rinsed from the replica. The structure of the surface of a film cast from a preplasticized polyvinyltoluene latex is shown in Fig. 9. This replica appears drastically different from those prepared from the unplasticized latex. It is rather difficult to interpret the surface structure of this film. It appears to be composed of long irregularly-shaped particles which are randomly intertwined. These may correspond to the individual particles which existed in the latex or may be aggregates of fused individual particles. Such a surface structure may also be formed by the soft latex particles fusing into a continuous mass followed by a drying process in which a flexible surface skin is first formed. The underlying material then dries and contracts, causing a severe wrinkling of the surface.

SUMMARY

It is possible to prepare silicon monoxide replicas of films cast from synthetic latices for study in the electron microscope. Replicas of surfaces of air-dried films cast from Saran latices containing up to 15 percent plasticizer (based on the polymer content in the latex) show the individual particles as they sinter into a continuous and durable film. Replicas of the surfaces of films cast from Saran, polystyrene, and polyvinyltoluene latices show the effect produced on the individual particles when plasticizer is added to the latex.

ACKNOWLEDGMENT

The author wishes to express his appreciation to R. D. Andrews, Jr., R. E. Dillon, and C. H. Gerould for their suggestions and criticisms of this work.

JOURNAL OF APPLIED PHYSICS VOLUME 23, NUMBER 6 JUNE, 1952

The Radiation Resistance of Resonant Transmission Lines

R. A. CHIPMAN, E. F. CARR,* N. A. HOY,* AND M. YURKO†
Electrical Engineering Department, McGill University, Montreal, Canada
(Received December 31, 1951)

For resonant sections of a transmission line consisting of parallel silver rods extending vertically above a metal ground plane, the resonance curves of input admittance as a function of line length have been drawn by a synchronized recording meter apparatus, and the effective total resistance of each resonant line calculated. This has been done for frequencies between 300 Mcps and 1400 Mcps, for resonant line lengths up to several wavelengths, for line sections with both open-circuit and short-circuit termination at the top, and in each case with and without a large metal pipe shielding the test line. Radiation resistance is obtained as the difference between the resistance calculations for any one resonant line section unshielded and shielded.

With a probable error of about 5 percent the radiation resistance is found to be proportional to the square of the frequency, and to be independent of line length and of whether the top termination is an open circuit or a short circuit. The absolute values agree reasonably well with the theory of Storer and King [Proc. Inst. Radio Engrs. **39**, 1408 (1951)] and disagree conclusively with some predictions of earlier theories.

1. INTRODUCTION

ALTHOUGH the question of the radiation losses from parallel wire and coaxial transmission lines has been a matter of controversy for fifty years, there seem to have been no attempts to test the matter experimentally.

This paper describes measurements of these losses for resonant sections of unshielded parallel wire line with both open-circuit and short-circuit terminations. The measurements show that the radiation resistance of such line sections is independent of the line length and of the nature of the terminations and is given approximately by $120\pi^2(d/\lambda)^2$ ohms, where d is the separation of the conductor centers and λ is the wavelength. It follows that the radiation losses can greatly affect the properties of resonant sections of parallel wire line at frequencies for which the conductor separation exceeds a very small fraction of a wavelength.

2. THEORIES OF RADIATION FROM TRANSMISSION LINES

The "telegraph equation" analysis of transmission lines, begun by Kelvin[1] and completed by Heaviside,[2] is based on assumptions which make it intrinsically incapable of revealing radiation phenomena. The application of electromagnetic theory to transmission line analysis, first carried out by J. J. Thomson for coaxial lines,[3] was extended to parallel wire lines by Mie,[4] who in 1900 concluded that "for an endless line, of which both wires are sufficiently uniformly cylindrical and parallel, regardless of frequency or wire separation there is not the slightest radiation to the surrounding space." Hertz[5] considered the matter, but interpreted his experimental observations in terms of the "surface waves" recently described by Goubau,[6] so that his conclusions are not relevant to the normal mode of transmission.

Mie's conclusion was upheld by Macdonald[7] in 1902. In 1909, however, and again in 1919, Steinmetz[8,9] published an analysis predicting a uniformly distributed radiation resistance for parallel wire lines. This was attacked by Carson[10] who, agreeing with Mie and Macdonald for the case of infinite lines, suggested that the discontinuities at the terminations of a line of finite length would result in radiation. For a section of parallel wire transmission line of conductor separation d and length L, terminated nonreflectively at each end, he derived an expression for the radiation resistance R_{rad} at wavelength λ:

$$R_{\text{rad}}=240\pi^2(d/\lambda)^2\{1-[\sin(4\pi L/\lambda)/4\pi L/\lambda]\} \text{ ohms.}$$

This does not include the radiation resistance of $80\pi^2(d/\lambda)^2$ of each of the terminations radiating as a current filament.[11] In a second paper Carson[12] analyzed transmission line radiation in terms of "complementary waves," the *TE* and *TM* waves of today.

Manneback[13] derived in 1923 an expression for the radiation resistance of a *resonant* section of parallel wire line, with open-circuit termination at each end,

* Now at General Electric Company, Syracuse, New York.
† Now at Department of National Defence, Ottawa, Canada.
[1] Lord Kelvin, *Mathematical and Physical Papers of Sir William Thomson* (Cambridge University Press, Cambridge, 1884), Vol. II, p. 61.
[2] Oliver Heaviside, *Electrical Papers* (Macmillan and Company, Ltd., London, 1892), pp. 119 and 309.
[3] J. J. Thomson, *Recent Researches in Electricity and Magnetism* (Oxford University Press, Oxford, 1893), p. 263.
[4] G. Mie, Ann. Physik IV, **2**, 201 (1900).
[5] H. Hertz, *Electric Waves* (Macmillan and Company, Ltd., London, 1893), p. 155.
[6] G. Goubau, Radio and Television News, Radio-Electronic Engineering Supplement **14**, 10 (1950).
[7] H. M. Macdonald, *Electric Waves* (Cambridge University Press, Cambridge, 1902), p. 106.
[8] C. P. Steinmetz, *Transient Electrical Phenomena and Oscillations* (McGraw-Hill Book Company, Inc., New York, 1909), p. 350.
[9] C. P. Steinmetz, Trans. Am. Inst. Elec. Engrs. **38**, 191 (1919).
[10] J. R. Carson, J. Am. Inst. Elec. Engrs. **40**, 789 (1921).
[11] M. Abraham and R. Becker, *The Classical Theory of Electricity and Magnetism* (D. Van Nostrand Company, Inc., New York, 1932), p. 228.
[12] J. R. Carson, J. Am. Inst. Elec. Engrs. **43**, 908 (1924).
[13] C. Manneback, Trans. Am. Inst. Elec. Engrs. **42**, 289 (1923).

TABLE I. Theoretical values for the radiation resistance of transmission-line sections. All figures shown are to be multiplied by $\pi^2(d/\lambda)^2$ to give radiation resistance in ohms.

Author and reference		Date	Line sections terminated nonreflectively at each end	Line sections terminated in open circuit at each end	Line sections terminated in short circuit at each end
Carson	(10)	1921	240[a,b]		
Manneback	(13)	1923		120	
Pistolkors	(14)	1929		120	
Carter	(17)	1932		120	
Sterba and Feldman	(18)	1932	160[b]	120	40[b]
Whitmer	(19)	1933		120	
Reukema	(20)	1937	160[a,b]	120[a]	40[a,b]
Storer and King	(24)	1951	240[a,c]	120[a]	120[a,c]

[a] For long lines or lines an integral number of half-wavelengths long. For lines less than a few wavelengths long, or reactively terminated resonant lines, the figures are modified somewhat by a term which is a function of line length.
[b] The figures do not include a contribution of 80 for each termination radiating as a current filament.
[c] The analytical method includes the terminations, and their radiation resistance is not additive as a separate component.

obtaining

$$R_{\text{rad}} = 120\pi^2(d/\lambda)^2 \text{ ohms}$$

subject to the inequality $(d/\lambda) \ll 1$.

Pistolkors,[14] using a method due to Brillouin,[15] has calculated the radiation resistance of various systems of parallel antennas. Two parallel, nonstaggered, half-wavelength dipole antennas separated by much less than a wavelength and carrying equal currents 180° out of phase are identical with the resonant transmission-line section considered by Manneback, and Pistolkors' theory gives the same result for this case. Bechmann[16] has shown that the two methods are equivalent.

Carter,[17] Sterba and Feldman,[18] and Whitmer[19] have made analyses which for the same case all lead to the same result obtained by Manneback. The theory of Sterba and Feldman, and another analysis by Reukema,[20] are more general than the rest and give values for the radiation resistance of line sections having open-circuit, short-circuit, or nonreflective terminations at each end. Brown and King[21] have made a distinctly different analysis of the case considered by Manneback, using a method due to Labus.[22] However, graphical computations were required,[23] and the accuracy of the published graphs for small values of (d/λ) does not permit useful comparison with the results of other theories. A recent analysis by Storer and King,[24] which corrects some earlier work by King,[25] finds the total radiation resistance of a resonant section of parallel wire line to be the same for a section with two open-circuit terminations as for a section with two short-circuit terminations.

The numerical results given by all the above theories are presented in Table I for comparison.

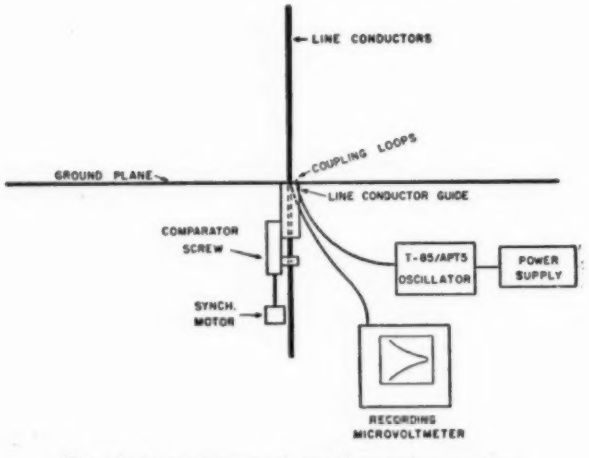

FIG. 1. Arrangement of experimental apparatus.

3. EXPERIMENTAL PROCEDURE

The experimental method used in the present work is illustrated by Fig. 1. The conductors of the parallel wire test line (0.100-in. diameter sterling silver rods with center spacing 1.00 in.) pass vertically through the center of a horizontal "ground plane" of 0.120-in. aluminum sheet, 6 feet by 8 feet. This plane is made of two sheets, the conductors of the test line passing through the plane on the line of contact of the sheets.

Radiofrequency power at frequencies between 300 Mcps and 1500 Mcps is obtained from a T85/APT-5 oscillator modified to give unmodulated output, and is fed to a small coupling loop at the base of the test line through several db of RG-21/U attenuating cable. The response of the test line, a measure of its input admittance, is detected by means of a uhf thermocouple, whose heater is connected to a second small coupling loop at the base of the line.

The output of the thermocouple (whose couple is insulated from its heater) is measured by a Leeds and Northrup Speedomax type G recording meter of unusual sensitivity (200 microvolts full scale), response time (1 second) and chart speed (up to 20 inches per minute).

With the oscillator supplying a signal of constant frequency and amplitude, the length of the line conductors above the plane is varied through resonance by means of a precision comparator screw, to the carriage of which the conductors are clamped below the plane. The screw is driven, via a reducing gear, by a synchronous motor. Since the chart of the recording meter is also driven by a synchronous motor, the final result

[14] A. A. Pistolkors, Proc. Inst. Radio Engrs. **17**, 562 (1929).
[15] L. Brillouin, Radio Electricite Sommaire, p. 147 (April, 1922).
[16] R. Bechmann, Proc. Inst. Radio Engrs. **19**, 1471 (1931).
[17] P. S. Carter, Proc. Inst. Radio Engrs. **20**, 1004 (1932).
[18] E. J. Sterba and C. B. Feldman, Proc. Inst. Radio Engrs. **20**, 1163 (1932).
[19] R. Whitmer, Proc. Inst. Radio Engrs. **21**, 1343 (1933).
[20] L. E. Reukema, Trans. Inst. Elec. Engrs. **56**, 1002 (1937).
[21] G. H. Brown and R. King, Proc. Inst. Radio Engrs. **22**, 457 (1934).
[22] J. Labus, Hochfrequ. und Elektroak. **41**, 17 (1933).
[23] G. H. Brown, Proc. Inst. Radio Engrs. **25**, 78 (1937).
[24] J. E. Storer and R. King, Proc. Inst. Radio Engrs. **39**, 1408 (1951).
[25] R. W. P. King, *Electromagnetic Theory* (McGraw-Hill Book Company, Inc., New York, 1945), Vol. I, p. 483.

is that the meter draws the resonance curve of input admittance of the line as the line length varies.

A chart speed of 2 inches per minute was used throughout the work. Two rates of line length variation were used at different times, 0.200 millimeter per minute and 1.072 millimeters per minute. One inch of chart therefore corresponded to 0.100 millimeter and 0.536 millimeter of line length variation, respectively, in the two cases. The time required to draw the resonance curves varied from about one-half minute to fifteen minutes. A sample curve is shown in Fig. 2.

The radiation resistance of the test line has been obtained by observing such resonance curves with and without a metal pipe shield surrounding the line. Brass tube of 4-in. i.d. and aluminum tube of $4\frac{1}{2}$-in. i.d. have been used as shields at different times.

Numerous checks and precautions have been required in the experimental work to insure that the interpretation of the final results is a correct one.

The constancy of the amplitude and frequency of the oscillator output, and the absence of frequency modulation are essential to the success of the method. A resonance curve having a Q of 2000 at a frequency of 500 Mcps, for example, will not be satisfactorily drawn unless the amplitude of the oscillator remains constant within less than 1 percent and the frequency drift or modulation does not exceed one or two kilocycles during the time required to draw the curve. Recording the response of the system both at and off resonance for several minutes at constant line length, and checking the nature of the signal and constancy of the frequency with a General Radio type 720-A heterodyne frequency meter, showed these requirements to be adequately met. The requirements were much less stringent than those stated (by a factor of 50 in some cases) for most of the experimental situations studied.

The coupling loops for the oscillator and detector at the base of the test line must be arranged so that there is negligible direct coupling between them, and so that they neither excite nor respond to the "antenna mode" of propagation on the line conductors, i.e., the mode for which the currents in the two conductors flow in the same direction. Several different positions of the loops have been used, with no detectable difference in results. The arrangement of Fig. 3 was used in a large part of the work. The slight vertical displacement of the two loops eliminates all evidence of direct coupling between them. When the input loop is parallel to the plane of the line conductors, it has minimum coupling to this "antenna mode" and maximum coupling to the "transmission line mode" for which the currents in the two line conductors flow in opposite directions. The output loop, located centrally between the line conductors with its plane parallel to the plane of the line conductors, has theoretically zero coupling to the "antenna mode" and the maximum possible coupling to the "transmission-line mode."

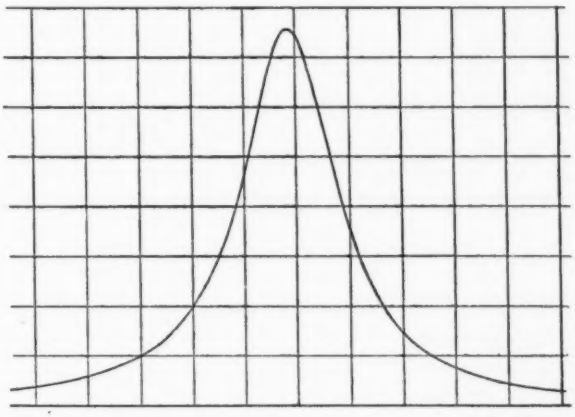

FIG. 2. Tracing of a typical resonance curve drawn with the apparatus of Fig. 1. This curve was obtained at a frequency of 600 Mcps, with a shielded line of resonant length $3\lambda/4$. The measured width of the curve at the half-power points is 0.21$_4$ mm, indicating a Q-value of 1730. One inch of chart corresponds to 0.1-mm change of line length, and the chart speed was 2 inches per minute.

It is clear from measurements on cylindrical antennas[26] that the resonant input admittance of the "antenna mode" for the conductors used will never be as great as 10 percent of the actual measured admittances in the present work, and for most cases will be less than 1 percent. For the coupling-loop positions used, the response of the system to the "antenna mode" for one of the line conductors alone should be far greater than the response to this mode for the two conductors together. Attempts to observe this response for a single conductor have shown that in typical cases it is 20 db to 30 db below the response to the "transmission line mode" for the two conductors, at the same frequency and resonant line length.

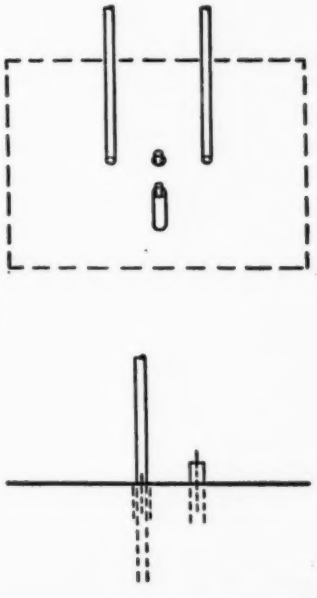

FIG. 3. Oblique view and side view of coupling loops at base of test line. One of several arrangements used, with identical results.

[26] G. H. Brown and O. M. Woodward, Proc. Inst. Radio Engrs. 33, 257 (1945).

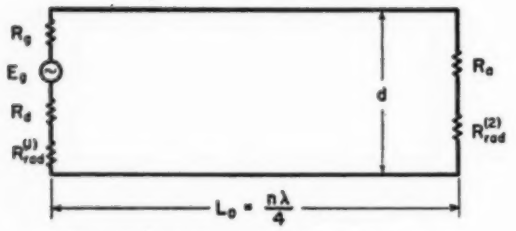

FIG. 4. Equivalent circuit of the test line.

It is concluded that any residue of coupling to the "antenna mode" affects the final calculated values of radiation resistance for the two-wire line by much less than 1 percent.

It is shown in the analysis below that the width of the experimental resonance curves at the half-power points is, with sufficient accuracy, a linear function of the radiation resistance of the line, the total resistance of the line conductors, and an equivalent terminal resistance, which represents losses coupled to the line by the input and output coupling loops, as well as the actual resistance of the terminations.

It is a necessary postulate in the radiation resistance calculations that this equivalent terminal resistance has the same value with and without the shield tube surrounding the line conductors. There is no satisfactory way of testing this assumption directly. Calculation shows that the actual resistances of the terminations are negligible compared with the observed values of equivalent terminal resistance, which must therefore represent losses coupled in by the coupling loops. The facts that the coupling loops are small (1 to 2 millimeters diameter), that they are considerably closer to the line conductors than to the shield, and that the losses they introduce are presumably due to losses in the cables to which they are connected, all suggest that the presence of the shield should not influence the equivalent coupling-loss resistance appreciably. The validity of the assumption is strengthened by the observation that even if this equivalent resistance is considerably increased by enlarging the coupling loops, the measured net value of radiation resistance for a given test line and frequency is not affected.

Some work to be published later shows that the Q of the unshielded line can be increased to within a few percent of the value for the shielded line by terminating the test line at the upper end in a horizontal plane of suitable size. This modification would obviously not affect the equivalent coupling-loss resistance, and it may be inferred from the result that this resistance is not appreciably changed by the presence of the shield tube.

The coupling-loss resistances measured for shielded line-sections amount to between 5 percent and 25 percent of the total effective resistance values calculated for the same line sections unshielded, and are less than 15 percent in most cases. Thus even if the value of this resistance should change by a few percent when the shield is added or removed, the effect on the calculated values of radiation resistance would be very small.

Other random deviations in the radiation resistance measurements are introduced by mechanical imperfections in the apparatus. The small conductor diameter, for example, makes it difficult to keep the conductors accurately straight, parallel, and perpendicular to the ground plane, particularly for line sections with open-circuit termination at the top. There may be some slight effects in certain frequency ranges caused by the finite size of the ground plane, and the finite distance to metal objects in the surroundings, which, however, was never less than several wavelengths even at the lowest frequencies used. The general consistency of the results suggests that these effects are not great.

Taking all of these effects into account, it is considered that the probable error of all the radiation resistance measurements made does not exceed 5 percent ± 0.05 ohm.

4. ANALYTICAL METHOD

The present project had its origin in some earlier work by one of us,[27] where an inference of radiation losses was made in connection with some impedance measurements involving an open wire line at 377 Mcps. The analytical method of that work could be applied to the present case, but the following modification of it is more convenient.

The equivalent circuit of the apparatus of Fig. 1 may be given as in Fig. 4. A generator of no-load voltage E_g and low internal resistance R_g in series with a detector of low internal resistance R_d and an equivalent radiation resistance $R_{rad}{}^{(1)}$ make up one termination of the test section of transmission line. The other termination may include some loss resistance R_a and may also include a radiation resistance component $R_{rad}{}^{(2)}$. The transmission line section is of some resonant length $n\lambda/4$, where n may be any integer. When n is odd, R_a and $R_{rad}{}^{(2)}$ are not required. The line conductors have total distributed resistance R_c ohms per meter. Dielectric losses are considered negligible.

It will be true in general that the impedances of the generator, detector, and second termination of the line will contain small reactance components. These have been ignored for two reasons. First, they are very small, as indicated by the fact that the measured resonant line lengths are always very close to $n\lambda/4$. Second, it is easily shown that the effect of terminal reactances on the measured resonance curves and calculated resistances is negligible even for reactances up to 20 percent of the characteristic impedance of the line, provided the sum of all the effective terminal resistances does not exceed a few percent of the characteristic impedance of the line, which is true for the present measurements.

[27] R. A. Chipman, J. Appl. Phys. **10**, 27 (1939).

The current through the detector for the equivalent circuit of Fig. 4 is given by

$$I_d = E_g/(R_{\text{rad}}{}^{(1)} + R_g + R_d + R_{\text{inp}}),$$

where R_{inp} is the input impedance of the line section of length L terminated in $(R_a + R_{\text{rad}}{}^{(2)})$. When the sum of all the resistances involved is small compared to the characteristic impedance of the line, I_d as a function of L will have sharp maxima at the resonant values of L given by $L = n\lambda/4$, the odd values of n corresponding to an open circuit for the second termination of the line, the even values corresponding to a short-circuit termination.

The approximate transmission line analysis that is valid under these conditions shows that the width ΔL_1 of any of these resonance curves of I_d between the half-power points ($I_d = 0.707 I_{d\max}$) is given by

$$\Delta L_1 = (2/\beta Z_0)\{\tfrac{1}{2}L_0 \cdot R_c + R_{\text{rad}}{}^{(1)} + R_{\text{rad}}{}^{(2)} + R_g + R_d + R_a\},$$

where L_0 is one of the resonant line lengths and β is the phase propagation constant of the line.

$L_0 \cdot R_c$ is the total resistance of the conductors for any actual resonant line. It is only half as effective as the same amount of resistance at a termination because of the approximately sinusoidal distribution of current on the conductors. All the other resistance terms are located at or referred to positions of maximum current in the line.

This equation may conveniently be rewritten

$$\Delta L_1 = (2/\beta Z_0)\{\tfrac{1}{2}L_0 \cdot R_c + R_{\text{rad}} + R_t\}, \qquad (1)$$

where $R_{\text{rad}} = R_{\text{rad}}{}^{(1)} + R_{\text{rad}}{}^{(2)}$ is now the total radiation resistance of the line, and $R_t = R_g + R_d + R_a$ is the total resistance accounting for all losses other than those due to radiation and conductor resistance.

If now a shield is put around the line conductors, all radiation is stopped. In general the total conductor resistance for the resulting shielded-pair line will be slightly different from the value R_c and the characteristic impedance will also change somewhat. Let the new values of these quantities be R_{cs} and Z_{0s}, respectively. The values of β and L_0 will not be affected appreciably, and it has been assumed that R_t does not change.

The width at the half-power points of any resonance curve for the shielded line will then be ΔL_2, given by

$$\Delta L_2 = (2/\beta Z_{0s})\{\tfrac{1}{2}L_0 \cdot R_{cs} + R_t\}. \qquad (2)$$

Solving Eqs. (1) and (2) for R_{rad} by eliminating R_t, gives

$$R_{\text{rad}} = \tfrac{1}{2}\beta Z_0 \cdot \Delta L_1 - \tfrac{1}{2}\beta Z_{0s} \cdot \Delta L_2 - \tfrac{1}{2}L_0(R_c - R_{cs}). \qquad (3)$$

It is shown below that R_c and R_{cs} differ by 1 percent or less for the lines used in the present measurements, so the final term in Eq. (3) may be dropped, giving

$$R_{\text{rad}} = \tfrac{1}{2}\beta Z_0 \cdot \Delta L_1 - \tfrac{1}{2}\beta Z_{0s} \cdot \Delta L_2. \qquad (4)$$

TABLE II. Constants of the test lines used in the experiments. Reference: S. Ramo and J. R. Whinnery, *Fields and Waves in Modern Radio* (John Wiley & Sons, Inc., New York, 1944), p. 332.

	(1) Two-wire line, sterling silver conductors 0.100-in. diam, center spacing 1.000-in.	(2) Two-wire line with coaxial brass shield 4-in. i.d.	(3) Two-wire line with coaxial aluminum shield, 4½-in. i.d.
Distributed resistance at frequency f_{Mcps} in ohms per meter	$0.0641(f_{\text{Mcps}})^{\frac{1}{2}}$	$0.0648(f_{\text{Mcps}})^{\frac{1}{2}}$	$0.0643(f_{\text{Mcps}})^{\frac{1}{2}}$
Characteristic impedance in ohms	359	344	347

The Q-value for any of the resonance curves will be given by $Q = L_0/\Delta L$. It is readily shown that if $R_{\text{rad}} = R_t = 0$, Eqs. (1) and (2) lead to the well-known expression $Q = \beta/2\alpha$. If, at a given frequency, the radiation resistance is independent of line length, the Q will increase asymptotically to the value $\beta/2\alpha$ as the line length is increased.

5. MEASUREMENTS AND CALCULATIONS

The dimensions and constants of the shielded and unshielded lines used are shown in Table II. Of the two shielded cases shown, the 4-in. i.d. brass pipe was used with all transmission line sections short-circuited at the upper end, while the 4½-in. i.d. aluminum pipe was used with all line sections open-circuited at the top. It should be noted that a true short-circuited shielded-pair line is not obtained by simply putting a shield around an open-wire line shorted by a linear conductor. It is necessary to use a shorting disk that terminates the line conductors and makes contact around its edges with the shielding pipe. Experimentally the addition of such a disk was found to make a significant difference in the resonance curve widths for the shielded shorted lines.

Table III shows the measured resonance curve widths for shielded and unshielded lines with short-circuit termination at the upper end, at various frequencies and resonant line lengths. Table IV gives the same data for lines with open-circuit termination at the upper end. Each value given is the average for at least two separate resonance curves recorded under identical conditions. In almost every case the widths of such duplicate curves agreed within 2 percent +0.01 mm.

The tables also show the resulting value of R_t calculated using Eq. (2), and the values of radiation resistance calculated using Eq. (4).

The radiation resistance values are plotted against frequency in Fig. 5, the range of values for all values of n being shown at each frequency. The broken line on the graph is for the equation

$$R_{\text{rad}} = 55\pi^2(d/\lambda)^2 \text{ ohms}.$$

TABLE III.

Frequency (1)	Resonant line length in quarter-wavelengths (2)	Resonant line length $=n\cdot(c/4f)$ (3)	Resonance curve width at half-power points for unshielded line (4)	Resonance curve width at half-power points for shielded line (5)	Q-value, unshielded circuits (6)	Q-value, shielded circuits (7)	Total effective resistance for shielded circuits, measured; $\frac{1}{2}\beta Z_0\cdot\Delta L_2=\frac{1}{2}L_0\cdot R_c+R_t$ (8)	Effective line resistance, calculated, $=\frac{1}{2}L_0\cdot R_c$ (9)	Terminal loss resistance R_t, $=(8)-(9)$ (10)	Total effective resistance for unshielded circuits, measured; $\frac{1}{2}\beta Z_0\cdot\Delta L_1=\frac{1}{2}L_0\cdot R_c+R_{rad}+R_t$ (11)	Radiation resistance, measured; $=(11)-(8)$ (12)
f Mcps	n	L_0 cm	ΔL_1 mm	ΔL_2 mm	$\frac{L_0}{\Delta L_1}$ Q	$\frac{L_0}{\Delta L_2}$ Q	$\frac{1}{2}\beta Z_0\cdot\Delta L_2$ ohms	$\frac{1}{2}L_0\cdot R_c$ ohms	R_t ohms	$\frac{1}{2}\beta Z_0\cdot\Delta L_1$ ohms	R_{rad} ohms
404	2	37.1	0.68	0.27	545	1370	0.39	0.24	0.15	1.03	0.64
	4	74.3	0.87	0.50	850	1490	0.73	0.48	0.25	1.32	0.59
	6	111.4	1.03	0.67	1080	1660	0.97	0.72	0.25	1.56	0.59
550	2	27.3	0.76	0.23	360	1190	0.46	0.21	0.25	1.57	1.11
	4	54.5	0.84	0.31	650	1760	0.61	0.41	0.20	1.74	1.13
	6	81.8	0.98	0.48	835	1700	0.95	0.62	0.33	2.03	1.08
	8	109.1	1.06	0.59	1030	1850	1.17	0.83	0.34	2.19	1.02
696	2	21.6	0.84	0.22	260	980	0.55	0.19	0.36	2.20	1.65
	4	43.1	0.92	0.31	470	1390	0.78	0.37	0.41	2.41	1.63
	6	64.6	0.98	0.33	660	1960	0.83	0.55	0.38	2.56	1.73
	8	86.2	1.08	0.45	800	1920	1.13	0.74	0.39	2.83	1.70
	10	107.8	1.17	0.52	920	2070	1.30	0.92	0.38	3.06	1.76
918	4	32.7	1.15	0.20	285	1630	0.66	0.32	0.34	3.97	3.31
	6	49.0	1.21	0.31	405	1580	1.02	0.48	0.54	4.18	3.16
	8	65.4	1.19	0.37	550	1770	1.22	0.64	0.58	4.11	2.89
	10	81.7	1.29	0.36	635	2270	1.19	0.80	0.39	4.45	3.26
	12	98.0	1.36	0.48	720	2040	1.58	0.96	0.62	4.69	3.11
	14	114.4	1.45	0.45	790	2540	1.49	1.12	0.37	5.00	3.51
1075	4	27.9	1.40	0.18	200	1550	0.70	0.30	0.40	5.66	4.96
	6	41.9	1.32	0.22	320	1900	0.85	0.45	0.40	5.33	4.48
	8	55.8	1.49	0.26	375	2150	1.01	0.59	0.42	6.02	5.01
	10	69.8	1.39	0.31	500	2250	1.20	0.74	0.46	5.62	4.42
	12	83.7	1.53	0.31	550	2700	1.20	0.89	0.31	6.18	4.98
	14	97.7	1.46	0.35	670	2790	1.35	1.04	0.31	5.90	4.55
	16	111.6	1.63	0.40	685	2790	1.55	1.19	0.36	6.59	5.04

6. DISCUSSION OF RESULTS

Because of the use of a ground plane, the radiation resistance measurements of Tables III and IV must be interpreted as representing one-half the radiation resistance of the test line and its image in the plane, in each case. For comparison with theory, therefore, the measured values must be doubled. Test lines of length $n\lambda/4$ with open-circuit termination at the top (n odd) are equivalent to theoretical lines of length $n\lambda/2$ with open-circuit termination at each end. Similarly test lines of length $n\lambda/4$ with short-circuit termination at the top (n even) are equivalent to theoretical lines of length $n\lambda/2$ with short-circuit termination at each end. The method is intrinsically incapable of measuring the radiation resistance of line sections terminated non-reflectively, or of the equivalent of line sections having a short-circuit termination at each end and a resonant length of an *odd* number of half-wavelengths.

It is clear from Fig. 5 that the theoretical prediction of radiation resistance varying as the square of the frequency (or of the conductor separation in wavelengths) is reasonably well verified. Considering an equation of the form

$$R_{rad}=k\pi^2(d/\lambda)^x \text{ ohms},$$

the data is best fitted by a value of x between 1.95 and 2.00. The best value of k, however, is appreciably lower than the theoretical value of 60 found by most theories for lines with open-circuit terminations, and by the recent theory of Storer and King[24] for lines with both open-circuit and short-circuit terminations. All of these theories assume line conductors with vanishingly small radius. For conductors of diameter 0.100 inch spaced 1.00 inch between centers, proximity effect reduces the square of the effective separation of the current centers by only $\frac{1}{2}$ percent. It seems probable, however, that when the diameter of one of the conductors of a line subtends an appreciable angle at the center of the other conductor, a mutual shielding will be created which is not described by the proximity effect. The first, somewhat less precise measurements, made in the present project involved line conductors of $\frac{3}{8}$-in. diameter, with

TABLE IV.

Frequency (1)	Resonant line length in quarter-wavelengths (2)	Resonant line length $=n\cdot(c/4f)$ (3)	Resonance curve width at half-power points for unshielded line (4)	Resonance curve width at half-power points for shielded line (5)	Q-value, unshielded circuits (6)	Q-value, shielded circuits (7)	Total effective resistance for shielded circuits, measured; $\frac{1}{2}\beta Z_0\cdot\Delta L_2=\frac{1}{2}L_0\cdot R_e+R_t$ (8)	Effective line resistance, calculated, $=\frac{1}{2}L_0\cdot R_e$ (9)	Terminal loss resistance R_t, $=(8)-(9)$ (10)	Total effective resistance for unshielded circuits, measured; $\frac{1}{2}\beta Z_0\cdot\Delta L_1=\frac{1}{2}L_0\cdot R_e+R_{rad}+R_t$ (11)	Radiation resistance, measured; $=(11)-(8)$ (12)
f Mcps	n	L_0 cms	ΔL_1 mm	ΔL_2 mm	$\frac{L_0}{\Delta L_1}$ Q	$\frac{L_0}{\Delta L_2}$ Q	$\frac{1}{2}\beta Z_0\cdot\Delta L_2$ ohms	$\frac{1}{2}L_0\cdot R_e$ ohms	R_t ohms	$\frac{1}{2}\beta Z_0\cdot\Delta L_1$ ohms	R_{rad} ohms
342	1	21.9	0.52	0.16	420	1370	0.20	0.13	0.07	0.67	0.47
	3	65.8	0.80	0.44	820	1530	0.54	0.39	0.15	1.03	0.49
452	1	16.6	0.70	0.20	240	830	0.33	0.12	0.21	1.19	0.86
	3	49.8	0.81	0.33	615	1510	0.54	0.34	0.20	1.38	0.84
	5	83.0	0.92	0.43	900	1930	0.71	0.57	0.14	1.56	0.85
602	1	12.5	0.74	0.13	170	960	0.28	0.10	0.18	1.67	1.39
	3	37.4	0.79	0.24	470	1560	0.53	0.30	0.23	1.79	1.26
	5	62.3	0.99	0.37	630	1680	0.81	0.49	0.32	2.24	1.43
691	1	10.9	0.78	0.13	140	840	0.33	0.09	0.24	2.03	1.70
	3	32.6	0.91	0.23	360	1420	0.58	0.28	0.30	2.37	1.79
	5	54.3	1.06	0.34	510	1600	0.85	0.46	0.39	2.76	1.91
898	1	8.4	1.00	0.25	84	335	0.82	0.08	0.74	3.38	2.56
	3	25.1	1.11	0.27	225	930	0.88	0.24	0.64	3.75	2.87
	5	41.8	1.09	0.29	385	1440	0.95	0.40	0.55	3.68	2.73
	7	58.5	1.22	0.31	480	1890	1.01	0.56	0.45	4.12	3.11
1045	1	7.2	1.18	0.13	61	550	0.49	0.07	0.42	4.64	4.15
	3	21.5	1.15	0.12	187	1790	0.45	0.22	0.23	4.52	4.07
	5	35.9	1.17	0.16	310	2240	0.61	0.37	0.24	4.60	3.99
	7	50.2	1.24	0.26	405	1930	0.99	0.52	0.47	4.87	3.88
1115	5	33.6	1.37	0.31	245	1080	1.26	0.36	0.90	5.74	4.48
	7	47.1	1.31	0.28	360	1680	1.13	0.51	0.82	5.49	4.36
	9	60.5	1.41	0.31	430	1950	1.26	0.65	0.61	5.91	4.65
1420	1	5.3	1.50	0.10	35	530	0.51	0.06	0.45	8.01	7.50
	3	15.8	1.66	0.18	95	880	0.93	0.19	0.74	8.86	7.93
	7	37.0	1.74	0.34	210	1090	1.75	0.45	1.30	9.29	7.54

the same 1-in. center spacing. A value of about 45 was obtained for k, while proximity effect indicates a value of about 54.

It is possible that the finite size of the ground plane in this work is at least partly responsible for k being less than 60.

The theories of Reukema[20] and of Sterba and Feldman[18] predict a theoretical value of k, for lines with short-circuit termination at each end, of $\frac{1}{2}(40+80+80)=100$, where the 40 represents radiation from the line conductors, and the two 80's represent radiation from the two terminations. The $\frac{1}{2}$ is because of the image effect in the present method. Sommerfeld[28] has shown that, when parallel current filaments are separated by half a wavelength or more, their radiations are independent and their radiation resistances are directly additive. The results of Fig. 5 disagree conclusively with this value of k, and show that, with a probable error not exceeding 5 percent, the radiation resistance is the same for lines with short-circuit termination as for lines with open-circuit termination.

Tables III and IV indicate that the variation of the radiation resistance values with n at constant frequency shows no consistent trend of any kind, which permits the conclusion that the radiation resistance is independent of n. While there is a regular oscillation of R_{rad} with n at 1075 Mcps in Table III, this does not appear at any other frequency. At 1045 Mcps in Table IV, R_{rad} diminishes steadily as n increases, while at 691 Mcps in the same table R_{rad} increases steadily as n increases.

While the spread of the radiation resistance values obtained for different resonant line lengths at constant frequency is somewhat larger than might be expected from the accuracy of repeatability of measurements of ΔL_1 and ΔL_2 for constant conditions, the randomness

[28] A. Sommerfeld, *Partial Differential Equations in Physics* (Academic Press, Inc., New York, 1949), p. 270.

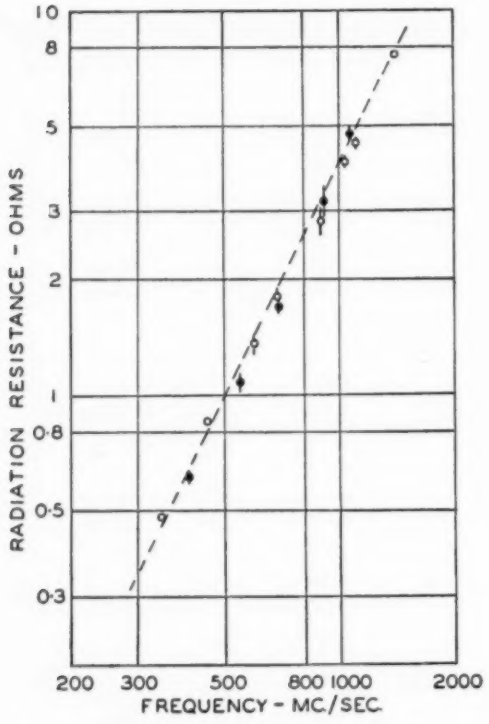

FIG. 5. Measured radiation resistance values plotted against frequency. ◊—average value and total range of measured values for line sections with open-circuit termination at top; ♦—average value and total range of measured values for line sections with short-circuit termination at top. The broken line is for the equation

$$R_{rad} = 55\pi^2(d/\lambda)^2 \text{ ohms.}$$

of the variations rules out any possibility of reducing the spread by simply changing the value of any one of the variables of which ΔL_1 and ΔL_2 are linear functions. No explanations involving partial excitation of undesired modes or inaccuracies in the values of the line conductor resistances or characteristic impedances can make any improvement.

The random variation of the values of ΔL_2 with n at constant frequency shows up in the values of R_t in Tables III and IV in considerably magnified form, due to the subtraction of the *calculated* effective line conductor resistance from the *measured* effective total resistance. Thus, when $\frac{1}{2}L_0 \cdot R_c$ is half as great as $\frac{1}{2}\beta Z_{0_t} \cdot \Delta L_2$, the probable error in the resulting value of R_t is twice as great as the probable error in ΔL_2. The actual values of R_t are by no means the minimum values that could be obtained experimentally, but were governed by the following experimental procedure. At a particular frequency a suitable amount of attenuation cable was connected between the oscillator and the input coupling loop at the test line. The size of the two coupling loops was then adjusted to give adequate detector response for a short, unshielded resonant line. All longer lines and all shielded lines would give greater response at resonance for the same frequency, and when necessary the response was reduced to bring it onto the scale of the detector by inserting further attenuation in the oscillator lead. The values of R_t were therefore determined primarily by the desirability of adequately decoupling the oscillator from its load.

The variation of R_t from one frequency to another is of no significance, since the oscillator output varied considerably over its frequency range and the coupling loops had to be adjusted accordingly.

While the *average* values of R_t at constant frequency and the variation of these average values with frequency are thus explained, the variations with n of the values at constant frequency remain somewhat larger than one would expect from the estimated accuracy of the method. Again, as with the R_{rad} values, these variations are apparently completely random, and no explanation can be based on a change in value of any of the line constants. If the indicated variations are real, they may indicate extra losses at some line lengths due to partial excitation of wave-guide modes in the shield pipe.

7. ACKNOWLEDGMENTS

We are very grateful to the National Research Council of Canada for a grant-in-aid supporting this project, both for purchases of equipment and for salary payments to three of us.

JOURNAL OF APPLIED PHYSICS VOLUME 23, NUMBER 6 JUNE, 1952

The Thermal Neutron Diffusion Length in a Heterogeneous Pile*

GILBERT N. PLASS
The Johns Hopkins University, Baltimore, Maryland
(Received December 18, 1951)

The diffusion equation for thermal neutrons in a pile with finite sides and having a three-dimensional lattice structure of fissionable material and moderator is solved to the first three orders by an expansion in spherical harmonics. This solution is used to calculate the difference in thermal utilizations of a pile of infinite extent and one with finite sides. From this difference is calculated an accurate expression, Eq. (24), for the diffusion length in a pile having a lattice structure. This expression is compared with the usual simplified equation for the diffusion length. The leakage of neutrons from a pile is also obtained from this calculation.

I. INTRODUCTION

THE theory of the diffusion of thermal neutrons involves a quantity, L, called the thermal diffusion length. For the case of diffusion in a homogeneous material, L can be calculated in terms of the nuclear constants of the material.[1] In the theory of piles the thermal diffusion length occurs in many different equations. It has been customary[1] to calculate L from the equation

$$L_a^2=(1/\kappa_1^2)(1-f_0), \tag{1}$$

where κ_1 is the reciprocal diffusion length in the pure moderator, f_0 is the thermal utilization in a pile with infinite sides, and L_a is the approximate value of the diffusion length obtained from this equation.

The justification for the use of the approximate Eq. (1) has been twofold. First, for a homogeneous mixture an elementary calculation shows that this equation is correct to within a few percent, provided that $N_0\sigma_0 \ll N_1\sigma_1$, where N_0 and N_1 are the number of atoms per unit volume in the fissionable material and moderator, respectively, and σ_0 and σ_1 are the total cross sections. Second, for a heterogeneous pile it can be shown, by weighting the cross sections with the average neutron density in the material, that Eq. (1) is approximately correct when the amount of fissionable material is such that only small changes in the thermal neutron distribution occur in the fissionable material.

In view of the very approximate nature of these derivations and of the importance of the thermal diffusion length, we have undertaken a more exact derivation of the relation of L to the fundamental nuclear constants of a heterogeneous pile containing spherical lumps of fissionable material arranged in a lattice structure. The method given here is an extension of the cellular method[1] which has been widely used to calculate the thermal utilization in piles. Our calculations are very similar to those of Bardeen[2] on metallic wave functions. The diffusion equation for a neutron in a pile of finite extent is solved to the first three orders by an expansion in spherical harmonics. This solution is used to calculate the thermal utilization for a finite pile. A relation between the thermal utilization and the diffusion length allows the accurate calculation of the latter quantity. This method allows for the change in L caused by both the varying neutron density inside a single cell and the finite over-all gradient of the neutron density across the pile.

II. RELATION BETWEEN DIFFUSION LENGTH AND THERMAL UTILIZATION

The fundamental equation of pile theory is[1]

$$-\nabla^2 n=(k-1)(L^2+L_f^2)^{-1}n, \tag{2}$$

where n is the thermal neutron density, L_f is the diffusion length for the slowing down process, k is the multiplication constant defined as the number of neutrons completing a cycle of slowing down, diffusion, capture, and fission per one neutron starting the cycle after fission. Thus

$$\eta\epsilon p_0 f_0=k, \tag{3}$$

for a pile with infinite sides, where η is the number of neutrons released per fission, ϵ is the number of neutrons gained through fast fission processes, f_0 is the probability that a neutron escapes resonance absorption during the slowing down process in an infinite medium. In an actual pile with finite sides neutrons are lost by diffusion through the sides. When the neutron distribution in such a pile is independent of time, it follows that

$$\eta\epsilon pf=1, \tag{4}$$

where f and p refer to the thermal utilization and probability of escaping resonance absorption for a pile with finite sides.

Consider a pile built in the form of a rectangular parallelopiped with sides of length l_1, l_2, l_3. Define a generalized reciprocal length of the pile, $\mathbf{s}$, by the

* This work originally appeared in 1943 as reports CP-992 and CP-1174 of the Metallurgical Laboratory, Chicago, Illinois. This work was declassified on July 31, 1951 by authority of the United States Atomic Energy Commission. The present paper is an expanded and improved version of these reports.

[1] See, for example, C. D. Goodman, Editor, *The Science and Engineering of Nuclear Power* (Addison-Wesley Press, Cambridge, Massachusetts, 1947); H. Soodak and E. C. Campbell, *Elementary Pile Theory* (John Wiley and Sons, Inc., New York, 1950).

[2] J. Bardeen, Phys. Rev. 49, 653 (1936); F. Seitz, *The Modern Theory of Solids* (McGraw-Hill Book Company, Inc., New York, 1940), Chapter IX.

equation,

$$\mathbf{s}=\mathbf{i}(\pi/l_1)+\mathbf{j}(\pi/l_2)+\mathbf{k}(\pi/l_3), \quad (5)$$

where the unit vectors point in the direction of the sides of the pile.

In the usual approximation which neglects the variations of neutron density in the individual lattice cells, choosing the origin of the coordinate system at the center of the pile, we have that

$$n=A\cos(\pi x/l_1)\cos(\pi y/l_2)\cos(\pi z/l_3). \quad (6)$$

Substituting this expression in the fundamental pile Eq. (2), using Eqs. (3) and (4) and the fact that $f_0-f\ll 1$ and $p_0-p\ll 1$, we may write

$$L_f^2+L^2=s^{-2}(k-1)=ks^{-2} \times\{p_0^{-1}(p_0-p)+f_0^{-1}(f_0-f)\}. \quad (7)$$

Therefore the desired relation between the thermal utilization and the diffusion length required by Eq. (2) is that

$$L^2=ks^{-2}f_0^{-1}(f_0-f). \quad (8)$$

Thus the calculation of the thermal utilization as a function of the size of a pile determines the diffusion length.

III. THE THERMAL UTILIZATION IN A FINITE HETEROGENEOUS PILE

The differential equation for the diffusion of thermal neutrons is[1]

$$-\nabla^2 n+\kappa^2 n=\delta\kappa^2(N\sigma_a v)^{-1}q, \quad (9)$$

where κ is the reciprocal diffusion length, N is the density of nuclei, q is the number of thermal neutrons produced per unit volume and time, $\delta=1$ in the moderator, and $\delta=0$ to a sufficient approximation in the heavy fissionable material. This is a good approximation unless only a very small amount of moderator is present.

Again taking the origin of our coordinate system at the center of the pile, the equation for the thermal neutron density can be written as

$$n=g(x,y,z)\cos(\pi x/l_1)\cos(\pi y/l_2)\cos(\pi z/l_3), \quad (10)$$

where the cosine terms represent the large scale variation of n over the pile and $g(x,y,z)$ represents the individual fluctuations of n in each lattice cell.

For purposes of calculation we shall write Eq. (10) as

$$n=(1/8)g(x,y,z)\exp[i\pi(x/l_1+y/l_2+z/l_3)] +\text{seven similar terms.} \quad (11)$$

The following calculations are made with only the first of the eight terms in Eq. (11). Since the final results only involve $\mathbf{s}^2$, it is seen that the same answers would have been obtained by using any of the eight terms. The same result follows from considerations of symmetry. For convenience, all of the following equations calculated from a single term in Eq. (11) are multiplied by eight to give the answer from all the terms.

The production of thermal neutrons can be written as

$$q=\exp(i\mathbf{s}\cdot\mathbf{r}). \quad (12)$$

Deviations from Eq. (12) introduce only negligible corrections to the present calculation. Substituting Eqs. (11) and (12) into (9) we obtain an equation for the unknown function $g(x,y,z)$,

$$-\nabla^2 g-2i\mathbf{s}\cdot\nabla g+(\kappa^2+s^2)g=\delta\kappa^2(N\sigma_a v)^{-1}. \quad (13)$$

We consider now a pile composed of spherical lumps of fissionable material in a simple cubic-, body-, or face-centered lattice. The unknown function g can now be considered as a function of the spherical polar coordinates r, θ, ϕ, where the origin for these coordinates is now taken at the center of the cell under consideration. We expand the solution of Eq. (13) in a power series in $\mathbf{s}$ and the Legendre polynomials,[2] so that

$$g(r,\theta,\phi)=g_s(r)+i\mathbf{s}\cdot\mathbf{m}g_p(r)+[3(\mathbf{s}\cdot\mathbf{m})^2-s^2]g_d(r), \quad (14)$$

where the unit vector in the r direction is written as $\mathbf{m}$. The radial functions within each cell associated with the first three spherical harmonics are $g_s(r)$, $g_p(r)$, $g_d(r)$. Unlike the cellular method in the theory of solids where the first two terms alone give a sufficient approximation, here the first three must be retained.

The solution of Eq. (13) correct to terms of order s^2 can be obtained by substituting Eq. (14) into (13) and using well-known vector identities. The solution is found to be

$$g_{s0}=ar^{-1}Sh\kappa_0 r+s^2\{-(1/6)ar\,Sh\kappa_0 r+(1/3)\kappa_0^{-1}b\,Ch\kappa_0 r\} \quad (15a)$$

$$g_{p0}=-a\,Sh\kappa_0 r+b(\kappa_0 r)^{-1}\{Ch\kappa_0 r-(\kappa_0 r)^{-1}Sh\kappa_0 r\} \quad (15b)$$

$$g_{d0}=-(1/6)ar\,Sh\kappa_0 r+b(3\kappa_0)^{-1}\{Ch\kappa_0 r-(\kappa_0 r)^{-1}Sh\kappa_0 r\}+c(\kappa_0 r)^{-1}\{[3(\kappa_0 r)^{-2}+1]Sh\kappa_0 r-3(\kappa_0 r)^{-1}Ch\kappa_0 r\} \quad (15c)$$

$$g_{s1}=\alpha r^{-1}Ch\kappa_1(r-r_0)+\beta r^{-1}Sh\kappa_1(r-r_0)+(vN_1\sigma_{a1})^{-1}+s^2\{-(1/6)\alpha r Ch\kappa_1(r-r_0)-(1/6)\beta r\,Sh\kappa_1(r-r_0) +(1/3)\gamma\kappa_1^{-1}Sh\kappa_1(r-r_0)+(1/3)\epsilon\kappa_1^{-1}Ch\kappa_1(r-r_0)-(\kappa_1^2N_1\sigma_{a1}v)^{-1}\} \quad (16a)$$

$$g_{p1}=-\alpha Ch\kappa_1(r-r_0)-\beta Sh\kappa_1(r-r_0)+\gamma(\kappa_1 r)^{-1}\{Sh\kappa_1(r-r_0)-(\kappa_1 r)^{-1}Ch\kappa_1(r-r_0)\} +\epsilon(\kappa_1 r)^{-1}\{Ch\kappa_1(r-r_0)-(\kappa_1 r)^{-1}Sh\kappa_1(r-r_0)\} \quad (16b)$$

$$g_{d1}=-(1/6)\alpha r\,Ch\kappa_1(r-r_0)-(1/6)\beta r\,Sh\kappa_1(r-r_0)+\gamma(3\kappa_1)^{-1}\{Sh\kappa_1(r-r_0)-(\kappa_1 r)^{-1}Ch\kappa_1(r-r_0)\} +\epsilon(3\kappa_1)^{-1}\{Ch\kappa_1(r-r_0)-(\kappa_1 r)^{-1}Sh\kappa_1(r-r_0)\}+\mu(\kappa_1 r)^{-1}\{[3(\kappa_1 r)^{-2}+1]Ch\kappa_1(r-r_0) -3(\kappa_1 r)^{-1}Sh\kappa_1(r-r_0)\}+\nu(\kappa_1 r)^{-1}\{[3(\kappa_1 r)^{-2}+1]Sh\kappa_1(r-r_0)-3(\kappa_1 r)^{-1}Ch\kappa_1(r-r_0)\}. \quad (16c)$$

The subscripts 0 and 1 refer to the fissionable material and moderator, respectively. These solutions contain nine arbitrary constants, a, b, c, α, β, γ, ϵ, μ, ν, which are determined from the boundary conditions. Let r_0 equal the radius of the sphere of fissionable material and $r_2=r_0+r_1$ equal the radius of a sphere having a volume equal to the volume of the unit cell.

In order to write the boundary conditions in a manageable form, we use the spherical approximation which replaces the actual polyhedra by spheres of equal volume. This approximation is familiar from the theory of solids and from the usual theory of piles. It has been shown that the effect of the spherical approximation on g_s is very small.[2] We assume that it would also introduce only second-order corrections to the calculation of L through g_p and g_d.

Three boundary conditions can be written in the form that g_s, g_p, g_d are separately continuous at $r=r_0$, thus assuring the continuity of n at this point. Three more boundary conditions result from the continuity of n at the outer boundary of the cell. These can be written as

$$g_{s1}'(r_2)=g_{p1}(r_2)=g_{d1}'(r_2)=0. \tag{17}$$

The final three boundary conditions result from equating the flow of neutrons in both directions at the point $r=r_0$. These equations can be written as

$$\begin{aligned}
R[g_{s0}'(r_0)-s^2g_{d0}'(r_0)]&=\kappa_0^2\kappa_1^{-2}[g_{s1}'(r_0)-s^2g_{d1}'(r_0)],\\
R[g_{p0}'(r_0)+g_{s0}(r_0)]&=\kappa_0^2\kappa_1^{-2}[g_{p1}'(r_0)+g_{s1}(r_0)],\\
R[3g_{d0}'(r_0)-g_{p0}(r_0)]&=\kappa_0^2\kappa_1^{-2}[3g_{d1}'(r_0)-g_{p1}(r_0)],
\end{aligned} \tag{18}$$

where $R=(N_0\sigma_{a0}/N_1\sigma_{a1})$. These nine boundary equations now determine the nine arbitrary constants in the solution given by Eqs. (15) and (16). Fortunately, in order to calculate f, it is not necessary to carry through the tedious solution of these equations for all the nine constants.

From the definition of the thermal utilization in an infinite pile,

$$f_0=\left[N_0\sigma_{a0}v\int_0^{r_0}n_0(r)r^2dr\right]\Big/\left[\int_{r_0}^{r_2}r^2dr\right]. \tag{19}$$

For convenience in further work, we define seven symbols,

$$\begin{aligned}
D&=Ch\kappa_0r_0-(\kappa_0r_0)^{-1}Sh\kappa_0r_0,\\
E&=Ch\kappa_1r_1-(\kappa_1r_2)^{-1}Sh\kappa_1r_1,\\
F&=Sh\kappa_1r_1-(\kappa_1r_2)^{-1}Ch\kappa_1r_1,\\
M&=E+\kappa_1r_0F,\\
G&=RSh\kappa_0r_0-2R(\kappa_0r_0)^{-1}D+2\kappa_0(\kappa_1^2r_0)^{-1}D,\\
H&=GM+\kappa_0r_0DE,\\
J&=R(\kappa_0^3\kappa_1r_0^3r_2)^{-1}MSh\kappa_0r_0+\kappa_1(\kappa_0^4r_0^2r_2)^{-1}DE.
\end{aligned} \tag{20}$$

From Eq. (19), a short calculation shows that

$$f_0=3MD/\kappa_0^4\kappa_1r_0r_2(r_2^3-r_0^3)J. \tag{21}$$

Similarly the thermal utilization in a finite pile is given by

$$f=\frac{N_0\sigma_{a0}v\displaystyle\int_\Omega\int_0^{r_0}\{g_{s0}(r)-(\mathbf{s}\cdot\mathbf{m})^2rg_{p0}(r)-\tfrac{1}{2}(\mathbf{s}\cdot\mathbf{m})^2r^2g_{s0}(r)\}r^2drd\Omega}{\displaystyle\int_\Omega\int_0^{r_0}\left\{1-\frac{r^2}{2}(\mathbf{s}\cdot\mathbf{m})^2\right\}r^2drd\Omega}. \tag{22}$$

Calculating f from this equation, substituting this answer and f_0 from Eq. (21) into Eq. (8), we find that

$$L^2k^{-1}=-(a_1/a_0)-(b/3\kappa_0^2a_0)-[(r_2^5-r_0^5)/10(r_2^3-r_0^3)], \tag{23}$$

where a_0 and a_1 are the first two terms in a power series expansion of the constant a in s^2, i.e., $a=a_0+s^2a_1$. Thus a calculation of the constant a to terms in s^2 and of b to terms independent of $\mathbf{s}$ determines the diffusion length.

The result of the long, but elementary, calculation of these constants is that L is given by the expression

$$L^2=\frac{k}{\kappa_1^2}\left\{1+\frac{2\kappa_1^3D}{3\kappa_0^3r_0JM}-\frac{\kappa_1^4r_2(Sh\kappa_1r_1+\kappa_1r_0Ch\kappa_1r_1)DG}{3\kappa_0^4r_0JHM}+\frac{\kappa_1^2r_0^2EG}{2H}+\frac{\kappa_1^3r_0^3FG}{6H}+\frac{\kappa_1^4r_0^3r_2G}{3HM}-\frac{\kappa_0\kappa_1^2r_0^2r_2D}{HM}-\frac{\kappa_1^4r_2D^2Sh\kappa_1r_1}{3\kappa_0^3JHM}-\frac{5\kappa_0\kappa_1^3r_0^4DEF}{3HM}-\frac{2\kappa_1^4r_0^4E^2G}{3HM}+\frac{7\kappa_0\kappa_1^2r_0^3DE}{6H}\right\}, \tag{24}$$

where the symbols appearing in this equation have been defined in Eqs. (20) and elsewhere. The terms are arranged in order of decreasing importance for a natural uranium pile with carbon for a moderator. In this particular case the first seven terms of Eq. (24) give a value of L^2 correct to about 1 percent for any radii that are likely to be of interest. However, as written Eq. (24) contains all the terms independent of $\mathbf{s}$ appearing in the expression for L^2 under the assumptions made in this article.

TABLE I. Diffusion length and neutron leakage from a finite pile.*

r_0	r_2	f_0	$\frac{f_0-f}{s^2}$	e/s^2	$\frac{f_{0m}-f_m}{s^2}$	L_a^2	L^2
2	6	0.9507	106.1	111.7	5.6	114.0	107.1
2	7	0.9216	163.3	177.4	14.1	181.2	184.5
2	8	0.8851	229.9	260.2	30.3	265.6	276.2
2	9	0.8418	301.3	358.6	57.3	365.7	375.4
2	10	0.7931	371.6	469.7	98.1	478.2	473.8
3	9	0.9366	129.8	138.7	8.9	146.5	139.1
3	10.5	0.8989	199.1	221.8	22.7	233.7	234.9
3	12	0.8522	277.0	325.7	48.7	341.6	344.4
3	13.5	0.7983	355.6	446.6	91.0	466.2	455.9
3	15	0.7390	427.3	580.1	152.8	603.3	558.3

* r_0 = radius of fissionable sphere in cm; r_2 = radius of sphere having same volume as unit cell; f_0 = thermal utilization for pile with infinite sides; f = same with finite sides; s = reciprocal length of pile defined by Eq. (5); f_m = fraction of neutrons absorbed in moderator in pile with finite sides; e_2 = fraction of thermal neutrons leaking from pile; L_a = approximate diffusion length in cm² from Eq. (1); L = exact diffusion length from Eq. (24). Calculated for a natural uranium-carbon pile with $R=(N_0\sigma_{a0}/N_1\sigma_{a1})=662.7$; $\kappa_0=0.732$; $\kappa_1=0.0208$ (diffusion lengths in pure uranium and carbon, respectively).

IV. NUMERICAL VALUES AND COMPARISON WITH SIMPLE FORMULA

The importance of the various terms in Eq. (24) depends on both the fissionable material and moderator used in the pile. As an example Table I shows results of exact calculations of the diffusion length for a natural uranium-carbon pile. The following values of the constants were used in these calculations: $R=662.7$; $\kappa_0=0.732$; $\kappa_1=0.0208$. The seventh column of the table gives the values of the approximate diffusion length, L_a, calculated from the Eq. (1). This is to be compared to the eighth column of the table giving the more exact diffusion length, L, calculated from Eq. (24). For the radii given in the table L_a and L do not differ by more than 10 percent. However, this difference becomes more marked for radii considerably different from those given in this table. For a natural uranium-carbon lattice, a series expansion shows that the first three orders of terms in Eqs. (1) and (24) agree, but the series converges so slowly as to be of little practical value. The functional form of these two equations is, however, quite different, and large deviations appear when the qualitative conditions mentioned in the introduction are not satisfied. For piles constructed with other materials, the ratio of the absorption cross sections and the magnitude of diffusion lengths in the pure moderator and fissionable material determine the region of validity of Eq. (1).

V. LEAKAGE OF NEUTRONS FROM A HETEROGENEOUS PILE

The number of neutrons diffusing from a pile per unit time divided by the production of thermal neutrons per unit time, e, can be calculated accurately from the results of the previous sections. From this definition and substituting for the neutron density from Eq. (14), we find that

$$e=N_1\sigma_{a1}vs^2\kappa_1^{-2}\{1-(r_0^3/r_2^3)\}^{-1}\{g_{s1}(r_2)+g_{p1}'(r_2)\}. \quad (25)$$

Using the results of the previous numerical calculation, the values of e for a natural uranium-carbon pile are given in the fifth column of Table I. Defining f_m and f_{0m} as the fraction of the thermal neutrons absorbed by the moderator in a pile with finite and infinite sides, respectively, it follows that

$$f_{0m}-f_m=e-(f_0-f). \quad (26)$$

From this equation the values given in the sixth column of Table I have been tabulated.

The writer wishes to express his gratitude to Professor E. P. Wigner, who suggested this problem and offered much helpful advice during the course of the work.

JOURNAL OF APPLIED PHYSICS VOLUME 23, NUMBER 6 JUNE, 1952

A Mathematical Analysis of Parallel-Connected Magnetic Amplifiers with Resistive Loads

LOUIS A. PIPES
Department of Engineering, University of California, Los Angeles, California
(Received December 31, 1951)

A mathematical analysis of a parallel-connected magnetic amplifier with a resistive load is presented. The analysis is based on two distinct analytical approximations of the magnetization curve of the core material; a polynomial and a hyperbolic function. The variation of the core flux and the output current of the amplifier as a function of time are determined by the solution of an integral equation. A finite difference method is developed to determine the response of the loaded amplifier that makes direct use of the magnetization curve of the core material.

1. INTRODUCTION

THE successful use of electronic amplifiers especially in communication circuits and in control systems has been responsible for a great deal of the important progress made in electrical engineering in the past thirty years. In spite of their excellent performance, electronic amplifiers have two serious disadvantages which limit their use particularly in military applications. First, the life of the vacuum tubes used in electronic equipment is limited, and second, shocks or vibrations may make them inoperative. Because of possible failure of electronic amplifiers resulting from these causes their use in military equipment is hazardous.

The magnetic amplifier, also called a dc controlled reactor, saturable reactor, and transductor being tubeless does not have the serious disadvantages of the electronic amplifier. Since the magnetic amplifier contains no moving parts and does not require servicing it is ideally suited for use in the control systems of military equipment and manufacturing processes.

The literature of magnetic amplifiers is growing very rapidly.[1] Many investigators have, in recent years, developed the theory of magnetic amplifiers basing their analyses on simplified idealized circuits and magnetization curves. In these studies, the effects of the resistances of the windings are usually neglected and the amplifier is assumed to operate under a condition of no load. In the present discussion a method of analysis is presented that is applicable to the study of typical magnetic amplifier circuits in the presence of resistive loads. The comparatively simple case of the parallel-connected magnetic amplifier is treated in detail in order to clarify the general procedure, however, the method involved is applicable directly to other types of amplifiers.

The amplifier under consideration is shown in Fig. 1. It consists of two identical toroidal cores with one pair of similar windings in series with a constant voltage source, and the other pair of windings in parallel with an alternating power source. The winding polarities are such that fundamental frequency voltages induced in the two control windings are in opposition so that no power frequency current flows in the control circuit.

[1] James G. Miles, "Bibliography of magnetic amplifier devices and the saturable reactor art," Am. Inst. Elect. Engrs. Technical Paper 51-388 (September, 1951).

2. NOTATION AND GENERAL EQUATIONS

Consider the circuit diagram of the magnetic amplifier of Fig. 1. The following notation will be used in the analysis of this circuit:

E_0 = the applied dc control potential.
$E_m \sin(wt)$ = the applied ac output potential.
R_0 = the total resistance of the control windings.
R_w = the resistance of the output windings.
R_L = the resistance of the load.
N_0 = the number of turns of the control windings.
N = the number of turns of the output windings.
ϕ_a = the magnetic flux of core a.
ϕ_b = the magnetic flux of core b.
l = the average length of the magnetic cores.
S = the cross-sectional area of the cores normal to the flux path.
B = the magnetic induction of a core.
H = the magnetic intensity of a core.
i_0 = the control current.
i_1, i_2 = the loop currents of the output circuits.
μ_0 = the initial permeability of the core material.
$L_0 = N^2 S\mu_0/l$ = the initial inductance of an output winding.
$m = 2R_L/L_0$ = a constant.
$T_0 = L_0/2R_L = 1/m$ = the effective time constant of the amplifier circuit.
$g_0 = N_0 L_0/NR_0$ = a constant.
$B = 2R_L N_0 E_0/R_0 N^2$.
$Z = (m^2+w^2)^{\frac{1}{2}}$ = a constant.
$\theta = \tan^{-1}(w/m)$ = a phase angle.
$H = k_1 B + k_3 B^3$ = an analytical approximation of the magnetization curve of the core material.
$k_1 = 1/\mu_0$, k_3 = constant, determined from the magnetization curve.
$H = U \sinh(k\phi)$ = an analytical approximation of the magnetization curve of the core material.
$Uk = 1/S\mu_0$, U and k constants determined from the magnetization curve.

$P=kg_0E_0/N$, $Q=kE_m/NZ$.

$I_n(x)$ = the modified Bessel function of the first kind of order n.[2]

$F(\phi)=(2R_Ll/N^2)H(\phi)$, $H(\phi)$ = the magnetization curve.

The Fundamental Equations of the Amplifier

If Kirchhoff's electromotive force law is applied to the three loop currents of Fig. 1, the following equations are obtained:

$$E_0=R_0i_0+N_0(\dot{\phi}_a+\dot{\phi}_b). \tag{2.1}$$

$$E_m\sin(wt)=R_L(i_1+i_2)+R_wi_1+N\dot{\phi}_a. \tag{2.2}$$

$$E_m\sin(wt)=R_L(i_1+i_2)+R_wi_2-N\dot{\phi}_b. \tag{2.3}$$

The following equations are obtained by applying Ampère's law to the magnetic circuits of the cores a and b.

$$N_0i_0+Ni_1=lH_a=lH(\phi_a). \tag{2.4}$$

$$N_0i_0-Ni_2=lH_b=lH(\phi_b). \tag{2.5}$$

The magnetization curve of the core material may be expressed in the form,

$$H_a=H_a(\phi_a). \tag{2.6}$$

$$H_b=H_b(\phi_b). \tag{2.7}$$

Equations (2.1)–(2.5) are five equation in the five unknown quantities, i_0, i_1, i_2, ϕ_a, and ϕ_b. The general solution of these equations presents formidable difficulties. However, in practice, the load resistance, R_L, is usually small in comparison with the winding resistance, R_w. If the assumption $R_w\ll R$, be made, then (2.2) and (2.3) reduce to

$$R_L(i_1+i_2)=E_m\sin(wt)-N\dot{\phi}_a=E_m\sin(wt)+N\dot{\phi}_b. \tag{2.8}$$

Hence,

$$\dot{\phi}_a+\dot{\phi}_b=0. \tag{2.9}$$

If now (2.3) is subtracted from (2.2) the result is,

$$0=R_w(i_1-i_2)+N(\dot{\phi}_a+\dot{\phi}_b). \tag{2.10}$$

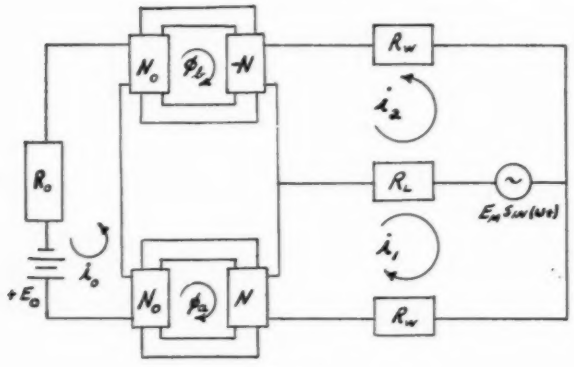

FIG. 1.

[2] Jahnke-Emde, *Tables of Functions* (Dover Publications, New York, 1943), pp. 232–233.

Hence,

$$R_w(i_1-i_2)=0, \tag{2.11}$$

or,

$$i_1=i_2. \tag{2.12}$$

Equations (2.9) and (2.12) greatly simplify the analysis.

The Flux Equation

As a consequence of (2.12), (2.2) may be written in the form,

$$2i_1R_L=E_m(\sin wt)-N\dot{\phi}_a. \tag{2.13}$$

(2.4) may be written in the form,

$$i_1=(lH_a-N_0i_0)/N. \tag{2.14}$$

If use is made of (2.9), (2.1) reduces to

$$i_0=E_0/R_0. \tag{2.15}$$

(2.14) and (2.15) may now be substituted into (2.13) and the result written in the following form,

$$\dot{\phi}_a+\frac{2lR_L}{N^2}H_a=\frac{E_m}{N}\sin(wt)+\frac{2R_LN_0E_0}{N2R_0}. \tag{2.16}$$

This equation determines the variation of the core flux, ϕ_a, with time. The load current, $i_L=2i_1$, may be obtained from (2.13) in the form,

$$i_L=[E_m\sin(wt)-N\dot{\phi}_a]/R_L. \tag{2.17}$$

Hence, if the core flux ϕ_a is determined by solving (2.16), the load current may then be determined by (2.17).

3. RESPONSE BASED ON A POLYNOMIAL MAGNETIZATION CURVE

In order to study the response of the magnetic amplifier mathematically, it is necessary to introduce the magnetization curve, $H(\phi)$, of the core material into Eq. (2.16). In this section the calculations will be based on the following polynomial representation of the magnetization curve of the material of the core,

$$H_a=k_1B_a+k_3B_a^3. \tag{3.1}$$

k_1 and k_3 are constants obtained so that (3.1) will give a good fit to the $B-H$ curve of the core material. It can be seen that $k_1=1/\mu_0$, where μ_0 is the initial permeability of the core material. Since the flux, ϕ_a, is given by $B_a=\phi_a/S$, (3.2) may be written in the form,

$$H_a=k_1\phi_a/S+k_3\phi_a^3/S^3=c_1\phi_a+c_3\phi_a^3. \tag{3.2}$$

If (3.2) is substituted into (2.16), the result is

$$\dot{\phi}_a+2R_L\frac{1}{N^2}(c_1\phi_a+c_3\phi_a^3)=\frac{E_m}{N}\sin(wt)+2R_L\frac{N_0E_0}{R_0N^2}. \tag{3.3}$$

This equation may be written in the form,

$$\dot{\phi}_a+\frac{2R_L}{L_0}\phi_a+2R_L\frac{lc_3}{N^2}\phi_a^3=\frac{E_m}{N}\sin(wt)+2R_LN_0E_0/R_0N^2, \tag{3.4}$$

where

$$L_0=N^2S\mu_0/l. \tag{3.5}$$

This is the effective initial inductance of a core winding. Equation (3.4) is a nonlinear differential equation for the determination of the core flux, ϕ_a. The transient and steady-state oscillations of the magnetic amplifier may be obtained on the supposition that the circuits are energized at $t=0$ so that we have the initial conditions, that at $t=0$, $\phi_a=0$. Write (3.4) in the form,

$$\dot{\phi}_a+m\phi_a=\frac{E_m}{N}\sin(wt)+A-a_3\phi_a^3, \tag{3.6}$$

where,

$$m=2R_L/L_0, \quad A=2R_LN_0E_0/R_0N^2,$$
$$a_3=2R_Lk_3/N^2S^3. \tag{3.7}$$

To solve (3.6) introduce the following Laplace transforms,

$$L\phi_a(t)=\bar{\phi}_a(p), \tag{3.8}$$

then the Laplace transform of the Eq. (3.6) is

$$(p+m)\bar{\phi}_a=\frac{E_mwp}{N(p^2+w^2)}+A-a_3L\phi_a^3(t).^3 \tag{3.9}$$

Therefore,

$$\bar{\phi}_a(p)=\frac{E_mwp}{N(p+m)(p^2+w^2)}+\frac{A}{(p+m)}-\frac{a_3L\phi_a^3(t)}{(p+m)}. \tag{3.10}$$

The inverse transform of (3.10) may be obtained by the use of a table of transforms and the Faltung theorem of the Laplace transform theory. It is given by,

$$\phi_a(t)=E_m\frac{w}{N}\left[\frac{e^{-mt}}{(m^2+w^2)}+\frac{\sin(wt-\theta)}{w(m^2)^{\frac{1}{2}}+w^2}\right]+\frac{A}{m}(1-e^{-mt})$$
$$-a_3\int_0^t e^{-m(t-u)}\phi_a^3(u)du, \quad \tan\theta=w/m. \tag{3.11}$$

Equation (3.11) is a form of Lalesco's nonlinear integral equation.[4] This integral equation may be written in the following form,

$$\phi_a(t)=\phi_0(t)-a_3\int_0^t e^{-m(t-u)}\phi_a^3(u)du, \tag{3.12}$$

where

$$\phi_0(t)=E_m\frac{w}{N}[e^{-mt}/Z_1^2+\sin(wt-\theta)/wZ]$$
$$+A(1-e^{-mt})/m \tag{3.13}$$

and,

$$Z=(m^2+w^2)^{\frac{1}{2}}. \tag{3.14}$$

The integral equation (3.12) may be solved by setting up the following sequence of equations,

$$\phi_1(t)=\phi_0(t)-a_3\int_0^t e^{-m(t-u)}\phi_0^3(u)du, \tag{3.15}$$

$$\phi_2(t)=\phi_0(t)-a_3\int_0^t e^{-m(t-u)}\phi_1^3(u)du, \tag{3.16}$$

$$\cdots\cdots\cdots\cdots\cdots\cdots\cdots\cdots$$

$$\phi_{r+1}(t)=\phi_0(t)-a_3\int_0^t e^{-m(t-u)}\phi_r^3(u)du. \tag{3.17}$$

It can be shown[5] that the foregoing sequence converges rapidly and that the solution of the integral Eq. (3.12) is given by

$$\phi_a(t)=\lim_{r\to\infty}\phi_r(t). \tag{3.18}$$

The function, $\phi_0(t)$, is the first approximation to the solution, the function, $\phi_1(t)$, is the second approximation, etc. It can be seen from the above, that the quantity e^{-mt} is of importance in the subsidence of the transient terms. By analogy with the theory of linear electrical circuits, the quantity,

$$T_0=L_0/2R_L=1/m, \tag{3.19}$$

may be defined as the effective time constant of the magnetic amplifier circuit.

The Steady-State Load Current

If ϕ_a from (2.16) is substituted for the expression given by (2.17) for i_L, the resulting equation for the load current is,

$$i_L=2N\phi_a/L_0-2N_0E_0/R_0N+21k_3\phi_a^3/NS^3. \tag{3.20}$$

The steady-state solution for the first approximation of the flux $\phi_a(t)$ is given by (3.13) for large values of time in the form

$$\phi_{0s}=\frac{A}{m}+E_m\frac{\sin(wt-\theta)}{N_Z}, \quad \theta=\tan^{-1}(w/m). \tag{3.21}$$

In the usual application, $w/m=wL_0/2R_L\gg1$, so that $\theta\approx\pi/2$. In this, we have,

$$\phi_{0s}=\frac{A}{m}-E_m\frac{\cos(wt)}{N_Z}. \tag{3.22}$$

This is the first approximation of the steady-state flux, ϕ_{as}. If (3.22) is substituted into (3.20) for ϕ_a, the first approximation of the steady-state load current,

[3] L. A. Pipes, *Applied Mathematics for Engineers and Physicists* (McGraw-Hill Book Company, Inc., New York, 1946), p. 587.

[4] E. G. Keller, *Mathematics of Modern Engineering* (John Wiley and Sons, Inc., New York, 1942), p. 294.

[5] Vito Volterra, *Leçons sur les Équations Intégrales* (Gauthier-Villars, Paris, France, 1910).

i_{Ls}, is obtained in the following form,

$$i_{Ls}=-2E_m\frac{\cos(wt)}{L_0Z}+\frac{2lk_3}{NS^3}[A/m-E_m\cos(wt)/NZ]^3$$

$$=\frac{2k_3l}{N^4S^3}\left[(g_0^3E_0^3+3g_0E_0E_m^2/2Z^2)-\frac{3\cos wt}{Z}\right.$$

$$\left.\times(g_0^2E_0^2E_m+E_m^3/4Z^2)-E_m^3\frac{\cos(3wt)}{4Z^3}\right]$$

$$+\frac{21k_3}{N^4S^3}\left[3g_0E_0E_m^2\frac{\cos(2wt)}{2Z^2}\right]-2E_m\frac{\cos(wt)}{L_0Z}, \quad (3.23)$$

where

$$g_0=N_0L_0/NR_0. \quad (3.24)$$

It is seen that to this approximation, the load current contains a direct current component as well as second and third harmonics of the output potential. The higher order approximations indicate the presence of harmonics of higher order and small amplitudes.

4. RESPONSE BASED ON A MAGNETIZATION CURVE REPRESENTED BY A HYPERBOLIC SINE FUNCTION

For purposes of comparison, the calculation of the response of the magnetic amplifier will now be based on the following representation of the magnetization curve of the material of the core,

$$H_a=U\sinh(k\phi_a), \quad (4.1)$$

where U and k are constants chosen in such a manner that (4.1) will be a good approximation to the magnetization curve of the core material. It is seen that for very small values of ϕ_a, we have,

$$H_a\approx Uk\cdot\phi_a. \quad (4.2)$$

Hence, it is seen that the constants U and k satisfy the following relation.

$$Uk=1/S\mu_0, \quad (4.3)$$

where μ_0 is the initial permeability and S is the cross-sectional area of the magnetic circuit.

In order to compute the flux variation on the basis of the hyperbolic sine approximation of the magnetization curve, (4.1) is substituted into (2.16) and the following equation obtained for ϕ_a.

$$\dot{\phi}_a+2lR_L\frac{U\sinh}{N^2}(k\phi_a)=\frac{E_m}{N}\sin(wt)$$

$$+2R_LN_0E_0/N^2R_0. \quad (4.4)$$

If the flux variation were such that the flux always remained small, then the approximation (4.2) indicates that in such a case the differential equation that governs the flux variation would be

$$\dot{\phi}_a+21R_L\frac{Uk}{N^2}\phi_a=\frac{E_m}{N}\sin(wt)+2R_LE_0/N^2R_0. \quad (4.5)$$

This is a linear differential equation and it is recognized that $Ukl/N^2=l/N^2S\mu_0=1/L_0$, where L_0 is the initial inductance of the core. This suggests adding the quantity $2R_L\phi_a/L_0$ to both members of Eq. (4.4) and writing it in the form,

$$\dot{\phi}_a+2R_L\phi_a/L_0=\frac{E}{N}\sin(wt)+A$$

$$+\frac{2R_L}{L_0}\left[\phi_a-\frac{1}{k}\sinh(k\phi_a)\right]. \quad (4.6)$$

This equation is similar to (3.4). By the same procedure explained in Section 3, it may be transformed into the following integral equation,

$$\phi_a(t)=\phi_0(t)+m\int_0^t e^{-m(t-u)}\left[\phi_a(u)-\frac{\sinh}{k}k\phi_a(u)\right]du. \quad (4.7)$$

In this case the solution is obtained as the limit of the following sequence,

$$\phi_1(t)=\phi_0(t)+m\int_0^t e^{-m(t-u)}\left[\phi_0(u)-\frac{\sinh}{k}k\phi_0(u)\right]du. \quad (4.8)$$

$$\phi_{r+1}(t)=\phi_0(t)+m\int_0^t e^{-m(t-u)}$$

$$\times\left[\phi_r(u)-\frac{\sinh}{k}k\phi_r(u)\right]du. \quad (4.9)$$

so that

$$\operatorname*{Limit}_{r\to\infty}\phi_r=\phi_a.$$

This process leads to the same for for the time constant, T_0, as the polynomial approximation of Section 3.

The Steady-State Solution

The steady-state current, i_L, may be obtained by substituting ϕ_a from (4.4) into (2.17) and obtaining,

$$i_L=\frac{2N}{L_0k}\sinh(k\phi_a)-2N_0E_0/R_0N. \quad (4.10)$$

To calculate the first approximation of the steady-state load current, ϕ_{0s} as given by (3.21) may be substituted for ϕ_a in (4.10) and the result written in the form,

$$i_L=\frac{2N}{L_0k}\sinh\left[\frac{kA}{m}-\frac{kE_m}{NZ}\cos(wt)\right]-2N_0E_0/R_0N. \quad (4.11)$$

The harmonic content of the steady-state load current may be obtained by means of (4.11) and the fol-

lowing expansions in terms of modified Bessel functions of the first kind, $I_n(x)$.

$$\cosh[x\cos(wt)]=I_0(x)+2\sum_{n=1}^{\infty}I_{2n}(x)\cos(2nwt) \quad (4.12)$$

$$\sinh[x\cos(wt)]=2\sum_{n=1}^{\infty}I_{(2n+1)}(x)\cos(2n+1)wt.^{6} \quad (4.13)$$

If the hyperbolic sine in (4.11) is expanded and the relations (4.12) and (4.13) are used, the steady-state load current may be written in the following form,

$$i_{LS}=\frac{2N}{kL_0}\sinh(P)[I_0(Q)+2\sum_{n=1}^{\infty}I_{2n}(Q)\cos(2nwt)]$$
$$-\frac{4N}{kL_0}\cosh(P)\sum_{n=4}^{\infty}\{I_{(2n+1)}(Q)\cos[(2n+1)wt]\}$$
$$-2E_0g_0/L_0 \quad (4.14)$$

where

$$P=kg_0E_0/N, \quad Q=kE_m/NZ. \quad (4.15)$$

The expression (4.14) indicates the relative magnitudes of the various harmonics of the steady-state load current.

5. THE RESPONSE OF THE AMPLIFIER CALCULATED BY THE METHOD OF FINITE DIFFERENCES

The two methods of analysis presented above are based on analytical approximations of the magnetization curve of the core material. A method based on the calculus of finite differences will now be presented for the computation of the amplifier response when the magnetization curve is given graphically.

The differential equation, (2.16), for the determination of the core flux, ϕ_a, is a nonlinear equation of the first order, and hence, an approximate solution may be effected by the method of finite differences. In order to do this, replace the continuous time variable, t, by

$$t=rh, \quad r=0, 1, 2, 3, 4, \cdots \quad (5.1)$$

and h, the tabular interval. A practical procedure is to take h a certain fraction of the period, $T=2\pi/w$, of the applied output potential, say,

$$h=T/24. \quad (5.2)$$

The derivative, $\dot{\phi}$, may be approximated by,

$$\dot{\phi}\approx(\phi_{r+1}-\phi_r)/h=\dot{\phi}_a. \quad (5.3)$$

If this is done, Eq. (2.16) may be replaced by the difference equation,

$$\phi_{r+1}=\phi_r+\frac{h}{N}E_m\sin(\pi r/12)+hA-hF(\phi_r)$$
$$r=0, 1, 2, 3, 4, \cdots, \quad (5.4)$$

where $\phi_0=0$, and

$$F(\phi)=\frac{2lR_L}{N^2}H(\phi), \quad A=2R_LN_0E_0/N^2R_0. \quad (5.5)$$

The function $F(\phi)$ is proportional to the magnetization curve $H=H(\phi)$. Equation (5.4) enables successive values of ϕ to be computed and thus ϕ_a may be obtained as accurately as desired. The load current, i_L, is obtained by substituting

$$\dot{\phi}_a=\dot{\phi}=\frac{E_m}{N}\sin(wt)+A-F(\phi), \quad (5.6)$$

into (2.17). This gives,

$$i_L=\frac{1}{R_L}[NF(\phi_r)-AN]=i_L(r) \quad \text{with} \quad i_L(0)=0. \quad (5.7)$$

This procedure gives an approximate method for determining the time required for the flux and current to reach a steady-state oscillation and thus enables the approximate time constant of the circuit to be determined.

VI. CONCLUSIONS

The above analysis indicates that the response of magnetic amplifiers of the type considered may be studied by the solution of a nonlinear differential equation of the first order. The methods presented show that in addition to the conventional treatment, it is possible to write the fundamental nonlinear differential equations of this type of circuit and that the application of the methods of nonlinear mechanics to their solution leads to interesting and useful results.

[6] N. W. McLachlan, *Bessel Functions for Engineers* (Oxford University Press, London, 1934), p. 50.

A Study of the Annealing Kinetics in Cold Worked Copper*

DWAIN BOWEN, R. R. EGGLESTON, AND R. H. KROPSCHOT
Atomic Energy Research Department, North American Aviation, Incorporated, Downey, California
(Received December 31, 1951)

The resoftening kinetics for cold work in copper have been studied using residual resistance as a measure of the degree of recovery. The specimens were quickly heated to the annealing temperature, held at temperature for a measured time, and quenched for measurement. It was assumed that the cold work could be characterized by a number of lattice defects n and that the residual resistance change produced by these defects obeyed Matthiessen's rule. It was found that the resoftening could be represented by a single process of activation energy 28.3 kilocalories per mole. The complete annealing kinetics are described by a fourth-order reaction, $dn/dt = -\nu n^4 e^{-E/RT}$.

I. INTRODUCTION

THE temperature dependence of the annealing of cold work in metals suggests that this process is governed by some type of kinetic reaction. To study these kinetics in detail it is necessary to know the dependence of the property measured on the configuration of the material during annealing. For this reason, residual resistance in copper was chosen as the property to be measured since it was felt a reasonable assumption could be made about its dependence on cold work. The degree of cold work was characterized by a concentration of lattice distortions that are annealed by thermal treatment. In the present fashion these distortions would be called dislocations, but since no detailed description of the distortion is required for this study the more general terms will be retained.

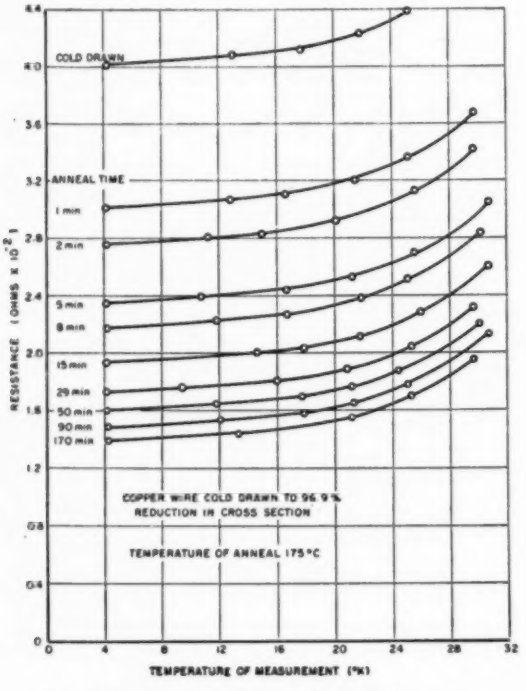

FIG. 1. Low temperature resistance of a copper wire—time of anneal as parameter.

It was assumed that the distortions change the scattering cross section for electron waves but do not change the number of carriers. If this be so, then Mattiessen's rule will be obeyed, and the change in residual resistance from the dead annealed condition will be proportional to the concentration of lattice distortions. On the basis of this set of assumptions a series of residual resistance measurements were analyzed.

II. EXPERIMENTAL

The low temperature measurements of resistance are made by standard potentiometric methods. The temperatures at which the measurements are made are determined from a calibrated platinum resistance thermometer. The required low temperature is obtained in a secondary cryostat as described by Smith and Kropschot.[1] It consists of three concentric Dewar flasks, the outside one containing liquid nitrogen, the intermediate one containing liquid helium, and the inner one containing the specimen, the platinum resistance thermometer, and a graphite heater. Liquid helium, supplied by a Collins helium cryostat, initially fills both the intermediate and center Dewars for a measurement at the helium point. Subsequently, the helium in the center Dewar is evaporated by using the graphite heater. A heat exchanger together with the above-mentioned graphite heater make it possible to attain the desired temperature with a temperature stability of 0.2°K. By placing the specimen and thermometer in close contact, the specimen temperature can be measured to an accuracy of 0.5°K in the range 10° to 40°K.

The very low resistivity of Cu at the liquid helium point made the use of long wires with small cross-sectional area desirable. The wire† was continuously cold drawn at room temperature from No. 25 to No. 40 B. and S. gauge, giving a reduction in cross-sectional area of 96.9 percent. It was assumed that the treatment produced uniform homogeneously cold worked wire of constant diameter. The purity of the copper was not definitely established, however; the copper plus silver

* This paper is based on studies conducted for the AEC under contract AT-11-1-GEN-8.

[1] C. A. Smith and R. H. Kropschot (to be published).

† Kindly furnished by the Anaconda Wire and Cable Company.

assay ran at a minimum of 99.952 percent and was oxygen free.

The specimens are approximately 14 inches long and are wound on a fired lavite form to avoid handling and prevent shorting. The lavite holder is designed so that the specimen is in contact with it over only a small fraction of its total length, thus giving the specimen a very fast response to temperature variations. The ends are silvered soldered to copper lugs on the lavite holder. This procedure undoubtedly anneals the ends; however, it is limited to less than 1/4 inch at the end, or less than 4 percent of the total length. There are no other opportunities for the specimens to receive an unknown thermal treatment.

The annealing of the specimen is done by subjecting it to "pulses" of temperature, with a measurement of residual resistance between each pulse. Ideally, the temperature pulse can be thought of as an instantaneous rise to the desired temperature, an accurately known time at temperature, and an instantaneous quench back again to the base temperature. Experimentally, the sample is immersed for a known time in a bath of molten wax maintained at the desired temperature, then quenched in a bath of carbon tetrachloride at room temperature. Uncertainties in time-temperature history of the pulses have been made as small as possible, both by favorable wire holder design as discussed above, and by making the heat capacity of the temperature bath orders of magnitude greater than the holder and its specimen. It is estimated that the time required to get to temperature is less than 4 seconds while the quench time is not greater than 1 second. The annealing and quench techniques were checked for possible chemical effects on the specimen but none were found.

The electrical resistance of the as-drawn copper wire and the resistance after successive anneals at 175°C, for periods varying from 1 to 170 minutes duration, are plotted against the absolute temperature of measurement in Fig. 1. In each test, the resistance was measured to 30°K as a partial check of the assumption that Matthiessen's rule is obeyed. If this be true, then the change in resistance on annealing should be the same at the various temperatures of measurement. These differences are plotted as a function of temperature of measurement in Fig. 2. The differences are sensibly constant to 20°K.

Since only differences in residual resistance are required, the value at the helium point (4.2°K) was used in all calculations rather than an extrapolation to 0°K. In the remainder of this paper, the resistance at 4.2°K will be referred to as the residual resistance.

By using this thermal pulsing technique the residual resistance can be obtained as a function of time for various annealing temperatures. These data are illustrated in Fig. 3, for annealing temperatures from 100°C to 250°C. For each temperature the annealing curve is obtained on a single sample, but the curves for the several temperatures had to be made on separate

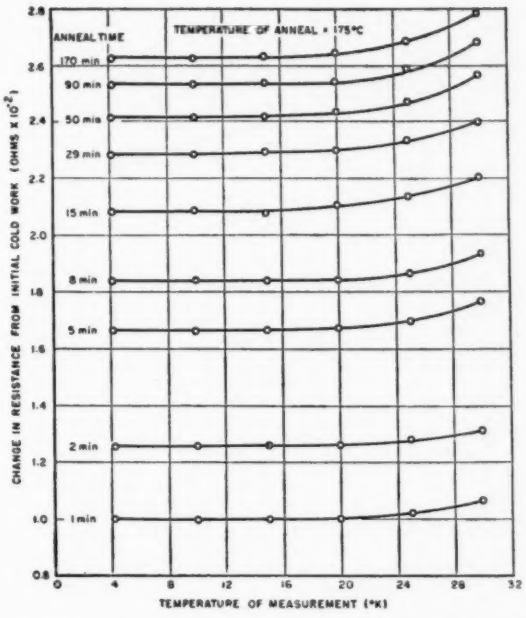

FIG. 2. Low temperature change of resistance of a copper wire—time of anneal as parameter.

samples. Since complete uniformity of the wire was assumed, the data were all normalized to an initial resistance of 0.0425 ohm.

III. TEMPERATURE DEPENDENCE

Using the isothermal data of Fig. 3, cuts were made at various values of residual resistance, and for each cut the logarithm of the time required to reach that value of resistance was plotted against the corresponding reciprocal of the absolute temperature of anneal. These data fall quite closely on straight lines as shown in Fig. 4. Since each cut gives a straight line and the lines are all reasonably parallel, one can infer that the rate of annealing is determined by a single activation process over the entire temperature range,

$$\text{rate} \sim e^{-E/RT}, \tag{1}$$

where E is the activation energy, R the gas constant, and T the absolute temperature. The activation energy is obtained from the slopes of the straight lines. The average value is 28.8 kilocalories per mole with a standard deviation of 3.9 percent.

This technique for analyzing the data for activation energy does not depend on knowing the connection between lattice distortion and property measured; in fact, any property sensitive to the annealing could be used in such a determination. Decker and Harker[2] used the intensity of x-ray diffraction lines to obtain a value of 22.4 kilocalories per mole for spectroscopic copper, and 29.9 kilocalories per mole for o.f.h.c. copper.

From these considerations a single activation energy (perhaps dependent on the purity of the sample used)

[2] B. F. Decker and D. Harker, Trans. Am. Inst. Mining Met. Engrs. 188 (1950).

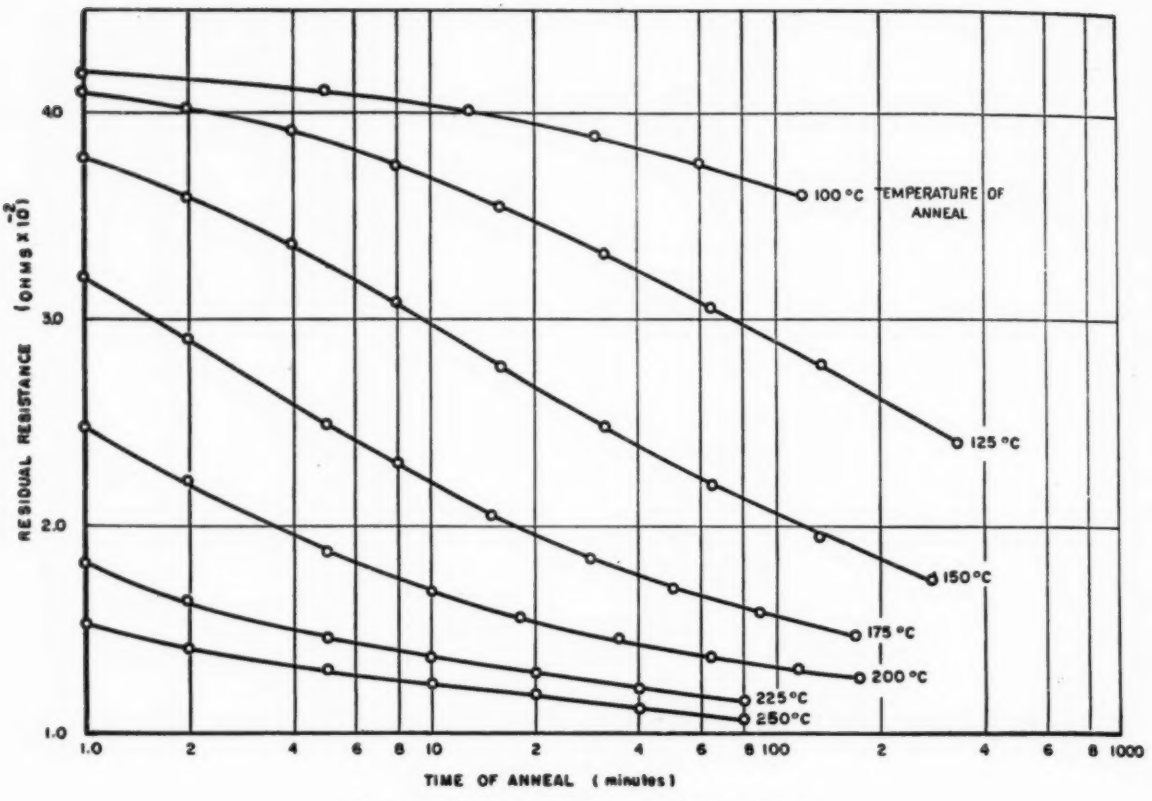

FIG. 3. Isothermal annealing of residual resistance.

appears to be valid over the entire temperature range that was investigated (100°C to 250°C). This covers the range that is usually described by the term resoftening and extends into the region of recrystallization. Any detailed kinetics that are proposed must be consistent with this phenomenological value of activation energy.

IV. DETAILED KINETICS

Let the number of lattice distortions per unit volume be designated by the symbol n. Equation (1) can then be written

$$dn/dt \sim e^{-E/RT}. \tag{2}$$

In accordance with chemical rate formalism this equation can be completed by setting the proportionality constant equal to $-\nu_\alpha' n^\alpha$,

$$dn/dt = -\nu_\alpha' n^\alpha e^{-E/RT}, \tag{3}$$

where α is the order of the reaction, and is probably an integer, and ν_α' is the frequency factor corresponding to the order α. Other investigators[2-7] have tried to interpret their data on the basis of a rate equation, but in each case they have tacitly assumed that the reaction was of first order ($\alpha=1$). In the present study the value of α was determined as the integer value that most adequately described the data according to Eq. (3).

By virtue of the assumption that Matthiessen's rule is obeyed, one can write

$$(\rho-\rho_0) \sim n, \tag{4}$$

where ρ is the residual resistance and ρ_0 is the residual resistance of the sample in the dead annealed condition. Combining Eqs. (3) and (4) one has

$$\frac{d(\rho-\rho_0)}{dt} = -\nu_\alpha(\rho-\rho_0)^\alpha e^{-E/RT}. \tag{5}$$

For an anneal at constant temperature such as was obtained in any one of the temperature pulses, Eq. (5) integrates to

$$\nu_\alpha e^{-E/RT} = K_\alpha(T)$$

$$= \frac{1}{(\alpha-1)(t_i-t_{i-1})}\left\{\frac{1}{(\rho_i-\rho_0)^{\alpha-1}} - \frac{1}{(\rho_{i-1}-\rho_0)^{\alpha-1}}\right\}, \tag{6}$$

where ρ_i is the residual resistance after the ith pulse in the data of Fig. 3 and (t_i-t_{i-1}) is the duration of the pulse.

The data for each temperature pulse were inserted in Eq. (6) for a variety of choices of α, and the corresponding $K_\alpha(T)$ computed. A value of 0.01 ohm was used as the dead annealed value of residual resistance.

[2] G. W. Brindley, Phys. Soc. Rept. Conference on Strength of Solids, **95** (1948).
[4] M. Balicki, J. Iron Steel Inst. **151**, 181 (1945).
[5] P. C. Varley, J. Inst. Metals, **75**, 185 (1948–49).
[6] M. Cook and T. Richards, J. Inst. Metals, **73**, 1 (1947).
[7] W. F. Brandsma, Z. Physik. **48**, 703 (1928).

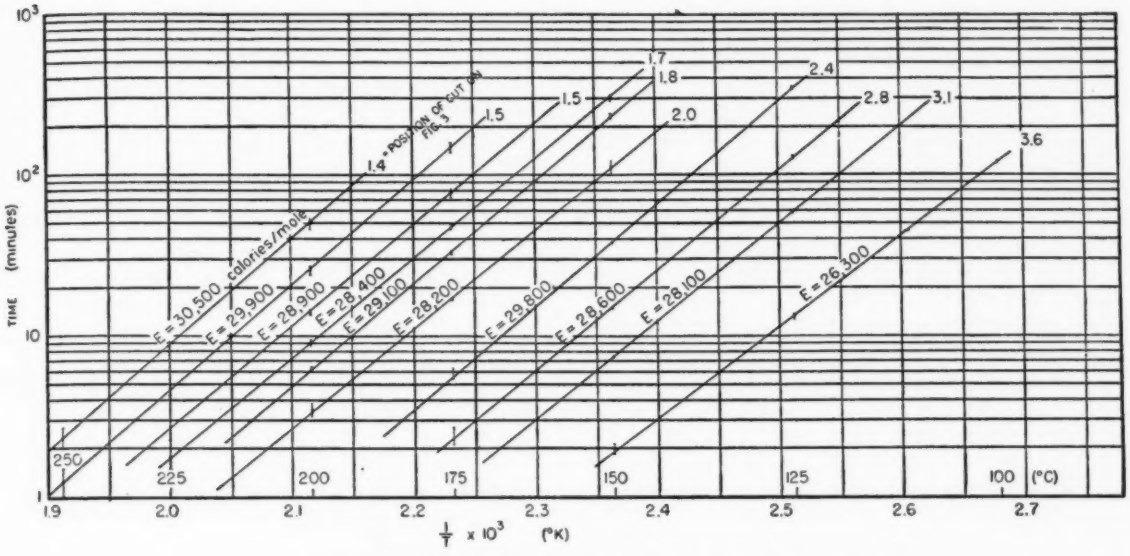

FIG. 4. Phenomenological determination of activation energy.

ρ_0. This value was chosen as the asymptote that the data of Fig. 3 were approaching. A long time anneal at 450°C gave a somewhat lower value, but the grain growth was extreme. In any case, the value of K_α is not sensitive to the choice of ρ_0 within a range that is reasonable, with the possible exception of the 250°C anneal. For this special case ρ_0 and α were both varied to give the most consistent K_α (250°C). A residual resistance of 0.0098 ohm was found best.

All $K_\alpha(T)$ having the same value of T and α were grouped together. One now has two criteria to decide the correct value of α: at a given temperature and order all the K_α should be equal; and when the logarithm of K_α is plotted against the reciprocal of the absolute temperature one should get a straight line with slope equal to the previously determined activation energy, 28.8 kilocalories per mole. These criteria are summarized in Figs. 5, 6, and 7. It is apparent that of these values for α, 4 is the best choice. It has the least spread in K at a given temperature, and the slope of 28.3 kilocalories per mole falls within the standard deviation of the previous determination of activation energy, while $\alpha=3$ or 5 have both a wide spread in K at each temperature, and the activation energies are more than 15 percent different from the previous determination. For α values of 2 and 6 the deviations are even larger. The data for the 100°C and 125°C anneal deserve special attention since they do not all fall on the 28.3 kilocalorie per mole line. The sequence of pulses (pulse number) has been indicated on Fig. 6 for these data. It is evident from this sequence that K_4 tends toward the 28.3 kilocalorie per mole line for large pulse numbers. This effect at the low temperatures of anneal could be produced by inhomogeneity in the initial cold work. In particular, a surface layer only a few ten thousandths of an inch thick with an appreciably higher concentration of lattice distortions than the bulk of the material could be responsible. In the 150°C anneal only the first pulse shows the effect (K_4 is too large). The data for the higher temperatures of anneal are not affected because the change in the bulk of the material is then large enough to mask the effect in the first few pulses when it should be observed. From this one can conclude that the annealing proceeds as

$$\frac{d(\rho-\rho_0)}{dt}=-\nu_4(\rho-\rho_0)^4 e^{-E/RT}, \tag{7}$$

or

$$\frac{dn}{dt}=-\nu_4' n^4 e^{-E/RT}, \tag{7a}$$

with an activation energy of 28.3 kilocalories per mole (the value as determined from Fig. 6 is taken as the

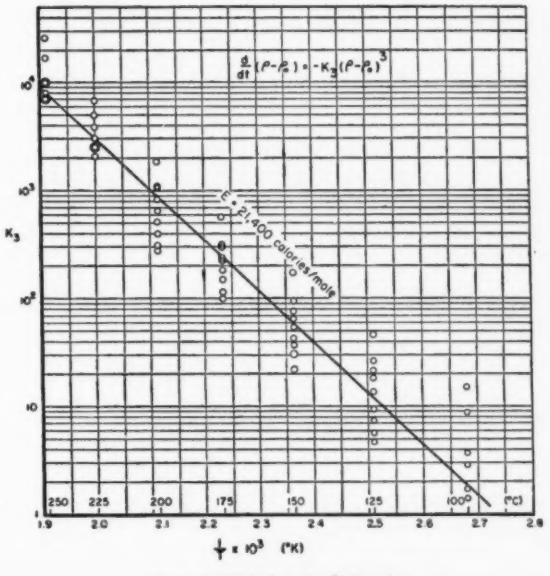

FIG. 5. Third-order kinetics.

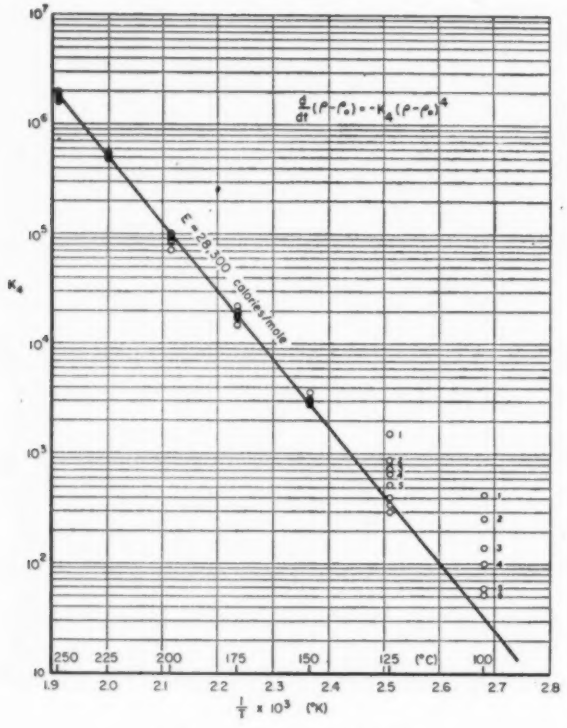

FIG. 6. Fourth-order kinetics.

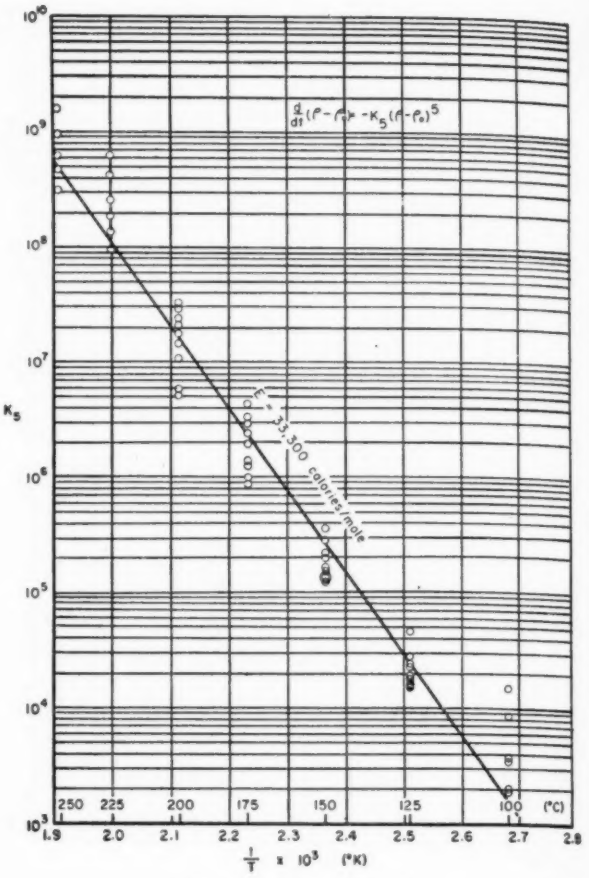

FIG. 7. Fifth-order kinetics.

most properly weighted average) and a frequency factor of 10^{18} ohm^{-3} minute^{-1} or 6.7×10^{33} ohm^{-3} centimeter^{-3} second^{-1}.

V. A RE-EXAMINATION OF ASSUMPTIONS

A fourth-order reaction kinetics is sufficiently unconventional that many may find it difficult to accept the usual implication that the order of the reaction indicates the number of reactants (in this case, lattice distortions) that cooperate in each individual event. It may be that the actual kinetic picture is different from this, but it must approximate this simple fourth-order reaction. It is possible that the assumptions concerning the connection between residual resistance and lattice distortions are in error. If one assumes that the lattice distortions anneal as a first-order reaction, but the connection between lattice distortions and change in residual resistance is such as to give a fourth-order reaction on resistance; then one must have that

$$n\frac{d(\rho-\rho_0)}{dn}\sim(\rho-\rho_0)^4 \tag{8}$$

or

$$-n\sim[e^{-(\rho-\rho_0)^3}-1]. \tag{9}$$

If one assumes a second-order reaction on n, then

$$\frac{1}{n}\sim\frac{1}{(\rho-\rho_0)^3}-\frac{1}{(\rho_i-\rho_0)^3}. \tag{10}$$

While it is possible that the residual resistance has one of these dependences (Eqs. (9) or (10)), it is difficult to appreciate why this would be so, particularly since they are both rather violent functions.

VI. DISCUSSION

If one accepts the implications of four-element cooperation contained in the previous formulation, then this represents a stringent boundary condition on any theory of plastic deformation. The lattice disorganization that results must be of such a nature that four element cooperation is possible. The authors have not investigated all the current theories in detail to see for which ones this is possible. In no case is it immediately apparent how to achieve the cooperative action.

The fourth-order kinetics is of such a nature that if one fits a first-order equation to the initial portions of a constant temperature annealing curve, then the latter portions will seem to be annealing too slowly for the first-order theory. This may be the reason several investigators have had to assume two processes taking place in the lattice in order to adequately describe their data. If this be so, then perhaps resoftening and recrystallization are only two aspects of the same process.

Chemical Reactions in Barium Oxide on Tungsten Emitters*

R. C. Hughes, P. P. Coppola and H. T. Evans
Philips Laboratories, Incorporated, Irvington-on-Hudson, New York
(Received January 10, 1952)

When barium carbonate is heated in vacuum in contact with tungsten, the following reactions may occur in sequence as progressively higher temperatures are reached: (1) $WO_3+BaCO_3 \rightleftarrows BaWO_4+CO_2$. (2) $3BaCO_3+W \rightleftarrows Ba_3WO_6+3CO$. (3) $BaCO_3 \rightleftarrows BaO+CO_2$. (4) $6BaO+W \rightleftarrows Ba_3WO_6+3Ba$.

At a temperature of approximately 600°C, reaction (2) begins to occur with appreciable speed. Reaction (3) proceeds at 800–900°C. Reactions (2) and (3) may be made to proceed simultaneously, the preponderance of one over the other depending upon state of subdivision and intimacy of admixture of the reactants. Under favorable conditions, reaction (2) may be driven to completion with almost total absence of reaction (3). Reaction (4) progresses with appreciable speed at temperatures over approximately 1000°C.

Activated cathodes of BaO on W will have an interface of Ba_3WO_6 formed by reactions (2) or (4), or both, unless unusual precautions are taken to avoid this. The end result of heating the cathode is the conversion of the entire thickness of the oxide coating to the basic tungstate. The resulting coating of Ba_3WO_6 on W is unreactive and nonvolatile at temperatures up to 1300°C, and provides no significant thermionic emission.

INTRODUCTION

A KNOWLEDGE of chemical reactions occurring in barium oxide on tungsten cathodes should aid in understanding many factors of interest, such as the processes determining life of the cathode, and the formation of interface layers possibly affecting electrical properties of the cathode.

A limited amount of previous work dealing primarily with the identification of the interface compounds formed in alkaline earth oxide on tungsten cathodes has been published; Rooksby and Steward[1] have first described the identification of compounds having the formula R_3WO_6 at the interface of alkaline earth oxide on tungsten cathodes. Subsequently, Hensley and Affleck[2] have studied the formation of interface compounds in barium oxide on tungsten cathodes. Though erroneously identifying the interface as barium tungstite, as admitted in a later publication,[3] Hensley and Affleck present interesting and useful information. They show that the interface compound is stable in air, at least for the time required to obtain the x-ray diffraction pattern. By evaporation of BaO onto a cold tungsten wire which had immediately before been cleaned by flashing to 1800°C, followed by heating the BaO coating on tungsten at 850°C for 24 hours, they find an interface compound (now known to be Ba_3WO_6) to be formed. From this experiment it might be concluded that Ba_3WO_6 can be formed by reaction at 850°C between W and BaO. Hensley and Affleck also show that, in the case of $BaCO_3$ coatings on W, an interface of 1.5×10^{-4} cm thickness is formed during the 10 minutes required for conversion of $BaCO_3$ to BaO, and that this thickness remains unchanged throughout 1000 hours subsequent operation at 875°C. The present authors consider this result inconsistent with the finding of reaction between BaO and W in 24 hours at 850°C or alternately, to indicate that equilibrium cannot be established at 850°C between the barium oxide and tungsten, when these are separated by an appreciable thickness of tungstate. Hensley and Affleck also report that when a mixture of powdered tungsten and barium carbonate was coated on a cathode sleeve and heated in vacuum, a large percentage of tungstite (actually Ba_3WO_6) was formed.

In a subsequent paper commenting on Hensley and Affleck's results, Rooksby and Steward[4] offer the following explanation:

"The observation that the barium compound could be formed from a mixture of $BaCO_3$ and powdered tungsten on heat treatment in a very high vacuum may be explained in the following manner. For production of the Ba_3WO_6 compound from such a mixture, limited oxidation of the tungsten is first of all required, and such oxidation is a possible consequence of degassing of the barium carbonate. It follows as a result of the limited oxidation that a high concentration of barium oxide in proportion to tungsten oxide exists in the mixture. Thus, Ba_3WO_6 is formed in preference to $BaWO_4$, provided a high reaction temperature, say, 1300°C or more, is reached. We have carried out similar heat treatments, both in vacuum and in an inert atmosphere, of mixtures of barium carbonate and metallic tungsten. The products from equimolecular mixtures often contained much Ba_3WO_6, but they invariably contained free tungsten and unreacted barium oxide as well."

Rooksby and Steward[5] have shown that Ba_3WO_6, which has a face-centered cubic lattice with a cell edge of $a_0=8.64$A, is isostructural with $(NH_4)_3FeF_6$ as described by Pauling.[6]

* Presented at the meeting of the Division of Electron Physics, American Physical Society, Washington, D. C., November 1, 1951.

[1] H. P. Rooksby and E. G. Steward, Nature **157**, 548 (1946).
[2] E. B. Hensley and J. H. Affleck, J. Appl. Phys. **21**, 938 (1950).
[3] E. B. Hensley and J. H. Affleck, J. Appl. Phys. **22**, 359 (1951).
[4] H. P. Rooksby and E. G. Steward, J. Appl. Phys. **22**, 358 (1951).
[5] H. P. Rooksby and E. G. Steward, Second Congress of International Union of Crystallography, Stockholm, June 1951.
[6] L. Pauling, J. Am. Chem. Soc. **46**, 2738 (1924).

In a very recent publication not available to us until the work described here was completed, Aldrich[7] has described an investigation by mass spectrometric means of the evaporation products of barium oxide from various metals, including tungsten. From the increased ratio of barium to barium oxide obtained (as compared with the ratio obtained in the case of BaO on Pt), he concludes that there is chemical reaction between BaO and the base metal, the effect occurring to a marked degree on Ta, and to a lesser extent on W and Mo.

A factor not taken into account by Aldrich is the possibility that his samples, initially consisting of a carbonate coating on the metal, may react to an appreciable extent during the conversion of carbonate to oxide. At least in all cases involving tungsten his measurements are not made on a sample consisting of BaO in contact with the metal; these are separated by a layer of interface compound. It is highly improbable that equilibrium for the reaction can be established, the rate of production of barium being limited by diffusion of barium oxide through the interface layer. We believe the low Ba/BaO ratios and failure to secure reproducible results are caused by this effect. These comments, however, do not in any way invalidate the results reported by Aldrich as to the actual species evaporated under a given set of conditions, but indicate that his choice of conditions is not such as to permit valid conclusions regarding equilibrium in the reaction between barium oxide and tungsten.

Thus the evidence presented in previous publications is to a considerable degree conflicting. The only conclusion which can be made with certainty is that basic barium tungstate (Ba_3WO_6) is the interface compound in BaO on W cathodes. Whether this is formed as a result of reaction between $BaCO_3$ and W or between BaO and W, or both, is not entirely clear. The temperature, and other conditions necessary for its formation are uncertain. Associated reaction products are completely unidentified.

The general approach employed in this investigation has been to apply simple chemical considerations to determine the probable nature of the reactions responsible for the formation of Ba_3WO_6 and, having so derived plausible hypotheses as to the equations for the reaction, to examine these by the application of critical tests. Two cases are considered:

1. *Formation of* Ba_3WO_6 *from* BaO *and* W—If we assume that BaO and tungsten react to form Ba_3WO_6 and free Ba, unaccompanied by any other reaction products, then the equation for the reaction must be

$$6BaO+W \leftrightarrows Ba_3WO_6+3Ba.$$

2. *Formation of* Ba_3WO_6 *from* $BaCO_3$ *and* W—If $BaCO_3$ reacts with W to give Ba_3WO_6, the W may be expected to reduce the carbonate to yield CO according to the following equation:

$$3BaCO_3+W \leftrightarrows Ba_3WO_6+3CO.$$

Much pertinent information concerning reaction between $BaCO_3$ and W is available. Barium carbonate is disassociated thermally in the following manner[8]:

$$2BaCO_3 \leftrightarrows BaO\cdot BaCO_3+CO_2$$

and

$$BaO\cdot BaCO_3 \leftrightarrows 2BaO+CO_2.$$

The partial pressure of CO_2 over the first of the above reactions is 0.4 mm at 915°C and for the second is 1.9 mm at 1020°C.

In practice, carbonate coatings are "broken down" in the temperature range of 800–900°C, where a small fraction of a millimeter of CO_2 pressure is produced.

Calculations made by Gulbransen and Andrew[9] show that if tungsten is heated, even to rather low temperatures, in an atmosphere containing CO_2, there is limited oxidation of the tungsten according to the equation

$$W+3CO_2 \leftrightarrows WO_3+3CO,$$

and at 400°C, the value for $\log PCO/PCO_2$ is -0.65, increasing with increasing temperature to -0.16 at 1000°C.

Normally, the oxide present on tungsten is partially protective[9] causing the rate of oxidation to decrease as the thickness of the film increases. However, when barium oxide (or carbonate) is in contact with tungsten oxide, there is reaction at low temperature to form a tungstate, thus exposing fresh tungsten to the oxidizing action of carbon dioxide. Thus, removal of CO_2 by reaction with tungsten drives the disassociation of $BaCO_3$ to completion, and by removal of the protective oxide coating the oxidation of tungsten is driven to completion.

The detailed course of the reaction may therefore be

$$3BaCO_3 \leftrightarrows 3BaO+3CO_2$$
$$3CO_2+W \leftrightarrows WO_3+3CO$$
$$3BaO+WO_3 \leftrightarrows Ba_3WO_6.$$

For the reaction between barium oxide and tungsten, less can be predicted from known chemical properties of the reactants. However, it has been suggested[10] and is now rather commonly accepted that free barium is produced by reduction of the barium oxide by any of various metals.

EXPERIMENTAL METHODS AND RESULTS

The experimental approach has been to determine (1) whether tungsten and barium oxide react:

(a) The products of the reaction between barium oxide and tungsten.

[7] L. T. Aldrich, J. Appl. Phys. **22**, 1168 (1951).

[8] *Gmelins Handbuch der anorganischen Chemie*, edited by R. J. Meyer (Verlag Chemie, Berlin, Germany, 1932), eighth edition, System No. 30, p. 305.

[9] E. A. Gulbransen and K. F. Andrew, J. Phys. and Colloid Chem. **53**, 690 (1949).

[10] J. P. Blewett, J. Appl. Phys. **10**, 831 (1939).

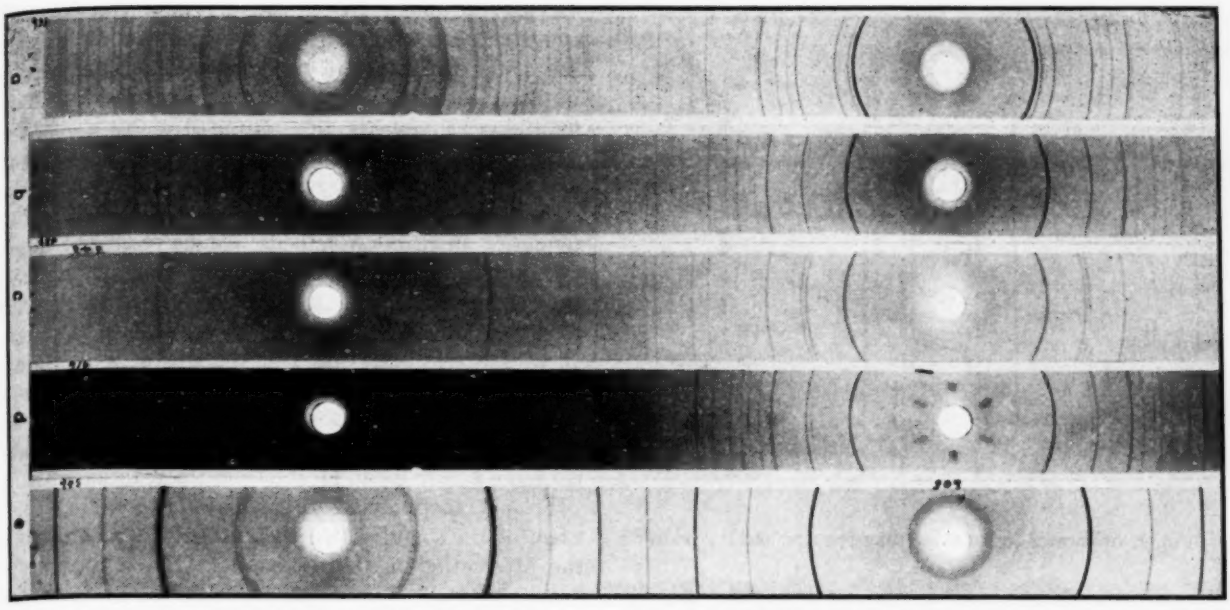

FIG. 1. (a) $BaWO_4$ prepared by precipitation. (b) Ba_3WO_6 prepared by reacting $BaCO_3$ and WO_3 in 3:1 mole ratio in-air at 1300°C. (c) Ba_3WO_6+W; residue from reaction between $BaCO_3$ and W, 3:2 mole ratio (excess W). (d) Ba_3WO_6; transparent film *in situ* on tungsten wire loop after heating wire coated with $BaCO_3$ to 1300°C in vacuum. (e) W.

(b) Quantitative relationships between reactants and products for the reaction between barium oxide and tungsten.

(2) whether tungsten and barium carbonate react:

(a) The products of the reaction between barium carbonate and tungsten.

(b) Quantitative relationships between the reactants and products for the reaction between barium carbonate and tungsten.

(3) some properties of Ba_3WO_6.

X-Ray Identification of Reaction Products

All solid reaction products were examined by x-ray diffraction methods. Powder photographs were made with Philips Debye-Scherrer cameras, 114.7-mm diameter, using CuKα radiation filtered through nickel foil. Specimens were prepared by suspending the finely powdered material in collodion and coating on a Lindemann glass fiber. Care was taken in the case of fired samples to keep exposure to air to a minimum. Standard patterns were prepared of barium tungstate compounds and reaction products, illustrated in Fig. 1(a) $BaWO_4$, (b) Ba_3WO_6, (e) W metal. The normal tungstate was prepared by precipitation from solution. Basic barium tungstate used as a standard was prepared by firing in air at 1300°C an intimate mixture of barium carbonate and tungsten trioxide in molecular proportions of 3:1. Typical patterns of reaction products are also shown in Fig. 1(c), where we see residue after reaction of the intimate mixture of three parts of barium carbonate and two parts of tungsten powder to 850°C (Ba_3WO_6+W), and (d) transparent film *in situ* on a tungsten wire loop after the wire coated with barium carbonate has been heated to 1300°C (Ba_3WO_6).

1. Reaction Between Barium Oxide and Tungsten

A study of the reaction between barium oxide and tungsten is complicated by the difficulty of obtaining pure barium oxide in the presence of tungsten. Barium oxide cannot be prepared and handled in air without the formation of the hydroxide and carbonate.

In the first experiment performed, it was sought only to determine the extent of reaction and conditions necessary for reaction between tungsten and barium oxide, and to determine qualitatively the reaction products. A barium carbonate coating (about 0.002 in. thick) was applied to a tungsten hairpin by a cataphoretic method. The hairpin was mounted for direct resistance heating, glassed in and attached to the vacuum system. Good practice for the processing and activation of cathodes was used. The coating was dissociated at low pressure in the temperature range of 800–900°C and good vacuum established. During this processing reaction between the carbonate and tungsten must have occurred. However, if we accept the data of Hensley and Affleck[11] this layer of reaction product should be of the order of 6×10^{-5} in. and should not constitute a larger proportion of the entire coating thickness of 2×10^{-3} in. than

$$(6\times10^{-5})/(2\times10^{-3})=3\times10^{-2},$$

or roughly 3 percent.

Upon heating the filament to 1100°C, reaction occurred, with the evaporation of material later found to consist of barium, and possibly some barium oxide. This reaction became more rapid as the temperature was increased to 1300°C. After some minutes dark

[11] See reference 2.

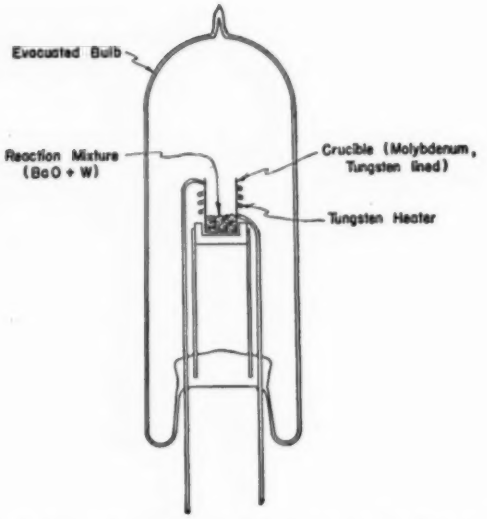

FIG. 2. Apparatus for reacting tungsten and barium oxide.

appearing spots appeared in the coating and gradually extended to cover the entire coated area. At this stage barium evolution ceased. The tube was now removed, the tungsten hairpin taken out, and the coating examined by x-ray diffraction. The coating was found to consist of Ba_3WO_6 (Fig. 1(d)). The dark appearance of this coating was found to be the result of its transparency, permitting the tungsten base to be seen through it.

Quantitative determination of the amount of barium evolved and of Ba_3WO_6 formed in relation to amounts of barium oxide and tungsten reacted, is complicated by the difficulty of obviating both the uncertainties due to the carbonate reaction, and by the direct evaporation of barium oxide. However, an experiment was devised in which both of these effects would be minimized.

An intimate mixture of tungsten and barium oxide, free of carbonate and hydroxide, was obtained by mixing together barium azide, barium formate, and tungsten in the desired proportions. This mixture was introduced into the reaction vessel shown in Fig. 2. At bakeout temperature, the azide decomposes to form barium, which in turn reacts with the formate to produce barium oxide. The net reaction appears to be

$$Ba(N_3)_2+Ba(COOH)_2\rightarrow 2BaO+3N_2+2CO+H_2.$$

Thus no constituent capable of oxidizing tungsten is produced, and after bakeout under vacuum, only barium oxide and tungsten remain. The mixture was prepared from carefully assayed materials and contained equimolar proportions of azide and formate, and a twofold excess of tungsten over that required to form Ba_3WO_6, in order to avoid limitations on the reaction due to depletion of tungsten.

Following bakeout and the establishment of a good vacuum, the mixture was heated to approximately 1100°C, and the evolution of barium followed by observing the effect on the work function of a nearby tungsten strip, and also by observing whether a barium arc could be sustained in the vicinity of the reaction mixture. Barium evolution was at first quite rapid, but became progressively slower, until finally it occurred at a rate insufficient to maintain a nearby heated tungsten surface at maximum activation. This occurred after two months of continuous heating. The observed reduction in reaction velocity is believed to be due to the formation of basic tungstate surrounding each tungsten particle, and the necessity for barium oxide to diffuse through and out of the tungstate. The presence of excess tungsten and the use of a mixture is thought to greatly retard the loss by evaporation of barium oxide, since, except for the surface, barium oxide vapor has many opportunities to come in contact with tungsten before it can escape from the reaction mixture.

From a reaction mixture calculated to contain 0.03216 gram of BaO, and which theoretically should result in the production of 0.0144 gram of Ba, a recovery of 0.0140 gram of Ba was experimentally obtained. This latter figure was obtained by conversion of the evaporated material to sulfate, ignition, weighing, and calculation to Ba. In view of the uncertainties in the method, this is considered to be in good agreement with the theoretical value, and to substantiate the equation

$$6BaO+W\leftrightarrows Ba_3WO_6+3Ba$$

for the reaction between barium oxide and tungsten.

2. *Reaction Between* $BaCO_3$ *and* W

An intimate mixture of barium carbonate (Mallinckrodt Ultra Pure) and tungsten powder (400 mesh and finer) in molar proportions of 3–1 was placed in a tungsten-lined molybdenum crucible suspended by platinum wire within a fused quartz vessel shown in Fig. 3. Provision was made for continuously pumping the vessel with a vacuum system capable of reaching an ultimate pressure of $<10^{-7}$ mm of mercury and for heating the crucible by an externally generated high frequency field. The crucible was brought up in temperature slowly, so as to prevent rise of pressure to a level permitting establishment of an electrodeless discharge within the quartz vessel. The final temperature reached was 800°C (uncorrected) as measured with an optical pyrometer. After about an hour at 800°C, the vacuum began to improve. The temperature was gradually elevated to 1300°C. No evidence of appreciable gas evolution was observed between 800 and 1300°C, thus indicating that the reaction was completed at 800°C. The reaction product was examined by x-ray diffraction and only Ba_3WO_6 detected. Examination under the microscope showed only an occasional particle of unreacted tungsten. We therefore conclude that the reaction occurs quantitatively at 800°C.

A similar mixture of barium carbonate and tungsten was prepared, but in the proportions of 3 moles of barium carbonate to 2 moles of tungsten, thus providing

an excess of tungsten. The barium carbonate was assayed by ignition to determine the true $BaCO_3$ content. The tungsten had been hydrogen fired at 1000°C to remove oxides. The tungsten-lined crucible was vacuum fired at 1300°C, cooled, weighed, and stored in a desiccator until used. A weighed quantity of the $BaCO_3$-W mixture was transferred to the crucible. The crucible was introduced into the reaction vessel, vacuum applied, and the apparatus baked out at 450°C. High frequency heating was applied at a rate sufficiently slow to prevent glow discharge in the reaction vessel. The vacuum was checked periodically. After about 3 hours heating to a final temperature of 800°C gas ceased to be evolved. The crucible was cooled, removed, and weighed promptly. The following results were obtained.

Wt of $BaCO_3$ taken	0.6528g
Wt of W taken	0.4056g
Calculated wt loss	0.0926g
Experimental wt loss	0.0929g

The loss in weight is therefore seen to agree with the calculated loss (for evolution of all carbon as CO) within the limit of error in weighing.

For the qualitative identification of carbon monoxide, apparatus was set up to permit excitation of the gas evolved from a reacting mixture of tungsten and barium carbonate and for recording the spectrum of the light emitted. Since CO_2 can be disassociated into the monoxide and oxygen by the action of an electrical discharge, special provisions were made to avoid this effect.

The reaction mixture, composed of 0.1 gram of

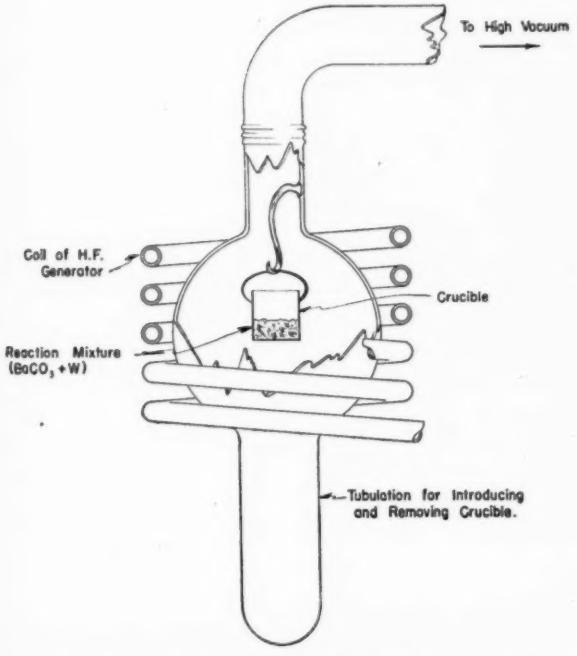

FIG. 3. Apparatus for quantitative study of reaction between barium carbonate and tungsten.

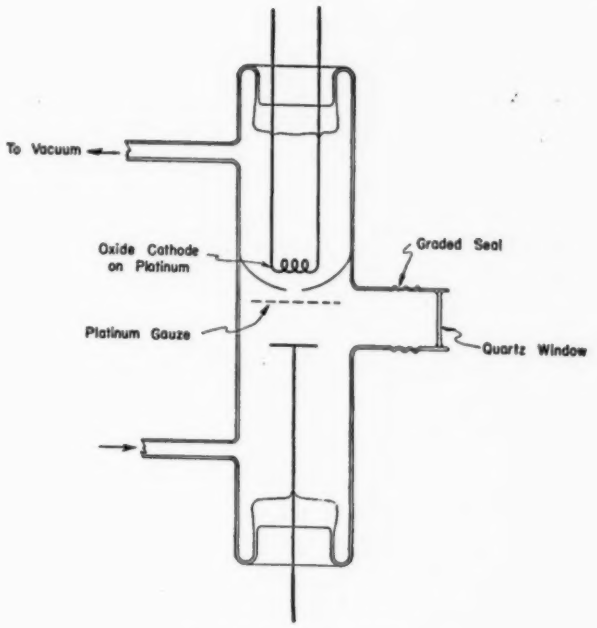

FIG. 4. Discharge tube.

$BaCO_3$ and 0.9 gram of W powder, was placed in a tungsten-lined molybdenum crucible. This in turn was inserted in a quartz capsule provided with a tubulation to lead the generated gas away. An electrically heated oven with Chromel-Alumel thermocouple was placed around the quartz capsule. The gas evolution tube was connected, via a graded seal, to a discharge tube of the type described by Duffendack and Fox.[12] In this tube, electrons for excitation of the gas are supplied by a BaSrO coating on a platinum filament. The electron beam is drawn through a small (1×8 mm) slot in a diaphragm and through a platinum gauze placed next to the diaphragm and supported by a U shaped anode. The gas is introduced so as to flow in a direction opposite to the electron flow. The radiation excited within the force-free volume formed by the U shaped cup closed on the end by platinum gauze is viewed through a fused quartz window. A schematic diagram of the tube and photograph are shown in Figs. 4 and 5, respectively. Radiation from the tube is focused by means of a quartz lens onto the slit of a Bausch and Lomb Medium Quartz Spectrograph. Eastman Spectrum Analyses No. 1 Plates, processed according to the Manufacturers' recommendations, were used for recording spectra. A schematic diagram of the assembled apparatus is shown in Fig. 6.

The gas composition evolved during the entire course of reaction was followed by continuously recording the spectrum. As the reaction mixture was brought up in temperature, sufficient gas to maintain a discharge began to be evolved at 300°C but it was necessary continuously to increase the temperature to maintain the

[12] O. S. Duffendack and G. W. Fox, Astrophys. J. 65, 214 (1927).

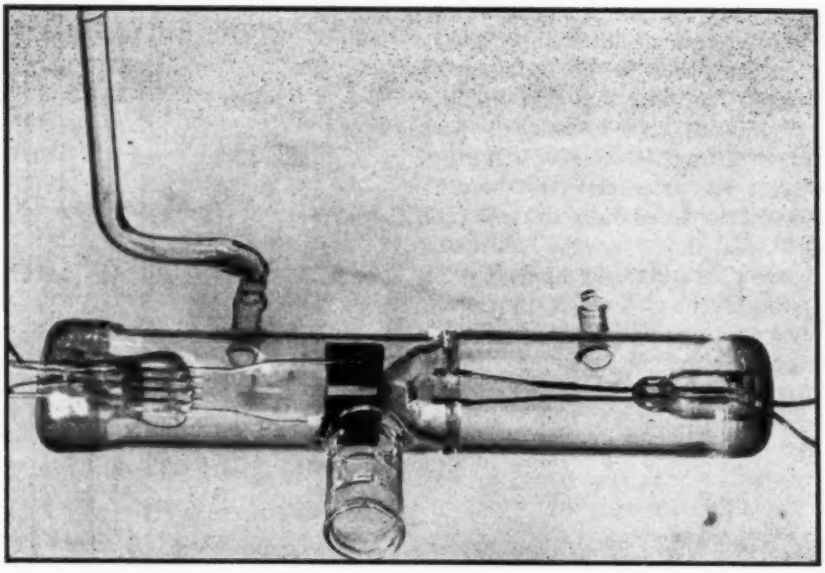

FIG. 5. Discharge tube.

discharge. At 600°C the gas evolution was steady, and continued for approximately 2 hours.

The spectra obtained are shown in Fig. 7 along with a comparison spectrum made with CO_2, introduced from a tank and flowing continuously through the excitation tube. It may be noted that when CO_2 is introduced, the spectrum obtained corresponds to that obtained by Fox, Duffendack, and Barker,[13] no trace of bands assignable to CO being obtained. The apparatus and method are therefore capable of distinguishing between CO_2 and CO. The spectrum of the gas evolved from the reaction between barium carbonate and tungsten shows the presence of predominant proportions of CO, and lesser proportions of CO_2 initially. The proportion of CO_2 present gradually diminishes, until, toward the end of the reaction, the strongest CO_2 bands are only rather faintly present.

The presence of minor proportions of CO_2 is to be expected from the following causes:

(a) Evolution of CO_2 from glass and metal parts of the apparatus, which, due to the relatively low temperature of reaction, cannot be outgassed prior to the run.

(b) Presence of a surface film of oxide on the tungsten powder. According to Gulbransen and Wysong[14] this must be present in a thickness of approximately 50 angstroms or more and corresponding to 0.8 micrograms or more per square centimeter of surface of the powder.

3. *Some Properties of* Ba_3WO_6

Basic barium tungstate was prepared by heating together stoichiometric proportions of WO_3 and $BaCO_3$ in air at 1300°C. A suspension in cellulose acetate binder was applied to a tungsten filament incorporated in a test diode. Following bakeout on the pump, the coated filament was gradually heated, while a positive potential was applied to the plate. No appreciable emission was detected up to an operating temperature of 1300°C.

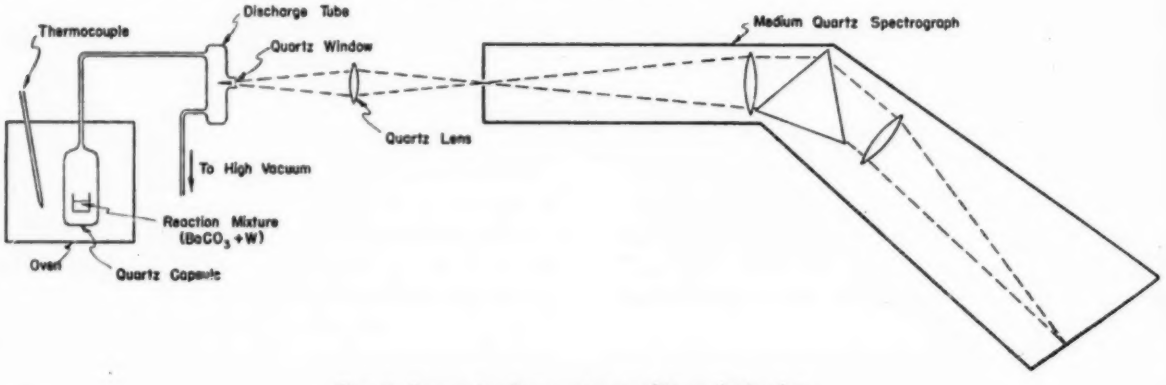

FIG. 6. Apparatus for spectrographic analysis of gas.

[13] Fox, Duffendack, and Barker, Proc. Nat. Acad. Sci., U. S. 13, 302 (1927).
[14] E. A. Gulbransen and W. S. Wysong, Metals Technol. 14, T.P. 2224 (September 1947).

Several hours of operation at 1300°C failed to produce a visible deposit on the wall of the bulb. The x-ray diffraction pattern of the coating, when made promptly after opening the tube, showed the coating to still consist of Ba_3WO_6. A week's exposure of similar coatings to the atmosphere prior to x-ray examination resulted in the formation of $BaWO_4$ and $BaCO_3$.

Coatings of Ba_3WO_6 were found to be evaporated from tungsten at temperatures in the range of 1300–1500°C, the rate of evaporation being rapid at the higher temperature.

Basic barium tungstate, when added to water, could be quantitatively titrated with standardized acid, $\frac{2}{3}$ of the barium oxide present reacting with the acid. An insoluble residue remaining from the titration was found to be $BaWO_4$. The Ba_3WO_6 is thought to hydrolyze in the following manner:

$$Ba_3WO_6+2H_2O\leftrightarrows BaWO_4+2Ba(OH)_2.$$

CONCLUSIONS

We conclude that the following reactions may occur when a barium oxide on tungsten cathode is prepared by applying barium carbonate to tungsten and proceeding with the customary schedule of processing and activation:

$$(1)\quad BaCO_3+WO_3\leftrightarrows BaWO_4+CO_2$$
$$(2)\quad 3BaCO_3+W\leftrightarrows Ba_3WO_6+3CO$$
$$(3)\quad BaCO_3\leftrightarrows BaO+CO_2$$
$$(4)\quad 6BaO+W\leftrightarrows Ba_3WO_6+3Ba.$$

The above reactions occur in sequence as successively higher temperatures are reached. Reaction (1) probably occurs in the range of 300–600°C. Reaction (2) begins to occur at appreciable speed at 600°C, while reaction (3) is normally made to occur at 800–900°C.

Reactions (2) and (3) may be made to occur concurrently, the preponderance of one over the other depending upon state of subdivision and intimacy of admixture of the reactants. Under favorable conditions reaction (2) may be made to proceed nearly quantitatively while reaction (3) is almost entirely suppressed. Reaction (4), required for activation of the cathode, normally is detected only at temperatures of 1000°C or over, and is rapidly driven to completion at 1300°C. All of these reactions result in the eventual production of basic barium tungstate at the interface of the cathode. By means of reaction (4) the entire volume of the oxide coating may be eventually converted to basic tungstate. A coating of basic tungstate is stable in contact with tungsten at temperatures up to approximately 1350°C, and does not emit appreciably. Exposure of the basic tungstate to air or moisture causes hydrolysis to $BaWO_4$ and barium hydroxide or carbonate, though the reactivity upon exposure to air is such as to easily escape detection. An emitter in which the interface of basic tungstate is eliminated or greatly reduced can probably be prepared by applying barium oxide to oxide-free tungsten and adding the necessary barium for activation from an outside source, the entire process being conducted in the absence of substances (other than barium oxide) capable of oxidizing tungsten.

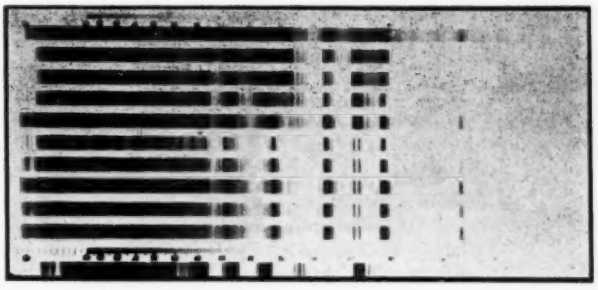

FIG. 7. Spectra of gas evolved during reaction between tungsten and barium carbonate. Spectra were recorded continuously from the beginning of the reaction (top spectrum) to the end of the reaction (next to bottom). The spectrum at the bottom of the figure is of CO_2, for comparison. These spectra show that the gaseous product of the reaction is predominantly CO, with minor proportions of CO_2.

While only barium compounds and tungsten have been dealt with here, we can safely predict that, in general, the activators employed in oxide cathodes will react in a similar manner with carbonates of the coating. Present knowledge of the interface compounds observed to occur will permit a prediction of the chemical reactions responsible for their formation. It is also to be expected that compounds of the other alkaline earth metals will behave similarly to the compounds of barium. Finally, it can be predicted with assurance that compounds other than the carbonate which are thermally decomposable to the oxide with the liberation of a substance capable of oxidizing tungsten will react in a manner similar to the carbonate.

Investigation is being continued on the thermodynamics and kinetics of the reactions between barium carbonate and tungsten and barium oxide and tungsten, and on the chemical and physical properties of basic barium tungstate.

ACKNOWLEDGMENT

It is a pleasure to acknowledge the technical assistance of Roy Anderson, George Beutel, Robert Bronnes, Miriam Ekstein, Martin Miller, and Robert Wassman in this work. This investigation arose from suggestions and observations by E. S. Rittner and O. G. Koppius concerning an unexpected reaction between barium carbonate and tungsten.

On the Kinetics of Ordering in Ni_3Mn

LEWIS R. ARONIN
Massachusetts Institute of Technology, Cambridge, Massachusetts
(Received February 4, 1952)

Kinetic behavior in specimens initially cooled through the ordering range is studied as a function of subsequent prolonged isothermal heat treatments. Room temperature measurement of electrical resistivity and saturation induction give evidence substantiating existence of ordered domains. Anomalous kinetic behavior at intermediate ordering temperatures is interpreted as due to growth of antiphase nuclei. Equilibrium values attainable at low ordering temperatures and multi-valued correspondence between resistivity and magnetic data exhibit dependence upon extent of domain growth.

BY means of resistivity and magnetic induction measurements at elevated temperatures, Thompson[1] observed that ordering in Ni_3Mn proceeded by complex kinetic behavior. It was suggested that two processes were taking place: first, the establishment of an equilibrium degree of local order, and second, a somewhat slower growth of antiphase nuclei. This hypothesis was in line with the earlier conclusion of Sykes and Evans[2] who suggested, from work on Cu_3Au, that the formation of large domains of order was favored by prolonged annealing just below the critical temperature and that local order within domains could follow temperature changes rather easily.

In the course of current studies on Ni_3Mn, further clarifying evidence that ordering in this alloy is a multiple-step process, rather than a simple diffusion characterized by a single activation energy, has been obtained as described below.

A high degree of order was first established in a 25.0 atomic percent alloy by slow cooling from 600°C to 300°C over a ten-day period. This resulted in a drop in room temperature resistivity from 70 microhm-cm to 38 microhm-cm. The alloy went from a paramagnetic condition to ferromagnetic with a saturation induction of 8000 gauss at 20°C.

Further isothermal heat treatment at 400°C and then at 375°C resulted in the growth of additional order as shown in the kinetic curves of Fig. 1. The resistivity values approach apparent limits in what appears to be a simple exponential behavior characterized by relaxation times of 180 hours at 400°C and 370 hours at 375°C.

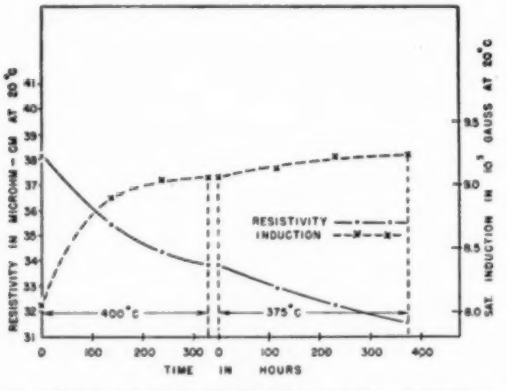

FIG. 1. Kinetic behavior in Ni_3Mn at 400°C and 375°C. Previously ordered by cooling 600°–300°C in 10 days.

Reheating the alloy to 425°C resulted in the unique and possibly most illuminating behavior shown in Fig. 2. Instead of a simple approach to a higher resistivity as might be expected with a decrease in order at 425°C, particularly after the close approach to an apparent equilibrium at the lower temperature of 375°C, there was at first a rather rapid increase in resistivity which reached a peak and then decreased considerably. Raising the temperature to 450°C resulted in similar behavior (Fig. 3) but with a much less pronounced peak.

Consistent with the views expressed above, it would appear that the behavior at 400°C and 375°C could be interpreted as essentially an increase in local order, the rate of cooling employed in the initial ordering treatment being too rapid to permit relaxation to complete equilibrium at these temperatures. Similarly the initial rise in resistivity at 425°C might be considered as being due to a decrease in local order at this temperature—the subsequent drop in resistivity indicating a growth of domain size. Inasmuch as 800 hours were required to observe a leveling off in changes at 425°C, it seems reasonable that the relaxation for growth of domains at 400°C and 375°C is so slow as to be virtually masked by the more rapid growth of order within domains. The lessened effect at 450°C indicates that substantial growth of nuclei occurred at 425°C and,

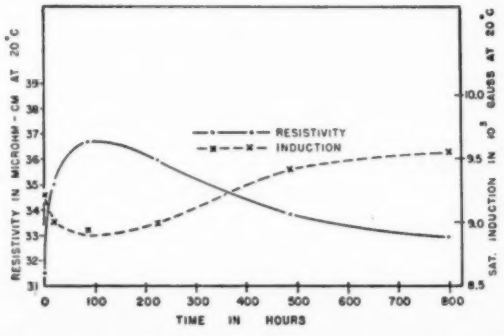

FIG. 2. Kinetic behavior in highly ordered Ni_3Mn at 425°C.

[1] N. Thompson, Proc. Roy. Soc. (London) **A52**, 217–228 (1940).
[2] C. Sykes and H. Evans, J. Inst. Metals **58**, 255–281 (1936).

hence, the effect due to decreasing local order predominates. Although the growth of nuclei is favored at temperatures just below the critical, it should be noted that an effective, though slow growth of domains, is here evidenced considerably below the critical temperature (510°C).

A consequence of this interpretation would be that the magnitude of the reversal observed at 425°C would be influenced by the size of the antiphase nuclei formed in the initial cooling through the ordering range. Measurements made on another melt of similar composition in which the initial cooling through the ordering range resulted in the attainment of higher order at the lower temperatures bear out this prediction inasmuch as the reversals obtained at 425°C and 450°C, although present, were smaller in magnitude. There is also evidence that the final equilibrium values approached at the lower temperatures are influenced by the extent of domain growth previously achieved at the intermediate temperatures.

It will be noted from Fig. 2 that a unique value of induction is not determined by a given value of resistivity, indicating that a given value of either parameter can represent a variety of internal structures as would be expected if the effects of domain growth were present.

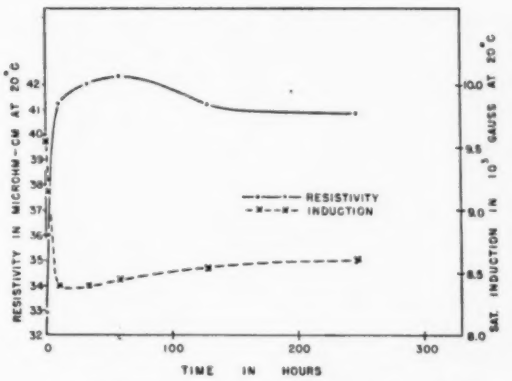

FIG. 3. Kinetic behavior in Ni_3Mn at 450°C. Previously held at 425°C.

Further studies are in progress at the M.I.T. Metallurgical Project under AEC Contract No. AT(30-1)-981.

JOURNAL OF APPLIED PHYSICS VOLUME 23, NUMBER 6 JUNE, 1952

Characteristics of the High Current Tungsten Arc in Argon, Helium, and Their Mixtures*

MERRILL SKOLNIK† AND T. B. JONES
Department of Electrical Engineering, The Johns Hopkins University, Baltimore, Maryland
(Received January 21, 1952)

An experimental study was made of the properties of the high current dc electric arc in argon, helium, and their mixtures at atmospheric pressure. Tungsten-rod electrodes were used over a current range from 10 to 100 amperes. Measurements of the voltage-current and the voltage-electrode separation characteristics were made along with the plasma voltage gradients in both the pure gases and in the mixtures.

It was found that this type of arc was very stable when the system was free from oxide impurities and that the cathodic processes played a major role in the arc mechanism. The results obtained suggest that the value of the anode voltage drop for the inert gas arc over the current range studied is negligibly small. At the higher currents or with smaller diameter cathodes, tungsten was able to evaporate from the cathode in sufficient quantities to influence the character of the discharge. It was observed that the properties of the arc in mixtures of gases were in between the properties observed in the pure gases. The lower ionization potential gas, argon, had more effect on the properties of the arc in mixtures than did helium. As long as there was at least 15 percent argon present in the mixture, the arc properties and appearance were more like those observed in argon than in helium.

INTRODUCTION

THIS paper presents the results of an experimental study of the high current dc electric arc in the inert gases argon, helium, and their mixtures at atmospheric pressure. The electrodes were tungsten rods and the current range was from 10 to 100 amperes. The use of inert gases and high melting-point electrodes permitted the study of the arc under controlled and reproducible conditions without being hindered by chemical reactions and excessive electrode consumption which usually accompanies the study of the arc in other gases.

Very little has been reported in the literature concerning the mechanism of this type of electrical discharge although it is not a new phenomenon and has been widely used in industry. The purpose of this investigation was simply to learn more about the fundamental properties and characteristics of the inert gas arc by carefully exploring its physical and electrical properties under controlled laboratory conditions.

* Assisted by the ONR.
† Submitted in partial fulfillment of the requirements for the degree of Doctor of Engineering at the Johns Hopkins University. Now at the Radiation Laboratory, the Johns Hopkins University, Baltimore, Maryland.

FIG. 1(a). Photograph of the arc chamber.

EXPERIMENTAL EQUIPMENT

The arc was operated in a horizontal position in a cross shaped chamber having approximate dimensions of two feet by two feet. A photograph of the chamber is shown in Fig. 1(a), and a cross section through the plane of the electrodes is shown in Fig. 1(b). This chamber was constructed from a six-inch diameter red brass pipe. The $\frac{1}{4}$-in. diameter tungsten rod electrodes were arranged horizontally and placed in opposite arms of the chamber. One of the electrodes was movable to provide adjustable electrode separation. A two-inch diameter plate glass window was provided in a third arm of the chamber through which a magnified image of the arc could be projected onto a screen for visual observation. The screen was calibrated to give the electrode separation. The fourth arm contained the vacuum outlet, the gas inlet, and a spring loaded pressure relief valve. The purpose of the pressure relief valve was to limit the pressure within the chamber to three psi ($\pm$ one psi) above atmospheric. This was the operating pressure used in these experiments, and for all practical purposes the difference between the results at this pressure and the results at atmospheric pressure was negligible. Water cooling tubes surrounded the chamber, and air blowers were used to limit the surface temperature. The current entered the chamber from each end through relatively large glass-to-metal lead-ins.

All measurements were made using current from a high capacity storage battery with an open circuit voltage of 100 volts. The starting of the arc was accomplished by a high voltage ac breakdown of the gap. The electrodes and gases used were of commercial purity and were claimed by the manufacturer to be better than 99.8 percent pure. The gases were used as received, but the electrodes were dipped before use in hot potassium hydroxide to remove the surface oxides. The presence of surface oxides caused the behavior of the arc to be erratic and produced fluctuations in the arc voltage. The removal of the oxides by this method eliminated these undesirable effects and produced a very stable arc.

METHOD OF MAKING MEASUREMENTS

Special procedures had to be observed in filling the chamber to insure reliable measurements. The filling was accomplished by first evacuating to a pressure of one micron (10^{-3} mm Hg). The chamber was flushed with the gas to be studied and re-evacuated to the one-micron level. The gas was again admitted to the chamber until the pressure was three psi above atmospheric, the operating pressure. The slight positive pressure in the chamber permitted gas to leak out rather than air to leak in through any minute leaks that may have been present. It was not found necessary to evacuate below a pressure of one micron prior to the admission of the test gas.

From the data that was obtained (voltage, current, and arc length), either voltage-current curves or voltage-arc length curves could be plotted. For the purpose of these measurements the electrode separation was taken to be a measure of the arc length. It is realized that the electrode separation is not always the same as the arc length, but it is a convenient approximation.

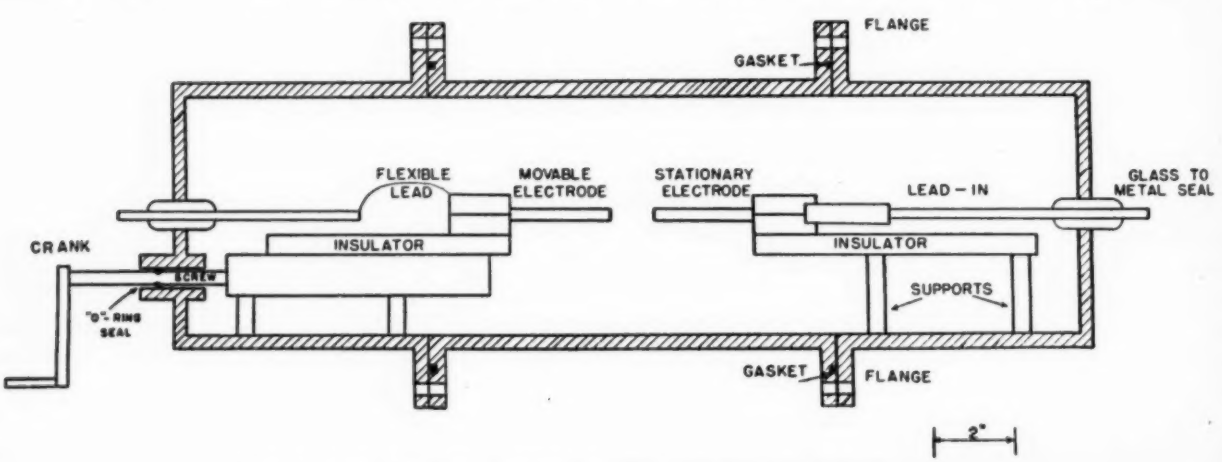

FIG. 1(b). Cross section of the arc chamber through the plane of the electrodes.

The ends of the electrodes were always flat when new. However, if the arc current were high enough to cause the anode to melt,‡ the surface tension of the liquid metal caused the tip of the electrode to become rounded as can be seen in Fig. 2.[1] The cathode, on the other hand, never became hot enough for the above to happen to it. Thus for, the sake of uniformity of the electrode appearance over the entire range of current the anode was rounded at the start of each test with new electrodes by passing a high current through the arc.

ARC APPEARANCE

The appearance of the arc in the inert gases was dependent upon the arc current and the electrode separation. In general, at close electrode separations (<0.3 in.) only the cathode flame was visible while at greater separations both the anode flame and the cathode flame appeared. With increasing current the cathode flame grew slightly in width and length and increased in intensity. When the electrode separation was increased at a constant current, the length of the cathode flame remained essentially constant, but the anode flame grew in length.

Argon

Figure 2(a) is a photograph§ of the argon-tungsten arc at a current of 30 amperes and an electrode separation of 0.2 in. The anode is the rounded electrode on the left. It can be seen that the arc consists chiefly of the cathode flame which was a bluish-white in color. Figure 2(b) shows the same arc at a current of 70 amperes. The chief effect of increasing the arc current is to increase the diameter and length of the cathode flame. In both these figures no flame is visible at the anode. This is similar to the "cathodic discharges" reported by Found[2] and by Druyvesteyn and Penning.[3] At greater separations (>0.3 in.) the anode flame is present (Fig. 2(c)). At low currents this flame is wider and less intense than the cathode flame. Figure 2(c) also shows how the anode and the cathode flame connect with one another. A dark space of approximately 0.04 in. can be seen separating the anode flame and the electrode. This dark space is similar to the dark space observed by Haynes[4] in short duration mercury sparks.

The configuration of the arc flames as illustrated by the three cases of Fig. 2 is termed the "normal" configuration for the flames. All measurements of the arc in argon were taken when the flames were in one of these three configurations. The flames may be above the axis of the electrodes as shown in these figures, or they may be below; there is no detectable difference in the arc characteristics. Because of thermal updraft, however, the flames were usually up.

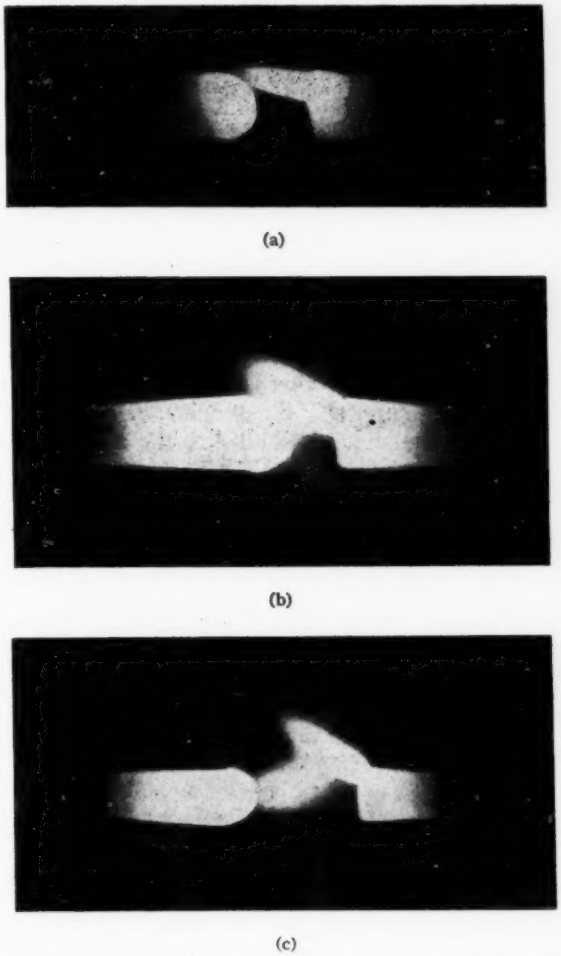

FIG. 2. Appearance of the arc in argon. (a) I=30 amps, electrode separation=0.2 in.; (b) I=70 amps, sep.=0.3 in.; (c) I=70 amps, sep.=0.4 in. The apparent tapering of the hot electrodes is caused by the photography and is not due to thermal expansion.

Photographs taken with color filters and kodachrome film help to resolve the structure of the arc flames. In Fig. 3 is shown a black and white reproduction of a kodachrome negative taken with a yellow filter. The cathode flame is composed of two parts, an intense inner core and a much dimmer outer sheath. A small bright spot can be observed on the anode.‖ This cannot be seen in Fig. 2 because the arc was too intense for it to be resolved on black and white film. If it is assumed that this bright spot represents the area over which the electrons enter the anode, then the anode current density at 35 amperes is of the order of 10^4

‡ In argon this current was about 85 amperes while in helium it was about 70 amperes. This difference in observed currents is probably due to the fact that the helium arc is a hotter arc because its arc voltage is higher for the same arc current.

[1] This phenomenon has also been observed with steel plates as anodes and tungsten rods as cathodes in both argon and helium under conditions simulating inert gas arc welding. See W. B. Kouwenhoven and T. B. Jones, Am. Inst. Elec. Engrs. Misc. Paper 49–129, April, 1949.

§ These photographs were made with a 35-mm camera at f/16, 1/1000-second exposure, and a red filter.

[2] C. G. Found, Gen. Elec. Rev. **37**, 269 (1934).

[3] M. J. Druyvesteyn and F. M. Penning, Revs. Modern Phys. **12**, 170 (1940).

[4] J. R. Haynes, Phys. Rev. **73**, 891 (1948).

‖ Because of loss of contrast in black and white reproduction, the anode spot cannot be seen distinctly in Fig. 3.

FIG. 3. Black and white reproduction of a kodachrome negative taken with a yellow filter. The two parts of the cathode flame may be seen. I=35 amps, electrode separation=0.5 in. The anode is on the left.

amperes/sq cm. This value is much higher than the values usually supposed for anode current densities. The spot on the anode is similar to the microspot observed by Finkelnburg with the high current carbon arc in air.[6] In his experiments the microspot wandered rapidly over the anode face causing voltage fluctuations. The spot in the inert gas arc, however, is stationary.

A qualitative estimate of the minimum value of the cathode current density may be made if the bright luminous area of the inner core of the cathode flame (as shown in Fig. 3) is taken as the area over which the electrons leave the cathode. On the basis of such an assumption the current density is 450 amperes/sq cm for an arc current of 35 amperes.

Helium

The characteristic shape of the flames in helium is much different than in argon, yet the basic phenomena in the two gases appear to be similar. For low currents (<30 amps) the only visible radiation from the helium arc was a flame issuing from the cathode. This is shown in the sketch Fig. 4(a) and was reddish-pink in color. The size of the cathode flame depended to some extent upon the current and was usually no longer than 0.3 in. nor wider than 0.2 in. (approximately). A change in arc appearance took place at a current between 40 and 50 amperes. The region between the electrodes became blue and was symmetrical in shape, Fig. 4(b). At higher currents the cathode flame was no longer visible and the blue region filled the entire space between the electrodes. (Fig. 4(c)). The disappearance of the cathode flame may be gradual or it may be abrupt and was accompanied by a decrease of several volts in the arc voltage drop. The helium arc, just as the argon arc, was very stable provided the electrodes were free from surface oxides.

Argon-Helium Mixtures

The appearance of the arc in mixtures of these gases depended upon the relative concentrations. For mixtures ranging from pure argon to mixtures containing 85 percent helium, the arc had essentially the properties and appearance of the argon arc. Its cathode and anode flames were similar to the arc in argon, and these flames had the characteristic bluish-white color. There was, however, one chief difference which made the presence of helium recognizable. While the inner core of the cathode flame in argon was an intense white, this inner core with mixtures was a reddish-pink, the characteristic color of the helium cathode flame. The length of the reddish-pink inner core increased with the amount of helium present. In a mixture containing 25 percent helium it was barely preceptible, but with a mixture containing 85 percent helium it had reached a length of from 0.2 in. to 0.3 in. Between 85 percent and 95 percent helium the arc looked more like the helium arc and less like the argon arc. Above 95 percent helium there was practically no resemblence to the argon arc.

In general, it may be stated that the appearance of the arc in mixtures was influenced more by small amounts of the lower ionization potential gas, argon, than by small amounts of helium.

Electrodes

While the arc was burning, the anode electrode appeared much hotter than the cathode electrode, except perhaps where the cathode flame attached to the cathode electrode. As can be seen from Fig. 3, the illumination from this spot was very intense. All indications were, however, that the anode was the hotter electrode. Examinations of the electrodes after a test showed that there was no appreciable loss of material from either electrode by melting. The tip of the anode was rounded and shiny while the cathode electrode was comparatively flat and appeared to be coated with a deposit of tungsten. This deposit was presumably vaporized from the hotter anode and transferred to the cathode. In Fig. 5 is illustrated the appearance of the electrodes after the tests in the two gases. In argon the deposit on the cathode extended about 2½ inches from the face

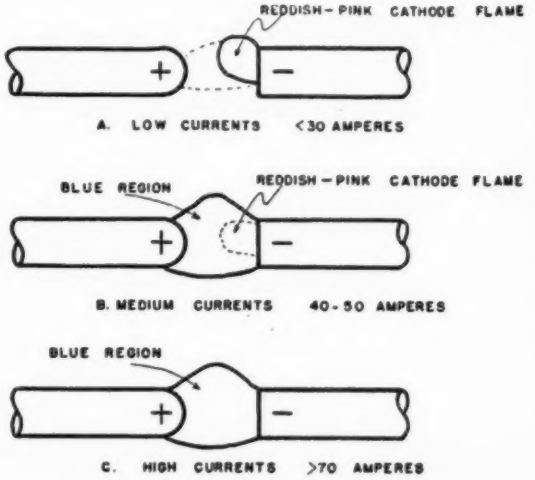

FIG. 4. Sketch of the arc appearance in helium.

[6] W. Finkelnburg, *The High Current Carbon Arc*, FIAT Final Report No. 1052, p. 27.

of the cathode while in helium the deposit extended only about $\frac{3}{8}$ inch but was thicker.

After the arc current had reached a value which caused the anode to liquify and form a rounded tip, a further increase in current caused a rise in the arc voltage making the slope of the voltage-current characteristic positive. This usually occurred with currents greater than those reported here. The rate of rise, however, was small. When the slope was positive, not only was the anode molten but the melted portions could be seen to rotate. It seems very likely that the increase in arc voltage when this occurred was distributed primarily at the anode.

The appearance of the electrodes in mixtures was in between the appearance of the electrodes in the pure gases. When argon was the dominant gas (mixtures with greater than 15 percent argon), the cathode had a deposit of tungsten metal for some length along the electrode; while if helium was the dominant gas, the tungsten was deposited over a shorter length of the electrode.

VOLTAGE-CURRENT CHARACTERISTICS

Argon

In Fig. 6 is plotted a family of voltage-current characteristics for the argon arc at various electrode separations up to one inch. Although the voltage as read on the voltmeter was actually the sum of the arc voltage plus the IR drop in the electrodes, both calculations and measurements indicated that the IR drop was small and could be neglected for the purpose of these measurements. The reproducibility of the data was good considering the nature of the measurements that were made. The curves presented here are believed to be reproducible within ± 0.5 volt if the arc has the same configuration as shown in Fig. 2. The curves of Fig. 6 were obtained with both increasing and decreasing current with no significant differences noted.

The voltage-current curves for the argon arc have the usual negative slope which is typical of low current dc arcs. At the higher currents and close electrode separations the arc voltage was less than the argon ionization potential (15.5 volts). This indicates that the metastable states of the argon atoms probably play an important role in the inert gas arc. The minimum arc voltage under these conditions seemed to approach close to the first excitation potential of argon (11.5 volts) which is near the metastable state.

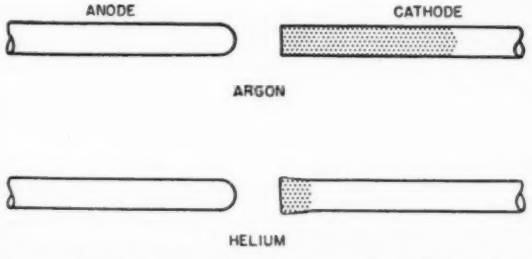

FIG. 5. Sketch of the characteristic shape of the electrodes in the two gases. The shaded areas on the cathode represent deposited tungsten transferred from the anode.

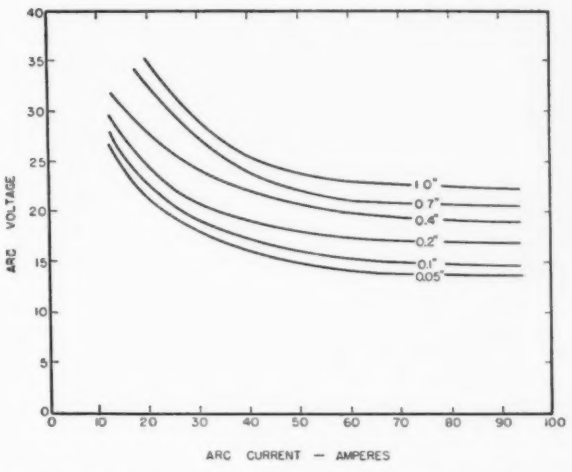

FIG. 6. Voltage-current characteristics of the arc in argon for various electrode separations.

Helium

The magnitude of the arc voltage in helium was almost twice that in argon for the same arc current. In Fig. 7(a) is plotted the arc voltage as a function of the arc current over the current range from 15 to 80 amperes with electrode separations of 0.1 in. and 0.3 in. Two different curves could be obtained for each separation. Over the current range where the two curves for the same separation overlap, the arc characteristic may follow either curve. In general, however, the voltage and current will follow the upper curve for low currents and make a transition to the lower curve at high currents. This transition is indicated by the dotted line connecting the curves for the 0.1 in. separation and represents an average occurrence. The jump from the upper curve to the lower curve was random and did not occur at any definable value of current. It may be an abrupt jump or it may be a gradual change. The transition is accompanied by the appearance of the blue flame of the arc and the disappearance of the reddish-pink cathode flame as described in the previous section. For decreasing current a jump from the lower to the upper curve occurred, but the rise in voltage usually occurred at a lower current and the reverse transition was more gradual.

In Fig. 7(b) is illustrated the voltage-current characteristics for separations of 0.05 in., 0.2 in., and 0.4 in. Figures 7(a) and 7(b) are drawn on separate coordinate axes because the curves for 0.05 in. and 0.1 in. separation lie very close to each other. The lower 0.4 in. curve actually lies below the upper 0.3 in. curve. Thus, in some cases it is possible to have a decrease in arc voltage as the arc length is increased at a constant current, an unusual condition for the electric arc. The curve for the 0.2 in. separation is the only curve which

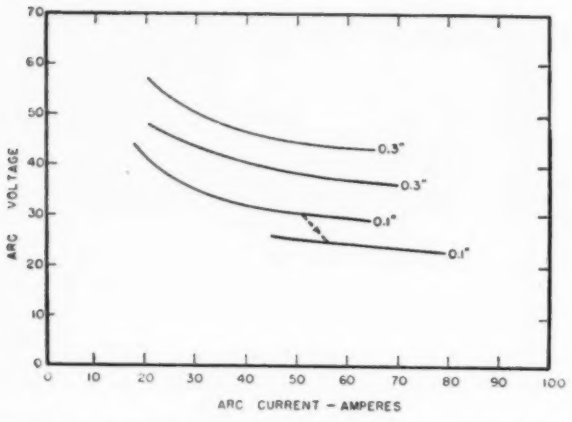

FIG. 7(a). Voltage-current characteristics of the arc in helium for electrode separations of 0.1 in. and 0.3 in.

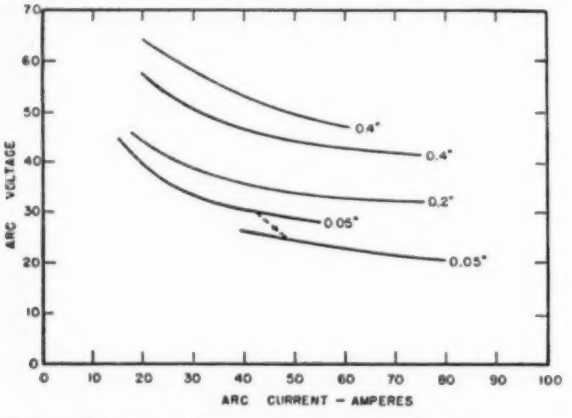

FIG. 7(b). Same as 7(a) but for separations of 0.05 in., 0.2 in., and 0.4 in.

did not show the dual-curve feature over the current range studied. It is not understood why this did not occur.

As the current was increased at close separations the arc voltage tended to approach a value near the first excitation potential (metastable state) of helium, 19.8 volts. The curves reported for helium were reproducible to within ± one volt. The dual curve feature of the helium arc will be explained in a later section.

Argon-Helium Mixtures

Just as in the case of the arc appearance the electrical characteristics of the arc in mixtures were a cross between the characteristics in the pure gases. Figure 8(a) shows a plot of the arc voltage as a function of the percentage of helium present in the mixture for an electrode separation of 0.05 in. and for arc currents of 20 and 60 amperes. As helium was added to pure argon, the arc voltage rose linearly until the mixture contained about 85 percent helium. Then the voltage rose sharply upward toward the arc voltage obtained

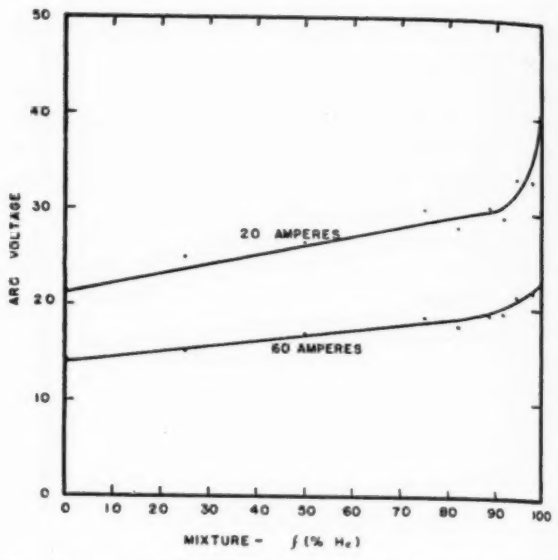

FIG. 8(a). Arc voltage as a function of the mixture for I=20 amps and I=60 amps. Electrode separation=0.05 in.

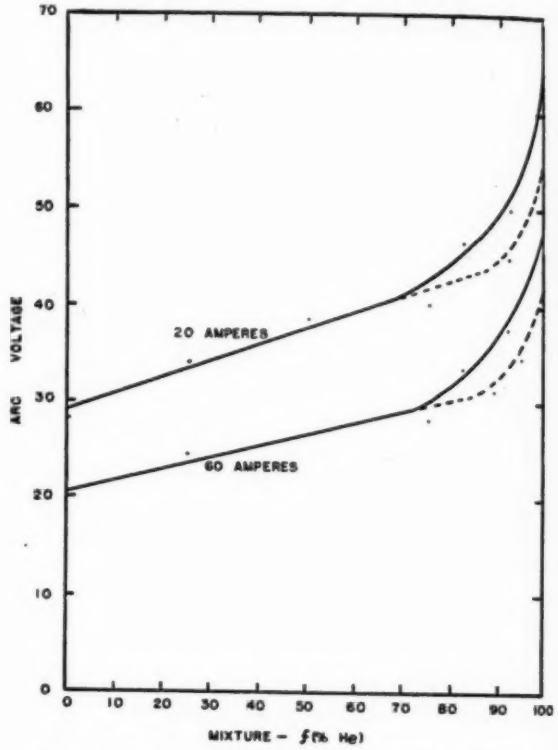

FIG. 8(b). Same as 8(a) but for a separation of 0.4 in.

in pure helium. The arc was strongly characteristic of argon until the sharp rise in voltage took place. The transition from the argon dominated arc to the helium dominated arc was continuous with increasing concentration of helium. For high concentrations of helium the dual curve feature, which was characteristic of the helium arc, was present. This illustrated by the dotted curve in Fig. 8(b).

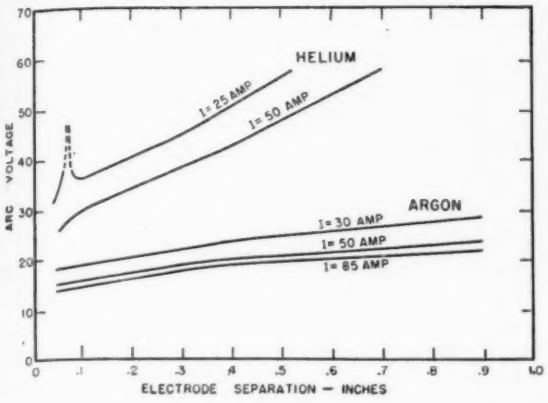

FIG. 9. Arc voltage as a function of the electrode separation.

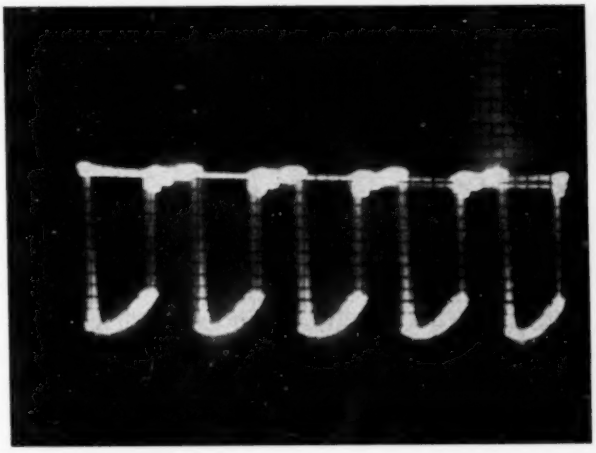

FIG. 10. Oscillogram of voltage oscillations observed in the helium arc at close separations and low currents.

VOLTAGE-ELECTRODE SEPARATION CHARACTERISTICS

Argon

The lower set of curves in Fig. 9 gives the arc voltage as a function of the electrode separation for the argon arc at three values of current. The slope of these curves is a measure of the voltage gradient of the region between the electrodes. The usual name for this region is the *plasma*. The voltage gradient in the plasma of the high current arc at atmospheric pressure is usually supposed to be a constant function of the arc length and decreases with increasing arc current. These curves, however, show that this is not exactly the case for this type of arc. Instead, there is a separate voltage gradient associated with both the anode flame and the cathode flame. For separations between 0.05 in. and 0.3 in. the plasma gradient was essentially constant over the current range studied and had an average value of 16.7 volts/in. This gradient appears to be associated with the cathode flame because the anode flame was not present at these separations. The slope of this curve at the longer separations (>0.3 in.) when the anode flame was present was less than the cathode gradient and decreased with increasing current. The actual values of the gradient are given in Table I.

These curves seem to indicate that at close separations the cathodic processes play a major role in the arc mechanism. It should be remembered, however, that the computation of the voltage gradient by this method assumes that the sum of the anode and cathode voltage drops (the voltage drops in the space charge at the electrodes) remains essentially constant for variations of the electrode separation at a constant current. This is generally thought to be a valid assumption.

TABLE I. Plasma voltage-gradients for the argon-tungsten arc.

Current	Gradient (volts/in.) Below 0.3 in.	0.3 in.—1.0 in.
30	16.8	9.5
50	16.5	7.0
85	16.9	6.5

TABLE II. Plasma voltage-gradients for the helium-tungsten arc.

Current	Gradient (volts/in.) 0.1 in.—0.3 in.	0.3 in.—0.7 in.
25	44	58
50	42	51

Helium

The voltage-electrode separation curves for the helium arc are also plotted in Fig. 9 for representative currents of 25 and 50 amperes. The results are similar to those in argon and the voltage gradients are listed in Table II. Between 0.1 in. and 0.3 in. the voltage gradient was essentially constant and seemed to be associated with the cathode flame. Above 0.3 in.

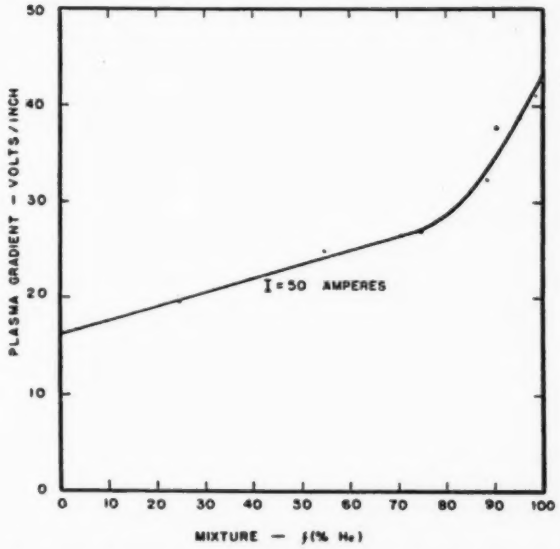

FIG. 11. Voltage gradient as a function of the mixture for I=50 amperes and for electrode separations between 0.1 and 0.3 in.

separation the gradient had the property of decreasing with increasing current. The chief difference between these curves and similar curves in argon is that voltage gradient in helium for longer separations was greater than for shorter separations. The reverse was true in argon.

With currents below 30 amperes in helium the voltage was found to rise 15 to 25 volts over a very narrow and critical range of electrode separation. The rise is shown by the dotted portion of the 25-ampere curve and it occurred somewhere between the 0.05-in. and 0.1-in. electrode separation. The width of the region in which this occurred was about 0.01-in. This phenomenon appeared when the cathode flame made direct contact with the anode electrode. The contact was very critical. The sharp rise in voltage was accompanied by a decrease in the size of the flame, the appearance of voltage oscillations, and an audible whistling sound from the arc. Noise was also heard on a radio receiver over certain narrow frequency ranges. An oscillogram of the arc-voltage oscillations is shown in Fig. 10. These oscillations have an amplitude of approximately 12 volts and a frequency between 8 and 8.5 kc. This phenomenon was not observed in arcs with currents greater than 35 amperes. It has also not been observed in argon at any current employed.

Argon-Helium Mixtures

The voltage-electrode separation curves for mixtures were similar to those in pure gases. In Fig. 11 is shown the voltage gradient of the cathode flame as a function of the mixture concentration at a current of 50 amperes. The general shape of this curve is similar to the curves shown in Fig. 8. The voltage gradient of the anode flame, however, did not follow the above type of characteristic exactly. For mixtures with less than 85 percent helium present the anode flame voltage gradient with a current of 50 amperes was essentially constant at about seven volts per inch, which is approximately equal to the gradient found in the pure argon arc (see Table I). For concentrations containing about 95 percent helium or more, the anode flame voltage gradient was close to that of the pure helium arc, about 50 volts per inch at the same current. In the transition region between 85 and 95 percent helium, the arc was unstable at separations where the anode flame should have appeared and no anode flame voltage gradients could be measured. Thus it seems that the anode gradient in mixtures is either that of argon or helium, since no in between values were measured.

SMALLER DIAMETER CATHODES

Several measurements were made using $\frac{1}{8}$-in. diameter tungsten-rod cathodes and $\frac{1}{4}$-in. diameter anodes. The appearance and behavior of the arc under these conditions was quite similar to the arc where both electrodes were $\frac{1}{4}$-in. diameter. One important difference was noted, however. The arc voltage in certain cases was found to be less than the minimum excitation potential of the gas. For a separation of 0.05-in. and at the higher values of current an arc voltage of 10.6 volts was found in argon and 17.5 volts in helium. Both values are about two volts lower than the excitation potential and these arcs may be classed as *low voltage* arcs. It was also noted that the smaller diameter cathode electrode in argon appeared to have vaporized in spots, while the $\frac{1}{4}$-in. cathode, it will be recalled, never appeared such. On the other hand, both the $\frac{1}{8}$-in. and the $\frac{1}{4}$-in. cathodes in helium appeared to have been vaporized. It is believed that the low voltage of the arc in these cases can be attributed to the presence of tungsten vapor in the cathode region. The tungsten with its lower ionization potential than either helium or argon is readily ionized and lowers the arc voltage. The result is a mixture of tungsten vapor and inert gas, and the effects are similar to those reported for gas mixtures.[6]

STARTING OF THE ARC

The phenomena associated with the starting of the arc are described in this section for the helium arc. Similar phenomena also occurred in argon.

A high voltage breakdown was used for the starting of the arc. A commercial arc starter, such as is used in inert-gas arc welding, was employed for placing a 60-cycle voltage of about 5000 volts across the electrodes which were separated by about 0.01 in. Under proper conditions the gap would break down and the arc would follow. The process of the initiation of the arc can be divided into three steps: (1) the ionization of the gap, (2) the cold cathode arc which follows almost immediately, and (3) the high temperature arc.

In helium there was usually a time delay in the initiation of the ionization of the gap. The time interval between the instant of the application of the high voltage and the breakdown of the gap varied from near zero duration to as much as twenty seconds. The longer delays occurred when the electrodes were hot, as was the case immediately after the arc had been extinguished. An average elapsed time of about fifteen seconds was required to allow the electrodes to cool after the arc was extinguished before the arc could be re-initiated. This was probably due to the fact that the breakdown of the gap depends to some extent on the amount of impurities present on the electrode.[7] The relatively long time interval seems necessary to allow the impurities present in the system to recondense on the cooling electrodes.

---

[6] This explanation of the low voltage of the arc as being due to the presence of evaporated cathode material may be applied to other cases reported in the literature. For example, see the following: Compton, Lilly, and Olmstead, Phys. Rev. **16**, 282 (1920). J. D. Cobine and C. J. Gallagher, paper presented at the Am. Inst. Elec. Engrs. Conference on Electric Welding, Detroit, April 1950. R. H. Gillette and R. T. Breymeier, The Welding Journal **30**, 146-*s* to 152-*s*, (1951).

[7] F. H. Newman, Brit. J. Appl. Phys. **2**, 303 (1951).

The cold cathode arc formed immediately after the ionization of the gap. This type of arc was not as intense as the high temperature arc and was characterized by a rapidly wandering cathode spot. This arc appeared bluish in color. If the arc current was low so that the electrodes could not become sufficiently hot, the cold cathode arc would wander rapidly over the electrode and be extinguished. However, if the current was sufficiently high so that the electrodes became hot enough, the cold cathode arc would change abruptly to the very stable high temperature arc with stationary cathode spot. There was a great difference in stability between the two types of arcs. In the case of the helium arc with $\frac{1}{4}$-in. diameter electrodes, the arc current had to be above 70 amperes for the high temperature arc to appear. If the arc current was not this high, the cold cathode arc would extinguish after one or two seconds. However, once the high temperature arc was established at this high current, it could still be maintained with currents as low as five amperes. The lowest current at which the high temperature arc could be maintained was not established.

In argon the phenomena described above were similar except that the steps occurred faster. The breakdown of the gap and the cold cathode arc was followed by the appearance of the high temperature arc in a fraction of a second. The minimum current necessary for the high temperature arc to appear was much lower than in helium and was about 30 amperes.

DISCUSSION

Helium Voltage-Current Characteristics

The transition that occurred in the voltage-current characteristics of Fig. 7 from the upper curve to the lower curve for increasing current and which was accompanied by a change in arc appearance seems to be caused by the presence of appreciable tungsten vapor near the cathode region. This could occur when the energy at the cathode electrode becomes high enough to generate the required heat to evaporate sufficient material. The tungsten vapor, because it has a much lower ionization potential (8.3 volts) than the minimum excitation potential of helium (19.8 volts), will be ionized by the excited helium and influence the character of the discharge near the cathode to a large extent, even though the quantity present may be small. The presence of a mixture of helium and tungsten vapor near the cathode produces a lower arc voltage than with pure helium.

It may be possible that vapor from the anode caused the lower voltage. This does not seem likely, however, since examination of the electrodes shows that the lower arc voltage occurred only when the face of the cathode had a shiny appearance, indicating that appreciable material had vaporized. the appearance of the anode remained unchanged, however, and gave indication that it was always hot enough to vaporize considerable material.¶

Distribution of Arc Voltage

The total voltage across the arc is made up of an anode drop, a cathode drop, and the drop between these two regions, usually known as the plasma drop. At very close separations the plasma drop is so small that it may be neglected, leaving the arc voltage composed primarily of the sum of the anode and cathode drops. In the case of the inert gas arc reported here, it was found that the minimum voltage is very nearly equal to the minimum excitation potential of the gas (assuming no appreciable electrode vapor present at the cathode). It is usually supposed that the cathode drop is never less than the minimum excitation potential of the gas in which the arc is maintained.[8]

Such an assumption leads to the conclusion that in the inert gas arc the *anode drop is zero or negligibly small.* If this is the case, the major portion of the heat generated at the anode is due to the electrons giving up their "heat of condensation." ** The watts input under these conditions is the product of the electron current times the work function of the anode. The electron current at the anode may be assumed equal to the arc current.

There are two indirect experimental checks that can be made to check this hypothesis:

(1) Data given by Jones and Langmuir[9] show that tungsten will reach its melting point when the power density (watts per unit surface area) is about 1200 watts per sq cm. If it is assumed that the input is given by $I\phi_e$, where I is the arc current and ϕ_e the electronic work function, and that this input distributes uniformly over the face of the anode so that the power density is $I\phi_e/0.317$ (for a $\frac{1}{4}$-in. diameter electrode) than the current at which the anode will melt is computed to be 85 amperes. This is close to the actual observed current necessary to cause the anode to melt.

(2) The axial, steady-state temperature distribution along the electrode may be given, with some assumptions, by[10]

$$T=T_0/4\pi kx, \tag{1}$$

where x is the axial distance from the end of the electrode at a temperature T_0; T is the temperature at the point x; k is the thermal diffusivity (for tungsten $k=0.54$). All units are cgs.

¶ Note that considerable electrode material may be vaporized at temperatures lower than the melting point. See reference 9.

[8] C. Eckart and K. T. Compton, Phys. Rev. **24**, 97 (1924). Note that when vapor is present, the cathode drop could be as low as the ionization potential of the vapor.

** There will be, of course, heat radiated from the plasma to the anode. For simplicity, however, this will be neglected.

[9] H. A. Jones and I. Langmuir, Gen. Elec. Rev. **30**, 312 (1927).

[10] H. S. Carslaw and J. C. Jaeger, *Conduction of Heat in Solids* (Oxford University Press, New York, 1947), p. 221.

Color photographs of the arc were obtained in which the change of color temperature along the electrode axis was quite well defined. The distance at which the color changed from white to bright orange could be easily measured. This corresponded to a temperature of 1500°K. For a 40-ampere arc in argon this distance was measured as 0.32 cm. For a 40-ampere arc the the power input is $40\times4.5/0.317=568$ watts/cm^2. Reference 9 shows that this corresponds to a surface temperature of 3100°K. By substituting $T_0=3100$ and $T=1500$ in Eq. (1) the distance x is found to be 0.30 cm.

The agreement between the calculated and observed values in the above two cases is good considering the nature of the assumptions made and tends to substantiate in an indirect way that the anode drop is zero or negligible. It seems likely, however, that at higher currents when the anode face is melted, the increase in arc voltage with current mentioned previously may be due to the presence of an anode drop. It would be very interesting if this could be checked in the future by suitably designed probe measurements.

CONCLUSIONS

The inert gas arc with tungsten electrodes is one of the most stable forms of the electric arc if the system is free from oxide impurities. Its electrical properties are very dependent upon the processes occuring in the cathode flame and in the cathode drop region.

The cathode voltage drop is probably very close to the minimum excitation potential of the inert gas except perhaps when the gas is a mixture of two gases. In this case the voltage drop at the cathode is believed to lie between the minimum excitation potentials of the two gases. When appreciable electrode vapor is present near the cathode, the effect is similar to that which occurs in a mixture of two gases.

The phenomena observed at the anode over this current range can be explained by assuming that there is no observable anode drop of voltage. Consequently most of the heat generated at the anode is due to the "heat of condensation" of the electrons entering the surface of the anode. At currents higher than those reported here it is believed that the rise in voltage is due to the presence of an anode drop which appears when the surface of the anode is at the melting temperature.

The dual curve feature of the voltage-current characteristics noted for the helium arc under certain conditions is thought to be due to tungsten vapor in the cathode region. When the cathode electrode is able to evaporate sufficient vapor into the cathode region, the arc voltage will drop since the ionization potential of the tungsten is much lower than the excitation potential of the gas. This indicates that the presence of small quantities of electrode vapor can have a large influence on the properties of the arc. Certain types of low voltage arcs reported in the literature may be explained on this basis.

Both the cold cathode and the high temperature forms of the arc were observed in these experiments. The cold cathode arc appeared on starting but did not last for more than a few seconds.

Quantitative measurements were obtained of the variation of arc voltage as a function of the composition of argon-helium mixtures. It was found that the properties of the arc in mixtures were a cross between the properties observed in the pure gases. With mixtures ranging from pure argon to mixtures containing 85 percent helium, the properties of the argon arc were more dominant, while the influence of the helium was more pronounced for concentrations containing greater than 85 percent helium. In general, the effect of small amounts of argon in helium is greater than small amounts of helium in argon. However, the effect of the inert gas with the lower excitation potential on the properties of the arc is not as striking as has been reported with the low pressure low current discharges, such as the glow.[11]

The experiments reported in this paper represent the results of a preliminary exploratory study of the high current inert gas arc. Spectroscopic studies and probe measurements are indicated as the next steps that should produce results of value. The authors believe that a complete understanding of this type of arc would contribute greatly to the understanding of the general mechanism of other forms of the arc, and for this reason its continued study is planned.

ACKNOWLEDGMENT

The authors wish to thank Dr. W. B. Kouwenhoven, Dean of the Johns Hopkins School of Engineering, for making this research possible and for his continued interest in this program.

[11] L. B. Headrick and A. S. Duffendack, Phys. Rev. **37**, 736 (1931).

JOURNAL OF APPLIED PHYSICS VOLUME 23, NUMBER 6 JUNE, 1952

Equivalences for the Analysis of Circuits with Small Nonlinearities

W. J. CUNNINGHAM
Yale University, New Haven, Connecticut
(Received February 4, 1952)

Equivalent forms may be useful in the analysis of the steady-state operation of circuits containing a nonlinear resistance element. Provided the amount of nonlinearity is not too large, the nonlinear element can be replaced by a linear resistance and several generators of voltage or current. The amplitude, phase, and frequency of these generators are determined by the nature of the nonlinearity and by the fundamental component of current in the nonlinear element.

I. DESCRIPTION OF NONLINEAR ELEMENT

CERTAIN types of electric circuit elements have an impedance which is not constant. The impedance may be a function of voltage or current in the element (e.g., impedance of a diode), or may be a function of some external control (e.g., grid-voltage control of the plate-cathode impedance of a triode). The analysis of a circuit containing an impedance element of this sort sometimes can be simplified through the use of an equivalent circuit. The equivalent circuit is composed of constant impedances and generators and is chosen to produce the same end result as the actual circuit. Such equivalences are widely used in the analysis of vacuum-tube circuits. For example, a triode, actually operating as a varying resistance controlled by grid voltage, is replaced by a fixed resistance and a generator of voltage or current.[1] Similar equivalent circuits are used in the analysis of a diode operating as a modulator or detector, where the resistance is a function of voltage across the diode.[2] This procedure of introducing equivalent circuits for varying elements can be extended profitably to sorts of circuits other than those just described.

The use of equivalent circuits in the analysis of varying or nonlinear impedance elements is practical only if the amount of variation or nonlinearity is not too large. The following discussion is confined to two-terminal electric circuit elements which are only slightly nonlinear and which are operating in the steady state. Such circuit elements can be described mathematically by a nonlinear equation in which the coefficients of the nonlinear terms are relatively small. A few examples of such elements are vacuum tubes, crystal diodes, thermistors, and incandescent lamps, operating in such a way that while there is nonlinearity present, its magnitude is small. Elements of this type are essentially resistive in nature, but small reactive effects may be present also.

A nonlinear element of the type under consideration can be described by an equation similar to the following

$$e=r\left[i+\alpha\left(\beta i^2+\gamma i^3+\delta di/dt+\epsilon\int idt\right)\right]. \quad (1)$$

Here, e is the instantaneous voltage across the element, i is the instantaneous current in it, t is time, and r, α, β, γ, δ, and ϵ are numerical coefficients. These coefficients have dimensions which can be determined from the way they enter Eq. (1). In particular, r is evidently a resistance. It is convenient for the purposes of discussion, however, to assume that e, i, and t are normalized dimensionless quantities, and therefore that the coefficients are dimensionless also. Throughout the discussion, the assumption is made that coefficient α, and all the products, $\alpha\beta$, $\alpha\gamma$, $\alpha\delta$, and $\alpha\epsilon$ are much smaller than unity. Under this assumption, the nonlinearity is small and the impedance element is approximately a simple constant resistance. Any actual circuit element most likely can be described by an equation such as Eq. (1) only within a limited range of the variables e and i. One or more of the coefficients may be zero, and additional terms of higher order may be present. An analysis based on Eq. (1), however, should yield results typical of this general sort of impedance element.

II. EQUIVALENT CIRCUIT FOR ELEMENT ALONE

A sinusoidal current in the element produces a nonsinusoidal voltage across it; a sinusoidal voltage across the element produces a nonsinusoidal current in it. These two cases can be represented by equivalent circuits in which the element is replaced by a resistance plus voltage or current generators operating at frequencies determined by the distortion.

The equivalent circuit for a sinusoidal current in the element can be obtained as follows. It is simplest to assume a cosinusoidal current, $i=I\cos\omega t$, of amplitude I and angular frequency ω, in the element. The voltage across the element is then

$$e=(rI+\tfrac{3}{4}r\alpha\gamma I^3)\cos\omega t+\tfrac{1}{2}r\alpha\beta I^2+\tfrac{1}{2}r\alpha\beta I^2\cos 2\omega t +\tfrac{1}{4}r\alpha\gamma I^3\cos 3\omega t-r\alpha I(\delta\omega-\epsilon/\omega)\sin\omega t. \quad (2)$$

Because of the nonlinearity, the voltage contains components at frequencies other than that of the current. Components at integral multiples of the fundamental frequency are introduced; the amplitude of the fundamental component is modified; an out-of-phase component is introduced. The relative amplitudes of the

[1] H. J. Reich, *Theory and Application of Electron Tubes* (McGraw-Hill Book Company, Inc., New York, 1944), p. 87.
[2] See reference 1, p. 323.

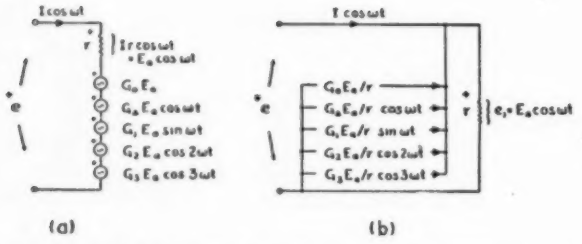

FIG. 1. Equivalent circuits for nonlinear element with cosinusoidal current supplied from infinite-impedance source.

various components are as follows:

$$\frac{\text{change in in-phase component}}{\text{linear in-phase component}}=G_\Delta=\tfrac{3}{4}\alpha\gamma I^2, \tag{3}$$

$$\frac{\text{out-of-phase component}}{\text{in-phase component}}=G_1=\frac{-\alpha(\delta\omega-\epsilon/\omega)}{1+G_\Delta}$$

$$\doteq-\alpha(\delta\omega-\epsilon/\omega), \tag{4}$$

$$\frac{\text{dc component}}{\text{in-phase component}}=G_0=\frac{\alpha\beta I/2}{1+G_\Delta}\doteq\alpha\beta I/2, \tag{5}$$

$$\frac{\text{second harmonic}}{\text{in-phase component}}=G_2=G_0, \tag{6}$$

$$\frac{\text{third harmonic}}{\text{in-phase component}}=G_3=\frac{\alpha\gamma I^2/4}{1+G_\Delta}\doteq\alpha\gamma I^2/4. \tag{7}$$

The second forms for all these equations apply only if $|G_\Delta|\ll 1$.

An equivalent circuit for the nonlinear element with a cosinusoidal current is shown in Fig. 1(a). The element is replaced by a constant resistance r and a number of voltage generators. The voltage and frequency of each generator are chosen to correspond to one of the terms of Eq. (2). Since the external current source, supplying the initial cosinusoidal current, has infinite internal impedance, the current in the circuit remains cosinusoidal while the voltage across the terminals is the sum of all component voltages.

A second form for the equivalent circuit is shown in Fig. 1(b). In this figure the voltage generators of Fig. 1(a) are replaced with current generators. The current supplied by any one of the generators is $1/r$ times the voltage of the corresponding generator of the first circuit. Currents from all these generators flow through the resistance r, and produce the voltage required by Eq. (2) across the terminals of the element. So far as effects at the terminals are concerned, circuits of Figs. 1(a) and (b) are the same.

The equivalent circuit for a sinusoidal voltage across the element can be found in a similar manner. Again it is simplest to assume a cosinusoidal voltage, $e=E\cos\omega t$, of amplitude E. The resulting current can be found by a process of successive approximations. The current can be assumed to be given by

$$i=i_0+\alpha i_1, \tag{8}$$

where i_0 and i_1 are two successive steps in the approximation and $\alpha\ll 1$.

Substitution of Eq. (8) into Eq. (1) with $e=E\cos\omega t$ gives

$$E\cos\omega t=r\left[i_0+\alpha\left(i_1+\beta i_0^2+\gamma i_0^3+\delta di_0/dt+\epsilon\int i_0dt\right)\right], \tag{9}$$

where the only terms retained are those with α to the powers zero and one. If it is required that Eq. (9) apply in the linear case of $\alpha=0$, then the first approximation is

$$i_0=E/r\cos\omega t=I_a\cos\omega t, \tag{10}$$

where $I_a\equiv E/r$. If, now, α is allowed to be different from zero, but small, it is necessary that

$$i_1=-\beta i_0^2-\gamma i_0^3-\delta di_0/dt-\epsilon\int i_0dt$$

$$=-\tfrac{1}{2}\beta I_a^2-\tfrac{1}{2}\beta I_a^2\cos 2\omega t-\tfrac{3}{4}\gamma I_a^3\cos\omega t$$

$$-\tfrac{1}{4}\gamma I_a^3\cos 3\omega t+(\delta\omega-\epsilon/\omega)I_a\sin\omega t. \tag{11}$$

To the second approximation, the current is given by Eq. (8) with the substitution of Eqs. (10) and (11); thus,

$$i=I_a\cos\omega t-\alpha[\tfrac{1}{2}\beta I_a^2+\tfrac{1}{2}\beta I_a^2\cos 2\omega t+\tfrac{3}{4}\gamma I_a^3\cos\omega t$$

$$+\tfrac{1}{4}\gamma I_a^3\cos 3\omega t-(\delta\omega-\epsilon/\omega)I_a\sin\omega t]. \tag{12}$$

The relative amplitudes of the various components of distortion to this degree of approximation may be collected as follows:

$$H_\Delta=-\tfrac{3}{4}\alpha\gamma I_a^2 \tag{13}$$

$$H_1=\frac{\alpha(\delta\omega-\epsilon/\omega)}{1+H_\Delta}\doteq\alpha(\delta\omega-\epsilon/\omega) \tag{14}$$

$$H_0=\frac{-\alpha\beta I_a/2}{1+H_\Delta}\doteq-\alpha\beta I_a/2 \tag{15}$$

$$H_2=H_0 \tag{16}$$

$$H_3=\frac{-\alpha\gamma I_a^2/4}{1+H_\Delta}\doteq-\alpha\gamma I_a^2/4. \tag{17}$$

As in Eqs. (4)–(7), the second forms of these equations apply only if $|H_\Delta|\ll 1$.

A comparison of Eqs. (3)–(7) with Eqs. (13)–(17) indicates that so long as $|G_\Delta|\ll 1$ and $|H_\Delta|\ll 1$, and further that $I=I_a=E/r$ or $E=E_a=Ir$, the corresponding G's and H's are equal in magnitude and opposite in

sign, i.e., $G_n=-H_n$. If this condition is satisfied, an equivalent circuit for the nonlinear element with a cosinusoidal voltage is shown in Fig. 2(a). The element is replaced by a constant resistance r and a number of current generators. The current and frequency of each generator are chosen to correspond to one of the terms of Eq. (12). Since the external voltage source, supplying the initial cosinusoidal voltage, has zero internal impedance, the voltage across the element remains cosinusoidal while the current in the external circuit is the sum of all the component currents.

A second form for the equivalent circuit is shown in Fig. 2(b). In this figure, the current generators of Fig. 2(a) are replaced with voltage generators. The voltage supplied by any one of these generators is r times the current of the corresponding generator of the first circuit. These generators produce currents in the circuit as required by Eq. (12). So far as the effects at the terminals are concerned, circuits of Figs. 2(a) and (b) are the same.

A comparison of Figs. 1 and 2 indicates that so long as $I=I_a=E/r$ or $E=E_a=Ir$, the circuits to the right of the terminals of Figs. 1(a) and 2(b) are identical, as are those of Figs. 1(b) and 2(a). The action as observed in the external circuit is different for Figs. 1 and 2 because of the difference in impedance of the external generator. For Fig. 1(a) the external impedance is infinite so that all distortion voltages appear across the terminals and the current into the terminals is undistorted. For Fig. 2(b) the external impedance is zero so that distortion currents flow in the external circuit while the voltage across the terminals is undistorted. Similarly, for Fig. 1(b) distortion currents flow through resistance r, leaving the current into the terminals undistorted; for Fig. 2(a) distortion currents flow in the external circuit leaving undistorted the voltage across the terminals.

The fact that the circuits of Fig. 1 are the same as those of Fig. 2 can be used occasionally to simplify the analysis of a nonlinear circuit. The characteristics of the generators of the distortion components can be found by considering the effect of either a sinusoidal current (Fig. 1) or a sinusoidal voltage (Fig. 2). It is sometimes much simpler to perform the analysis in terms of one of these quantities than it is in terms of the other.

As is generally true for approximate analyses of nonlinear problems, it is difficult to assess the error when these equivalent circuits are used in a particular situation. If the nonlinearity is not sufficiently small, several things happen to introduce errors. Odd-order terms of Eq. (1) (only the third-order term is included) modify the amplitude of the component at the fundamental frequency; in other words, $|G_\Delta|$ may not be small compared with unity. Because of this effect alone, typical distortions produced by sinusoidal current and by sinusoidal voltage will be in the ratio

$$|G_n/H_n|=(1-G_\Delta)/(1+G_\Delta)\doteq 1-2G_\Delta. \qquad (18)$$

Since $G_\Delta=3G_3$, from Eqs. (3) and (7), this effect becomes appreciable for relatively small values of third-order distortion. Higher odd-order distortion produces a similar result. The effect is increasingly important for larger values of I_a, since G_Δ varies as I_a^2.

Furthermore, if the nonlinearity is not sufficiently small, the second approximation for the current given by Eq. (12) is not adequate. If Eq. (12) is substituted into Eq. (1), with $e=E\cos\omega t$, an identity results for those terms containing α to the powers zero and one. Terms with α to powers higher than one are left over, and are error terms if Eq. (12) is taken as the solution for Eq. (1). If this substitution is carried out, a typical error term in voltage is found to be

$$2r\alpha^2\beta^2 I_a^3\cos^3\omega t=\tfrac{1}{2}r\alpha^2\beta^2 I_a^3(3\cos\omega t+\cos 3\omega t).$$

The amplitude of the third harmonic in this error term is $\frac{1}{2}r\alpha^2\beta^2 I_a^3$. The amplitude of the second-harmonic voltage produced by the current of Eq. (12) is $\frac{1}{2}r\alpha\beta I_a^2$. Thus, the error term considered above has an amplitude $\alpha\beta I_a$ times the amplitude of the second-harmonic voltage of the approximate solution, Eq. (12). Only if the magnitude of $\alpha\beta I_a$ is sufficiently small can this error term be ignored. Again the error increases as I_a is increased.

III. EQUIVALENT CIRCUIT FOR ELEMENT PLUS A RESISTOR

If the nonlinear element is placed in series with a linear resistance and a sinusoidal voltage, both the voltage and current for the individual elements will be nonsinusoidal. Similarly, if the nonlinear element is placed in parallel with a linear resistance, and the combination supplied with a sinusoidal current, both the voltage and the current for the individual elements will be nonsinusoidal. Equivalent circuits for these cases can be found.

If a linear resistance R is placed in series with the nonlinear element, the voltage across the combination is given by

$$e=(r+R)i+r\alpha\left(\beta i^2+\gamma i^3+\delta di/dt+\epsilon\int i\,dt\right). \qquad (19)$$

This equation is the same as Eq. (1) with R introduced.

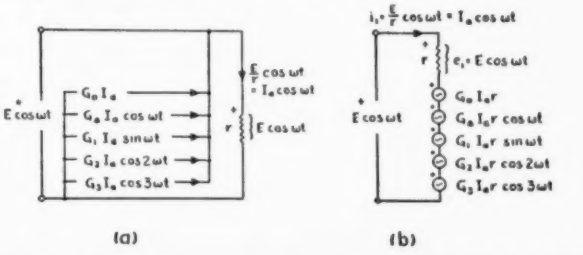

FIG. 2. Equivalent circuits for nonlinear element with cosinusoidal voltage supplied from zero-impedance source.

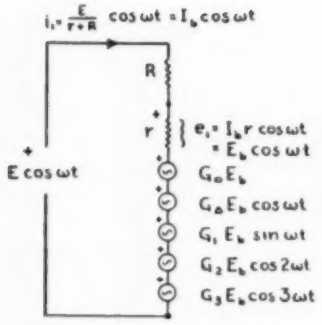

FIG. 3. Equivalent circuit for series combination of nonlinear element and linear resistance supplied with cosinusoidal voltage from zero-impedance source.

If $e=E\cos\omega t$, the current will be given by an equation similar to Eq. (12). The difference will be that the coefficient of the first approximation, which was $I_a\equiv E/r$ in Eq. (10), is instead $E/(r+R)$, which can be defined as $I_b\equiv E/(r+R)$. In the second approximation, all terms in i_1, given by Eq. (11), will be multiplied by the factor $r/(r+R)$. The approximate solution for Eq. (19) is then like Eq. (12), but with I_a replaced by I_b and with all terms that are multiplied by α having the extra factor $r/(r+R)$. Equations for the relative distortions are analogous to Eqs. (13)–(17), again with I_b in place of I_a and with the extra factor $r/(r+R)$.

An equivalent circuit for the nonlinear element in series with the linear resistance and cosinusoidal voltage is shown in Fig. 3. For this figure, $I_b\equiv E/(r+R)$ and $E_b\equiv I_b r=Er/(r+R)$. The G's are found from Eqs. (3)–(7) with the fundamental component of current I_b used in place of I. It is evident that the circuit of Fig. 3 is the same as the circuit of Figs. 1(a) or 2(b) with the addition of the resistance R.

The voltages of the generators at the distortion frequencies in the circuit of Fig. 3 vary with the factor $r/(r+R)$. Therefore, the relative distortions in the current in this circuit also vary with this factor. If the resistance R becomes very large, the current becomes sinusoidal with zero distortion.

A discussion, similar to that used to obtain the circuit of Fig. 3, can be used to obtain the equivalent circuit for the case of the parallel combination of the nonlinear element, a linear resistance, and a generator of sinusoidal current. The details will not be given here, but the resulting circuit is shown in Fig. 4. For this circuit, $I_c\equiv IR/(r+R)$ and $E_c\equiv I_c r=IrR/(r+R)$. The G's are found from Eqs. (3)–(7) with the fundamental component of current I_c used in place of I. It is evident that

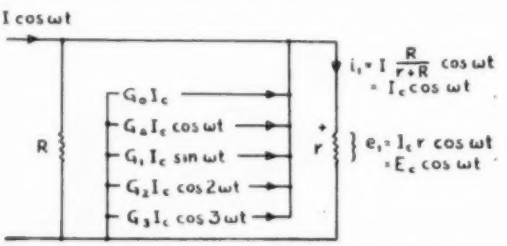

FIG. 4. Equivalent circuit for parallel combination of nonlinear element and linear resistance supplied with cosinusoidal current from infinite-impedance source.

the circuit of Fig. 4 is the same as the circuit of Figs. 1(b) and 2(a) with the addition of the resistance R.

The currents of the generators at the distortion frequencies of the circuit of Fig. 4 vary with the factor $R/(r+R)$. Therefore, the relative distortions in the voltage across the circuit also vary with this factor. If the resistance R becomes very small, the voltage becomes sinusoidal with zero distortion.

By a simple extension of the argument leading to Figs. 3 and 4, circuits can be set up for more complicated combinations of linear impedances with the nonlinear element. The equivalence for the element itself is always the same. The fundamental component of current in the nonlinear element is found through the usual methods of linear circuit theory. The amplitude for the voltage or current generators of distortion components is found from Eqs. (3)–(7). The value of I for these equations is the fundamental component of current in the nonlinear element, calculated first. A solution for the operation of the entire circuit, then, involves two steps: first, the calculation as a linear

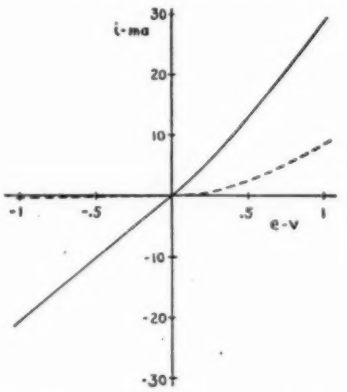

FIG. 5. Dotted curve is current-voltage characteristic for a 1N34 crystal diode. Solid curve is characteristic for the same 1N34 in parallel with a 50-ohm resistor.

circuit; second, the calculation of the effects of the distortion generators. If complex impedances occur in the circuit, note must be made of the fact that their values are different at different frequencies.

IV. EXPERIMENTAL MEASUREMENTS

A crystal diode is a nonlinear resistance element. The amount of nonlinearity represented by such a diode is too large to be treated by these approximate circuits, since the diode is equivalent to a very low resistance for conduction in one direction and to a very high resistance for conduction in the opposite direction. If a linear resistance of suitable value is connected in parallel with the diode, the resulting combination is still nonlinear, but the amount of nonlinearity may be small enough for the approximate analysis. In Fig. 5, the dotted curve is the current-voltage characteristic for a 1N34 crystal diode. The solid curve is the characteristic for the 1N34 in parallel with a 50-ohm resistor. The nonlinearity represented in the combined elements is small enough that the approximate analysis is applicable.

If a sinusoidal current is applied to the combined elements, the voltage across them is nonsinusoidal. The wave form of the voltage can be found by graphical construction[3] as in Fig. 6, where the current amplitude is 24 ma. It is apparent that the voltage wave has its negative peak accentuated. Similarly, if a sinusoidal voltage is applied, the current is nonsinusoidal with the positive peak of the current wave accentuated. In Fig. 6 is shown also the construction when the voltage amplitude is 1.0 volt. The harmonic components in the distorted waves can be found by any of a number of procedures for numerical analysis; the Chaffee[4] method is quite applicable here. The results of such an analysis for the waves of Fig. 6 are given in Table I.

For the data of Table I, the amplitudes of the fundamental components in the two cases have been made the same. The relative amplitudes of the components at the second and third harmonic frequencies are not exactly the same, but are essentially so. This is the result predicted from the equivalent circuits of Figs. 1 and 2. Any of the various effects considered in connection with these circuits might lead to differences of the sort observed here. For many purposes, however, the relative distortions could be considered the same.

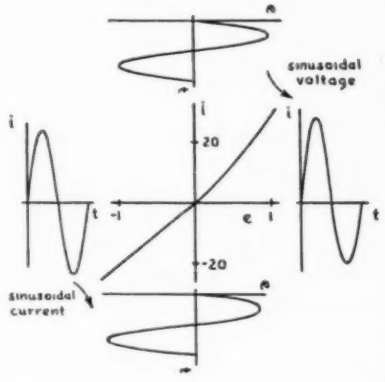

FIG. 6. Construction for obtaining the nonsinusoidal voltage, or current, resulting from the application of a sinusoidal current, or voltage, to the nonlinear element of Fig. 5.

If a linear resistance is inserted in series with the parallel combination of the 1N34 and the 50-ohm resistor, and the circuit supplied with a sinusoidal voltage, the current is nonsinusoidal. The wave forms of the current and of the voltage across the parallel elements can be found by the usual graphical construction employing a load line.[3] Again, the harmonic components in the nonsinusoidal waves can be found by a numerical analysis. In Fig. 7(a) are shown the results of such an analysis. Data for this figure were obtained with the amplitude of the sinusoidal driving voltage adjusted always so that the fundamental component of current in the 1N34–50-ohm combination was 24 ma. The relative amplitudes of the second and third harmonic currents, compared with the fundamental current, are plotted against the factor $r/(r+R)$. In this factor, r is the linear resistance for the nonlinear element, and is about 40 ohms for the 1N34 in parallel with the 50-ohm resistor. The value of the series resistor is R.

[3] See reference 1, Chap. 4.
[4] E. L. Chaffee, Rev. Sci. Instr. **7**, 384 (1936).

TABLE I. Harmonic components of wave forms of Fig. 6.

Sinusoidal driving quantity amplitude	Current 24 ma	Voltage 1.0 volt
Nonsinusoidal response	Voltage	Current
amplitude of fundamental	1.0 volt	24 ma
amplitude of 2nd harmonic	0.079 v	2.14 ma
amplitude of 3rd harmonic	0.018 v	0.57 ma
2nd/fundamental	0.079	0.088
3rd/fundamental	0.018	0.023

Similarly, a linear resistance connected in parallel with the nonlinear element and supplied with a sinusoidal current leads to a nonsinusoidal voltage across the 1N34. The harmonic components in this voltage can be found by a process analogous to that just described. In Fig. 7(b) are shown the results of such an analysis where the amplitude of the sinusoidal driving current was adjusted always so that the fundamental component of voltage across the 1N34 was 1.0 volt. Relative amplitudes of the harmonic voltages are plotted against the factor $R/(r+R)$, where R is the value of the parallel resistor.

It is evident from Figs. 7(a) and (b) that the relative distortions vary linearly with the factors used as abscissas in the two cases. This is the result predicted from the equivalent circuits of Figs. 3 and 4.

Only a single example is given here. Calculations have been carried out as numerical analysis of graphical data. Similar experimental data have been obtained on actual circuits where harmonic components as high as the sixth have been measured with a wave analyzer. Circuits having nonlinearities predominantly of even order (as in the example) and of odd order were considered. In all cases where the relative distortion was less than about ten percent, the equivalent circuits were found to hold quite well.

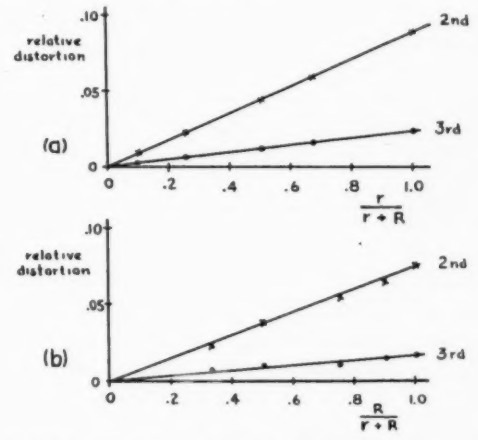

FIG. 7. (a) Relative second and third harmonic components of current in a series circuit of a resistance R and the nonlinear element of Fig. 5, supplied with a sinusoidal voltage. (b) Relative second and third harmonic components of voltage across a parallel circuit of a resistance R and the nonlinear element of Fig. 5, supplied with a sinusoidal current.

Incandescent Lamp Bulbs in Voltage Stabilizers

W. J. CUNNINGHAM
Yale University, New Haven, Connecticut
(Received February 4, 1952)

High vacuum incandescent lamp bulbs have been used as sensitive elements in stabilizing systems for ac power sources. Such a lamp is a nonlinear element and accordingly introduces distortion components into the stabilizer circuit. An analysis of the operation of the lamp is given, based on rather simple assumptions. This analysis allows the prediction of the distortion for given operating conditions and shows the effects of changes in frequency and current.

I. USE OF LAMPS IN STABILIZERS

CIRCUITS used for automatically stabilizing the output voltage of any source of electric power require some standard of reference against which the voltage of the power source can be compared. The standard of reference used in stabilizers for sources of direct-current power is usually the constant voltage developed across a gas-discharge tube or a battery. The standard of reference for use with a source of alternating-current power is not easily obtainable as an analogous device producing constant voltage across its terminals. The difficulty here lies in the fluctuating nature of the ac power. An element that has been used as a standard in stabilizers for ac power is an incandescent lamp, having a metal filament in a high vacuum bulb.[1] The resistance of the filament of such a lamp varies rapidly with changes in its temperature and therefore with changes in voltage across or current through the filament. The lamp is used in one or more arms of a bridge composed of resistors adjusted so that the bridge is most nearly balanced when the desired operating voltage appears across the input terminals of the bridge. Variation of the rms voltage from its desired value produces a change in the resistance of the lamp so that an unbalance voltage appears at the output terminals of the bridge. The magnitude and phase of this unbalance voltage are such that it can be used to control elements which ultimately adjust the output voltage of the power source.

Investigation of the performance of such a lamp carrying an alternating current shows that its operation is somewhat more complicated than might appear at first examination. A sinusoidal current in the lamp leads to fluctuations in temperature, and therefore in resistance, of the lamp. These fluctuations in resistance cause the voltage across the lamp to be nonsinusoidal. A sinusoidal current of a given frequency leads to a component of voltage at that frequency in phase with the current. In addition, however, a component of voltage out of phase with the current appears, as does a component of voltage at three times the frequency of the current. Other components of voltage may appear also, but with amplitudes smaller than those of the components mentioned first. These extra components appear across the terminals of the bridge used in the stabilizing system and ultimately limit its successful operation.

Analyses of the operation of an incandescent lamp used in a circuit of this sort have been given, with various more-or-less valid assumptions taken as a starting point. The nature of these assumptions is usually such that the results are applicable if the current in the lamp is not too large, or if the frequency is not too low. The analysis given here is only an approximate one also, and is based on relatively simple assumptions. It appears to lead to useful results over a relatively wide range of the operating parameters.

II. ANALYSIS FOR ZERO OR INFINITE FREQUENCY

While it is the current-voltage characteristic of the lamp that is of most interest, the analysis is simpler if carried out initially in terms of the temperature. To a first approximation, the resistance of the filament is proportional to its temperature, so that

$$e=c\theta i, \tag{1}$$

where e is the voltage across the filament, i is the current in it, θ is the absolute temperature of the filament, and c is a constant for a given lamp. Numerical values found using the equation for the resistance of tungsten as a function of temperature,[2] indicate that Eq. (1) is fairly accurate if the temperature is not too high. More accurate results would be obtained if a constant temperature were subtracted from the actual temperature before substitution in Eq. (1). The error is not too serious, however.

If the temperature of the filament changes with time, the following equation is approximately true,

$$d\theta/dt=a\theta i^2-b(\theta^4-\theta_0^4), \tag{2}$$

where θ_0 is the ambient absolute temperature, t is time, and a and b are constants for a given lamp. The first term on the right side of Eq. (2) represents the rate of temperature change produced by heat supplied to the filament by the electric power. Parameter a is smaller for a filament of large heat capacity. The second term

[1] G. N. Patchett, Electronic Eng. **22**, 371, 424 (1950). An extensive bibliography appears in this reference.

[2] *International Critical Tables* (McGraw-Hill Book Company, Inc., New York, 1929), Vol. VI, p. 136.

represents the rate of temperature change produced by heat radiated from the hot filament to its surroundings.

Ambient temperature θ_0 is in the order of 300°K. The filament of a lamp used in a stabilizer circuit is usually operated so that it glows visibly and its temperature θ is then in the order of at least 1000°K. If this is the case, $\theta_0^4/\theta^4 \ll 1$, and the term in θ_0 appearing in Eq. (2) can be neglected. In all the succeeding analysis θ_0 will be ignored. This situation is desirable, since it means that the operation of a stabilizer using the lamp is essentially independent of the ambient temperature.

If a steady current I_0 is passed through the lamp, and if enough time to achieve a steady state has elapsed, then $d\theta/dt=0$, and

$$\theta=(a/b)^{1/3}I_0^{2/3}. \tag{3}$$

The voltage across the lamp is

$$E_0=c(a/b)^{1/3}I_0^{5/3}. \tag{4}$$

These equations are valid for a current of zero frequency; they are valid also for an alternating current of very high frequency having I_0 as its rms value. This equivalence results because the heating effect, which governs the resistance, is the same for the two currents. If the frequency of the alternating current is not sufficiently high, the temperature of the filament changes during each cycle of the current and the situation is more complicated. Published data[3] from a number of experimenters indicate that the current-voltage relation for a high vacuum lamp in the steady state is of the form $E_0=\text{constant}\ (I_0)^n$. Experimental values of n always seem to be quite close to 5/3, thus lending support to the assumptions that were made at the beginning of the analysis.

III. ANALYSIS FOR EXTREMELY LOW FREQUENCY

In order to proceed toward a more general solution for the alternating-current case, the current will be assumed sinusoidal of angular frequency ω,

$$i=2^{1/2}I_0\sin\omega t. \tag{5}$$

If the frequency is extremely low, approaching zero, the temperature of the filament will follow the fluctuating current, so that

$$\theta=2^{1/3}(a/b)^{1/3}I_0^{2/3}\sin^{2/3}\omega t \tag{6}$$

and

$$e=2^{5/6}c(a/b)^{1/3}I_0^{5/3}\sin^{5/3}\omega t. \tag{7}$$

Since the temperature varies as $\sin^{2/3}\omega t$, it never becomes negative and goes through two cycles during each single cycle of the current, as shown in Fig. 1. A Fourier analysis of $\sin^{2/3}\omega t$ shows that, approximately,

$$\sin^{2/3}\omega t=0.71-0.37\cos2\omega t-0.14\cos4\omega t -0.10\cos6\omega t-0.06\cos8\omega t\cdots. \tag{8}$$

The temperature has a mean value and a number of components at frequencies that are even multiples of the frequency of the current.

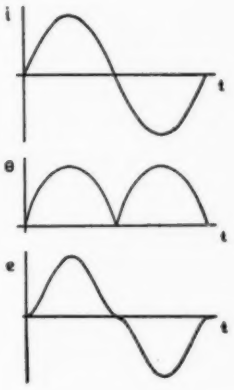

FIG. 1. Extremely low frequency sinusoidal current in lamp, and resulting variation in temperature and voltage across the lamp.

The voltage across the lamp, also shown in Fig. 1, varies as $\sin^{5/3}\omega t$. This function can be analyzed, approximately, as

$$\sin^{5/3}\omega t=0.90\sin\omega t-0.12\sin3\omega t-0.02\sin5\omega t\cdots. \tag{9}$$

Components of the voltage occur at odd multiples of the frequency of the current. The amplitudes of the higher order components of the voltage are of relatively less importance than those of the temperature.

IV. ANALYSIS FOR RELATIVELY HIGH FREQUENCY

If the frequency of the current is neither extremely low nor extremely high, then neither Eqs. (3) and (4) nor Eqs. (6) and (7) are applicable. At relatively high frequencies, the temperature fluctuates during the cycle of the current, but only by a small amount. In such a case, the temperature might be approximated by

$$\theta=\theta_1-\theta_2\sin(2\omega t+\phi). \tag{10}$$

The two terms here can be considered as the first two terms of a series such as Eq. (8). A phase angle ϕ is necessary to allow for the lag in temperature variation as compared with the current.

A combination of Eqs. (1), (5), and (10) leads to the equation

$$e/(2^{1/2}cI_0)=(\theta_1+\theta_2/2\sin\phi)\sin\omega t -\theta_2/2\cos\phi\cos\omega t+\theta_2/2\cos(3\omega t+\phi). \tag{11}$$

The ratio of the amplitude of the out-of-phase component to that of the in-phase component of voltage may be defined as G_1, and is

$$G_1=\cos\phi/(2\theta_1/\theta_2+\sin\phi). \tag{12}$$

The ratio of the amplitude of the third-harmonic component to that of the in-phase component may be defined as G_3, and is

$$G_3=1/(2\theta_1/\theta_2+\sin\phi). \tag{13}$$

Since the out-of-phase component is relatively small compared with the in-phase component, the denominator of Eqs. (12) and (13) is almost the same as the total fundamental component.

[3] G. N. Patchett, J. Inst. Elec. Engr. 93, III, 305 (1946).

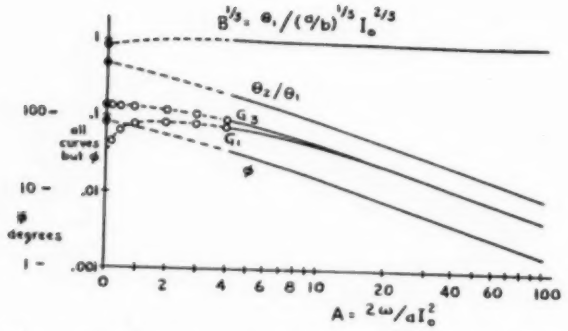

FIG. 2. Significant operating data for the lamp carrying a sinusoidal current of rms amplitude I_0. Scales are logarithmic except for the abscissa for $0<A<4$, which is linear. Dotted portions of the curves are estimates, with some experimental points indicated.

A combination of Eqs. (2), (5), and (10) leads to a long equation involving sine and cosine terms of angular frequencies that are integral multiples of 2ω. In order to simplify this equation, it is convenient to assume that $\theta_2/\theta_1 \leq 0.2$, so that approximately, $\theta^4 = \theta_1^4 - 4\theta_1^3\theta_2 \sin(2\omega t+\phi)$. From Eq. (8) it is evident that at extremely low frequencies $\theta_2/\theta_1 = 0.52$, so that this assumption is not valid; it is valid at higher frequencies, however. Since the long equation must hold identically at all times, it can be broken into individual equations involving the coefficients of the sine and cosine terms of each frequency. These equations are

$$\text{constant:}\quad aI_0^2\theta_1 + \tfrac{1}{2}aI_0^2\theta_2 \sin\phi - b\theta_1^4 = 0 \tag{14}$$

$$\cos 2\omega t:\quad 2\omega\theta_2 \cos\phi - aI_0^2\theta_2 \sin\phi - aI_0^2\theta_1 + 4b\theta_1^3\theta_2 \sin\phi = 0 \tag{15}$$

$$\sin 2\omega t:\quad 2\omega \sin\phi + aI_0^2 \cos\phi - 4b\theta_1^3 \cos\phi = 0. \tag{16}$$

Terms of angular frequency higher than 2ω are neglected as having little effect upon the components of lower frequencies.

Solution of Eq. (16) for $\sin\phi$ gives

$$\sin\phi = (4B-1)/[A^2+(4B-1)^2]^{1/2} \tag{17}$$

where $A \equiv 2\omega/aI_0^2$ and $B \equiv b\theta_1^3/aI_0^2$. Substitution of Eq. (17) into Eq. (15) gives

$$\theta_2/\theta_1 = 1/[A^2+(4B-1)^2]^{1/2}. \tag{18}$$

Substitution of Eqs. (17) and (18) into Eq. (14) gives

$$2(B-1) = (4B-1)/[A^2+(4B-1)^2]. \tag{19}$$

If the frequency is sufficiently high, the temperature of the filament is constant, and is given by Eq. (3). For this condition of high frequency, $B=1$. If the frequency is not so high as to maintain constant temperature in the filament, but still high enough that $\theta_2/\theta_1 \leq 0.2$, then the value of B remains very nearly unity. This is evident from Fig. 2, which shows that B is almost constant with respect to A. If the assumption is made that within the region of interest, always $B=1$, then Eq. (17) becomes

$$\sin\phi = 3/(A^2+9)^{1/2} \tag{20}$$

and Eq. (18) becomes

$$\theta_2/\theta_1 = 1/(A^2+9)^{1/2}. \tag{21}$$

Equations (20) and (21) can be combined with Eqs. (11), (12), and (13) to allow calculation of the components of voltage across the lamp for any value of the parameter A, so long as A is not too small.

The results of such calculations are shown in Fig. 2. Numerical values for $A \geq 4$ were obtained from the equations of Sec. IV. Numerical values for $A \to 0$ were obtained from the equations of Sec. III. The dotted portions of the curves for $0<A<4$ are merely interpolated, since none of the equations are strictly valid in this region.

If parameter $A(=2\omega/aI_0^2)$ is large enough that $A^2 \gg 9$, then approximately $\theta_2/\theta_1 = 1/A$, $\sin\phi = 3/A$, and $G_1 = G_3 = 1/2A$. These relations, then, are applicable for high frequencies or small currents. If A is not sufficiently large, $G_1 \neq G_3$, and the out-of-phase component of voltage is not of the same amplitude as the third-harmonic component.

A curve showing the instantaneous current in the lamp as a function of the instantaneous voltage across

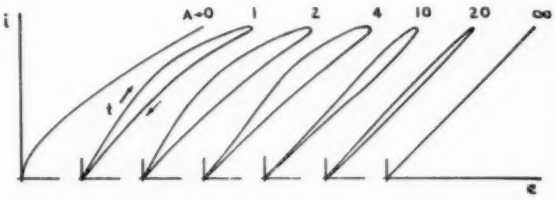

FIG. 3. Current-voltage characteristics for the lamp carrying a sinusoidal current. Only the portion of the characteristic in the first quadrant is shown; an exactly similar curve should appear also in the third quadrant. Values of A are indicated.

it, with time as a parameter, presents a picture of its operation. Because of the variation of the extra components of voltage with the quantity A, this current-voltage characteristic assumes different forms as A varies. In Fig. 3 are shown several such characteristics plotted from the equations previously developed, with the numerical value of A corresponding to each being indicated. These characteristics are for a sinusoidal current, and only the portion of the curve in the first quadrant is plotted. An exactly similar curve should appear also in the third quadrant.

If A approaches zero, the characteristic is a single-valued curve, $e = c(a/b)^{1/3} i^{5/3}$. As A is made larger, the characteristic becomes a double-valued curve, with time increasing clockwise around the loop. The loop assumes its maximum opening when A is about two. If A approaches infinity, the characteristic is a straight line, $e = c(a/b)^{1/3} I_0^{2/3} i$. The opening of the loop comes about, of course, because of the time delay in the temperature of the filament with respect to the current in it.

V. LAMP IN BRIDGE CIRCUIT

The foregoing analysis applies to the case of a sinusoidal current in the lamp and leads to expressions for the nonsinusoidal voltage across it. A similar analysis could be used to obtain the nonsinusoidal current in the lamp for a sinusoidal voltage applied across it. However, if the amount of nonlinearity is not too large, it is not necessary to repeat the analysis. An equivalent circuit,[4] generally valid for the lamp, is shown in Fig. 4. In this circuit, r is the equivalent resistance for the lamp and is very nearly $r=c(a/b)^{1/3}I_0^{2/3}$. Factors G_1 and G_3 are given by Eqs. (12) and (13); the polarities of the generators are chosen to fit Eq. (11). Fundamental components of current and voltage are i_1 and e_1, respectively.

As the lamp is normally used in a stabilizer, it is a portion of a bridge, the other elements of which are linear resistances. A possible configuration is shown in Fig. 5. An equivalent for this bridge circuit is shown in Fig. 6, where an equal-arm bridge is assumed. Voltage E_0 is the fundamental component of voltage across the lamp, and is $E_0=Er/(r+R)$. For the equal-arm bridge adjusted for best balance, $E_0=E/2$. For this condition of best balance the voltage appearing across

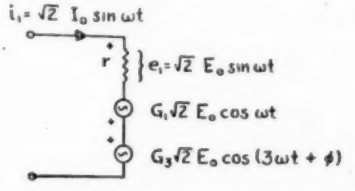

FIG. 4. Equivalent circuit for the lamp. Fundamental rms amplitudes of current and voltage are I_0 and E_0, respectively.

the output terminals of the bridge is

$$e_b=2^{1/2}E[r/(r+R)][-G_1\cos\omega t+G_3\cos(3\omega t+\phi)]. \quad (22)$$

This voltage, representing the effects of nonlinearities in the lamp, limits the optimum performance of the stabilizing system.

It is desirable that the voltage of Eq. (22) be minimized in any actual stabilizing system. Ideally, it may be reduced by increasing the magnitude of quantity A. If the frequency is assumed fixed, A can be increased for a given lamp by reducing the current in it. Too small a current will cause the operating temperature to become so low that it is no longer much higher than the ambient temperature, which is undesirable. Alternatively, A can be increased by choosing a lamp for which parameter a is small. This parameter is related to the heat capacity of the filament, and will be reduced by increasing the heat capacity, i.e. choosing a lamp of higher wattage rating. Either of these procedures for increasing A will tend also to make the stabilizer sluggish in its response to changes in input voltage.

Once the lamp and its operating conditions are chosen, the effect of the distortion voltages may be reduced by balancing them from the output of the bridge.[1] In particular, the out-of-phase component can be removed by adding a capacitor to the arm of the bridge in series with the lamp. This capacitor may go either in series or in parallel with the resistor, and its value must be chosen so as to introduce an out-of-phase voltage sufficient to cancel that produced by the lamp. It is not difficult to show from the circuit of Fig. 6 that the value of capacitance needed for compensation is given by the following equations:

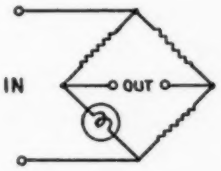

FIG. 5. Possible bridge circuit with lamp for use in stabilizer system.

$$\text{parallel connection: } C=1/2AR\omega=aI_0^2/4R\omega^2 \quad (23)$$

$$\text{series connection: } C=2A/R\omega=4/aI_0^2R. \quad (24)$$

In these equations, R is the resistance of one arm of the equal-arm bridge, and it is assumed that $A^2\gg9$. It is evident from Eqs. (23) and (24) that the series connection is desirable in that compensation is then independent of frequency. However, the value of capacitance needed in the series connection is so much larger than that in the parallel connection that the latter is commonly used.

A further result predicted by the analysis is that the reference voltage obtained from the balanced bridge is not entirely independent of frequency. Balance of the bridge is dependent upon the resistance of the lamp, which can be found from Eq. (11) as

$$r=c(a/b)^{1/3}I_0^{2/3}(1+\theta_2/2\theta_1\sin\phi). \quad (25)$$

In writing this equation, θ_1 is taken to be constant at $(a/b)^{1/3}I_0^{2/3}$, which has been shown to be nearly true. If conditions are such that $A^2\gg9$, then Eq. (25) becomes*

$$r=c(a/b)^{1/3}I_0^{2/3}(1+3/2A^2). \quad (26)$$

Since A depends upon frequency, both r and the balance conditions of the bridge will vary with frequency. In practice usually A is large enough that this change with frequency is quite small. If the frequency is zero, from Eq. (4) the resistance is

$$r=c(a/b)^{1/3}I_0^{2/3}. \quad (27)$$

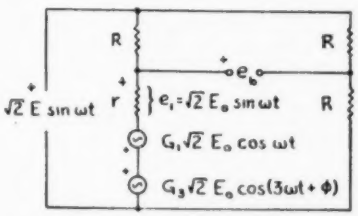

FIG. 6. Equivalent circuit for lamp in equal-arm bridge. Fundamental rms voltage across lamp is E_0.

[4] W. J. Cunningham, J. App. Phys. **23**, 653 (1952).

* *Note added in proof:* A value for B, more accurate than $B=1$ but subject to the condition that $A^2\gg9$, is $B=(2A^2-1)/(2A^2-4)=1+3/2A^2$. With this value, Eq. (26) becomes

$$r=c(a/b)^{1/3}I_0^{2/3}(1+3/2A^2)^{4/3}.$$

Thus, the resistance is the same at zero and very high frequencies, but is slightly larger at intermediate frequencies.

VI. EXPERIMENTAL MEASUREMENTS

As is true for most nonlinear circuits, the preceding analysis is only approximately correct. The physical assumptions leading to Eqs. (1) and (2) are only partially justified but serve to give a simple form to these equations. The resulting current-voltage relation, Eq. (4), does agree well with that found by experimenters. Further analysis based on Eqs. (1) and (2) contains a number of mathematical approximations. Whether or not these approximations are justified will depend upon actual experimental conditions.

Measurements have been carried out on several high vacuum lamps, including a 115-volt, 6-watt lamp, and several 6-volt pilot lamps. The current-voltage characteristics, such as shown in Fig. 3, are easily observed with an oscilloscope and are found to agree well with these curves. These characteristics can be observed at frequencies from almost zero upwards. The distortion voltages produced by the lamp when used in a bridge, such as Fig. 5, are readily measured. Such measurements carried out over a wide range of both frequency and current in the lamp show the proper variation of distortion voltages with both these quantities. The observed amounts of distortion indicate that the value of parameter A for typical operation of the lamp is usually much greater than ten. If A, I_0, and ω are known, then parameter a can be found. For the 115-volt, 6-watt lamp, parameter a is about $a=9000$ amp^{-2} sec^{-1}.

The theory is inadequate for values of A just greater than zero but less than four, for which the curves of Fig. 2 are shown dotted. Indicated on these curves are points obtained from experimental measurements with the 115-volt, 6-watt lamp.

The value of the parallel compensating capacitance, as found from Eq. (23), is readily checked. The series capacitance, required by Eq. (24), is so large that measurement becomes difficult. In all cases where experimental measurement is possible, the agreement of the measured data with that predicted by the equations is within the error of the measuring techniques.

VII. ACKNOWLEDGMENT

The theory of the operation of an incandescent lamp was brought to the attention of the author by Professor J. C. May of this laboratory. He also provided special equipment for experimental measurements at extremely low frequencies.

APPENDIX. STEP-FUNCTION RESPONSE

The response of the lamp to a step wave of voltage applied across it can be approximated also. Equations (1) and (2) can be combined to eliminate θ, giving

$$c^3i^3de/dt-c^3i^2edi/dt=ac^3i^5e-be^4, \tag{A.1}$$

where the ambient temperature θ_0 is neglected as in the steady-state analysis. A type of step wave occurring often in practice is that in which the voltage e changes suddenly at time equal to zero from an initial constant value E_1 to a final constant value E_2. Except at the instant of change, $de/dt=0$. Following the change, $e=E_2$, so that the equation applying for positive times, $t>0$, is

$$di/dt=-ai^3+(b/c^3)E_2^2i^{-2}. \tag{A.2}$$

For negative times, $t<0$,

$$i=I_1=(b/ac^3)^{1/5}E_1^{3/5}=g_1E_1, \tag{A.3}$$

where g_1 is the initial conductance of the lamp. Just at $t=0$, the current jumps to the value

$$i=I_m=g_1E_2=(b/ac^3)^{1/5}E_1^{-2/5}E_2, \tag{A.4}$$

since the temperature and conductance cannot change instantaneously. After a very long time, $t\to\infty$, the current becomes

$$i=I_2=(b/ac^3)^{1/5}E_2^{3/5}. \tag{A.5}$$

While the current is assuming its final value, it is given approximately by

$$i=I_2-(I_2-I_m)\exp(-\alpha t). \tag{A.6}$$

If this approximate solution, Eq. (A.6), is substituted into Eq. (A.2), a series of terms with factors $\exp(-n\alpha t)$ results, where n is an integer. Since the solution must hold at all values of t, terms for any given n must satisfy the conditions of the equation. From these conditions it is not difficult to show that

$$\alpha=5(a^3b^2/c^6)^{1/5}E_2^{6/5}. \tag{A.7}$$

A time constant for the lamp may be defined as

$$\tau\equiv 1/\alpha=(\tfrac{1}{5})(c^6/a^3b^2)^{1/5}E_2^{-6/5}. \tag{A.8}$$

In other words, the time constant for any given lamp varies with $E_2^{-6/5}$. This variation is essentially the same as that found from experimental tests.[5] The time constant is reduced by operating at a higher voltage and, accordingly, a higher current.

The approximate solution, Eq. (A.6), is reasonably accurate so long as the voltage change is not too large, i.e., so that the ratio E_2/E_1 is nearly unity. If this ratio departs considerably from unity the solution is not correct.

In this analysis a unidirectional voltage was assumed. The same analysis is applicable for an alternating voltage of relatively high frequency having rms amplitudes of E_1 and E_2.

---

[5] See reference 3, p. 315.

X-Ray Absorption Corrections for Single Crystals*

HOWARD T. EVANS, JR.
Laboratory for Insulation Research, Massachusetts Institute of Technology, Cambridge, Massachusetts

(Received January 28, 1952)

It is shown in this paper that exact expressions may be derived for the absorption factor for the intensity of Bragg reflection by a small euhedral crystal completely bathed in a parallel x-ray beam. The expression is a sum of terms evaluated for subdivisions of the crystal determined according to discontinuities in boundary conditions imposed by the distribution of edges between the plane faces of the crystal. For a prismatic crystal of constant cross section, general expressions are derived for five general types of subdivisions in terms of the linear absorption coefficient and certain linear dimensions. Other expressions are also given for other types of subdivisions which arise in certain cases. The application of the method, including corrections for secondary extinction, is illustrated by calculations on tetragonal barium titanate.

INTRODUCTION

As demands on the precision of crystal structure analysis increase, more emphasis is being placed on accurate measurement of diffraction intensities. One of the most troublesome factors opposing this trend is the effect of absorption of x-rays in the crystal used to measure these intensities. Several methods have been suggested which allow for the absorption effect by some approximate method.[1] This paper describes how the absorption effect on diffraction intensities may be determined by means of exact expressions for single crystals of known shape and dimensions.

THE ABSORPTION EFFECT

The total diffraction energy E of a given diffraction beam for a single crystal rotating at an angular velocity ω is

$$E\omega = AQVI_0, \tag{1}$$

where I_0 is the intensity of the incident x-ray beam, V is the volume of the crystal, Q is a function of the structure factor and includes the Lorentz and polarization effects, and A is a factor caused by absorption and is different for each reflection. The factor A is a function of the physical properites μ (linear absorption coefficient) and Q (as a result of extinction), the geometrical properties 2θ (Bragg angle), the shape, dimensions and position in the beam of the crystal. It is the ratio of the diffraction intensity given by the crystal with absorption to that which would be given without absorption. With absorption, according to Fig. 1,

$$E\omega = I_0 Q \int e^{-\mu(t_1+t_2)}dv;$$

therefore,

$$A = \frac{\int e^{-\mu(t_1+t_2)}dv}{\int dv}. \tag{2}$$

The exponential integral in Eq. (2) cannot be carried out exactly for crystals whose boundaries are curved (cylinders or spheres), but exact solutions are possible for crystals bounded by plane surfaces. The integration must be carried out in sections according as the boundary conditions change at the edges of the crystal. To make the problem practicable, we must assume that the crystal is prismatic and consider only diffraction angles in a plane perpendicular to the axis of the crystal. The more general cases have not been studied, but they become so involved that it will be very seldom that a case will arise in which it will be worth while to consider them. The two-dimensional case can be generalized to some degree, as will be described below.

BOUNDARIES

In a general case we may divide the crystal section into areas with boundaries formed by the surfaces of the crystal and by lines drawn parallel to the incident and diffracted beams. Thus, a crystal of rectangular cross section is divided into four areas in the case shown in Fig. 2a. The limits of the exponential integral in Eq. (2) are different for each area j, so that Eq. (2)

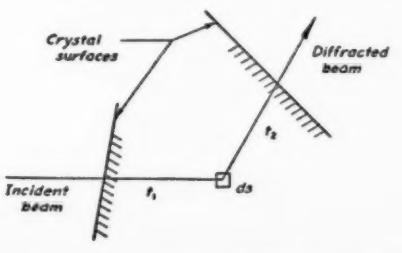

FIG. 1. X-ray beams in the crystal.

* The work described in this paper was carried out mainly under ONR Contract N5ori-07801, and in minor part at Philips Laboratories, Inc. The author's present address is United States Geological Survey, Washington, D. C.

[1] G. Albrecht, Rev. Sci. Instr. **10**, 221 (1939); O. P. Hendershot, Rev. Sci. Instr. **8**, 324 (1937); R. G. Howells, Acta Cryst. **3**, 366 (1950).

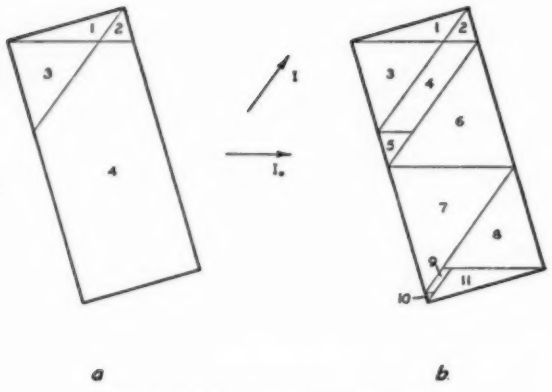

FIG. 2. Subdivision of crystal section.

becomes

$$A=\frac{\sum_j^j \int_j e^{-\mu(t_1+t_2)}ds}{\int ds}=\frac{\sum^j Z_j}{\mu^2 S}, \tag{3}$$

where Z_j is the exponential integral of each subdivision multiplied by μ^2, and S is the area of the section for the two-dimensional case. The areas $j=1$, 2, and 3 are triangles and can be integrated at once, but the area $j=4$ must be further subdivided into areas of simpler shapes. This can be done to give eight areas as shown in Fig. 2b. All areas can now be classified into five types, as follows:

I. A parallelogram in the crystal interior, the direct and diffracted beam both passing through distant surfaces.

II. A triangle adjacent to a crystal surface, through which both the direct and diffracted beam pass.

III. A triangle adjacent to a crystal surface, through which the diffracted beam passes, the direct beam passing through a distant surface.

IV. A triangle adjacent to a crystal surface through which the direct beam passes, the diffracted beam passing through a distant surface.

V. A triangle adjacent to a crystal surface, both the direct and diffracted beam passing through distant surfaces.

These five general types are illustrated in Fig. 3, in which certain dimensions are defined.

ABSORPTION INTEGRALS

As typical examples, the absorption expressions are derived for types I and II. In all five cases double integration is carried out parallel to the x-ray beams, which are taken as the direction of x and y. The area element $ds=\sin 2\theta dxdy$, where 2θ is the Bragg angle.

For type I, the absorption differential from Eq. (3) becomes

$$\frac{1}{\mu^2}dZ_{\mathrm{I}}=e^{-\mu(t_1+t_2)}ds=e^{-\mu(x+x_1+k_x y)}e^{-\mu(y+y_1+x/k_y)}\sin 2\theta dxdy,$$

where

$$k_x=x_2/y_0, \quad k_y=x_0/y_2;$$

$$\frac{1}{\mu^2}Z_{\mathrm{I}}=e^{-\mu(x_1+y_1)}\sin 2\theta\int_0^{y_0}\int_0^{x_0}e^{-\mu(1+k_x)y}e^{-\mu(1+1/k_y)x}dxdy$$

$$Z_{\mathrm{I}}=\frac{k_y\sin 2\theta e^{-\mu(x_1+y_1)}}{(k_x+1)(k_y+1)}[e^{-\mu(x_0+y_2)}-1][e^{-\mu(x_2+y_0)}-1].$$

For type II

$$\frac{1}{\mu^2}dZ_{\mathrm{II}}=e^{-\mu[x-k_0(y_0-y)]}e^{-\mu[y-(x_0-x)/k_0]}\sin 2\theta dxdy$$

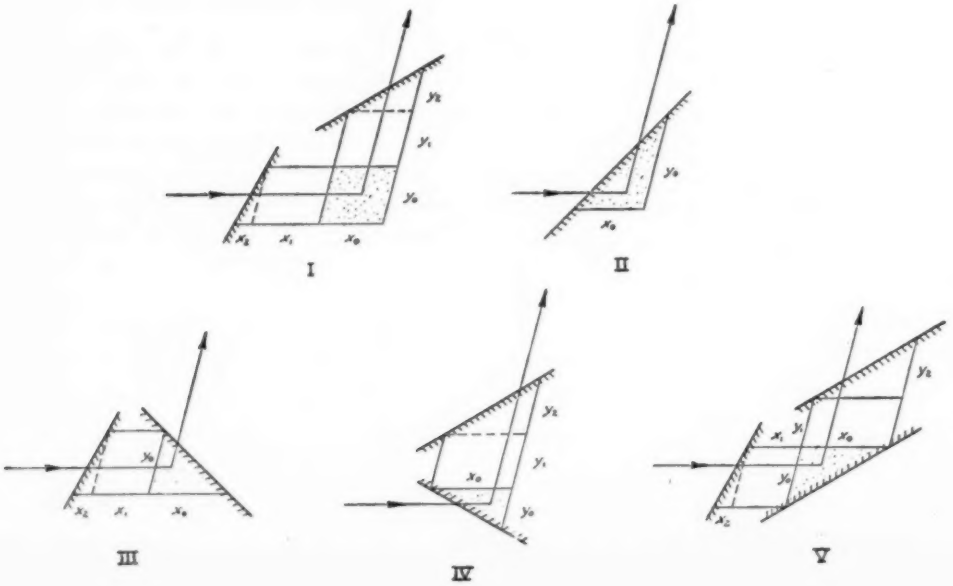

FIG. 3. Five general types of subdivision.

TABLE I. Expressions for Z_j, general types I to V (Fig. 3).
$k_0=x_0/y_0 \quad k_x=x_2/y_0 \quad k_y=x_0/y_2$

Type	Z_j
I	$e^{-\mu(x_1+y_1)}\dfrac{k_y \sin 2\theta}{(k_x+1)(k_y+1)}[e^{-\mu(x_0+y_2)}-1][e^{-\mu(x_2+y_0)}-1].$
II	$\dfrac{k_0 \sin 2\theta}{(k_0-1)^2}[e^{-\mu(x_0+y_0)}+\mu(x_0+y_0)-1].$
III	$e^{-\mu x_1}\dfrac{k_0 \sin 2\theta}{(k_x+1)(k_0-1)(k_0+k_x)}[(k_x+1)e^{-\mu(x_0+x_2)}-(k_0+k_x)e^{-\mu(x_2+y_0)}+(k_0-1)].$
IIIa ($k_0=-k_x$)	$e^{-\mu x_1}\dfrac{k_0 \sin 2\theta}{(k_0-1)^2}[e^{-\mu(y_0-x_0)}+\mu(y_0-x_0)-1].$
IIIb ($k_0=k_x=1$)	$e^{-\mu x_1}\dfrac{\sin 2\theta}{4}[1-e^{-2\mu x_0}(2\mu x_0+1)].$
IV	$e^{-\mu y_1}\dfrac{k_y \sin 2\theta}{(k_y+1)(k_0-1)(k_0+k_y)}[(k_0+k_y)e^{-\mu(x_0+y_2)}-k_0(k_y+1)e^{-\mu(y_0+y_2)}+k_y(k_0-1)].$
IVa ($k_0=-k_y$)	$e^{-\mu y_1}\dfrac{k_0 \sin 2\theta}{(k_0-1)^2}[e^{-\mu(x_0-y_0)}+\mu(x_0-y_0)-1].$
IVb ($k_0=k_y=1$)	Same as IIIb.
V	$e^{-\mu(x_1+y_1)}\dfrac{k_y \sin 2\theta}{(k_y\{k_y+1\}-k_0\{k_y+1\})(k_x+1)(k_y+1)}$ $\times[k_0(k_y+1)e^{-\mu(x_2+y_0)}-k_y(k_x+1)e^{-\mu(x_0+y_2)}+(k_y\{k_x+1\}-k_0\{k_y+1\})].$

where

$$k_0=x_0/y_0;$$

$$\frac{1}{\mu^2}Z_{II}=e^{-\mu(k_0y_0+x_0/k_0)}\sin 2\theta \times\int_0^{y_0}\int_{k_0(y_0-y)}^{x_0} e^{-\mu(1+k_0)y}e^{-\mu(1+1/k_0)x}dxdy$$

$$=\frac{k_0 \sin 2\theta}{\mu(k_0+1)}\int_0^{y_0}[e^{-\mu(k_0+1)y}-1]dy$$

$$Z_{II}=\frac{k_0 \sin 2\theta}{(k_0+1)^2}[e^{-\mu(x_0+y_0)}+\mu(x_0+y_0)-1].$$

The expressions for Z_j for the five types are given in Table I. Occasionally these expressions degenerate to simpler forms, when certain relations between the x-ray beams and the crystal faces obtain. Such expressions must be derived from the original integrals. Some of these expressions are given in Table I.

In some cases it is more convenient to subdivide the crystal section by lines parallel to the crystal edges when such a process results in fewer areas and simpler forms for Z_j. For example, the section of Fig. 2 may be subdivided as in Fig. 4. Another type of subdivision which has been encountered is shown in Fig. 5. Expressions for Z_j are derived by double integration parallel to the crystal edges and are given for these special types in Table II.

Thus it appears that the analysis of a crystal section can be generalized only to a limited extent, when the five types of subdivisions of Table I can be applied. There are cases when such a subdivision is not possible (except in part), or where another kind of subdivision is more convenient. For any case, however, exact expressions for Z_j can always be found, and, when special

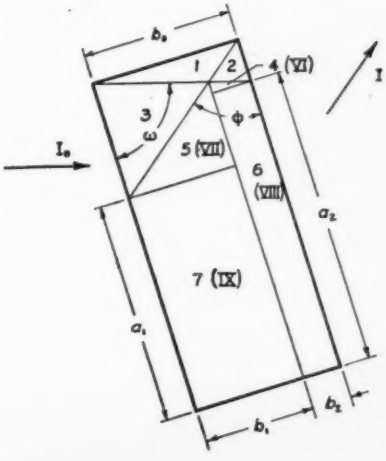

FIG. 4. Special subdivision.

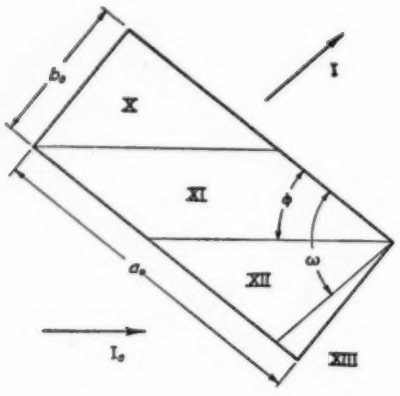

FIG. 5. Special subdivisions.

expressions are necessary, it will usually be found that such expressions will be applicable to an appreciable number of reflections for a given crystal.

CALCULATION OF ABSORPTION FACTORS

In calculating the absorption effect for a large number of reflections, each reflection must be treated separately. The procedure adopted for the present work consisted first of drawing a sketch of the crystal and its subdivisions. The dimensions necessary according to Fig. 3 or 4 are either calculated or measured from the scale drawing. All dimensions are multiplied by μ, the linear absorption coefficient. If secondary extinction is included μ will be different for each reflection.

As examples we cite two reflections from a tetragonal barium titanate crystal whose dimensions in cross section are 0.160×0.071 mm. The (203) reflection is produced under the conditions shown in Fig. 6. The linear absorption coefficient μ_0 calculated for this crystal is 198 cm^{-1}, and for this reflection we include a small extinction, giving $\mu=205$. The dimensions of the crystal multiplied by μ are $X=1.456$, $Y=3.280$, area $\mu^2S=4.771$ (in dimensionless units). The summation of formulas is as follows:

Subdivision j in Fig. 6	Type	Z_j
1	X	0.325
2	IV	0.058
3	I	0.130
4	IIIa	0.073
5	IVa	0.004
6	I	0.025
7	III	0.007
8	X	0.086
		$\Sigma Z_j=0.708$

$$A=\frac{\Sigma Z_j}{\mu^2 S}=\frac{0.708}{4.771}=0.148.$$

The reflection (501) as illustrated in Fig. 4 has a larger extinction correction giving $\mu=215$. Then $X=1.528$, $Y=3.440$, and $\mu^2S=5.250$ (dimensionless

TABLE II. Expressions for Z_j, special types VI to XIII.

$$s=\frac{1}{\sin\phi}-\frac{1}{\sin\omega}.$$

Type	Figure	Z_j
VI	4	$\dfrac{e^{-\mu b_0/\sin\omega}}{s^2\tan\omega}[1-e^{-\mu s b_2}(\mu s b_2+1)]$.
VII	4	$\dfrac{e^{-\mu b_0/\sin\phi}}{s^2\tan\phi}[1+e^{-\mu s b_1}(\mu s b_1-1)]$.
VIII	4	$\dfrac{e^{-\mu b_0/\sin\omega}}{s}[1-e^{-\mu s b_2}]\mu a_2$.
IX	4	$\dfrac{e^{-\mu b_0/\sin\phi}}{s}[e^{+\mu s b_1}-1]\mu a_1$.
X	5	$\dfrac{\cot\omega}{s}[\sin\phi e^{-\mu b_0/\sin\phi}-\sin\omega e^{-\mu b_0/\sin\omega}+(\sin\omega-\sin\phi)]$.
XI	5	$\dfrac{\mu(a_0-b_0\cot\omega)}{s}[e^{-\mu b_0/\sin\omega}-e^{-\mu b_0/\sin\phi}]$.
XII	5	$\dfrac{(\cot\phi-\cot\omega)}{s^2}[(\mu s b_0+1)e^{-\mu b_0/\sin\phi}-e^{-\mu b_0/\sin\omega}]$.
XIII	5	$Z_X\dfrac{\cot\phi}{\cot\omega}$.

units). The summation is as follows:

Subdivision j in Fig. 4	Type	Z_j
1	II	0.149
2	IV	0.031
3	III	0.216
4	VI	0.004
5	VII	0.239
6	VIII	0.085
7	IX	0.412
		$\Sigma Z_j = 1.136$

$$A = \frac{1.136}{5.250} = 0.216.$$

THE ABSORPTION TOPOGRAPHY

Where extinction is not important some saving in time may be gained by plotting a number of strategic values of A on Weissenberg coordinates. The values of 2θ and ω (angular position of the crystal) for MoKα reflections ($h0l$) of tetragonal $BaTiO_3$ are plotted in Fig. 7, and produce the familiar Weissenberg pattern. Superimposed on this pattern are contours representing the variation of A as a function of 2θ and ω. The discontinuities in this function correspond to the conditions of grazing incidence of either the direct or diffracted beam with the surfaces of the crystal. This phenomenon is identical with that described by Buerger[2] and by MacGillavry and Vos.[3] If the crystal is producing fluorescent scattering, this scattering will be uniform over 2θ and ω, and, except for the absorption factor A, the same as for Bragg reflection (without extinction). MacGillavry has shown that a photometric measurement of such a background on a Weissenberg film may be used to determine approximately the shape of the function $A(2\theta, \omega)$ in order to estimate the corrections for the Bragg reflections. Such measurements will be useful when the absorption coefficient is not very different for the incident and fluorescent wavelengths, that is, for the paths t_1 and t_2 of Fig. 1. More generally, the shape of the function may be approximated by computing a few strategic values of A, using the methods described above.

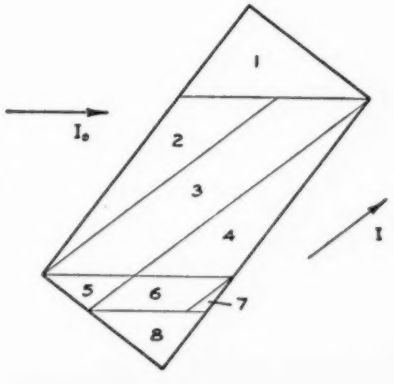

FIG. 6. Example of calculation of absorption factor.

[2] M. J. Buerger, Z. Krist. **99**, 189 (1938).
[3] C. H. MacGillavry and H. J. Vos, Z. Krist. **105**, 257 (1943–44).

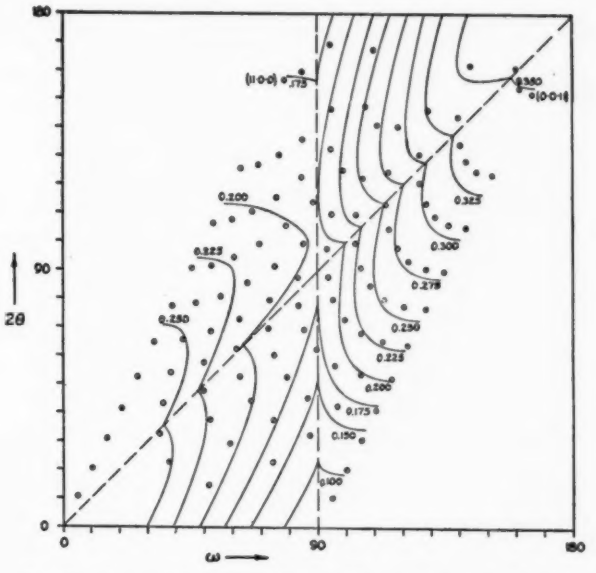

FIG. 7. Absorption topography on Weissenberg coordinates.

SECONDARY EXTINCTION

Because of the drain of radiation energy from the x-ray beam as a result of the diffraction process as it passes through the crystal, the ordinary linear absorption coefficient μ_0 will be increased by an amount proportional to Q,

$$\mu = \mu_0 + gQ.$$

When Q is not known, some method of intensity measurement must be used in which secondary extinction does not play a part. For example, the strong, low-Bragg-angle reflections may be measured from powder patterns, although in such methods preferred orientation is always a hazard, sometimes very serious. When Q is known, at least approximately, the value may be estimated by trial. This was the procedure used for tetragonal barium titanate. In this case, A for twelve strong, low-Bragg-angle reflections was calculated for various values of g, and the quality of it estimated by computing the usual reliability factor,

$$R = \frac{\sum \big| |F_{obs}| - |F_{calc}| \big|}{\sum |F_{obs}|},$$

where we set

$$\sum |F_{obs}| = \sum |F_{calc}|.$$

The results of this work are shown in Table III. The best value is seen to be near $g = 5.06 \times 10^3$, and this was used finally in calculating all absorption factors.

As far as the importance of secondary extinction is concerned, it is felt that since the magnitudes of ordinary absorption and extinction effects vary roughly as the average electron density of the crystal, the average influence of extinction will increase, as the ordinary absorption effect increases. That is, extinction will generally be more important for highly absorbing crys-

TABLE III. Determination of secondary extinction in barium titanate.

hkl	$g\times10^{-5}=1.45$ μ	A	2.90 μ	A	4.35 μ	A	5.06 μ	A	5.80 μ	A	6.50 μ	A
100	214	0.230	230	0.208	246	0.179	254	0.169	262	0.159	270	0.151
200	258	0.175	318	0.117	378	0.079	409	0.066	438	0.056	467	0.048
300	202	0.248	206	0.242	210	0.236	211	0.235	214	0.230	217	0.229
001	214	0.062	230	0.052	246	0.045	254	0.043	262	0.041	270	0.039
002	258	0.071	318	0.050	378	0.039	409	0.035	438	0.033	467	0.031
003	202	0.131	206	0.128	210	0.125	211	0.124	214	0.122	215	0.122
101	257	0.137	317	0.094	376	0.080	406	0.058	436	0.050	466	0.044
102	205	0.149	210	0.147	216	0.145	218	0.144	222	0.142	229	0.141
103	211	0.109	224	0.097	237	0.088	243	0.085	250	0.081	257	0.078
201	204	0.228	210	0.220	216	0.212	219	0.208	222	0.205	225	0.201
202	226	0.159	254	0.132	282	0.111	296	0.104	310	0.097	324	0.092
301	211	0.222	224	0.205	237	0.187	243	0.177	250	0.168	256	0.161
	$R=0.129$		0.097		0.083		0.079		0.082		0.089	

tals, and generally less important for low absorbing crystals.

TETRAGONAL BARIUM TITANATE

The methods for correction of intensity measurements for absorption and secondary extinction have been applied to a detailed crystal structure study of tetragonal barium titanate. The factor A was calculated for 99 reflections with secondary extinction included. The factor ranged from 0.035 to 0.325. The success of the calculations is indicated somewhat by the reliability factors which were obtained for the final structure. The intensities were measured on the previously mentioned crystal with a Geiger counter, using techniques which will be described in detail elsewhere. The calculated values are based on three structure parameters and nine temperature parameters. For 99 reflections, $R=4.72$ percent. If low-angle reflections are omitted, the remaining 83 reflections give a factor $R=3.72$ percent. In this case, A ranges from 0.085 to 0.325. The larger deviations at low angles may be caused in part by the presence of a small amount of primary extinction, or to the departure of the true crystal structure from the Hartree atom model used for the calculated structure factors. The details of the structure analysis will appear in another place.

Physical Processes in the *L* Cathode

D. L. SCHAEFER AND JOHN E. WHITE
General Electric Company, Tube Department, Schenectady, New York
(Received January 30, 1952)

The activity of this barium-on-tungsten cathode is maintained by dispensing barium from a pellet of barium compound. The dispensing mechanism is shown to be controlled by surface diffusion of barium over tungsten. Despite incomplete coverage of the emitting surface with barium, and almost complete absence of streaming of active material out through pores in the surface material, evaporation of barium is sufficient to be of concern in certain applications.

I. INTRODUCTION

THE monolayer-activated thermionic cathode, given its initial stimulus by Langmuir,[1] is intrinsically a very attractive source of electrons. The fact that active material evaporates more slowly at a given temperature from a monolayer than from bulk material has made it possible to heat low-work-function materials very hot in monolayer form. Furthermore, the work function of a material one atom layer thick is often lower than that of the same material in bulk. Some thirty years after its announcement Langmuir's thoriated tungsten cathode, which is activated by a monolayer of Th, continues to be the best emitter in many applications. Difficulty has been experienced in producing stable monolayer emitters from materials with lower work functions than thorium because of the higher volatility of such substances. The problem was attacked by Hull,[2] who devised a monolayer cathode in which the active layer was continuously replenished by a "dispenser" containing a barium compound. The dispenser idea has been applied to a barium monolayer on tungsten,[3] and publicized by the Philips Company as their *L* cathode.

II. DESCRIPTION AND PERFORMANCE

The *L* cathode has been constructed by Philips in several forms, all of which operate with a basic design consisting of a cavity containing active material and connected to the vacuum space only through pores in a tungsten compact whose surface serves as the electron emitter. The particular form which has been most available is illustrated in Fig. 1; the experiments to be described were carried out on this type. The diameter of the emitting surface (tungsten compact) is nominally 3 mm. The cavity originally contains barium carbonate, usually with some strontium carbonate as well. Activation is obtained, after degassing the cathode, by thermal breakdown of the carbonate at about 1100–1200°C and operation in about this temperature range until emission stabilizes.

The performance of the cathode is evident from the I–V plot shown in Fig. 2. Such curves reproduce quite well from one cathode to another. Current densities of 20 or 30 amperes per cm² can readily be obtained, but only at high operating temperatures. In any contemplated application, one must take into account both the emission capabilities and the evaporation rate, discussed later.

III. PROPOSED OPERATING MECHANISM

F. K. duPré and E. S. Rittner[4] have described the operating mechanism of this cathode as constituted of the following processes:

1. Thermal decomposition of the $BaCO_3$ to BaO.
2. Evaporation of BaO as oxide within the cavity.
3. Streaming of BaO vapor into the pores of the tungsten compact.
4. Reaction of BaO with tungsten, producing barium.
5. Surface migration of Ba atoms along the pores and over the emitting area.
6. Evaporation of active material from the emitting surface.
7. Electron emission from a layer of Ba on O on W.

Even if the general correctness of this plausible mechanism be accepted, important unanswered questions remain, such as:

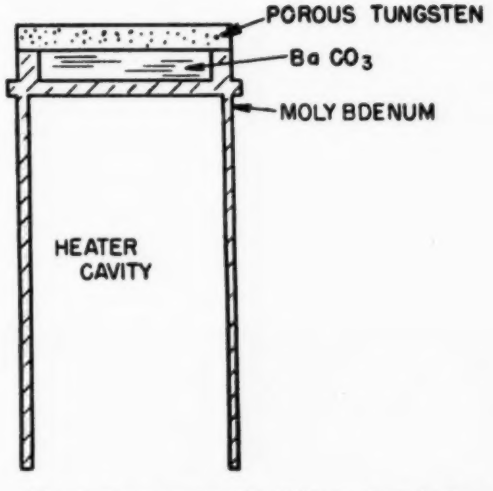

FIG. 1. Cross section of a disk-type *L* cathode.

[1] I. Langmuir, Phys. Rev. **22**, 357 (1923).
[2] A. W. Hull, Phys. Rev. **56**, 86 (1939).
[3] Lemmens, Jansen, and Loosjes, Philips Tech. Rev. **11**, 341 (1950).
[4] F. K. duPré and E. S. Rittner, Symposium on Electron Emission of the Division of Electron Physics, A.P.S., New York, January, 1951.

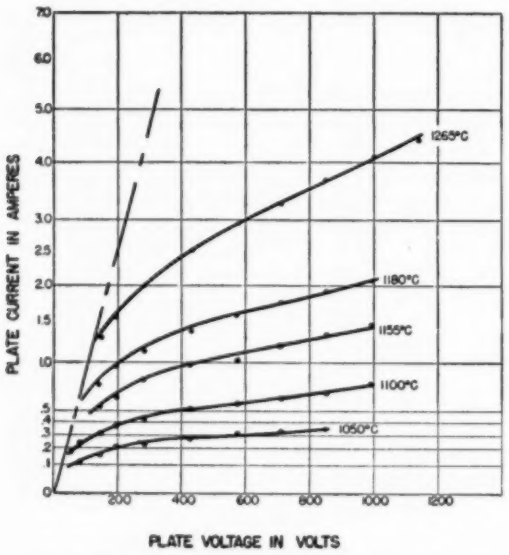

FIG. 2. $I^{\frac{1}{2}}-V$ plot of pulse emission data taken on 3-mm diameter L cathodes.

1. Is it possible to draw higher emission densities than those so far attained from such a cathode?

This question depends on whether or not the tungsten surface is completely covered by barium, and if so whether the coverage is more than a monolayer thick.

2. Is it possible to reduce a reportedly high rate of evaporation from the cathode surface?

This question, as well as the first, is related in part to the degree of surface coverage existing under operating conditions. It also depends on whether BaO streams out the pores in parallel with the surface diffusion process. In general the question depends on which of the seven previously-mentioned processes determines the evaporation rate.

3. There appears to be some doubt whether the chemisorbed layer of oxygen, assumed by duPré and Rittner to underlie the surface barium, is really stable enough to remain through the life of the tube as barium diffuses over and evaporates from the tungsten cathode surface.

The purpose of this paper is to provide such experimental evidence of the physical processes at work in the cathode that answers to these and other questions relating to this emitter are possible.

FIG. 3. Emission micrographs of an L cathode with two conditions of surface coverage. Total area represents a circle 0.030" in diameter at the center of the cathode.

IV. EXPERIMENTAL STUDY

Various features of the cathode mechanism have been studied separately; the experimental procedures and results will be discussed individually in the following sections.

All temperatures given are true temperatures. These were determined by a blackbody study of one of the cathodes carried out by drilling a small hole through the porous tungsten. The spectral emissivity of the porous tungsten compact was found to be 0.7 at 0.65-micron wavelength in the temperature range of interest.

(a) Degree of Surface Coverage

The most direct method of showing whether the tungsten surface is completely or partially covered with barium is by means of emission microscopy. We have employed this method by sealing an L cathode into a cathode-ray tube structure and focusing a picture of the emitting surface onto the phosphor screen of the tube. A 10-inch cathode-ray tube without an ion trap was used. The gun consisted of a first and second grid and a cylindrical anode as normally used in the 10FP4 tube.

Emission micrographs are best when taken at relatively low cathode temperatures and high accelerating voltages to avoid space-charge effects. Such conditions were used in these studies. Low cathode temperatures have the added advantage of "freezing" the surface distribution of barium while the photograph is taken. The procedure used was to operate the cathode at the desired temperature for a time sufficient to assure equilibrium surface coverage. The cathode temperature was then suddenly reduced to a low "measurement" temperature, where the coverage would not change for a long period, and a photograph with adequate exposure time was made.

Emission micrographs made in this way are shown in Fig. 3. The photograph on the left was taken from an equilibrium operating temperature of 1230°C, the one on the right from a temperature of 980°C. In both cases, the emission pattern was photographed at the same "measurement temperature" of 760°C. To insure that any differences in the two photographs were differences in the actual emission patterns both photographs were taken side by side on the same piece of film under the same exposure conditions and were processed simultaneously.

The photograph on the left clearly shows the grainy emission pattern to be expected from incomplete surface coverage. Although the bright spots cannot be exactly identified as individual pores their number is about right for such identification rather than for identification as separate crystal faces on the tungsten.

The photograph on the right, corresponding to equilibrium coverage at a lower temperature, shows a more uniform brighter pattern corresponding to a higher more uniform coverage of the surface of the tungsten by barium. This result may be generalized by the state-

ment that surface coverage in these cathodes increases as the operating temperature decreases.

A further inference of incomplete coverage was obtained by making a Richardson plot of data from operating cathodes. This plot gave an effective work function of 1.67 volts. This work function could correspond to a partially covered surface, since the work function of W covered by a monolayer of Ba is given in the literature[5] as 1.56 volts. It could not correspond to a heavy layer of bulk, Ba, the work function of which is over 2 volts.

Our study of the degree of surface coverage was concluded by an experiment which confirmed the emission micrograph finding that the cathode surface is more completely covered at low operating temperatures than at high. The results of this experiment are shown in Fig. 4. Peak emission was first measured, as shown on the curve at zero time, after a period of operation to establish equilibrium surface coverage at the initial temperature of 1255°C. Heating power was then suddenly reduced to a value which ultimately gave a temperature of 990°C. As the temperature fell, emission fell accordingly, dropping from 0.62 ampere to 0.11 ampere as the cathode temperature reached its lower value. After a period of about four minutes, the emission began to rise, indicating an increase in barium coverage. The increased coverage at the lower temperature resulted in an increase of emission from 0.11 ampere to 0.14 ampere or 27 percent. The converse effect, showing an emission maximum on a sudden increase in temperature, was also observed.

It seems well established that L cathodes now furnished by Philips operate with a surface incompletely covered with active material and that the degree of coverage rises with decreasing temperature.

(b) Evaporation Rate

We have employed a method which measured evaporation from the emitting surface alone and thus provided an intrinsic parameter of the cathode. Our method is subject to some error caused by lack of collimation of the stream of evaporant; but is quite reproducible and gives directly and accurately the quantity needed in some studies such as grid emission.

The evaporation rate was measured in a tube arranged as shown schematically in Fig. 5. Referring to the figure, the L cathode is spaced 0.015 inch from a plate or anode of 0.005-inch thick tantalum. The anode is perforated with a 0.030-inch hole, above the center of which is stretched a 0.005-inch tungsten wire. The wire-anode spacing is 0.010 inch.

Evaporant from the cathode passed through the hole onto the tungsten wire which was held at a constant temperature. Observation of the electron emission from the wire as a function of time gave the now familiar[6]

[5] A. L. Reimann, *Thermionic Emission* (Chapman and Hall, Ltd., London, England, 1934).
[6] J. A. Becker, Phys. Rev. **34**, 1323 (1929).

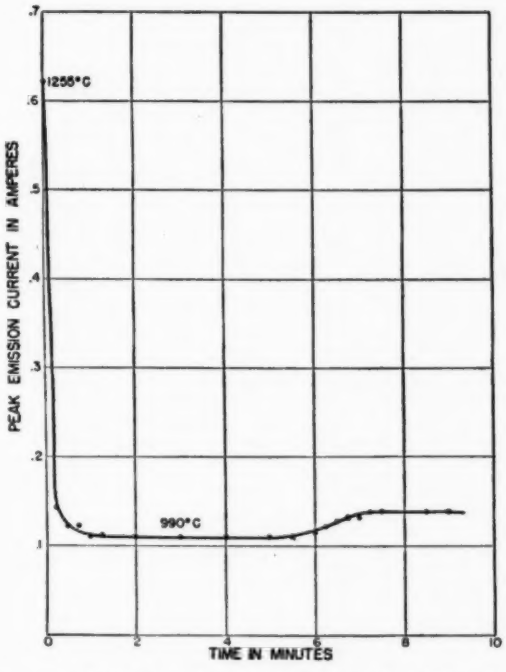

FIG. 4. Emission transient showing first the effect of cooling the cathode and finally the effect of increasing coverage of the surface with barium at a lower temperature.

curve shown in Fig. 6, with a maximum occurring at approximately monolayer coverage. The time to reach a maximum in the curve is obviously the inverse of the evaporation rate in monolayers per unit time for the specific temperature at which the cathode is operating. The tungsten wire used to intercept evaporant from the cathode could be heated to high temperatures for thorough initial cleaning and outgassing as well as to drive off evaporant collected during previous runs.

(c) Nature of Evaporant

The work function of the coated portion of the wire used in the evaporation studies could readily be studied by Richardson plots under any desired degree of coverage. Such plots were made under two particular conditions of coverage which were of especial interest. The first condition of interest was the condition of single monolayer coverage, corresponding to the maximum of the emission-time curve of Fig. 6. A Richardson plot made under this condition gave a work function of 1.58 volts which agrees within experimental error

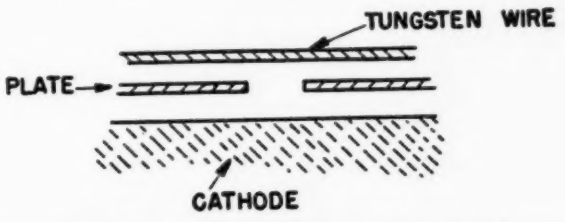

FIG. 5. Schematic arrangement of electrodes for evaporation rate measurements.

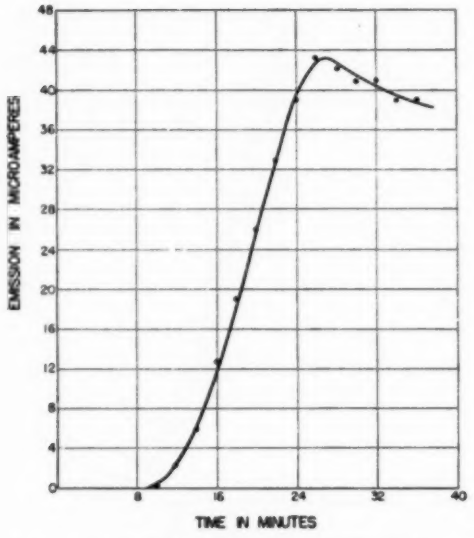

FIG. 6. Increasing emission from the evaporation-measuring wire as surface coverage increases, and reduction of emission beyond monolayer coverage.

with the value of 1.56 volts taken from the literature[5] for a monolayer of Ba on pure tungsten. If the evaporant had been BaO, the work function expected with complete coverage would have been 1.0 volt.[7]

The nature of the evaporant from the cathode was studied further by continuing evaporation from the cathode to far beyond the maximum of the emission-time curve, Fig. 6, when a layer of evaporant many atomic layers thick had been built up. A Richardson plot made under these conditions indicated a work function of 2.02 volts as compared with a value of 2.1 volts given in the literature[8] for bulk barium.

These experiments have provided rather convincing evidence that the active material which evaporates from the L cathode is barium metal with no more than insignificant quantities of BaO. Some additional evidence will appear in the next section, incidental to a study of the mechanism of barium transfer.

(d) Mechanism of Barium Transfer

Since the experimental evidence indicates that the L cathode normally operates with somewhat less than complete coverage of Ba on the surface, it is natural to suppose that the process controlling evaporation rate will be one of three:

1. The rate of Knudson flow of BaO vapor into the pores of the tungsten compact.
2. The rate of BaO reduction on contact with the tungsten.
3. The rate of diffusion of Ba over the tungsten surface.

It has seemed reasonable to exclude the chemical reduction process as a likely bottleneck since similar reduction processes are known to be extremely efficient.[9] A study of the activation energy of barium transfer was used to distinguish between the two remaining processes.

Figure 7 shows a graph of the results of the barium-evaporation-rate studies with the log of evaporation rate plotted against $1/T$, where T is the equilibrium temperature in deg K. The data are plotted for four different tubes. The slope of this curve gives an activation energy of 2.61 electron volts per atom. This value differs so widely from the value given in the literature for the latent heat of evaporation of BaO from itself, which is 3.91 volts,[10] that evaporation of BaO is excluded as the controlling process in the barium-transfer mechanism. The essential constancy of the slope of the curve over its length also indicates that no significant quantity of BaO streams out the pores in a parallel transfer mechanism, thus confirming the findings of the last section that little BaO is present in the evaporant.

By a process of elimination, it is found that Ba evaporates from the cathode, the rate of evaporation being controlled by the rate of diffusion of Ba over the surface of the tungsten compact. However, it has not been demonstrated whether the diffusion takes place over pure tungsten or over a chemisorbed layer of oxygen. A separate experiment was performed to provide evidence on this point.

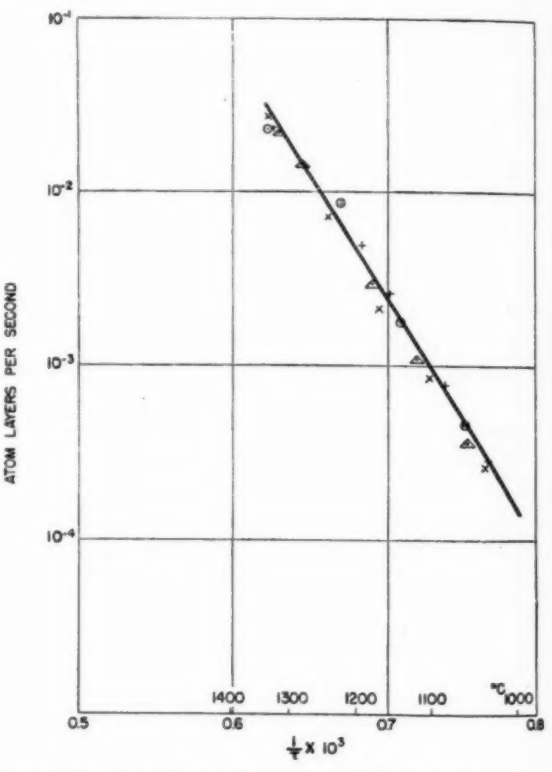

FIG. 7. Evaporation rate from L cathodes as a function of temperature. Different type points correspond to each of the four tubes used in the measurements.

[7] G. E. Moore and H. W. Allison, Phys. Rev. **77**, 246 (1950).
[8] H. B. Michaelson, J. Appl. Phys. **21**, 536 (1950).
[9] Moore, Allison, and Morrison, Phys. Rev. **75**, 347 (1949).
[10] J. P. Blewett, J. Appl. Phys. **10**, 668 (1939).

A tube was built to determine the activation energy for diffusion of Ba over clean tungsten. It is recognized that this energy varies with degree of coverage, reducing as the coverage grows; however, since the presence of oxygen would change the diffusion energy much more than would moderate changes in coverage, a diffusion experiment should have considerable weight in deciding whether a layer of oxygen is present.

The tube for diffusion study is shown schematically in Fig. 8. Barium was evaporated from a barium berylliate plus tantalum source to a depth of four atomic layers onto the rear side of the tungsten ribbon. The thickness of barium deposition was determined by observing emission to the rear anode, which made it possible to find the rate of monolayer deposition as described above in connection with Fig. 6. The tungsten ribbon was flashed to high temperature for cleaning before the start of barium deposition and was held at a constant low "measurement temperature" during deposition. A small negative potential was held on the guard plates during emission measurements to prevent current from flowing to the front anode because of the barium on the back side of the ribbon. The diffusion study was then carried out by operating the ribbon at a "diffusion temperature" for a sufficient period of time (sometimes lasting well over 24 hours) to enable the emission from the front side of the ribbon, observed periodically at the "measurement temperature," to reach a specified value. The time required to reach this specified emission value at the "measurement temperature" must correspond to the time required to obtain a certain degree of coverage of Ba on the front side of the ribbon. The reciprocal of this time is a measure of the rate of diffusion or of the coefficient of diffusion in arbitrary units. A plot of the logarithm of this reciprocal time against the reciprocal of the temperature in degrees Kelvin is a straight line, as expected; the activation energy for diffusion may be calculated from its slope. Figure 9 shows the curve obtained from the observed data. Since fewer points are available on this curve than might be desired for accurate slope

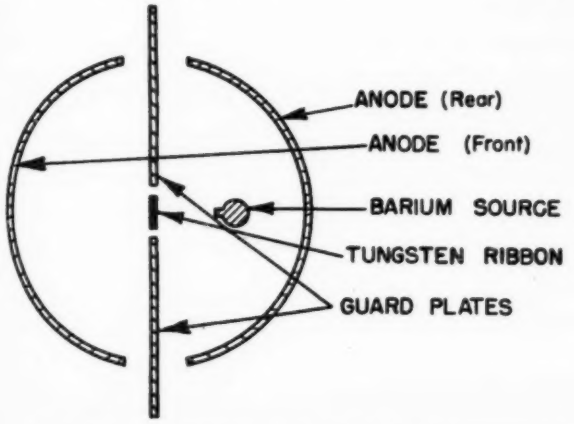

FIG. 8. Schematic arrangement of electrodes for measurement of diffusion rates of Ba on W.

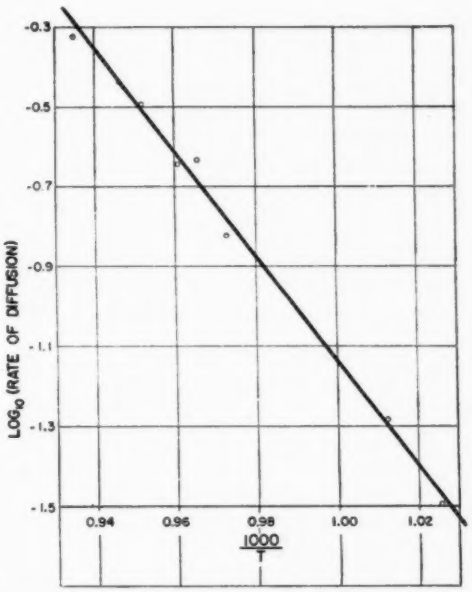

FIG. 9. Log of diffusion rate plotted against reciprocal temperature of tungsten over which barium is diffusing.

determinations, the best straight line was determined by the method of least squares. The activation energy of diffusion determined from the slope of this curve is 2.58 electron volts per atom which agrees surprisingly well with the value of 2.61 electron volts per atom obtained from the slope of the *L* cathode evaporation rate curve in Fig. 7. One is forced to the conclusion that on and near the emitting surface barium transfer occurs by diffusion over clean tungsten rather than over a sorbed layer of oxygen.

If this conclusion represents the facts, it is natural to raise the question, "What happens to the oxygen monolayer which Langmuir's work has shown always to be present on tungsten unless special measures are taken to remove it?" We have calculated the time required to remove this monolayer by simple evaporation, assuming the normal operating temperature for the Philips cathode and evaporation rates of oxygen quoted by Langmuir.[11] It turns out that nearly two years would be required to evaporate half of the oxygen monolayer under these conditions.

However, one might consider another mechanism for oxygen removal from the tungsten surface. This mechanism involves the occasional removal of an oxygen atom from the surface with the Ba as the Ba evaporates. The literature gives no direct information on this subject but the recent work of L. T. Aldrich[12] gives data on the related problem of Ba *vs* BaO evaporation from bulk BaO on tungsten. Although this is not the monolayer condition found in the *L* cathode, it contributes to the logic that the evaporation of Ba from the surface may enhance the removal rate of oxygen to orders of

[11] I. Langmuir, J. Am. Chem. Soc. **54**, 2798 (1932).
[12] L. T. Aldrich, J. Appl. Phys. **22**, 1168 (1951).

magnitude above that calculated from Langmuir's figures. Aldrich's work points to an evaporation rate of Ba atoms about equivalent to that of BaO molecules in the vicinity of 1100°C. If the same ratio were obtained under monolayer conditions, Fig. 7 shows that a monolayer of oxygen would be removed from the L cathode of 1100°C in about 10^3 seconds. Even if the BaO/Ba ratio were reduced two orders of magnitude under monolayer conditions, a monolayer of oxygen would be removed from the L cathode in 10^5 seconds or about 32 hours, which is early in the life of a cathode.

V. CONCLUSIONS

According to the evidence, the L cathode operates with its outer tungsten surface partially covered by Ba, but without a significant amount of sorbed oxygen on the emitting area or the surface of the capillaries near the outside. The evaporation rate of barium from the surface is controlled by the activation energy of diffusion of barium over clean tungsten. Within the capillaries near the cavity itself sorbed oxygen may be present, with the diffusion rate of Ba maintained by a high concentration gradient, Ba possibly occurring in layers many atomic diameters thick. The oxygen involved in the reduction of BaO must appear as compounds of barium, tungsten, and oxygen near the cavity.

The authors are indebted to C. R. Knight for the suggestion to study these cathodes and for useful discussion during the course of the work to Dr. Edith B. Fehr for valuable suggestions.

JOURNAL OF APPLIED PHYSICS VOLUME 23, NUMBER 6 JUNE, 1952

Electrical Noise from Instrument Cables Subjected to Shock and Vibration*

THOMAS A. PERLS
National Bureau of Standards, Washington, D. C.
(Received February 7, 1952)

Existing information on the reduction of spurious signals from instrument cables is reviewed. A tentative theory is formulated to account for the known data. Subsequent experiments confirm this theory and allow the formulation of a detailed mechanism of noise generation in cables. The noise may be eliminated for practical purposes (reduced by a factor of 500 or more in some cases) by having continuous electrical conduction between both surfaces of the insulating dielectric and the adjacent conductors. A simple procedure is outlined to make short lengths of this cable for laboratory use, and an industrially applicable method is suggested. There appears to be no limit on how small the diameter of such cables could be made.

INTRODUCTION

PIEZOELECTRIC gauges have been used for many years for the measurement of transient pressures, accelerations, and forces. Since the charge developed by a piezoelectric crystal leaks off at a rate determined by the effective resistance across the crystal, it is necessary to connect the output of crystal-type gauges to circuits having an extremely high effective input impedance, if it is desired to obtain good low frequency response from these devices. Considerable development work has gone into high input-impedance preamplifiers such as cathode followers, so that effective resistances of the order of 100 to 200 megohms are commonly achieved. Since the crystal-type gauges are often exposed to conditions of shock sufficient to cause spurious signals in the preamplifier, it is in general necessary to connect the gauge to the preamplifier by a short length of cable which thus joins two extremely high impedances. Two difficulties commonly arise in this type of connection:

(1) The cable readily picks up signals from electrostatic fields. This is usually remedied by careful shielding and care in the selection of a single point to which the entire instrumentation is grounded.

(2) It is found in general that the cables generate spurious signals when subjected to shock and vibration. The mechanism of this effect has not been well understood and is usually assumed to be somehow related to the (converse) electrostrictive effect in the cable dielectric,[1] changes in the electrical capacitance of the cable,[1,2] "generation of small potentials in the dielectric itself due to intermolecular friction,"[2] or "static charges developed on the outer braided shield, as a result of friction between the dielectric and shield."[3] It is the investigation of this effect which is the subject of this paper.

With the advent of barium titanate, it has become possible to build crystal-type transducers which combine small size, low cost, high output, and large internal

* This investigation was conducted under a cooperative program of Basic Instrumentation Research and Development sponsored by the ONR, U. S. Air Force, and AEC.

[1] H. C. Roberts, *Mechanical Measurements by Electrical Methods* (The Instruments Publishing Company, Inc., Pittsburgh, 1951), p. 180.
[2] R. M. Peirce and V. Siegfried, "Noise Suppression in Coaxial Cable," Annual Report, 1948, Conference on Electrical Insulation, National Research Council, Washington, D. C., March 15, 1949, p. 36.
[3] R. H. Cole, *Underwater Explosions* (Princeton University Press, Princeton, New Jersey, 1948), p. 163 and 195–198.

capacitance (see, for example, references 4 and 5). The main limitation on the use of these transducers has come from the deficiencies in the available cables. Commercially-available "low noise" cable† is bulky, heavy, and rigid, and still develops signals which are comparable with the output of crystal-type transducers under some conditions. A cable to be used with a small barium-titanate accelerometer,[4] for example, should be small, light, and flexible, in order to minimize the mechanical loading effect on the crystal due to the moving portion of the cable. It was therefore thought worth while to re-examine current theories on cable noise and to test several types of cables in an effort to determine whether it might be possible to make or obtain a very small, light, and flexible cable with a sufficiently low sensitivity to shock and vibration.

AVAILABLE "LOW NOISE" CABLES

Means of reducing spurious cable signals are reviewed as of 1946 in Cole's book on underwater explosions.[3] At that time, the most successful solution to the problem was provided by copper-tubing cable developed at the David Taylor Model Basin;[6] in another approach, tests were in progress on the effect of making the outside surface of the dielectric a relatively good conductor. Since then, special "low noise" Simplex cable has been used by several government agencies. Because of its size (0.4-in. o.d.) and considerable rigidity, this cable could unfortunately not be considered for use with very small transducers.

It is understood from representatives of various manufacturers that comparative tests among small, flexible, shielded, commercially available cables have already been conducted, with results showing large variations in spurious noise from one type of cable to another and among different samples of the same type of cable. None of the cables tested gave entirely satisfactory results.

DISCUSSION OF VARIOUS THEORIES

Experimental tests of several types of cables showed that the capacitance change which can be made by mechanically distorting or flexing the cables ranges from 0.4 to 2 micromicrofarads. This capacitance change appears in parallel with a combined gauge and cable capacitance (in a typical case) of a few hundred micromicrofarads. In the presence of a signal from the crystal, this effect would be expected to cause a noise signal of not more than 1 percent of the gauge signal, and would in general be entirely negligible.

On the other hand, it is experimentally observed that the signal induced by moving or flexing the cable may be several times (under some conditions several hundred times) the signal from the gauge itself. This has sometimes been ascribed to either a (converse) electrostrictive[1] or a piezoelectric‡ effect in the cable dielectric. Data on these effects for rubber[7] show very little consistency and indicate in many cases that insufficient precautions were taken against surface effects (see, for example, references 8 and 9). The converse electrostrictive and piezolectric sensitivities of other "amorphous" dielectrics are too small by several orders of magnitude to account for the observed effects.

The tests reported in this paper started from the assumption that the observed effects were due to a combination of frictional separation of charges and electrostatic induction, and that the generation of cable noise depended on the ability of either of the conductors (central conductor or shield, in the case of coaxial cables) to deposit charges on the surface of the dielectric insulator. On this assumption, the noise could be eliminated if the dielectric were coated with a reasonably good conductor, so that charges transferred to the dielectric from either the central conductor or the shield of the cable could immediately leak off. In order to gain a complete understanding of the effects involved, it appeared that tests should be conducted with coaxial cables having conducting coatings on the inside, on the outside, and on both.

A "standard" test set-up was made to compare the performance of various experimental and commercial cables when connected between a small barium titanate accelerometer and a cathode follower (Gulton type F403). The output of the cathode follower was recorded through a dc amplifier (Brush type BL932) on a direct inking oscillograph (Brush type BL222). A signal equivalent to a step loading of about 300 g could be obtained by loading the accelerometer with a 1-pound weight which was then suddenly removed. This served mostly as a check on the over-all operation of the system and as a detection device for accidental shorts in the experimental cables. The amplitude of this signal depended a great deal on the speed with which the weight was removed, since the time constant of the system was only about 40 milliseconds, and a quantitative reference signal was therefore provided from the built-in calibration voltage of the Brush amplifier. The "standard" test for cable noise consisted in grasping a

[4] L. T. Fleming, Instruments **24**, 968 (1951).

[5] G. K. Guttwein and A. I. Dranetz, Electronics **24**, No. 10, 120 (1951).

† Manufactured on special order, for example, by the Simplex Wire and Cable Corporation. See also reference 2.

[6] U. S. Patent No. 2,442,785 to M. M. Shapiro and B. Stiller, "Signal-Transmitting Cable Insensitive to Explosion Pressure Pulses"; see also A. R. Cohen and B. Stiller, "A Tourmaline Crystal Gage for Underwater Explosion Pressure," Report R-157. David Taylor Model Basin, Washington 7, D. C.; and M. A, Greenfield and M. M. Shapiro, "Instrumentation for Measurement of Underwater Explosion Pressures," Report 523, David Taylor Model Basin, Washington 7, D. C.

‡ A piezoelectric effect is limited, by definition, to materials with a crystalline structure. X-ray and other evidence shows crystal formation in many "amorphous" dielectrics, especially for rubber under stress (see reference 7).

[7] C. C. Davis, and J. T. Blake, Editors, *The Chemistry and Technology of Rubber* (Reinhold Publishing Corporation, 1937), with extensive bibliography.

[8] H. F. Richards, Phys. Rev. **22**, 122 (1923).

[9] K. R. Brain, Proc. Phys. Soc. (London) **36**, 81 (1924).

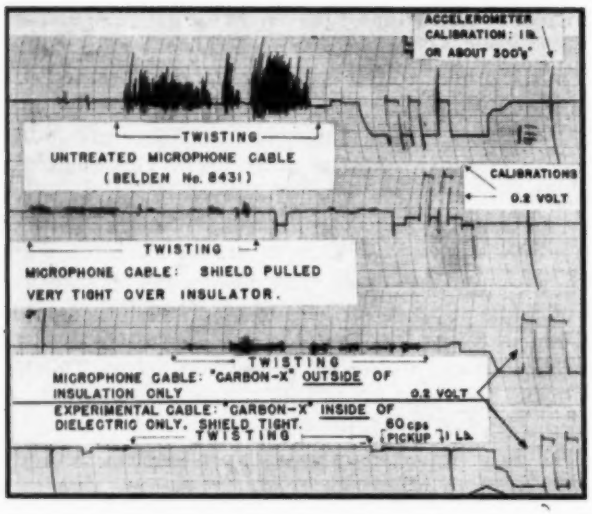

FIG. 1. Cable noise from concentric cables, 0.070-in. o.d.

short section of the cable and subjecting it to severe strains by twisting and bending, while making sure that no strains or motion were transmitted to the accelerometer itself. Another test consisted in using a pair of pliers to compress and release alternately a short section of the cable. A few typical records obtained in this fashion for some commercial as well as experimental laboratory-made cables are shown in Figs. 1, 2, and 3.

RESULTS

It was found that standard microphone or phonograph pick-up cable (Belden No. 8431 about 0.070-inch o.d.) gives signals under these conditions of up to 500 millivolts peak to peak (see Fig. 1). This was definitely lowered (to about 60 mv peak to peak) by tightening the braided shield over the dielectric, thus improving the contact between the dielectric and the shield (Fig. 1).

A colloidal suspension of graphite, in benzene, "Carbon *X*"§ (manufactured by the General Cement Manufacturing Company, Rockford, Illinois) was then used in experiments with the coating on the inside and/or outside surfaces of the dielectric. It was found that no further reduction in noise, over the previous test, was obtained by coating only the outside of the dielectric (Fig. 1). In another test, only the inside of the dielectric was coated with Carbon *X*. This markedly reduced the cable signal due to mechanical flexing, provided the shield remained tight over the dielectric, the residual noise being less than 3 mv peak to peak (Figs. 1 and 2); the cable signals were reduced to a minimum by coating both inside and outside of the dielectric with Carbon *X* (Fig. 2).

In yet another series of tests, a test cable was made up consisting of an outer braided shield, the same rubber-like dielectric as above, and a Formex-insulated central conductor. This cable was found to be quite noisy and was not materially improved by filling the inside of the dielectric with Carbon *X*; there was also no significant improvement when the outside of the dielectric was subsequently also coated with Carbon *X*.

Analysis of the above results, together with other reported data[3] on cable noise has led to the formulation of a theory completely describing the mechanism of generation of noise in instrument cables. There appears to be no evidence that any additional assumptions need be made to account for at least that portion of the generated noise which has proved troublesome in instrumentation applications.

DETAILED THEORY

The mechanism described in this section applies to all cases where two conductors are separated by a dielectric and one or both of these conductors is capable of slight motion with respect to the dielectric. The actual amount of the motion may be extremely small, and it is sufficient that there be a temporary loss of electrical contact between a small region on the surface of the dielectric and either conductor. The mechanism is most easily visualized by having only one conductor free to move, while the other is rigidly bonded to the dielectric (see Fig. 4). Suppose, now, that there is a small area, say 1 mm^2, over which the movable conductor can make intermittent electrical contact with the dielectric. (There is evidence that such a situation exists in most cables, usually for

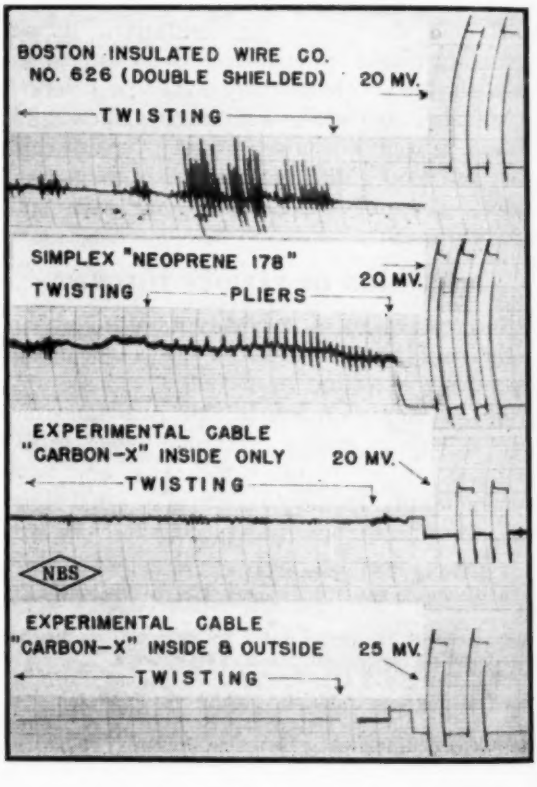

FIG. 2. Cable noise for several low noise cables, observed at high gain. The "experimental cable" is described in the text.

§ Subsequent tests with other conductive paints and suspensions have shown similar results. See also footnote ‖.

both the central conductor and the shield.) Some experiments reported as long as thirty years ago[10] have shown that a separation of charge occurs under these conditions resulting in a surface charge on the dielectric and an opposite "bound" charge on the conductor. It would appear at first that since the electrons are "free" in the conductor to a greater extent than in the dielectric, the surface charge left on the dielectric would always be negative. A complete theory must, however, take into account the degree to which electrons are free to leave the surface of the material, i.e., the material's "work function." Experimental data on polarity of "triboelectric" charges (see, for example, references 10 and 11) show serious differences from one investigation to another. These differences have been attributed to contamination, films (e.g., oxides), adsorbed gases,[11] and other conditions,[8] and appear to warrant considerable additional investigation. In the discussion which follows, the easily remembered, although oversimplified, assumption is made that the conductor loses electrons and is positively charged after separation. When this situation is reversed, for some dielectrics, the polarity of all resulting signals will also be reversed.

As the conductor separates from the dielectric, a small air capacitor is formed whose capacitance decreases as the gap becomes larger. It is well known that if this gap can be made large in a short enough time to avoid appreciable leakage, potentials of thousands of volts can be developed.

In the case of a cable, only a small portion of this potential will appear across the terminal impedance, since the capacitance of the small air capacitor can never become sufficiently small to release a large fraction of the "bound" separated charge on the moving conductor. Assume that the moving conductor is the shield of a concentric cable, and that a positive charge is left on the shield upon separation. The inner conductor is momentarily at a negative potential, and a negative voltage pulse appears across the input to the amplifier. The potential is subsequently neutralized by a transfer of electrons from the central conductor through the terminal impedance, at a rate determined by the time constant of the system. On the subsequent contact between the moving shield and the dielectric, the redistribution of charge takes place in the opposite direction, and a positive pulse is recorded.

It is seen that this mechanism will function for the central conductor as well as for the shield, if both are able to move with respect to the dielectric, and we can predict that pressure on the inside conductor will produce output pulses in a direction opposite to pressure on the shield, since the separation of charge leaves similar charges on both surfaces of the dielectric.

To provide quantitative predictions against which the theory might be tested, an attempt will be made to express the generated voltage signal in terms of the separated charge and the electrical characteristics of the system.

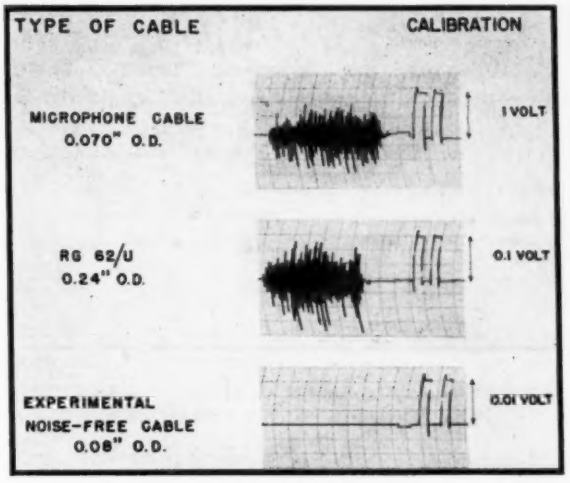

FIG. 3. Noise signals generated by severe whipping of three types of cable.

QUANTITATIVE CONSIDERATIONS

Let σ be the surface charge separated per unit area (see Fig. 4), and let A be the affected area. The total separated charge is σA. Since the two conductors must eventually reach the same potential, there will be a redistribution of charge. Let C_1 be the capacitance of the small air capacitor, C_2 the capacitance of the dielectric between the surface charge and the fixed conductor, Q_1 and Q_2 the final charges on C_1 and C_2, respectively; then Q_2 is the charge transferred through the input impedance of the amplifier, and $Q_1/C_1=Q_2/C_2$; $Q_1+Q_2=\sigma A$, which yield $Q_2=\sigma AC_2/(C_1+C_2)$. The transfer of charge can be represented approximately as an exponential decay of the charge on the moving conductor: $Q=Q_2e^{-(1/RC_3)t}$, where R is the terminal impedance (assumed mainly resistive) of the cable and C_3 is the cable capacitance, including any parallel capacitances. The current pulse through the terminal resistance R is given by $i=-(dQ/dt)=(Q_2/RC_3)e^{-(1/RC_3)t}$, and the observed voltage will be

$$V=iR=\frac{Q_2}{C_3}e^{-(1/RC_3)t}=\frac{\sigma A}{C_3}\cdot\frac{C_2}{C_1+C_2}e^{-(1/RC_3)t}.$$

The above derivation was made on the assumption of an instantaneous separation of charge. The maximum

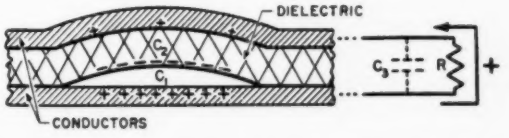

FIG. 4. Schematic diagram showing a separation of charges due to relative motion between one of the conductors and the dielectric.

[10] H. F. Richards, Phys. Rev. **16**, 290 (1920).

[11] F. B. Silsbee, "Static Electricity," U. S. Department of Commerce, National Bureau of Standards Circular C438, (1942).

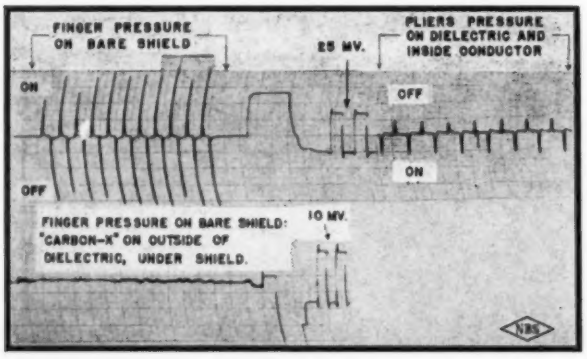

FIG. 5. Cable signals obtained with a 2-foot length of RG8/U cable. Note increased sensitivity in lower trace.

voltage

$$V_{max}=\frac{\sigma A}{C_3}\cdot\frac{C_2}{C_1+C_2}$$

will be attained only if the separation of charge takes place in a time short compared to the time constant RC_3 of the exponential decay curve. Within this limitation, it is seen that this maximum voltage is independent of the terminal resistance of the cable.

It is also seen, that the maximum generated voltage

(1) can be calculated (as an upper limit) from the maximum charge density (2.65×10^{-9} coulomb/cm^2)[11] allowed by the breakdown voltage of the airgap;

(2) is proportional to the affected area of cable;

(3) is inversely proportional to the total capacitance C_3 of the cable and parallel capacitors;

(4) decays with a time constant (time to be reduced to 37 percent of its maximum value) in seconds, equal to the product of the terminating resistance, in ohms, by the capacitance C_3 in farads;

(5) is reduced if the relative motion between conductor and dielectric is kept small, so that the capacitance C_1 always remains large;

(6) may be reduced to zero if good electrical conduction is maintained between the conductor and all points on the surface of the dielectric, thus preventing the separation of change. (In this case, it is no longer necessary to prevent motion of either conductor with respect to the dielectric.)

Qualitatively, at least, available data on cable noise[3] verify points 2, 3, and 5, while the success of flexible experimental cables having conductive coatings both inside and outside of the dielectric appears to confirm point 6. A series of simple experiments was set up to test quantitatively all of the above predictions.

TEST OF THE THEORY

A two-foot length of RG8/U cable (concentric, with polyethylene dielectric) was stripped of its rubber-like outer jacket. The braided copper shield thus uncovered was slightly expanded (by longitudinal compression) over a 2-inch section of the cable and was taped off in this position. One end of the cable was left "open," while the other was connected to the Brush dc amplifier and recorder. It was found that no signal was obtained from touching the shield with the fingers, but that sufficient finger pressure to make the shield touch the dielectric caused a positive signal of about 50 millivolts and that releasing this pressure caused an approximately equal negative signal. The signals were of opposite polarity (and somewhat smaller) when a pair of long-nose pliers was slipped inside the shield and pressure was exerted on the dielectric, squeezing it on the inner conductor (see Fig. 5).

These tests were repeated after coating the outside of the dielectric with Carbon X. The signal from finger pressure on the shield sufficient to make contact with the dielectric was less than 0.3 millivolt (see Fig. 5). The signal from compressing the dielectric and inner conductor was unchanged. These results appear to be in complete agreement with the theory of the preceding section: The Carbon X maintains good electrical contact between the shield and the outside surface of the dielectric. It appears that a resistance of the order of 10 to 50 megohms per inch of cable is sufficiently low for this purpose.

In the first set of tests above, the affected area A may be roughly estimated at 0.5 cm^2, and the separation at 2 mm, hence $C_1=0.2$ $\mu\mu$f; over the same area, with a larger spacing and higher dielectric constant, $C_2=0.2$ $\mu\mu$f. With a capacitance C_3 of about 100 $\mu\mu$f, the maximum permissible charge density $\sigma=2.6\times10^{-9}$ coulomb/cm^2 would yield a signal of about 66 millivolts. This result is in good agreement with the observed value of 50 millivolts and indicates that the final density of separated charge is about as great as is allowed by the breakdown voltage gradient for the air dielectric.

In another test, a large capacitor (0.02 μf) was connected across the uncoated cable, in order to lengthen the time constant of the system. The shape of the pulses was found to agree with point 4 of the preceding section, and the maximum observed voltage was independent of the amplifier input impedance in the range from 180 megohms to 0.9 megohm. At still lower input resistances ($RC_3<18$ millisec), the separation of charge did not take place in a time short enough to be negligible with respect to the time constant, and the observed voltage decreased. A subsidiary test set-up was made in which various dielectric sheets could be bonded to a flat brass plate, and blocks of various metals could be alternately placed on and removed from the free surface of the dielectric. The brass plate and metal block were connected through a short length of noise-free cable to the input of a Cathode follower and the Brush equipment previously used. Pulses of 5 to 28 volts were obtained from all dielectrics tested, with only insignificant differences among different metals (copper, brass, aluminum, steel) for any given dielectric. The pulses obtained for different dielectrics, however, fell into two groups, one group of dielectrics acquiring electrons from the metals (polyethylene, Teflon, and the dielectric from 0.07-in. microphone cable) while the other group became positively charged (Lucite, glass, glass wool, and Neoprene).

A sheet of conductive rubber bonded to the dielectric eliminated the triboelectric pulses in all cases. It was also found that the observed peak voltage was approximately proportional to the area of contact. The difficulties due to surface films encountered in these tests showed how differences among "triboelectric series" of various investigators could easily arise. Thus, copper loses electrons to cellulose acetate when both surfaces are freshly cleaned with tissue paper and alcohol, but successive pulses become gradually smaller until the polarity of the pulses is reversed, indicating that the copper now gains electrons from the dielectric. Renewed cleaning of the surfaces again reverses the polarity of the separated charges.

CONSTRUCTION OF LOW NOISE CABLE

It appears from the above theory and tests that in order to make a cable which does not suffer from the usual sensitivity to shock and vibration, it is only necessary to insure continuous electrical conduction between each conductor and the surfaces of the dielectric between conductors (in the case of doubly-shielded cable, the above also applies, of course, to the dielectric between shields, unless the electrical resistance between these shields is very low). The conductive covering on the outside surface of the dielectric in the special Simplex cable is quite effective in this respect, and the residual noise in this cable can be definitely ascribed to the inner conductor. The inner conductor and its separate strands are embedded in a soft, nonadhesive conductive material. When relative motion occurs between the inner conductor and the dielectric, the conductive material partially separates from the dielectric, allowing a separation of charge to take place at some points. Because of the high rigidity of this cable, very little motion is allowed between the inner conductor and the dielectric, except under extremely severe conditions, and it is for these reasons that this cable has been found quite satisfactory in applications where its bulk and rigidity can be tolerated. In attempting to construct a very light, small, and flexible cable, it is not practicable to prevent relative motion between the dielectric and either conductor, and a method must therefore be found for providing a good conductor bonded to both the inside and outside surfaces of the dielectric (see Fig. 6). Possible methods of achieving this result appear to have been thoroughly investigated in connection with the reduction of corona discharge in high voltage cables,[12] and a large variety of conductive paints, colloidal suspensions of graphite, and conductive rubbers is commercially available for this purpose. The electrical resistance of the coatings may have any value up to 50 megohms per inch of cable, but a resistance of the order of 0.3 megohm per inch appears to be both practicable and very effective. A promising method for industrial application would consist in extruding concentric layers of conductive rubber, nonconductive dielectric, and more conductive rubber over the central conductor, with provision for vulcanizing or otherwise bonding together the three layers. This treatment could be given to all conductors in a multiple-conductor cable. It is to be noted that it is not necessary to bond the conductive layers to the cable conductors, and it is actually preferable to have them loose, to increase the flexibility of the cable. A conductive coating is *not* necessary between the shield and any protective insulating outside jacket. There appear to be no limitations, except considerations of total cable capacitance, to how small the diameter of such a cable might be made.

[12] See, for example, U. S. Patents: 2,059,146 to Roeterink; 2,074,826 to C. P. Boggs; 2,081,517; 2,096,840 to E. Bormann; 2,142,625 to D. A. C. Zoethout; *2,165,238;* 2,234,068 to R. J. Wiseman; *2,304,210 to T. R. Scott; 2,377,153 to P. V. Hunter;* 2,427,700 to W. B. Atkinson, *et al.; 2,446,387.* Patents listed in italics appear most pertinent.

PROCEDURE FOR MAKING SHORT LENGTHS OF LOW NOISE CABLE

Until suitable cable of this type becomes commercially available, short lengths of this cable (6 ft or less) may be readily made as follows:

(1) Start with the desired length of three different cables:

(a) Insulated wire with about AWG No. 20 conductor. This wire should have a thin, rubber-like or impermeable plastic insulation which is easily removed from the solid conductor (push-back, hook-up wire). It must be possible to perform operation 8, below, on this wire. (Only the dielectric of this cable will be used.)

(b) Microphone or phonograph pick-up cable about 0.070 inch o.d. with a readily removable braided shield, e.g., Belden No. 8431 (shield, only, to be used.)

(c) Lamp cord with stranded copper conductors, the individual strands being 0.006 to 0.007 inch in diameter. (Strands will be used to make central conductor.)

(2) Straighten the hook-up wire (a) by stretching it slightly.

(3) Coat the outer surface of the insulation of wire (a) with a conductive paint|| leaving about 1 inch on each end unpainted. Let dry.

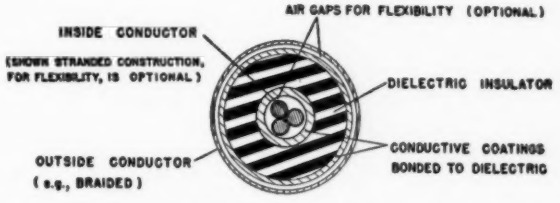
AIR GAPS FOR FLEXIBILITY (OPTIONAL)
INSIDE CONDUCTOR
(SHOWN STRANDED CONSTRUCTION, FOR FLEXIBILITY, IS OPTIONAL)
DIELECTRIC INSULATOR
CONDUCTIVE COATINGS BONDED TO DIELECTRIC
OUTSIDE CONDUCTOR (e.g., BRAIDED)

FIG. 6. Structure of noise-free coaxial cable. An insulating overall protective jacket is optional and does not require a conductive coating.

|| Carbon *X* was used in the initial experimental cables. It was found, however, that a small fraction of the "noise" reappears after prolonged use of cable made with this material, presumably because some of the graphite coating flakes off. Conductive suspensions in a "vehicle" designed to bond firmly to the cable dielectric are much more desirable for this application. Such special paints are available from most manufacturers of conductive paints and suspensions (see reference 13), but generally are not sufficiently flexible. A mixture of finely divided Carbon Black (18 to 25 millimicrons, e.g., "Halo Black" distributed by Binney and Smith, New York) with "Pliobond 30" (a Goodyear adhesive distributed by the W. J. Ruscoe Company, Akron, Ohio) and Methyl Ethyl Ketone Solvent has been found quite satisfactory. The proportions used were 3 parts "Halo Black" to 10 parts "Pliobond 30" and 60 parts Methyl Ethyl Ketone, by weight. The

(4) Strip the shield from cable (b) in such a way that the inside diameter of the shield is somewhat increased. This may be done by pushing the shield toward the center of the cable and slipping it off after it has been compressed in length (and correspondingly expanded).

(5) From the lamp cord (c), pull out the stranded copper conductor and separate out five or six of the strands.

(6) Holding one end of these strands in a vise and the other end in the chuck of a hand or electric drill, tightly twist together the strands, occasionally smoothing them to obtain a uniform wire.

(7) Push the hook-up wire through the shield of point 4 above.

(8) Strip off about ½ inch of the insulation from each end of the painted length of hook-up wire. Hold one end of the bare wire in a vise, the other with a pair of pliers, and stretch the wire at least 10 percent of its length, being careful not to stretch the insulation. If this cannot be done, a different type of push-back wire should be used.

(9) Pull out the wire from the insulation of cable (a).

(10) About ¼ inch from one end, tape a piece of transparent plastic tubing to the outside of the dielectric-tube insulation.

(11) Connect this plastic tubing to a vacuum line (this can also be done by mouth suction) and dip the other end of the insulation into conductive paint. When the paint appears in the plastic tube, it should be blown out again and drawn up at least once more, if this is necessary to insure thorough coating of the entire inside surface of the dielectric. Let dry, after blowing out enough of the paint to leave a sufficient opening for the inside conductor. Remove plastic tubing and tape.

(12) Push the stranded wire through the painted insulation of the hook-up wire.

(13) Stretch shielding over the entire length of the cable.

USES OF LOW NOISE CABLES

One of the attractive possible uses for very small barium titanate accelerometers is to serve as monitors for small electromagnetic shakers in vibration tests and calibrating procedures for vibration pickups of various types. The usefulness of the small crystal-type transducers for this application was severely limited by the large, nonreproducible signal due to the cable used with these devices. Under typical conditions, the combined signal from the accelerometer and cable could be changed by a factor of three at 20 cycles per second, depending on the method by which the cable was supported. At 40 cps, the corresponding range of readings was still ±30 percent, while the readings began to have good consistency in the vicinity of 100 cps. The use of experimental low noise cables made by the method outlined in the previous section, has made possible the reliable monitoring of the motion of a small shaker down to 7 cps with a suitable cathode follower. The only remaining uncertainty in this case is due to the reaction of the mass of the cable on the crystal, and this is easily remedied by fastening the cable to a point close to the accelerometer which moves together with the accelerometer.

In addition to applications to piezoelectric accelerometers, examples of need for a low noise cable can be found in research on pressures from underwater explosions, especially with small charges; in connection with piezoelectric pressure gauges in air-blast and rocket research; in crystal-type microphones, hearing aids and phonograph pick-ups, and, in general, wherever the cable may be subjected to shock, vibration, pressure, or stress, and the terminating impedance of the cable is not very low.

ACKNOWLEDGMENT

It is a pleasure to thank W. A. Wildhack for suggestions related to both the experimental and commercial construction of low noise cables, B. L. Davis, W. C. Nyberg, and Mrs. B. B. Stackig for their cooperation in developing a suitable flexible conductive coating, and F. B. Silsbee for a clarification of several important points in the detailed mechanism of cable-noise generation. I would also like to thank R. O. Smith and J. H. Pinkard for helping to make the test cables and conducting some of the tests.

container should have a tight cover. Considerable mixing is required to insure uniform distribution of the conductive material. This may be done by adding porcelain or glass balls to the mixture and rotating the closed container about its axis in a horizontal position for at least 24 hours after the initial mixing and for at least 15 minutes before use.

Recent experiments have been made with different kinds of flexible conductive paints, after it was found that the "Pliobond" mixture previously used changes properties quite rapidly if it is not applied immediately after mixing. These recent tests have shown that a mixture of one part acetylene black, 6 parts Stoner-Mudge No. 67 adhesive (Ethyl-Methacrylate and Vinylite Resin Mixture), and about 30 parts methyl isolbutyl ketone makes an even better, flexible, well-bonded, conductive coating which may be kept indefinitely once it has been mixed by milling and filtered through a 200-mesh screen.

[13] See, for example, Annual Buyers' Guide Issue, Electronics **24**, No. 6A, listings under "*Coatings*—Conductive," p. D-23, "*Graphite*—Colloidal," p. D-51, and "*Paints*—Conductive," p. D-84 (1951).

Determination of the Transverse Permeabilities of Large Core Samples from Petroleum Reservoirs

R. E. COLLINS
Magnolia Petroleum Company, Field Research Laboratories, Dallas, Texas
(Received February 4, 1952)

The solution of the problem of determining the permeabilities of petroleum reservoir rocks from measurements employing the flow of a gas through large cylindrical cores, transverse to the axis of the cores, is presented. This solution is obtained by solving the corresponding problem in potential theory, the method of conformal transformations of complex variables being employed. An electrolytic model study of this problem is described and a comparison of the theoretical and experimental solutions presented.

INTRODUCTION

THE permeability of a porous medium to the flow of a fluid is defined in terms of what is commonly called Darcy's Law, which is expressed symbolically as

$$v=\frac{-k}{\mu}\nabla P, \tag{1}$$

where v=volumetric flux density of flow, μ=fluid viscosity, P=pressure, and k is defined as the permeability of the porous medium to the flow of the fluid. Permeability has the dimensions of length squared.

The usual procedure for determining the permeability of a sample of porous petroleum reservoir rock is to employ the linear flow of a fluid through a specimen of either circular or rectangular cross section. The method of calculation of permeability for such procedure is well established and can be found elsewhere.[1]

Generally sedimentary reservoir rocks are anisotropic; hence, they possess one permeability parallel to the bedding planes and another perpendicular to the bedding planes. Since the fluids entering a well bore flow approximately parallel to the bedding planes, it is the permeability parallel to the bedding planes which is the more critical as regards the flow of oil and/or gas from the surrounding porous medium toward the vertical well bore.

Now the definition of permeability as given in Eq. (1) applies only on a macroscopic basis, that is, the size of the rock sample must be much greater than the size of individual pores in the rock. Hence, if rocks containing fractures or solution cavities are to be considered, large samples must be used.

For the above reasons apparatus has been developed for flowing a gas through large cylindrical samples, tranverse to the cylindrical axis of the samples. In this apparatus the ends of the samples are sealed, as are two portions of the lateral surface. The gas is introduced through one portion of the lateral surface at pressure P_1 and leaves through the opposite side of the core at a pressure P_2. A plan view of the flow geometry is shown in Fig. 1. The equation for the calculation of permeability from this arrangement is developed in the next section.

[1] M. Muskat, *Flow of Homogeneous Fluids Through Porous Media* (McGraw-Hill Book Company, Inc., New York), p. 76.

THEORETICAL SOLUTION

The equation of continuity for the flow of a compressible fluid through a porous medium is

$$\nabla\cdot(\rho v)=-\phi\partial\rho/\partial t, \tag{2}$$

where ρ=fluid density, v=volumetric flux density, and ϕ=porosity of the porous medium, defined as the ratio of pore volume to the bulk volume.

If the fluid is a gas, then for moderate pressures and pressure gradients

$$\rho=AP, \tag{3}$$

where

$$A=\text{const.}$$

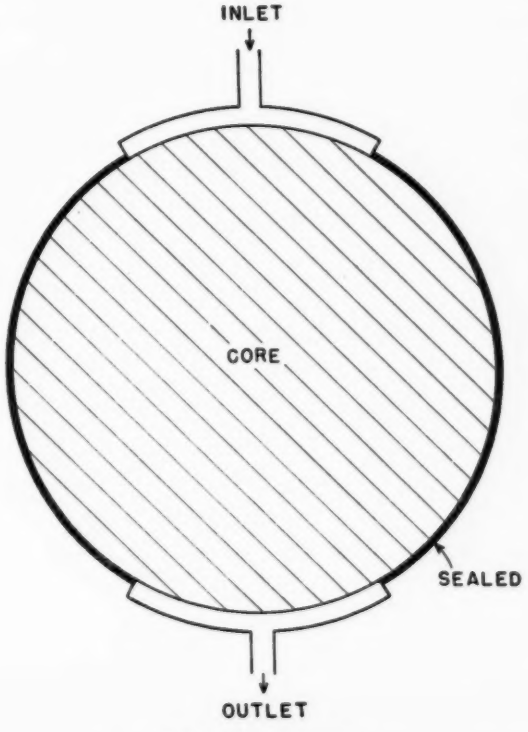

FIG. 1. Flow geometry.

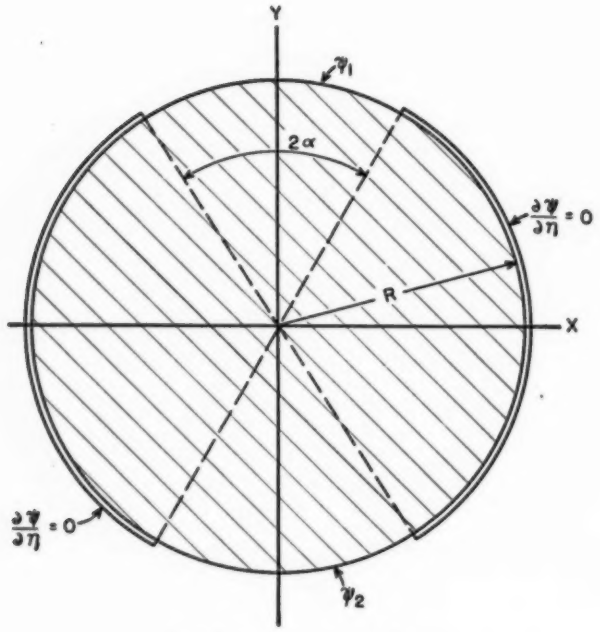

FIG. 2. Boundary conditions.

Combining Eqs. (1) and (3) gives

$$\rho v = -AkP\nabla P/\mu, \tag{4}$$

or assuming μ independent of the pressure in the range of pressures considered,

$$\rho v = -\nabla(AkP^2/2\mu), \tag{5}$$

which assumes that k is independent of the space coordinates. Now for steady flow Eq. (2) becomes

$$\nabla \cdot (\rho v) = 0. \tag{6}$$

Thus, substitution of (5) in (6) yields Laplace's equation

$$\nabla^2(AkP^2/2\mu) = 0 \tag{7}$$

or

$$\nabla^2\psi = 0, \tag{8}$$

where

$$\psi = AkP^2/2\mu \tag{9}$$

is the potential function of the mass flux density as shown by (5). Thus, this is a problem in potential theory with the boundary conditions as shown in Fig. 2.

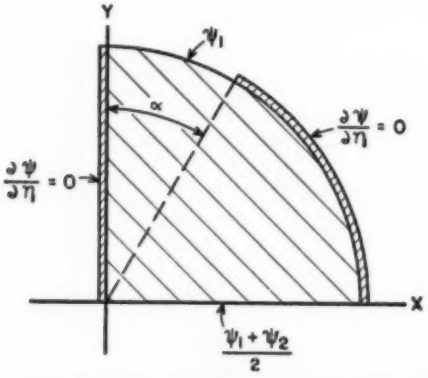

FIG. 3. Simplification of boundary conditions.

From the principles of potential theory and examination of Fig. 2 it is evident that there are two lines of symmetry: One is the x axis, which must be an equipotential at the potential $(\psi_1+\psi_2)/2$ and the other is the y axis across which no fluid flows, i.e., on the y axis $\partial\psi/\partial n = 0$.† These symmetry conditions permit the problem to be reduced to that shown in Fig. 3. Note that exactly one-half of the two-dimensional flow passes through this domain.

Now if in this figure all dimensions are expressed in units of R, the radius of the core, then the radius of the semicircle is unity. Then, treating this plane as the complex z plane, this domain is transformed to that shown in Fig. 4 by the conformal transformation

$$W = \ln i/z. \tag{10}$$

This set of boundary conditions can be altered to correspond to the classical problem of seepage under a

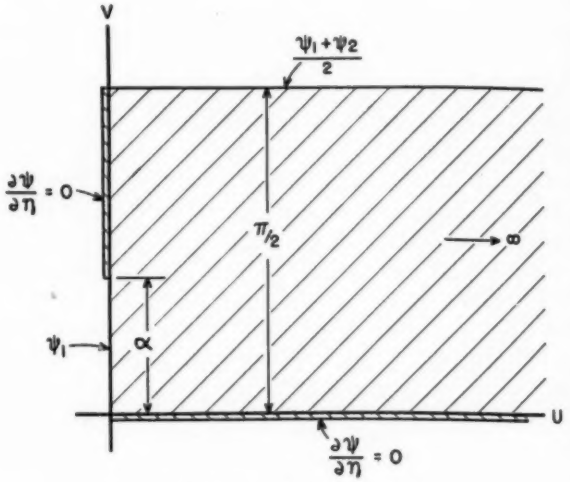

FIG. 4. Transformed domain.

coffer-dam if on the negative u axis it is required that $\partial\psi/\partial n = 0$ and along the line $V = \pi i/2$ for $U < 0$ ψ is such that

$$\psi - \psi_1 = \left(\frac{\psi_1+\psi_2}{2} - \psi_1\right), \tag{11}$$

which leaves the boundary conditions of the original domain unchanged. This gives for ψ on this boundary $\psi = (3\psi_1 - \psi_2)/2$. Thus the problem is now as shown in Fig. 5, which is a coffer-dam in a porous bed of finite thickness with no excavation below the dam. This problem has been solved previously.[2] Muskat gives for the total two-dimensional flux under the dam

$$K'\Delta\psi/2K, \tag{12}$$

† Throughout this paper $\partial\psi/\partial n$ denotes the gradient in the direction of positive normal n.

[2] Reference 1, p. 221.

where for the geometry and boundary conditions given here

$$\Delta\psi=\frac{3\psi_1-\psi_2}{2}-\frac{\psi_1+\psi_2}{2}=\psi_1-\psi_2,$$

and K'=complete elliptic integral of the first kind with modulus $\sin\alpha$ and K=complete elliptic integral of the first kind with modulus $\cos\alpha$. This solution is obtained by Muskat employing Schwartz-Christoffel transformations resulting in a rectangular domain with two opposite boundaries at uniform potentials and the other two boundaries having $\partial\psi/\partial n=0$.

Since this solution was arrived at employing a domain through which only one-half of the flux passes it must be multiplied by two; also by multiplying by L, the length of core, the total flux is obtained, thus

$$Q_1\rho_1=\frac{L}{G}(\psi_1-\psi_2), \tag{13}$$

where Q_1=volumetric flow rate at P_1, ρ_1=gas density at P_1, and $G=K/K'$.

Substitution of the expression for ψ given in Eq. (9) gives

$$Q_1\rho_1=\frac{L}{G}\frac{Ak}{2\mu}(P_1^2-P_2^2). \tag{14}$$

Since with the apparatus employed Q is measured at the downstream pressure, this is expressed as

$$Q_1\rho_1=Q_2\rho_2=Q_2AP_2=\frac{L}{G}\frac{kA}{2\mu}(P_1^2-P_2^2), \tag{15}$$

whence k is given by

$$k=G\frac{Q_2\mu}{L}\frac{2P_2}{P_1^2-P_2^2}. \tag{16}$$

The geometrical factor G is plotted in Fig. 6 *versus* 2α, where 2α is the angular opening on one side of the core.

Thus with Eq. (16) and the curve of Fig. 6 the measured rate of flow, pressures, etc., can be used to calculate the transverse permeability of the samples.

MODEL STUDY

Prior to the development just presented, an electrolytic model study was conducted as a method of determining the equation to be used for calculating permeabilities. This model consisted of a plastic cylindrical vessel, having a flat bottom, into which were placed two $\frac{1}{32}''$ copper plates, curved to fit the wall of the vessel. Another vessel of rectangular cross section was fitted with flat copper plates at each end to serve as a conductivity cell. Both vessels were filled to a known depth with KCl solutions and the two vessels connected in series with an ammeter to a current source of 5000 cycles having a voltage regulator. The voltage drop

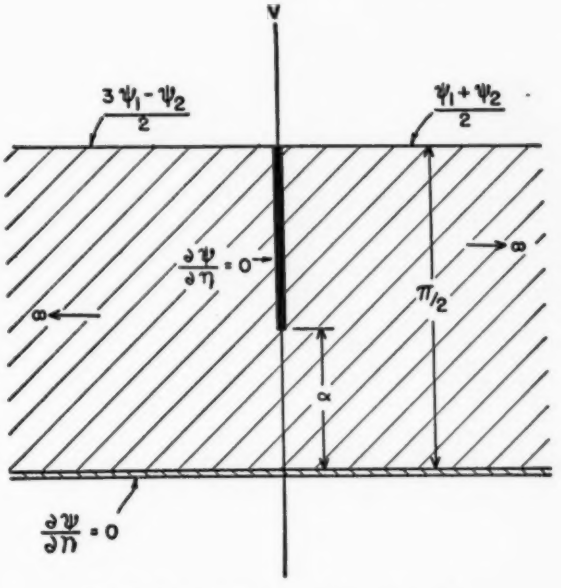

FIG. 5. Extension of transformed domain.

across each vessel was measured. This circuit is shown in Fig. 7. In this model the analogy is the electric current to total mass flux, electric potential drop to mass flux density potential difference, and conductivity of electrolyte to permeability/viscosity ratio.

This study was made using two sizes of circular vessel, 7″ and 12″ in diameter. In each case a number of

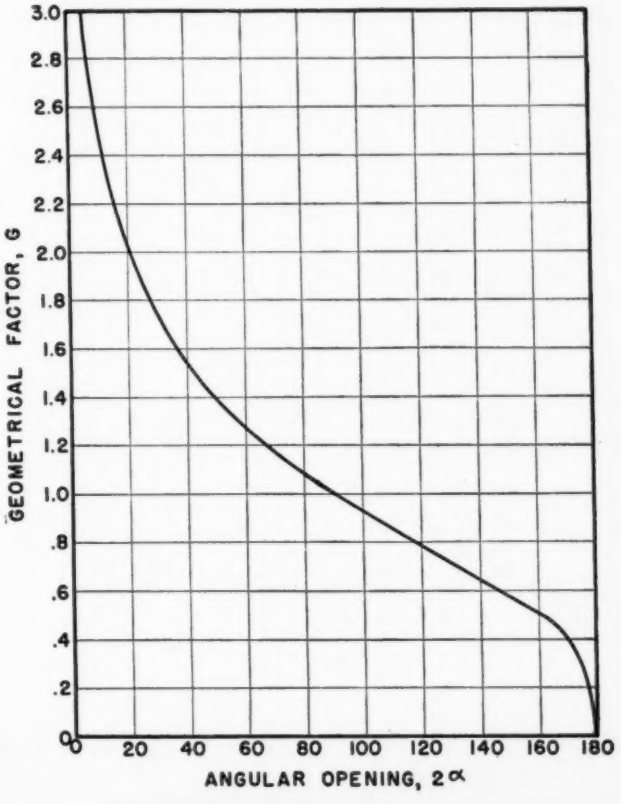

FIG. 6. Theoretical curve, G *versus* 2α.

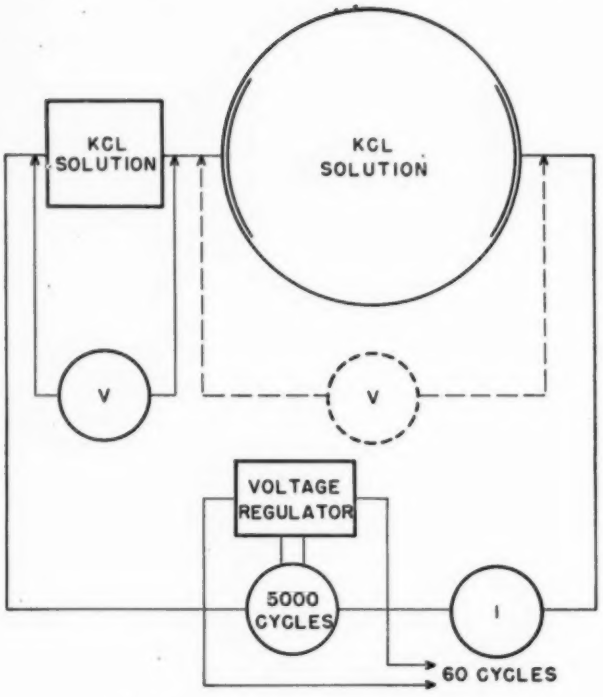

FIG. 7. Circuit diagram (model study).

different values of S, the arc length of the electrodes, were used. The results of the measurements were used in the equation

$$G = L'CV/I, \tag{20}$$

where G = geometrical factor, V = potential difference, I = current, C = conductivity of electrolyte, and L' = depth of electrolyte, which is analogous to Eq. (16) to calculate G. These results are plotted as dashed curves in Fig. 8.

DISCUSSION

It is obvious that the two sizes of model gave slightly different results, which in both cases differ from the theoretical curve. These differences are probably due to the fact that the electrodes used did not fit flush into the walls of the vessel but extended $\frac{1}{32}''$ from the wall into the vessel.

An interesting feature of the theoretical curve shown in Fig. 6 is that G is exactly one for an angular opening of 90° for inlet and outlet. This is approximately the size opening usually used.

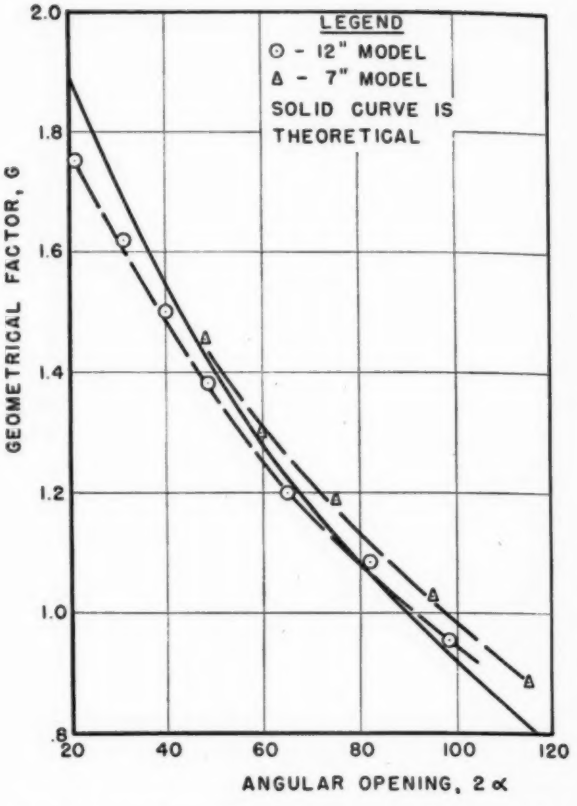

FIG. 8. Comparison of theoretical and experimental results.

One qualifying statement should be made regarding both the theoretical and the experimental solutions; both solutions assume that the transverse permeability of the core is independent of space coordinates.

ACKNOWLEDGMENT

Acknowledgment is made to the management of the Field Research Laboratories, Magnolia Petroleum Company, for permission to publish this paper. The writer acknowledges his appreciation to Mr. E. M. Landsbaum who designed and conducted the model study reported herein.

Conical Surfaces of Fracture Produced by Asymmetrical Impulsive Loading*

JOHN S. RINEHART AND JOHN PEARSON
Michelson Laboratory, United States Naval Ordnance Test Station, Inyokern, China Lake, California
(Received March 10, 1952)

Conical surfaces of fracture generated in thick-walled cylinders that were asymmetrically and impulsively loaded through the use of internal explosive charges are presented. It is deduced from qualitative considerations that the conical fractures result from the interaction between transient tensile stress waves. The two tensile stress waves that are responsible for the fracture arise from a single compressional stress wave that is reflected from two inclined free surfaces. The angle of fracture associated with these conical surfaces has been used to measure the velocity of propagation of the stress waves in low-carbon steel, brass, copper, lead, and 24ST aluminum alloy.

INTRODUCTION

FRACTURES are quite commonly found within metal bodies that have been explosively or impulsively loaded. It is known that many of these fractures result from interference between stress waves. For example, observations reported in an earlier paper[1] established that the transient stress wave induced in a metal by an exploding charge can cause fracturing (or scabbing) near a free surface as the result of interference between the incident and reflected waves.

A conical fracture surface that appears to be generated by the highly localized stress concentration set up by the interference of two sharp-fronted high intensity tensile stress waves is discussed in this paper. Such a conical fracture surface is often generated at the base of a thick-walled explosive-filled cylinder when the explosive is detonated at the opposite end. A rigorous treatment of the problem is not attempted. It is demonstrated, however, that the conical fracture surface formed at the base of such a cylinder can be explained qualitatively on the basis of interacting reflected stress waves. The interference results from division of a single compressional wave into two tensile waves as a result of reflection of the wave from two inclined free surfaces.

EXPERIMENTS

In previous work conducted by the authors[2] on thick-walled hollow steel cylinders internally loaded with explosives, it was noticed that when the explosive was detonated from one end, fracture cones were formed at the opposite end of the cylinder. The origin of these cones was not discussed in that paper. The present paper discusses their origin and extends the experimental observations regarding the cones to cylinders machined from metals other than steel. The particular cylinders that were fired are listed in Table I.

TABLE I. Test cylinders.[a]

Material	Outside diameter (in.)
1020 steel	4
1020 steel	5⅛
1020 steel	5⅞
1020 steel	6⅛
Copper	4⅞
Brass	5⅛
24ST aluminum alloy	5⅜
Lead[b]	3

[a] All cylinders 8 in. long with 1-in. i.d., except as noted.
[b] This cylinder 5¼ in. long with 0.22-in. i.d.

Cylinders of 1020 steel, copper, brass, and 24ST aluminum alloy were machined from solid round stock, the diameter of which was at least ⅛ inch greater than the finished outside diameter of the cylinder. The lead cylinder was first cast as a solid piece and then machined to shape. The low-carbon steel cylinders were annealed in a reducing atmosphere at about 1600°F after machining. Each cylinder, with the exception of one lead cylinder, had a one-inch inside diameter, was eight inches long, and was loaded internally with Composition *C*-3 explosive.

The explosive was detonated by an Engineer Special Cap which was inserted in the explosive at the upper end of the cylinder. All of the cylinders were mounted in a vertical position on several layers of Celotex sheeting which were placed on the bottom of shallow holes located in sandy soil. The outer surfaces of the cylinders were free from any restraint.

A fracture cone formed at the base of each of the eight cylinders used in the tests. In each case the remainder of the cylinder broke into numerous long fragments. However, for each of the four low-carbon steel cylinders and for the lead cylinder the fracture cones remained intact. For the other three cylinders used in the tests the cones broke into several pieces with the fractures extending radially through the cone. Typical fracture cones from two 1020 steel cylinders are shown in Fig. 1.

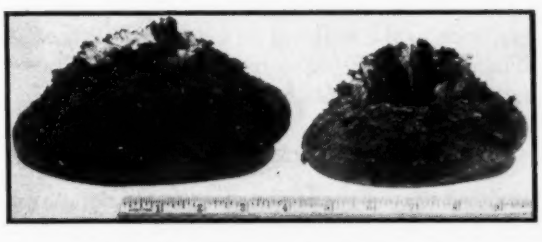

FIG. 1. Fracture hubs from steel cylinders.

* Work supported by Armament Branch, ONR.
[1] J. S. Rinehart, J. Appl. Phys. **22**, 555 (1951).
[2] John Pearson and J. S. Rinehart, J. Appl. Phys. **23**, 434 (1952).

DISCUSSION

The stress situation in a cylinder, shortly after initiation of the explosive, is shown schematically and much simplified in Fig. 2. When detonated in contact with the metal, the charge initiates a sharp-fronted high intensity stress wave within the wall of the cylinder. The loading produced by the detonating explosive is asymmetrical since the detonation proceeds through the explosive with a finite velocity D. The induced stress wave moves both outward and downward through the cylinder. For a purely elastic wave the velocity of propagation C of the wave would be given by

$$C^2=2G(1-\nu)/\rho(1+2\nu), \qquad (1)$$

where ρ is the density of the cylinder material, G is its modulus of rigidity, and ν is its Poisson's ratio. As the stress wave propagates through the cylinder wall there exist simultaneously a very high tensile stress σ_θ in the circumferential direction, a compressive stress σ_r in the radial direction, and a compressive stress σ_z parallel to the longitudinal axis of the cylinder. The magnitudes of

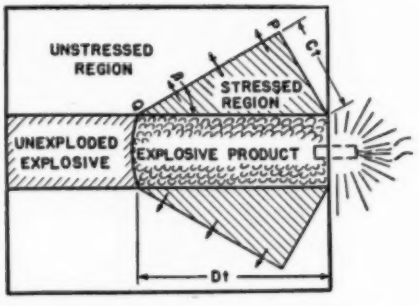

FIG. 2. Generation of stress wave in internally loaded metal cylinder.

these three stresses decrease quite rapidly as the wave propagates through the cylinder wall. A circular cross section of the cylinder would show the vector component of the stress wave in that plane as a circularly expanding wave with the intensities of the normal and tangential stresses decreasing considerably as the wave progresses radially outward in the plane of the cross section.

After a time interval t a conical portion of the cylinder will be in a stressed condition, and the remaining portion will be at rest in an unstressed condition. It is assumed here that at any particular point on the inner surface of the cylinder the stress rises abruptly to a high value and then remains substantially at that value for some time thereafter. At this instant the maximum depth of the stressed area in the wall will be Ct and will extend down a distance of Dt. The wave front PQ will be inclined at an angle β with the axis of the cylinder, where β is given by

$$\beta=\sin^{-1}(C/D). \qquad (2)$$

It is realized that in the region close to the detonator the over-all picture is quite complex, and the situation in that region has been much simplified in Fig. 2.

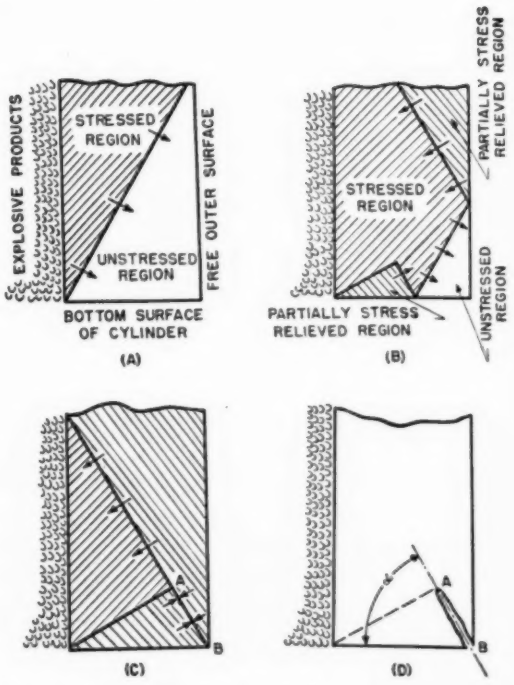

FIG. 3. Propagation and interaction of stress waves in wall of a cylinder.

When this stress wave strikes the outer free surfaces of the cylinder, it will be reflected. In examining the effects of these reflections it is helpful to consider the stress wave as a combination of a wave of high circumferential tensile stress that advances simultaneously with a compression wave. The latter wave involves both radial stress and axial stress. A study of particle motion within the reflected stress wave indicates that the circumferential stress component remains a tensile stress and tends to reinforce the normal stress established in the cylinder wall by the incident stress wave. The compressive stress component of the incident stress wave, however, appears as a tensile stress in the reflected wave.

Certain qualitative aspects of the propagation and interaction of the incident compressive stress component and its reflected tensile counterparts are indicated in Fig. 3. During the initial period of loading, the high intensity compressional stress wave advances into the unstressed region of the cylinder wall [Fig. 3(A)] leaving behind it a region subjected to radial and axial compression. When the incident compression stress wave component strikes the outer and bottom surfaces of the cylinder, tensile waves comprised of radial and axial stresses are propagated back into the compressed region [Fig. 3(B)]. Part of the energy of the incident compression wave appears in the form of shear waves which are initiated at the free surfaces. These waves are not shown in Fig. 3. Because of the generation of the shear waves, absorption of energy by the material, and divergence of the wave, the magnitude of the reflected

TABLE II. Angles of fracture and stress wave velocities.

Material	Angle of fracture (degrees)	Velocity (ft/sec) Calculated from angle of fracture	Reference values		
Aluminum	42–43	19,300–19,000	20,900[b]		
Steel	44–45	18,700–18,400	19,300[b]	19,522[c]	19,500[d]
Brass	59–62.5	13,400–12,000	14,080[b]		
Copper	62–64	12,200–11,400	12,850[a]		
Lead	72–74	8,000– 7,200	7,045[c]		

[a] Calculated from bulk modulus.
[b] Reference (6).
[c] Reference (4).
[d] Reference (5).

tensile stress wave will be less than that of the original compression wave. As the reflected tensile waves eat back into the compressed region, they will leave behind them partially stress-relieved regions which will be in a state of reduced radial and axial compression. Eventually, the fronts of these two waves will meet. The encounter will take place over a definite surface. The intersection of this surface with the plane of the drawing is labeled A–B in Fig. 3(C). The result of this meeting will be the initiation of a region of high tensile stress. If the magnitude of this resulting tensile stress is greater than the critical normal fracture stress of the material, fracturing will occur over the surface [Fig. 3(D)].

It is not readily apparent just what part, if any, the circumferential stress component plays in the formation of the fracture cones, although it is known[2] that the internal fracturing in the walls of thick-walled steel cylinders and the fragmentation of these bodies does result from the high tangential stresses induced by internal explosive loading.

A more rigorous treatment of the present problem would involve considerations of the propagation of waves in a cylinder with conclusions based on the application of appropriate partial differential equations and suitable boundary conditions. The authors have not yet carried out this more rigorous treatment.

The angle of fracture α in Fig. 3(D), can be used to calculate the velocity C of the stress waves provided the detonation velocity D of the explosive is known. The stress wave velocity will be given by

$$C = D\cos\alpha. \tag{3}$$

It is seen that a large angle of fracture corresponds to a low stress wave velocity.

It was found experimentally that the angle of fracture varied with cylinder material in the manner indicated by Eq. (3). It is important that only that portion of the fractured surface which has been subjected to the interacting tensile waves, i.e., A–B in Fig. 3, be used to determine the angle of fracture. During the formation of the cone, the fracture may extend beyond A [Fig. 3(C)], but this additional fracturing will not be directly caused by the interacting stress waves. The length of the fracture A–B is proportional to the wall thickness. Thicker-walled cylinders, therefore, increase the accuracy with which α can be measured.

The angles of fracture and the stress wave velocities computed from them are given in Table II. A detonation velocity of 26,000 ft/sec was used in the computations. Included in this table are values for the velocity of dilatational waves, i.e., C of Eq. (2), in these metals taken from several sources.[4–6] Photographs of cross-sectional views of the hubs or hub fragments for copper, brass, 1020 steel, and lead are reproduced in Fig. 4. Of the four metals shown, it can be seen that steel, with the highest stress wave velocity, has the smallest angle of

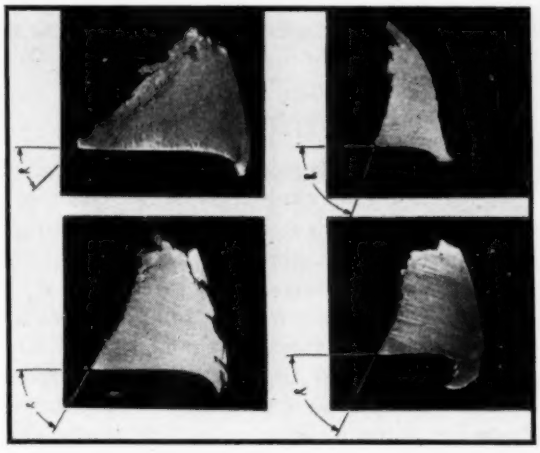

FIG. 4. Cross sections of metal hubs showing angles of fracture; upper left, steel; upper right, lead; lower left, brass; and lower right, copper.

fracture, while lead, with the lowest velocity, has the greatest angle of fracture. Brass and copper have almost the same angle of fracture and approximately the same stress velocity. The aluminum alloy, which is not shown in Fig. 4, had the greatest stress wave velocity of the five metals tested and also the smallest angle of fracture. The quantitative agreement is good between published values of stress wave velocities and those determined here.

In conclusion, the authors wish to acknowledge the assistance of Mr. J. Craig McLaughlin who performed the tests.

[4] Pack, Evans, and James, Proc. Phys. Soc. (London) **60**, 1 (1948).
[5] R. D. Fay and O. V. Fortier, J. Acoust. Soc. Am. **23**, 339 (1951).
[6] Hughes, Pondrom, and Mims, Phys. Rev. **75**, 1522 (1949).

Radiation Characteristics of a Turnstile Antenna Shielded by a Section of a Metallic Tube Closed at One End*

ALFREDO BAÑOS, JR.,† DAVID S. SAXON,‡ *Physics Department, University of California, Los Angeles, California*

AND

LOUIS L. BAILIN,§ *National Bureau of Standards, Institute for Numerical Analysis, Los Angeles, California*

(Received March 10, 1952)

Radiation characteristics are established for a turnstile antenna in a cylindrical shield. The antenna consists of perpendicularly crossed wires driven by a sinusoidal current distribution, harmonic in time, and differing in phase by 90° between members of the cross. The shield is assumed to be a perfectly conducting cylindrical can open at one end and its diameter is taken to be of the order of a fraction of the driving wavelength. The axis of the shield is perpendicular to the plane of the antenna, passing through its center. The excitation of an infinitely long circular wave guide by the above current distribution is considered first, and conditions under which only the dominant (TE_{11}) mode is important are determined. The essential radiation problem can then be regarded as one in which a semi-infinite circular guide, excited by a TE_{11} mode, radiates into free space. This problem has been formally solved by Levine and Schwinger and, using their results, values of the reflection coefficient and gain function have been computed by the National Bureau of Standards, Institute for Numerical Analysis, University of California, Los Angeles. The results of this theory are compared with experiment and with the Kirchhoff method.

I. INTRODUCTION

A PROBLEM of considerable interest in antenna design is the determination of the behavior of a turnstile antenna which is shielded by a cylindrical can open at one end as illustrated in Fig. 1. This antenna consists of perpendicularly crossed wires of equal length excited by a sinusoidal current distribution which differs by 90° in time phase between the members of the cross. The shield is assumed to be a perfectly conducting cylindrical can open at one end, and its diameter is taken to be of the order of a fraction of the driving wavelength. The axis of the shield is so aligned that it passes through the center of the crossed wires and is perpendicular to them. Further, the effect of the wire supports is assumed to be negligible. Under these conditions, it is desired to calculate the radiation properties of the antenna such as the far field radiation pattern and polarization, the impedance seen by the antenna, and the field and power gain functions.

The radiation field can be approximated by following the classical procedure of Kirchhoff. According to this procedure, it is assumed that the lateral surface of the shield is infinitely long, and the field inside this cylinder produced by the crossed wires and their image with respect to the closed end of the shield is determined.[1] The equivalent electric and magnetic current densities produced by the above field at the position of the open end are then obtained, and the radiation field is assumed to be equivalent to the field which would be radiated by these currents. However, recent investigations by J. Schwinger and others have shown that the Kirchhoff method is not always reliable for aperture dimensions of the order of or smaller than the wavelength. The reliability of the Kirchhoff method as applied to this problem is also investigated here.

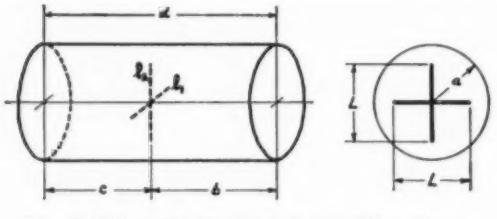

FIG. 1. Schematic diagram of turnstile antenna.

It will be the purpose of this paper to make use of the powerful methods established by Levine and Schwinger[2] to obtain, approximately, the radiation characteristics of the above turnstile antenna. The analysis will essentially consist of two parts, as follows: First, the excitation of an infinite circular guide by the prescribed current source distribution is determined. Having thus obtained a complete description of the field (mode structure, relative amplitude, and phase) incident upon the open end, the second part of the analysis will consist of a mode-by-mode analysis of the radiation from a *semi-infinite* guide into free space. It turns out that, with a suitable choice of wavelength and dimensions, there is only one propagating mode excited by the radiator and that, at distances of only a small fraction of wavelength from the cross, the amplitudes of all attenuated modes have dropped sharply. Hence, the far radiation field of the one propagating mode will very accurately represent the radiation from the described antenna.

The theoretical problem which will be explicitly

* The preparation of this paper was sponsored (in part) by the ONR.

† Consultant for the Natl. Bur. Standards.

‡ Presently at the Natl. Bur. Standards, Institute for Numerical Analysis, Los Angeles, California.

§ Present address: Hughes Aircraft Company, Culver City, California.

[1] H. Buchholz, Ann. d. Phy. (5) **39**, 81 (1941).

[2] H. Levine and J. Schwinger, Phys. Rev. **73**, 383 (1948), and "Electromagnetic Radiation from a Circular Guide into Free Space" (unpublished but privately communicated to the authors).

solved, as already mentioned, is the radiation from a *semi-infinite* guide into free space. That is to say, the cylindrical shield of length d in the actual antenna is replaced in the theoretical problem by a semi-infinite guide containing a short-circuiting plunger a distance d from the open end (Fig. 2). Such an approximation, which is essential for the application of the Schwinger and Levine method and results, must be carefully considered because the metallic extension introduces boundary conditions which the fields of the actual antenna need not satisfy. We may argue, however, from the physical nature of the antenna, that the radiation is strongly directed outward from the open end, with only a small amount of the energy being radiated in the backward direction. Thus, it is reasonable to assume that the metallic extension has little effect on the far radiation field in the forward direction. This directivity will be explicitly demonstrated in the final results of Levine and Schwinger. Alternatively, it can be shown that the surface current induced on the shield (which can be regarded as the source of radiation) is exponentially attenuated in the negative direction. Hence, the contribution from those elements of the surface current, which are far removed from the mouth of the antenna, is a small one.

II. DESCRIPTION OF FIELDS INSIDE AN INFINITE CIRCULAR GUIDE

To determine the excitation of an infinitely long circular guide by the cross, we now show that the total field produced can be obtained from the longitudinal components of the electric and magnetic fields. However, in carrying out this analysis, we shall proceed first in complete generality and consider the excitation of an infinite cylindrical guide with an arbitrary cross section by an arbitrary, prescribed current distribution. In the following, we shall choose the axis of the cylinder coinciding with the z axis of coordinates, and e_z shall denote a unit vector along this axis.

The inhomogeneous Maxwell's equations, under the assumption that the source oscillates with harmonic time dependence $e^{-i\omega t}$, can be written as

$$\text{(I)}\ \nabla\times E=ik\zeta H \qquad \text{(III)}\ \nabla\cdot H=0$$
$$\text{(II)}\ \nabla\times H=-ik\eta E+J \quad \text{(IV)}\ \nabla\cdot E=\rho/\epsilon_0=(\zeta/ik)(\nabla\cdot J),$$

where the time dependence has been suppressed. Here ζ, the intrinsic impedance of free space for plane homogeneous waves, is given by

$$\zeta=1/\eta=(\mu_0/\epsilon_0)^{\frac{1}{2}}$$

and $k=2\pi/\lambda$, where λ is the free space wavelength corresponding to the driving frequency ω.

The integration of these vector equations, in general, can be effected using a dyadic Green's function.[3] However, we shall proceed directly by separating the field equations into two inhomogeneous scalar equations

[3] See, for example, P. H. Morse and H. Feshbach, *Methods of Theoretical Physics* (M.I.T. Press, Cambridge, 1946), Chap. VI.

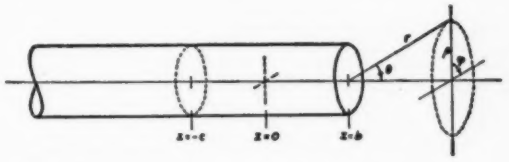

FIG. 2. Idealized antenna and coordinate system.

governing the longitudinal components of E and H and into two vector equations for the transverse components. Since the total fields can be obtained from the longitudinal components, it is only necessary to determine explicitly the solutions of the scalar equations.

Thus, taking the vector and scalar products of e_z with (I) and (II), respectively, and making use of (IV) to eliminate the transverse components of E, we find for E_z

$$(\nabla^2+k^2)E_z=-ik\zeta J_z-(i\zeta/k)(\partial/\partial z)(\nabla\cdot J). \quad (2.01)$$

Proceed similarly to find the corresponding scalar equation for H_z,

$$(\nabla^2+k^2)H_z=-e_z\cdot\nabla\times J. \quad (2.02)$$

From the solutions of these equations the rest of the field is easily obtained since, after some manipulation, the transverse fields E_t and H_t can be expressed in terms of the longitudinal components E_z and H_z by the differential equations

$$[(\partial^2/\partial z^2)+k^2]E_t=(\partial/\partial z)(\nabla_t E_z) -ik\zeta(e_z\times\nabla_t H_z)-ik\zeta J_t, \quad (2.03)$$

and

$$[(\partial^2/\partial z^2)+k^2]H_t=ik\eta(e_z\times\nabla_t E_z) +(\partial/\partial z)(\nabla_t H_z)-(\partial/\partial z)(e_z\times J), \quad (2.04)$$

in which the subscript t denotes the transverse component of the vectors in question.

In the present instance the current density vector J refers to the prescribed current distribution over the antennas l_1 and l_2 (Fig. 1) which is assumed to be given by

$$I_1=I_0e^{-i\omega t}\cos(\pi\rho/L) \quad \text{and} \quad I_2=I_0e^{i\pi/2-i\omega t}\cos(\pi\rho/L),$$

where L is the length of the antennas and ρ measures the distance from the center of the cross. Thus, suppressing the exponential time dependence factor and using cylindrical coordinates (ρ, φ, z), with the center of the turnstile antenna at the origin of coordinates (Fig. 2), the current density vector J becomes

$$J(\rho,\varphi,z)=e_\rho(I_0/\rho)\cos(\pi\rho/L)\delta(z) \times\sum_{s=0}^{3}e^{is\pi/2}\delta(\varphi-s\pi/2), \quad 0\leqslant\rho\leqslant L/2; \quad (2.05)$$

$$J(\rho,\varphi,z)=0, \quad \rho>L/2,$$

where e_ρ denotes the unit vector along ρ.

Substituting this expression for J into (2.01) there results an inhomogeneous, scalar Helmholtz equation for E_z which is readily solved using the Green's function expressed in terms of an expansion into normal TM or E modes. Briefly, E_z can be expanded as

$$E_z=\sum_{m,n}\Phi_{mn}=\sum_{m,n}A_{mn}\varphi_{mn}(\rho,\varphi)\frac{z}{|z|}e^{ih_{mn}|z|}, \quad (2.06)$$

where we have

$$\varphi_{mn}(\rho,\varphi)=N_{mn}J_m(\gamma_{mn}\rho)e^{im\varphi}, \quad J_{mn}(\gamma_{mn}a)=0;$$
$$1/N_{mn}^2=\pi a^2[J_m'(\gamma_{mn}a)]^2, \quad h_{mn}^2=k^2-\gamma_{mn}^2;$$
$$A_{mn}=\frac{2(\pi)^{\frac{1}{2}}i\zeta I_0}{akLJ_m'(\gamma_{mn}a)} \times\int_0^{L/2}J_m(\gamma_{mn}\rho')\sin(\pi\rho'/L)d\rho', \quad (2.07)$$

and in which $m=4p+1$, with p any integer including zero, and $n=1, 2, \cdots$. A similar calculation for H_z in terms of normal TE or H modes yields

$$H_z=\sum_{m,n}\Psi_{mn}=\sum_{m,n}A_{mn}'\psi_{mn}(\rho,\varphi)e^{ih_{mn}'|z|}, \quad (2.08)$$

with

$$\psi_{mn}(\rho,\varphi)=N_{mn}'J_m(\gamma_{mn}'\rho)e^{im\varphi},$$
$$J_{mn}'(\gamma_{mn}'a)=0;$$
$$1/N_{mn}'^2=\pi a^2[1-(m/\gamma_{mn}'a)^2]J_m^2(\gamma_{mn}'a),$$
$$h_{mn}'^2=k^2-\gamma_{mn}'^2;$$
$$A_{mn}'=\frac{2mI_0}{\pi^{\frac{1}{2}}ah_{mn}'[1-(m/\gamma_{mn}'a)^2]^{\frac{1}{2}}J_m(\gamma_{mn}'a)} \times\int_0^{L/2}J_m(\gamma_{mn}'\rho')\cos(\pi\rho'/L)\frac{d\rho'}{\rho'}, \quad (2.09)$$

where again $m=4p+1$, with $p=0, \pm1, \pm2, \cdots$, and $n=1, 2, \cdots$.

It is evident from the above expansions that the prescribed cross excites only modes which have alternate odd angular mode numbers or an odd number of nodal planes (i.e., $m=\cdots, -7, -3, 1, 5, 9, \cdots$) for both TE and TM waves. The fields associated with these modes rotate with an angular velocity which depends upon the mode number where positive mode numbers indicate the positive direction and negative mode numbers the negative direction. We see, therefore, that there is no possibility of obtaining angular standing wave patterns, since the fields rotating in one direction and those rotating in the opposite direction have different angular velocities and, therefore, cannot couple together to form a standing wave. Thus, the total field inside the guide consists of partial fields which rotate with angular velocities which are consecutive odd submultiples of the angular velocity of a dominant mode and whose direction of rotation alternates with the increase in mode number (i.e., 1, −3, 5, −7, ···).

TABLE I.[a] $ka=1.928$.

mode	γa	ha
TE_{11}	1.841	.576
TM_{11}	3.832	$3.310i$
TE_{31}	4.201	$3.732i$
TE_{12}	5.331	$4.970i$

[a] These numerical values will be used frequently in subsequent calculations.

We now determine explicitly the modes present and the character of their propagation constants by rewriting the expressions for h_{mn} and h_{mn}', as found in (2.07) and (2.09), in terms of the dimensionless parameter ka which is proportional to the driving frequency, obtaining

$$(h_{mn}a)^2=(ka)^2-(\gamma_{mn}a)^2 \quad (2.10)$$

and

$$(h_{mn}'a)^2=(ka)^2-(\gamma_{mn}'a)^2, \quad (2.11)$$

where it is recalled that γ_{mn} and γ_{mn}' are determined as the nth roots, respectively, of $J_m(\gamma_{mn}a)=0$ and $J_m'(\gamma_{mn}'a)=0$. If we now choose, as an example, $ka=1.928$, a value which has been encountered in an experimental model of this antenna, we can then list a few of the modes excited by the cross and the transverse and longitudinal wave numbers associated with them in the order of increasing cut-off frequency. This is done in Table I. It is evident from this table that for the frequency parameter chosen, only the TE_{11} mode propagates since only h_{11}' is real and that all the higher modes are attenuated. The attenuation constants for all TM modes are defined by writing

$$iK_{mn}=h_{mn}, \quad (2.12)$$

and those for all TE modes other than the TE_{11} are given by

$$iK_{mn}'=h_{mn}'. \quad (2.13)$$

III. REDUCTION OF THE ACTUAL ANTENNA TO A SEMI-INFINITE GUIDE

With a knowledge of the fields excited by the sources in the infinite guide, we may now describe the nature of the fields inside the actual antenna based on our fundamental assumption that it behaves essentially as a semi-infinite guide containing a short circuiting plunger to the left of the source (Fig. 2). Providing that there is very little coupling between modes of the same type and angular distribution, the analysis will then consist of a mode by mode determination of the radiation from an unflanged semi-infinite guide. Such radiation problems have been considered by Levine and Schwinger but were explicitly formulated for only a few of the lower modes. Thus, it becomes essential for the present problem to determine, at least approximately, the

relative power radiated by the various modes excited by the source. From this information, we may determine how many "Schwinger-like-problems" are required to represent accurately the far radiation field of the antenna.

The fields inside of the semi-infinite guide can be regarded as the sum of an exciting field given by (2.06) or (2.08) and appropriate solutions of the homogeneous Eq. (2.01) or (2.02), so chosen that the total field will satisfy the boundary conditions imposed by the plunger representing the closed end of the actual antenna and the discontinuity at the open end. The boundary condition at the open end is very complicated, of course, since each incident mode sets up a higher mode field of infinite order, but the effects upon a given incident mode can be accounted for by considering the open end to be a partially reflecting surface characterized by a complex reflection coefficient r of magnitude less than or equal to unity.‖ The reflection coefficient associated with each mode excited by the source can be determined by the methods given by Levine and Schwinger. A rigorous calculation of the total power radiated by the guide would thus seem to require accurate description of these complex reflection coefficients. However, we shall now show that the power radiated by each attenuated mode, i.e., TM_{11}, TE_{31}, TE_{12}, etc., is small in comparison to that radiated by the propagating TE_{11} wave, since an upper limit to the small amount of power radiated by each attenuated mode can be obtained without any precise information about its reflection coefficient. Consequently, the radiation from the antenna can be accurately described in terms of the solution of just one "Schwinger-like-problem," namely, that for the TE_{11} mode.

As has been already mentioned, the fields in the semi-infinite guide that represents the actual antenna are obtained as a superposition of the appropriate solutions of the homogeneous Eqs. (2.01) and (2.02) and the expansions (2.06) and (2.08). Thus, if we normalize with respect to the transverse field and drop the subscripts, we may write for each TM mode

$$\Phi_{mn}/\varphi_{mn}=\varphi(z)=A(|z|/z)e^{ik|z|}+Be^{ikz}+Ce^{-ikz}, \quad (3.01)$$

and for each TE mode

$$\Psi_{mn}/\psi_{mn}=\psi(z)=A'e^{ik'|z|}+B'e^{ik'z}+C'e^{-ik'z}, \quad (3.02)$$

where the B's and C's are constants to be determined by the boundary conditions at the short-circuiting plunger, $z=-c$, and at the open end, $z=b$ (see Fig. 2). They will, of course, turn out to be proportional to the amplitudes A of the exciting fields. Upon application of these boundary conditions, we find after solving for the B's and C's,

$$C=rA(1-e^{-2ikc})/(r-e^{-2ikd}), \quad (3.03)$$

$$B=-A(r-e^{-2ikb})/(r-e^{-2ikd}), \quad (3.04)$$

‖ This assumes that the coupling between modes of interest, which is introduced at the open end, is negligible.

and

$$C'=r'A'(-1+e^{-2ik'c})/(r'+e^{-2ik'd}), \quad (3.05)$$

$$B'=-A'(r'+e^{-2ik'b})/(r'+e^{-2ik'd}). \quad (3.06)$$

The constants given in (3.03) and (3.04) for TM modes and (3.05) and (3.06) for TE modes thus permit us to express the total field vectors anywhere inside the shield for any type of mode in terms of the appropriate reflection coefficients.

Let us now examine the power radiated by or supplied to each mode and in addition the impedance of the antenna referred to the input current I_0. The total complex power supplied to a volume V by external sources can be written as

$$\text{total input power}=-\frac{1}{2}\int_v E\cdot J^*dv, \quad (3.07)$$

which is merely a generalization of Ohm's law. From a simple consideration of Maxwell's equations, the real part of this integral can be shown to equal the average power radiated out of the volume V, as expected, and hence a mode-by-mode evaluation of (3.07) yields directly the power radiated by each mode. Further, an impedance can be defined for the antenna by expressing the total input power, real and reactive, as

$$-\frac{1}{2}\int_v E\cdot J^*dv=\tfrac{1}{2}I_0^2Z, \quad (3.08)$$

whence Z is seen to be the impedance of the antenna referred to the input current I_0.

For an extended source, the integral in (3.08) can be evaluated by obtaining E from the inhomogeneous Eqs. (2.01) and (2.03) by the methods previously outlined. However, in the present simpler case, the source is concentrated in a transverse plane and for each TE mode, for example, we may write at once, as in (3.02),

$$[H_z]_{mn}=\Psi_{mn}=\psi_t(A'e^{ik'|z|}+B'e^{ik'z}+C'e^{-ik'z}). \quad (3.09)$$

Thus from (2.03), the corresponding electric field is given by

$$[E]_{mn}=[E_t]_{mn}=(ik\zeta/(\gamma')^2)(e_z\times\nabla\psi)(A'e^{ik|z|}+B'e^{ik'z}+C'e^{-ik'z}) \quad (3.10)$$

and is a continuous function of z. Hence, upon substitution of this expression and the current distribution (2.05) into the volume integral in (3.01), we obtain after some elementary integrations

$$-\frac{1}{2}\int_v E\cdot J^*dv'=\frac{k\zeta h}{(\gamma')^2}|A'|^2\times\left[1-\frac{r'+e^{-2ik'b}}{r'+e^{-2ik'd}}-\frac{r'-r'e^{-2ik'c}}{r'+e^{-2ik'd}}\right], \quad (3.11)$$

if h' is real, and

$$-\frac{1}{2}\int_v E\cdot J^*dv' = -\frac{ik\zeta K'}{(\gamma')^2}|A'|^2 \times\left[1-\frac{r'+e^{2K'b}}{r'+e^{2K'd}}-\frac{r'-r'e^{2K'c}}{r'+e^{2K'd}}\right] \quad (3.12)$$

for $h'=iK'$. The real and imaginary parts of (3.11) can conveniently be written as

$$-\tfrac{1}{2}Re\int_v E\cdot J^*dv' = (k\zeta h'/(\gamma')^2)|A'|^2 2f(r')\sin^2(h'c), \quad (3.13)$$

where

$$f(r')=(1-|r'|^2)/(|r'+e^{-2ih'd}|^2) \quad (3.14)$$

and

$$-\tfrac{1}{2}Im\int_v E\cdot J^*dv' = \frac{k\zeta h'}{(\gamma')^2}|A'|^2 \times\frac{2Im[r'^*(e^{-2ih'd}-e^{-2ih'b})]-[1+|r'|^2]\sin^2(h'c)}{|r'+e^{-2ih'd}|^2}. \quad (3.15)$$

It should be noted that, since $\sin^2(h'c)$ appears as a factor in (3.13), the position of the short-circuiting plunger strongly influences the power radiated, the power being in fact zero when c is a half-integral number of guide wavelengths and a maximum when c is an odd integral number of quarter wavelengths—all as anticipated from elementary considerations, of course.

Similarly, for attenuated modes, where $h'=iK'$, the real and imaginary parts of (3.12) become

$$-\tfrac{1}{2}Re\int_v E\cdot J^*dv' = \frac{k\zeta K'}{(\gamma')^2}|A'|^2e^{2K'b} \times\frac{[e^{2K'c}-1]^2}{|r'+e^{2K'd}|^2}Im[r'], \quad (3.16)$$

$$-\tfrac{1}{2}Im\int_v E\cdot J^*dv' = -\frac{k\zeta K'}{(\gamma')^2}|A'|^2(e^{2K'c}-1) \times\frac{|r'|^2+e^{2K'(d+b)}+e^{2K'b}(e^{2K'c}+1)Re[r']}{|r+e^{2K'd}|^2}. \quad (3.17)$$

For TM modes, we need consider only $h=iK$, and we find in a similar way that

$$-\tfrac{1}{2}Re\int_v E\cdot J^*dv' = \frac{k\eta K}{\gamma^2}|A|^2e^{2Kb}\frac{(1-e^{2Kc})^2}{|r-e^{2Kd}|^2}Im[r] \quad (3.18)$$

and

$$-\tfrac{1}{2}Im\int_v E\cdot J^*dv' = \frac{k\eta K}{\gamma^2}|A|^2(1-e^{2Kc}) \times\frac{[-|r|-e^{2K(b+d)}+e^{2Kb}(1+e^{2Kc})Re[r]]}{|r-e^{2Kd}|^2}. \quad (3.19)$$

It should perhaps be mentioned that Eqs. (3.13), (3.16), and (3.18), which give the average power supplied to the antenna and, hence, the average power radiated in a given mode, can be verified by calculating the radiated power directly using Poynting's theorem; i.e., we must have

$$-\tfrac{1}{2}Re\int E\cdot J^*dv = \tfrac{1}{2}Re\int_S e_z\cdot[E\times H^*]dS,$$

where S is a cross section of the guide located anywhere to the right of the source ($z>0$). That this expression indeed reduces to (3.13), (3.16), or (3.18), as the case may be, is easily established by direct substitution of the appropriate fields.

Having obtained explicit expressions for the power radiated by various types of modes, we can now calculate, at least approximately, the average power radiated by or supplied to each mode as compared to the propagating TE_{11} mode. Considering first the power radiated by the TM_{11} mode, it is easily seen from (3.18) that, considered as a function of the reflection coefficient r_{11}, this power has the upper limit

$$P(TM_{11})\leq(k\eta K_{11}/\gamma_{11}^2)|A_{11}|^2e^{-2K_{11}b}. \quad (3.20)$$

This rough, but sufficient, result is obtained by putting $Im(r_{11})=1$ and neglecting r_{11} and unity in comparison to the exponentials in (3.18). Thus we have at once, using (3.13),

$$\frac{P(TM_{11})}{P(TE_{11})}\leqq\frac{(K_{11}a)(\gamma_{11}'a)^2|A_{11}|^2}{(h_{11}'a)(\gamma_{11}a)^2\zeta^2|A_{11}'|^2} \times\frac{e^{-2K_{11}b}}{2f(r_{11}')\sin^2(h_{11}'c)}, \quad (3.21)$$

where $f(r_{11}')$ is given by (3.14) and where the result has been expressed in terms of the dimensionless quantities $K_{11}a$, $\gamma_{11}a$, $h_{11}'a$, and $\gamma_{11}'a$. Similarly, for the TE_{31} and TE_{12} modes we obtain

$$\frac{P(TE_{31})}{P(TE_{11})}\leqq\frac{(K_{31}'a)(\gamma_{11}'a)^2}{(h_{11}'a)(\gamma_{31}'a)^2}\frac{|A_{31}'|^2}{|A_{11}'|^2} \times\frac{e^{-2K_{31}'b}}{2f(r_{11}')\sin^2(h_{11}'c)} \quad (3.22)$$

and

$$\frac{P(TE_{12})}{P(TE_{11})}\leq\frac{(K_{12}'a)(\gamma_{11}'a)^2}{(h_{11}'a)(\gamma_{12}'a)}\frac{|A_{12}'|^2}{|A_{11}'|^2}\times\frac{e^{-2K_{12}'b}}{2f(r_{11}')\sin^2(h_{11}'c)}. \quad (3.23)$$

We have thus been able to obtain upper bounds for the power ratios without requiring a precise knowledge of the reflection coefficients of the attenuated modes. Since expressions for r_{11}' were derived by Levine and Schwinger and its numerical values as a function of ka have been computed by the National Bureau of Standards, these ratios may be evaluated for any desired set of parameters. In particular, using the following parameters which have been encountered in an experimental antenna: $KL=2.438$; $kc=1.519$; $kd=3.192$; $kb=1.673$ and using also the numerical values listed in Table I, we find that

$$\frac{P(TM_{11})}{P(TE_{11})}\leqq\frac{.258}{f(r_{11}')}e^{-2K_{11}b},$$

$$\frac{P(TE_{31})}{P(TE_{11})}\leqq\frac{.00801}{f(r_{11}')}e^{-2K_{31}'b},$$

$$\frac{P(TE_{12})}{P(TE_{11})}\leqq\frac{.136}{f(r_{11}')}e^{-2K_{12}'b}.$$

If we now make use of the value of $r_{11}'\simeq-0.39-i(0.12)$ for $ka=1.928$ interpolated from the results of Levine and Schwinger which are tabulated in Sec. IV, we find $f(r_{11}')\simeq.44$ and, hence,

$$P(TM_{11})/P(TE_{11})\leq.59e^{-2K_{11}b},$$

$$P(TE_{31})/P(TE_{11})\leq.018e^{-2K_{31}'b},$$

$$P(TE_{12})/P(TE_{11})\leq.31e^{-2K_{12}'b}.$$

Since the dimensionless parameters $2Kb$ are

$$2K_{11}b=5.745;\quad 2K_{31}'b=6.474;\quad 2K_{12}'=8.625,$$

for the experimental antenna, it is evident that for the given parameters the power radiated by each attenuated mode is less than 0.2 percent of the propagating mode. Thus, we have ample justification for the assumption that the actual antenna behaves as if it were excited by a TE_{11} wave alone.

From (3.17) and (3.19), it can be easily shown that, to a first approximation, the reactive power in the attenuated TE modes can be given by

$$Q(TE)\simeq-(k\zeta K/(\gamma')^2)|A'|^2, \quad (3.24)$$

and for the attenuated TM modes by

$$Q(TM)\simeq(k\eta K/(\gamma)^2)|A|^2. \quad (3.25)$$

These results have been obtained by neglecting terms of order unity compared to the exponentials. Such an approximation is equivalent to neglecting, for the attenuated modes, the reactive power contributed by the fields reflected from both the open and closed ends of the antenna. Finally then, if we let

$$z=R-iX \quad (3.26)$$

and neglect as before terms of $0(e^{-2Kb})$ arising from the attenuated modes, we obtain, to good approximation,

$$R\simeq\frac{2k\zeta h_{11}'}{(\gamma_{11}')^2}\frac{|A_{11}'|^2}{I_0^2}f(r_{11}')\sin^2(h_{11}'c), \quad (3.27)$$

and

$$X\simeq-\frac{k\zeta h_{11}'}{(\gamma_{11}')^2}\frac{|A_{11}'|^2}{I_0^2}\times\frac{2Im[r_{11}'^*(e^{-2ih_{11}'d}-e^{-2ih_{11}'b})]-[1+|r_{11}'|^2]\sin 2h_{11}'c}{|r_{11}'+e^{-2ih_{11}'d}|^2}-\sum_{m,n}\frac{k\eta K_{mn}}{\gamma_{mn}^2}\frac{|A_{mn}|^2}{I_0^2}+\sum_{m,n}\frac{k\zeta K_{mn}'}{\gamma_{mn}'^2}\frac{|A_{mn}'|^2}{I_0^2}. \quad (3.28)$$

From the above expressions for the resistive and reactive parts of the impedance seen by the antenna, we note that, to good approximation, the resistance depends only on the characteristic parameters and the reflection coefficient associated with the *propagating* mode and upon the distance from the source to the open and closed ends of the antenna. The reactance, however, is composed of a term which involves the parameters of the TE_{11} mode and which is either capacitive or inductive, depending upon the position of the source with respect to the ends plus an infinite series of inductive terms, one for each attenuated TM mode, and an infinite series of capacitive terms, one for each attenuated TE mode. Because of the approximate treatment of the attenuated modes, each term in these series depends only upon the field amplitudes excited by the source and not upon the reflection coefficients or position of the source.

IV. ELECTROMAGNETIC RADIATION FROM A CIRCULAR GUIDE INTO FREE SPACE

In the preceding sections, we have shown to good approximation that the field incident upon the open end of the antenna is that of a TE_{11} mode. Thus, to obtain the characteristics of the given antenna, we must consider the radiation from a circular guide which is so excited. The formal solution of this problem has already been obtained by Levine and Schwinger¶ using a

¶ As yet unpublished because of the extensive computations required. However, these calculations have now been performed by the National Bureau of Standards and early publication in the Physical Review is expected. Thanks are due Dr. Levine and Dr. Schwinger for the private communication of their solution.

TABLE II. $r_{11}'=X+iY$.

ka	X	Y	$\lvert r_{11}'\rvert$
1.841183790	−1.000	−0.000	+1.000
2.000	−0.234	−0.152	0.279
2.400	−0.054	−0.073	0.091
2.800	−0.023	−0.038	0.045
3.200	−0.016	−0.022	0.027
3.600	−0.016	−0.011	0.019
3.831705970	−0.024	+0.003	0.024

method similar to that employed in a previous paper by the same authors.[2] In this section, we will make repeated use of this formal solution and the numerical values computed from it by the National Bureau of Standards. We now summarize the pertinent results of Levine and Schwinger with occasional trivial modifications as required by the present problem. For convenience these results will be given essentially in their notation.

The reflection coefficient r_{11}', referred to in Sec. III, for the magnetic field (called voltage reflection coefficient by Levine and Schwinger) in the guide is given by

$$r_{11}'=-\frac{L_+(h_{11}')}{L_+(-h_{11}')}\frac{(k+h_{11}')/(k-h_{11}')+iS}{(k-h_{11}')/(k+h_{11}')+iS}, \quad (4.01)$$

where

$$S=A\frac{ka}{2}\left(1+\frac{\zeta_0 a}{ka}\right)^2\exp\left[\left(2i\frac{ka}{\pi}\right)+2i\right.$$
$$\left.\times\sum_{n=1}^{\infty}\left[\sin^{-1}\left(\frac{k}{\gamma_n}\right)-\frac{ka}{n\pi}\right]-2i\sum_{n=2}^{\infty}\left[\sin^{-1}\left(\frac{k}{\gamma_n'}\right)-\frac{ka}{n\pi}\right]\right]$$

and

$$A=\exp\left\{\frac{-1}{\pi}\int_0^{\infty}\frac{dx}{x}\left(1-\frac{ka}{[x^2+(ka)^2]^{\frac{1}{2}}}\right)\right.$$
$$\times\left(\tan^{-1}\frac{K_1(x)}{\pi I_1(x)}+\tan^{-1}\frac{-K_1'(x)}{\pi I_1'(x)}\right)\frac{-i}{2\pi}\int_0^{\infty}\frac{dx}{x}$$
$$\left.\times\left(1-\frac{ka}{[x^2+(ka)^2]^{\frac{1}{2}}}\right)\log\frac{1+[\pi I_1'(x)/K_1'(x)]^2}{1+[\pi I_1(x)/K_1(x)]^2}\right\},$$

where I_1 and K_1 are first-order cylinder functions of imaginary argument and $a\zeta_0=\alpha_0+\beta_0$ is defined by

$$H_1^{(1)\prime}[(k^2-\zeta_0^2)^{\frac{1}{2}}a]=0 \quad \text{for} \quad -\frac{\pi}{2}<arg(k^2-\zeta_0^2)^{\frac{1}{2}}<0.$$

Its value can be obtained from

$$(a\zeta_0)^2=(ka)^2-(x_0-iy_0)^2,$$

where $x_0=.50118351$ and $y_0=.64354502$.** As before, $J_1(\gamma_n a)=0$ and $J_1'(\gamma_n' a)=0$. Also

$$\frac{L_+(h_{11}')}{L_+(-h_{11})}=\frac{\zeta_0+h_{11}'}{\zeta_0-h_{11}'}\left[\frac{k-h_{11}'}{k+h_{11}'}\right]^{5/4}$$
$$\times\exp\left[-2i\sum_{n=2}^{\infty}\left(\sin^{-1}\frac{h_{11}'}{(\gamma_n^2-\gamma_1^2)^{\frac{1}{2}}}-\frac{h_{11}'a}{n\pi}\right)\right]$$
$$\times\exp\left[2i\frac{h_{11}'a}{\pi}\left(\log\frac{2\pi}{Cka}+2\right)\right]\times B,$$

where C = Euler's constant and where

$$B=\exp\left\{\frac{ih_{11}'a}{2}\int_0^{\infty}\frac{xdx}{x^2+(\gamma_1'a)^2}\frac{1}{(x^2+(ka)^2)^{\frac{1}{2}}}\right.$$
$$\times\log\left[\left\{1+\left(\frac{\pi I_1'(x)}{K_1'(x)}\right)^2\right\}e^{-4x}\right]+\frac{h_{11}'a}{\pi}$$
$$\left.\times\int_0^{\infty}\frac{xdx}{x^2+(\gamma_1'a)^2}\frac{1}{(x^2+(ka)^2)^{\frac{1}{2}}}\tan^{-1}\left(\frac{-K_1'(x)}{\pi I_1'(x)}\right)\right\}$$
$$\times\exp\left[\left(-2i\frac{\gamma_1'a}{\pi}\right)\sin^{-1}\frac{h_{11}'}{k}-h_{11}'a\right].$$

Numerical values of r_{11}' as a function of ka were obtained from (4.01) by the National Bureau of Standards and are exhibited in Table II and plotted in Fig. 3. Although a great deal of care was taken with these calculations and convenient checking methods were used to insure correct results, the necessarily large interval in ka did not permit the use of differencing as an absolute mathematical check.

Other important results which can be obtained from the equations of Levine and Schwinger are the expressions for the magnetic and electric fields at large distances from the mouth of the guide. From the components of these fields a study can be made of the polarization of the far fields as a function of the azi-

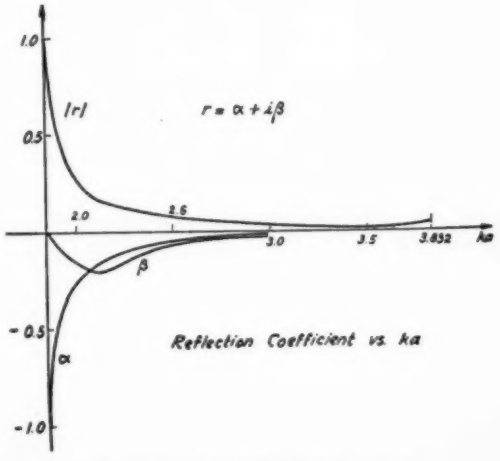

FIG. 3. Reflection coefficient *vs* ka.

** Numerical values obtained by the National Bureau of Standards with the aid of the values given by Jahnke-Emde, "Tables of Functions" (Dover Publications, New York, 1943), fourth edition, p. 242.

muthal and polar angles measured with respect to the axis of the guide. This study indicates that, in general, the far fields are elliptically polarized. However, owing to the complexity of the functions involved, it is not possible to discuss accurately the characteristics of the polarization ellipse without an enormous amount of numerical calculation, except in the forward direction. In this direction, the functions simplify greatly, and it is easily shown that the fields are circularly polarized, which is in agreement with experiments performed on the actual antenna.

The power gain function defined as in Silver[5] is given by Levine and Schwinger as

$$G(\theta)=2\frac{h_1'}{\gamma_1'}(ka)\frac{J_1(\gamma_1'a)}{H(ka,h_1'a)-H(ka,-h_1'a)}\times\left[\frac{J_1'(ka\sin\theta)}{1-(k\sin\theta/\gamma_1')^2}H(ka,ka\cos\theta)+\frac{2J_1(ka\sin\theta)}{\sin\theta}E(ka,ka\cos\theta)\right],$$

$$E(x,y)=\frac{e^y}{(x+y)^{\frac{1}{2}}}\times\exp\left[-\frac{1}{\pi}\int_0^\infty\frac{tdt}{(t^2+x^2)^{\frac{1}{2}}}\tan^{-1}\frac{K_1(t)}{\pi I_1(t)}\times\left\{\frac{1}{(t^2+x^2)^{\frac{1}{2}}+y}+\frac{1}{(t^2+x^2)^{\frac{1}{2}}+x}\right\}\right], \quad (4.02)$$

$$H(x,y)=\frac{(x+y)^{5/2}e^y}{|x+\zeta_0a|^2|y+\zeta_0a|^2}\left|\frac{x-y}{x+y}+iS\right|^2\times\exp\left[\frac{1}{\pi}\int_0^\infty\frac{tdt}{(t^2+x^2)^{\frac{1}{2}}}\tan^{-1}\left(\frac{-K_1'(t)}{\pi I_1'(t)}\right)\times\left\{\frac{1}{(t^2+x^2)^{\frac{1}{2}}+y}+\frac{1}{(t^2+x^2)^{\frac{1}{2}}+x}\right\}\right].$$

$G(\theta)$ as function of θ and ka is tabulated in Table III and plotted in Fig. (4), and here again differencing could not be used as an absolute check.

V. COMPARISON WITH KIRCHHOFF THEORY AND WITH EXPERIMENT

In Sec. IV, the radiation characteristics of the antenna were computed from the rigorous solutions obtained by Levine and Schwinger for the radiation from a circular guide excited by a TE_{11} mode. With these results which are admittedly very complex, we may proceed to investigate the reliability of the classical

[5] S. Silver, "Microwave antenna theory and design," Radiation Laboratory Series, No. 12 (1949).

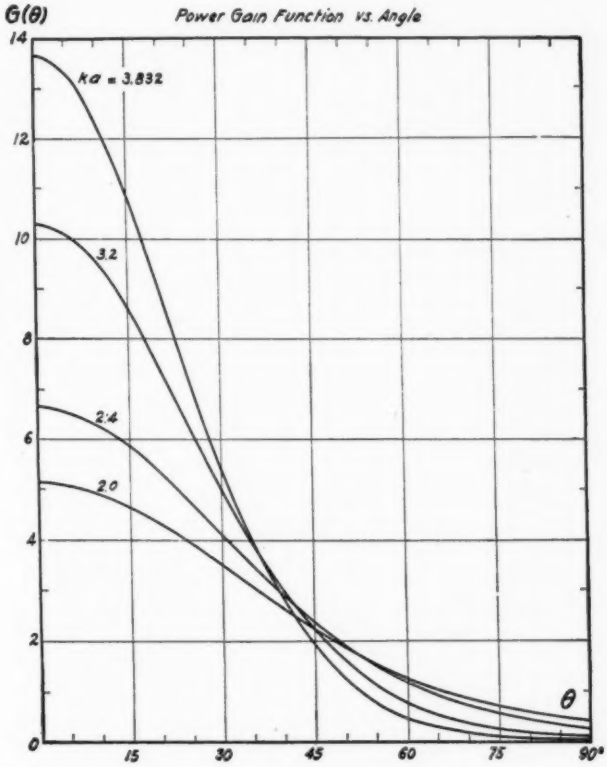

FIG. 4. Power gain function *vs* angle.

Kirchhoff method as applied to this type of radiation problem. For this comparison, we will assume that the exciting fields are linearly polarized and study the power gain functions in both the $E(\varphi=\pi/2)$ and $H(\varphi=0)$ planes. This will give a more detailed comparison than would a study of just the circularly polarized field; indeed, this latter is merely a superposition of the former two cases. We will also compare these theoretical results with some accurate experimental data obtained by Mr. L. E. Swarts of the Antenna Laboratory of the University of California, Berkeley.††

The power gain functions which correspond to (4.02) for exciting fields which are linearly polarized are given by

$$G(\theta,0)=2A\frac{J_1'(ka\sin\theta)}{1-(ka\sin\theta/\gamma_1'a)^2}H(ka,ka\sin\theta) \quad (5.01)$$

for the H-plane and

$$G(\theta,\pi/2)=2A\{[2J_1(ka\sin\theta)/\sin\theta]E(ka,ka\cos\theta)\} \quad (5.02)$$

for the E-plane. The constant A is the coefficient of the bracket in (4.02), and the functions $E(x,y)$ and $H(x,y)$ are as defined in (4.02).

†† The authors are indebted to Professor S. Silver and Mr. L. E. Swarts for these measurements which were privately communicated to them.

The Kirchhoff solution of this particular problem is obtained in Sec. 10.2 of Silver[5] from the radiation field vectors derived by Chu.[6] Thus, in the notation of this report and normalized to the same exciting power incident upon the opening in the guide as in (5.01) and (5.02), the Kirchhoff method yields the power gain function as

$$G(\theta,0)=\frac{2(ka)^3}{ha(\gamma_{11}^2a^2-1)}\left[\cos\theta+\frac{ha}{ka}\right]^2\times\left[\frac{J_1'(ka\sin\theta)}{1-(ka\sin\theta/\gamma_1''a)^2}\right]^2 \quad (5.03)$$

and

$$G(\theta,\pi/2)=\frac{2(ka)}{ha(\gamma_{11}^2a^2-1)}\left[1+\frac{ha}{ka}\cos\theta\right]^2\times\left[\frac{J_1(ka\sin\theta)}{\sin\theta}\right]^2. \quad (5.04)$$

From the above equations, we may now compare the corresponding gain functions as functions of θ for various values of ka. In Fig. 5 are compared the theoretical results obtained by Levine and Schwinger for the two planes of observation and the approximations to these results obtained by the Kirchhoff method. It is also of interest to normalize these curves with respect to the forward direction, $\theta=0$, so as to exhibit explicitly the angular dependence by eliminating amplitude factors. In Fig. 6 we compare the relative power gain function of the theoretical results with the experimental data obtained by Swarts.

TABLE III. $G(\theta)$.

θ \ ka	1.8411···	2.0	2.4	2.8	3.2	3.6	3.831···
0	4.597	5.131	6.630	8.342	10.262	12.379	13.647
5	4.551	5.075	6.538	8.201	10.054	12.084	13.293
10	4.417	4.909	6.271	7.793	9.457	11.244	12.290
15	4.203	4.647	5.853	7.161	8.547	9.980	10.791
20	3.923	4.307	5.320	6.371	7.428	8.458	9.008
25	3.596	3.913	4.714	5.495	6.218	6.854	7.159
30	3.240	3.487	4.079	4.601	5.023	5.322	5.428
35	2.872	3.054	3.452	3.749	3.924	3.969	3.935
40	2.510	2.632	2.864	2.980	2.973	2.851	2.734
45	2.165	2.237	2.334	2.317	2.192	1.978	1.827
50	1.847	1.878	1.873	1.767	1.578	1.332	1.178
55	1.562	1.560	1.485	1.328	1.114	0.873	0.736
60	1.312	1.287	1.166	0.986	0.775	0.560	0.447
65	1.097	1.056	0.911	0.727	0.534	0.354	0.266
70	0.915	0.864	0.709	0.535	0.367	0.222	0.156
75	0.763	0.707	0.553	0.395	0.253	0.139	0.091
80	0.638	0.581	0.433	0.293	0.176	0.088	0.053
85	0.536	0.479	0.342	0.220	0.124	0.057	0.032
90	0.453	0.399	0.273	0.168	0.090	0.039	0.021
95		0.336					0.014
100		0.286					0.011
105		0.248					0.009
110		0.220					0.008
115		0.199					0.008
120	0.225	0.185	0.107	0.058	0.028	0.012	0.008
125		0.177					0.008
130		0.175					0.008
135		0.181					0.009
140		0.195					0.010
145		0.221					0.011
150	0.333	0.264	0.140	0.073	0.037	0.019	0.013
155		0.327					0.017
160		0.411					0.023
165		0.499					0.035
170		0.567					0.055
175		0.603					0.073
180	0.704	0.615	0.424	0.277	0.174	0.106	0.078

[6] L. J. Chu, J. Appl. Phys. **11**, 603 (1940).

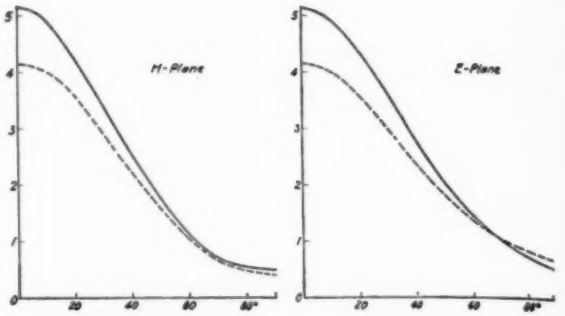

FIG. 5. Power gain function *vs* angle for $ka=2.0$. —— Rigorous theory. – – – Kirchhoff theory (normalized to same incident power.)

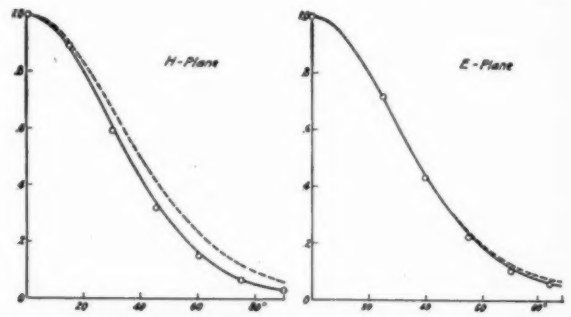

FIG. 6. Relative power gain *vs* angle for $ka=2.4$. —— Rigorous theory. – – – Kirchhoff theory. ○ Experimental points.

From Fig. 5, it is evident that the Kirchhoff approximation may give results which are as much as 20 percent too small in the forward direction for both types of polarization. However, from Fig. 6, we notice that the form of $G(\theta)$ is surprisingly accurate in the E-plane but is much less so in the H-plane. We also notice that the Schwinger and Levine results agree remarkably well with the experimental results in both planes of observation. Thus, we may conclude from this comparison that for this problem the Kirchhoff approximation will not suffice, if one desires absolute results which are with 20 percent of the correct values. On the other hand, if only the form of the gain function is required, as is usually the case, then the Kirchhoff approximation is very satisfactory in the E-plane but somewhat less so in the H-plane.

Letters to the Editor

The Change of the Elastic Constants of β-Brass with Composition

H. JONES
Imperial College, London, England
(Received February 11, 1952)

IN a letter in these columns, Artman and Thompson[1] have given the results of their determination of the elastic constants of β-brass at a composition of 55.12 atomic percent copper, and have compared their values with those determined by Lazarus[2] for brass of 51.74 atomic percent copper. They find that the shear constants $\frac{1}{2}(c_{11}-c_{12})$ (denoted for brevity by c') and c_{44}, and the bulk modulus K, are diminished by increasing the copper concentration. In a short paragraph at the end of their letter they discuss the significance of the diminution of c', and suggest that this is due to an increase in the non-Coulomb ion−ion interaction which might be expected to result from the substitution of the relatively large copper ions for the smaller zinc ions.

There are serious difficulties, however, in this interpretation because the same effect would certainly *increase* both c_{44} and K, contrary to observations. For a pure metal with body centered cubic structure, it is well known that

$$(c_{44}/c')_{\text{ion}}=(r^2w''+2rw')/3rw', \tag{1}$$

where r is the distance between nearest ions and $w(r)$ is the energy associated with the non-Coulomb interaction between a pair of ions. Many lines of approach suggest that, for ions which have closed electronic shells (as both Cu^+ and Zn^{++} have), $w(r)$ varies as $\exp\times(-r/\rho)$, where ρ is a length of about 0.3 au, and hence the right-hand side of (1) becomes $-\frac{1}{3}\left(\frac{r}{\rho}-2\right)$. Thus, if increasing the copper concentration by 3.38 percent changes c' by $\delta c'$, and if we attribute this change to an increase in the average negative value of $\frac{4}{3}rw'$, then we must expect, from the same cause, a change in c_{44} given by

$$\delta c_{44}=-\frac{1}{3}\left(\frac{r}{\rho}-2\right)\delta c'=-2.17\delta c', \tag{2}$$

since $r=2.549$ au for β-brass. As c' is observed to decrease from 0.974 to 0.833 (10^{11} dynes/cm²) as the copper concentration increases from 51.74 to 55.12 we see that $\delta c'=-0.141\ 10^{11}$ dynes/cm² and, therefore, δc_{44} should be $+0.306\ 10^{11}$ dynes/cm². The experimental results, however, show that the change is in the opposite sense and $(\delta c_{44})_{\text{obs}}=-0.804.10^{11}$ dynes/cm².

In a similar way the contribution to the bulk modulus K from the ion-ion interactions can be expressed

$$(K/c')_{\text{ion}}=(r^2w''-2rw')/3rw', \tag{3}$$

from which we may deduce $\delta K=-3.50\,\delta c'$. Thus again, if we attribute the change in c' to ion-ion interaction we should expect K to increase by $0.493.10^{11}$ dynes/cm². In fact K *decreases* by $0.83.10^{11}$ dynes/cm².

In a recent paper,[3] I have considered the way in which the shearing of the Brillouin zone affects the Fermi energy of the conduction electrons, and have shown that this effect leads to a contribution of about 1.2 and 1.8 (10^{11} dynes/cm²) to c' and c_{44}, respectively. Since these contributions depend upon the number of conduction electrons per unit volume of the metal it is clear that they must change as the composition changes. If Eqs. (16) and (17) of reference (3) are differentiated with respect to n, the number of conduction electrons per atom, it follows that

$$\delta c_{44}{}^F=\left\{-\frac{1}{2}\nu+\frac{4(1-\lambda)(2+3\lambda)}{3(2+\lambda)}\right\}\frac{\kappa(2)^{\frac{1}{3}}}{\pi}\delta n, \tag{4}$$

and

$$\delta c'^F=\left\{-\frac{5}{4}\nu+\frac{4(1-\lambda)(2+3\lambda)}{3(2+\lambda)}\right\}\frac{\kappa(2)^{\frac{1}{3}}}{\pi}\delta n. \tag{5}$$

Hence, since $\kappa=2.416\ 10^{12}$ dynes/cm², $\nu=0.6752$ and λ was taken equal to 0.15, $\delta c_{44}{}^F=10.374.10^{11}\delta n$ and $\delta c'^F=4.867\ 10^{11}\delta n$. As the copper concentration increases from 51.74 to 55.12, n decreases from 1.4826 to 1.4488 and therefore $\delta n=-.0338$. Thus the calculated changes in the Fermi energy contributions amount to $\delta c'^F=-.164\ 10^{11}$ and $\delta c_{44}{}^F=-.351\ 10^{11}$ dynes/cm². The change in c'^F is quite close to the observed value, but that for $c_{44}{}^F$, although now in the right sense, is only about half of the measured change.

The agreement with regard to c_{44} is improved by taking into account the change in the electrostatic contribution to the shear constants. If it may be assumed that the charge distribution of the conduction electrons is approximately uniform throughout the metal the effective ionic charge, which gives the electrostatic term, will be $Z_{\text{eff}}=1+x$, where x is the fraction of zinc atoms in the alloy. In these circumstances the contribution to each shear constant is proportional to $(1+x)^2\Omega^{-4/3}$, where Ω is the atomic volume. Neglecting changes in volume, which can easily be shown to give an effect an order of magnitude smaller, we may write

$$\frac{\delta c'^E}{c'^E}=\frac{\delta c_{44}{}^E}{c^E{}_{44}}=\frac{2\delta x}{1+x}, \tag{6}$$

where the superscript E denotes the electrostatic contribution. In reference (3) c'^E and $c_{44}{}^E$ were estimated to be 0.61 and 4.55, respectively, and thus $\delta c'^E=-0.028$ and $\delta c_{44}{}^E=-0.210$ (10^{11} dynes/cm²). When these contributions are added to the contributions from the Fermi energy the total changes in c' and c_{44} are found to be -0.192 and -0.561 (10^{11} dynes/cm²) respectively, which are not far from the observed values.

Finally with regard to the bulk modulus it is known that the conduction electrons, if regarded as "free", contribute a term which is proportional to $n^{5/3}$ and therefore $\delta K^F/K^F=(5/3)\delta n/n$. Since n diminishes as the copper concentration increases we see that K^F varies in the same sense as the observed modulus. The magnitude of δK^F is, however, only about one-half of the observed change; this is no doubt due to the fact that the bulk modulus, unlike the shear constants, is sensitive to changes in the energy of of the lowest level of the conduction band.

[1] R. A. Artman and D. O. Thompson, J. Appl. Phys. **22**, 358 (1951).
[2] D. Lazarus, Phys. Rev. **76**, 545 (1949).
[3] H. Jones, Phil. Mag. **43**, 105 (1952).

A Receiver of High Effective Absorption for Penetrating Radiation*

RUDOLF FRERICHS
Department of Physics, Northwestern University, Evanston, Illinois
(Received March 5, 1952)

CRYSTAL phosphors with well-developed electron traps, i.e., with persistent luminescence, change their dielectric constant (and dielectric loss) if they are exposed to radiation. The radiation must be able to lift up electrons and consequently to fill the traps. This change in dielectric constant is attributed to the high polarizability of the trapped electrons. The effect has been well known for many years.[1] Earlier experiments have been made with thin sandwiches consisting of a phosphor layer arranged between two transparent electrodes. Generally, excitation by light is used, but L. Wesch reports two experiments performed with x-rays and cathode-rays on such sandwiches.[2] It appears to me that this effect has a few properties that make it useful for the measurement of penetrating radiation. A number of such sandwiches can be piled up similar to a paper condenser to make a receiver of any desired effective absorption. Such consensers can be easily made from thin aluminum foil, covered with a thin (0.5-mm) layer consisting of a suitable crystal phosphor (No. 1300 du Pont) and

a highly insulating binder, such as polystyrene dissolved in benzene. Preliminary experiments were made by the author with such a condenser consisting of ten layers with a thickness of 10 mm and an effective area of 4×4 cm². The condenser was mounted in a paraffin-filled aluminum box in order to avoid ionization of the surrounding air.

In a preliminary experiment x-rays were pulsed (60/sec) and their intensity was reduced by large distance, small tube current, and filtering (13 mm Al) to 0.001 R/min. The condenser was charged with 250 volts over 2.5 megohms. The signal due to the periodic change in capacity of the condenser was preamplified (500 times) and observed at an oscilloscope. It amounted to 160 microvolts corresponding to a capacity change of 0.57×10^{-6}. In a similar experiment 50 R of gamma-irradiation (radium) changed the capacity (3040 $\mu\mu f$) of a condenser (50×60×11 mm) by 30 $\mu\mu f$, as measured by a capacity bridge.

If the condenser is exposed to strong irradiation (about 1000 R), the occupancy of the traps and the change in capacity reaches a saturation value and therefore the ac signal, caused by the intermittent irradiation, disappears completely. The traps in the phosphor discharge almost completely in about one day, and then the original state of the condenser is restored. It is well known that the discharging of the traps can be accelerated by heating of the condenser (250–300°C), but in this case the phosphor has to be used without a polystyrene binder.

The excitation process itself, i.e., the lifting up of electrons into the conduction band and filling of the traps, does not have any time lag. Therefore, also pulses of gamma-radiation of a few microseconds duration, produced by beta-ray pulses of accelerators, should be effective in such receivers. The experiment mentioned was undertaken with a wide band amplifier; the sensitivity of the receiver can be greatly increased by tuned amplification using narrow bands.

Such receivers can be used with x-rays and beta-rays, which do not affect phosphors. It is obvious that in such condensers cadmium electrodes can be used for the detection of neutrons, as has been proposed for the combination of crystal phosphor and photomultiplier.[3] Also experiments with lead foils inserted for the production of pairs seem to be possible with such condensers. If the radiation is not periodically chopped, the change in dielectric constant can be measured with a heterodyne circuit of high sensitivity. It is even possible, if the decay curves of the dielectric change are determined for all energy levels, to measure the change in capacity at a given time after the irradiation and to extrapolate to the value obtained during the irradiation.

It is intended to continue this investigation.

The author wishes to express his thanks to the General Electric X-ray Department, Milwaukee, Wisconsin for the loan of the x-ray apparatus and to E. I. duPont de Nemours and Company, Towanda, Pennsylvania for help in selecting the phosphor used.

[*] This work is sponsored by the Bureau of Ships, Department of the Navy, Washington 25, D. C.
[1] See G. F. J. Garlick, *Luminescent Materials* (London, 1949), pp. 130 *ff.*
[2] L. Wesch, Ann. Physik. **40**, 263 (1941).
[3] W. H. Jordan and P. R. Bell, Nucleonics **4–5**, 30 (1949).

Intensity Calculation for Determining Weight Percentage in a Binary Alloy by X-Ray Fluorescent Analysis

P. K. Koh, B. Caugherty, and R. E. Burket
Research Laboratories, Allegheny Ludlum Steel Corporation, Brackenridge, Pennsylvania
(Received March 17, 1952)

THE difficulties encountered in the theoretical calculation of fluorescent intensity for the determination of the percentage of a component element in metallic alloys have been enumerated in a paper by the writers.[1] When a binary alloy consisting of two neighboring elements in the periodic table is concerned, the effect of mutual excitation, absorption edge, and difference in absorption becomes insignificant so that a simple calculation gives weight percentages of the alloying elements in good agreement with chemical analysis.

TABLE I.

Specimen	$I_{K\alpha}$ Cobalt / $I_{K\alpha}$ Iron	Calculated atomic percent Fe	Co	Calculated wt percent Fe	Co
Small crystal	2.066	32.33	67.67	31.17	68.83
Tape	1.883	34.39	65.61	33.19	66.81
Comparison standard	1.002	49.60	50.40	48.25	51.75
Chemical analysis of comparison standard:				Fe 48.80 weight percent Co 50.59 weight percent	

An occasion arose when it was necessary to compare the cobalt content of two iron-cobalt alloys; one in the form of a 3×3×0.1 mm small single crystal, and the other, 5×0.1 mm thin tape. Since it was essential that the specimen be preserved in the original form, no microchemical technique could be used.

An iron-cobalt alloy of known chemical analysis was used as a standard of comparison. The intensity ratio of $Co_{K\alpha}$ to $Fe_{K\alpha}$ on each specimen was obtained under identical operating conditions. The intensity in counts per second was the average of several readings obtained by scaling at ½ to 2 percent relative probable error (16,384 to 1024 total counts, respectively).

The relative excitation efficiency of cobalt *versus* iron was obtained as follows:

$$\frac{\text{(excitation efficiency) cobalt}}{\text{(excitation efficiency) iron}} = \frac{I_{K\alpha}}{I_{K\alpha}}\frac{\text{(remelted carbonyl cobalt)}}{\text{(electrolytic iron)}} = 0.987.$$

The atomic percentage of Fe in the Co-Fe alloys was calculated according to the following equation:

$$\text{Fe}\left(\frac{I_{K\alpha}\text{ cobalt}}{I_{K\alpha}\text{ iron}}\times\frac{1}{0.987}+1\right)=100.$$

The results in Table I show the validity of the preceding equation.

[1] P. K. Koh and Betty Caugherty, J. Appl. Phys. **23**, 427 (1952).

Energy Transference between Wave Numbers in Isotropic Turbulence

Hiroshi Sato
Institute of Industrial Science, University of Tokyo, Chiba City, Japan
(Received March 18, 1952)

ONE of the most important features of turbulent motion is the energy transference between different ranges of wave numbers. Experimental information on this subject has recently

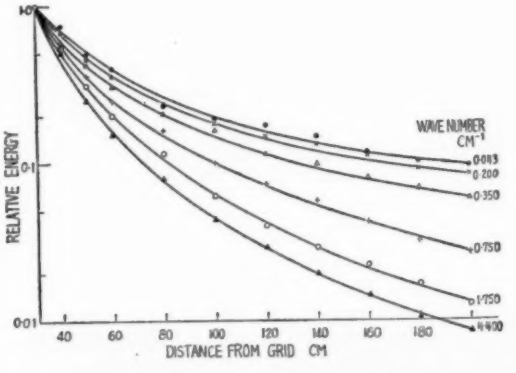

FIG. 1. Decay of spectral components.

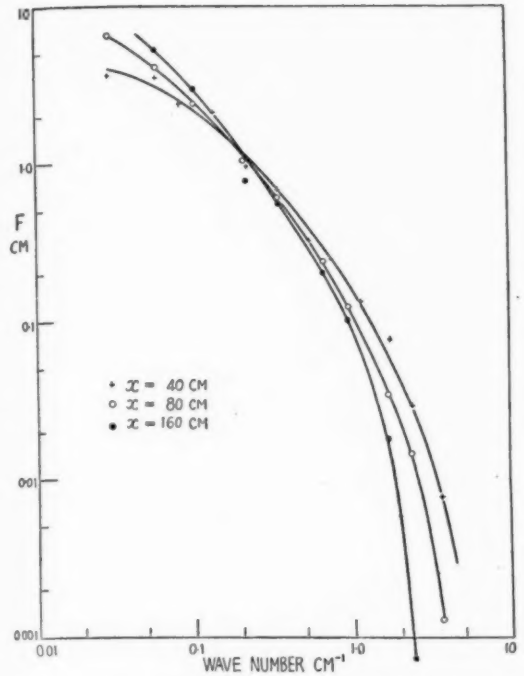

FIG. 2. One-dimensional spectrum of $\bar{u}^2$.

been obtained by measuring the triple correlation of velocity fluctuations.[1] It is possible, however, to estimate the transference directly from energy spectrum. With usual notations, the Fourier transform of Kármán-Howarth's equation of correlation propagation is

$$\frac{\partial}{\partial t}(\bar{u}^2F)+2(\bar{u}^2)^{\frac{1}{2}}W(k)=-2\nu k^2\left(Fk^2+4\int_k^\infty Fkdk\right), \qquad (1)$$

where k the wave number, F the one-dimensional spectrum of $\bar{u}^2$, and W is the energy transference function. The first term on the left side may be derived from measurement of decay of spectral components, an improved method being proposed by the present author.[2] Terms on the right side may be obtained from the measured curve of spectrum.

Experiments were made in a closed wind tunnel with a grid of 1-in. mesh length and at a wind speed of 10 m/s. Relative energy of spectral components was observed by traversing hot wire longitudinally with tuning frequency of filter fixed (Fig. 1). Decay of components is found to become more severe as the wave number increases, whereas a somewhat complicated tendency was observed in a previous study,[2] where the measurements were carried out in an open jet-type wind tunnel. Figure 2 shows the energy spectrum obtained at various positions, from which we estimated terms on the right side of Eq. (1). From faired curves of results, the energy transference is determined as Fig. 3, where positive value of W denotes flow-out of energy and negative value flow-in. It is seen that the wave numbers of no transference as well as of maximum flow-in decrease wtih decay of turbulence. Integral $\int_0^\infty Wdk$ becomes nearly zero, indicating the reliability of results.

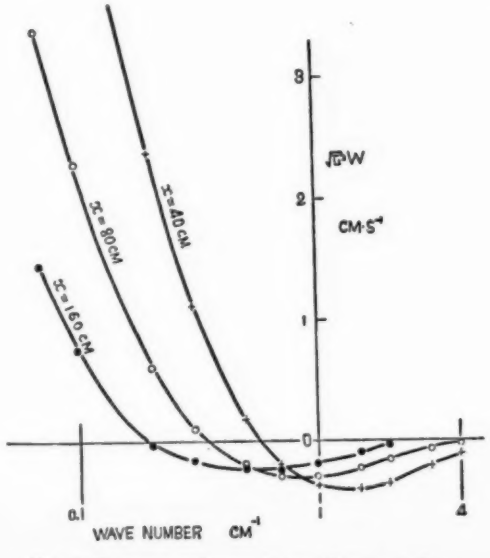

FIG. 3. Energy transference between wave numbers.

The author wishes to thank Professor I. Tani and Professor H. Kumagai for their valuable advice.

[1] R. W. Stewart, Proc. Cambridge Phil. Soc. **47**, 146 (1951).
[2] H. Sato, J. Appl. Phys. **22**, 525 (1951); H. Sato, J. Phys. Soc. (Japan) **6**, 387 (1951).

Dielectric Image Line

D. D. KING
Radiation Laboratory, The Johns Hopkins University, Baltimore, Maryland
(Received March 19, 1952)

THE behavior of dielectric rods as wave guides has been discussed both experimentally and theoretically.[1,2] It is the purpose of this note to describe a modification of the dielectric wave guide which offers several important advantages over the simple rod.

Inspection of the theoretical expressions for the fields in a rod excited in the lowest or dipole mode shows that the distribution possesses a plane of symmetry. This permits the use of a half-round rod and an image plane, as shown in Fig. 1.

The extent of the field is determined by the ratio of conductor diameter to the wavelength. The percent power within a radius b for a dielectric rod of radius a is shown in Table I for the case $2a/\lambda_0=0.282$.

TABLE I.

b/a	3.5	10.6	35.5
%	30.5	82.5	99.9

For relatively thin rods such as this, most of the power is carried outside the rod, and the field intensities are, therefore, relatively low. The losses in the dielectric, and in the image conductor are minimized by the resulting low displacement and conduction current densities.

A polystyrene image line with $2a=0.42$ cm for use at $\lambda_0=1.23$ cm was constructed on a dural image surface 20 cm wide. A resonator was obtained by mounting 10×20 cm vertical end plates on the image surface. Holes in the base of the end plates permitted the polystyrene half-round rod to pass through the end faces. By measuring the Q of this resonator as a function of line length, the attenuation was determined as $31.5db/100$ ft.

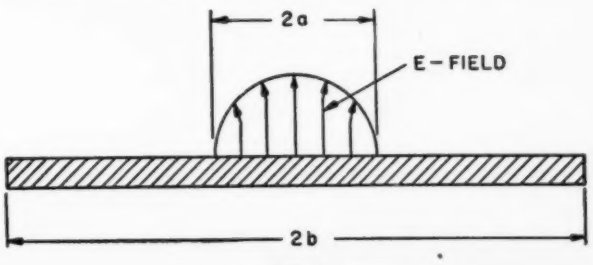

FIG. 1.

This compares with the calculated value of $18db/100$ ft assuming a loss tangent for the dielectric $\tan\delta = 0.001$, and an infinite perfectly conducting image surface. The calculated value is about equal to the attenuation of $\frac{1}{4} \times \frac{1}{2}$ in. (*RG-53/u*) brass wave guide. The attenuation may be decreased without limit by decreasing the ratio $2a/\lambda$. However, this requires a wider surface.

Advantages of the image line may be summarized as follows:

(1) no supports are required,
(2) coupling from the rear through slots is facilitated,
(3) the space required for the field is positively indicated by the width of the image plane,
(4) minimal attenuation at millimeter wavelength is afforded by choosing a large enough image screen and a thin dielectric filament,
(5) construction is simple, since the exact cross section of the dielectric filament is immaterial; the dielectric may be deposited in liquid form if desired.

[1] W. M. Elsasser, J. Appl. Phys. **20**, 1193 (1949).
[2] C. H. Chandler, J. Appl. Phys. **20**, 1188 (1949).

New Booklets and Other Publications

National Bureau of Standards Handbook 48 entitled "Control and Removal of Radioactive Contamination in Laboratories" is available from Government Printing Office, Washington 25, D. C. Price 15 cents.

The JAP has received a copy of No. 91 (1951) *Acta Polytechnica*. This publication is devoted to original contributions to engineering sciences and is published at Stockholm, Sweden, by the Royal Swedish Academy of Engineering Sciences in collaboration with the State Council of Technical Research, The Royal Institute of Technology, the Chalmers' University of Technology (Gothenburg), The Association of Engineers and Architects, and other bodies. Interested readers should write to Lennart Simonsson, Secretary to the Executive Committee of *Acta Polytechnica*, Stockholm 5, Sweden.

A booklet entitled "Electrodeposited Tin-Nickel Alloy Coatings" has been issued by Tin Research Institute, which describes work done in the Institute's laboratories during the past two years. Copies of this booklet are available, without charge from: Tin Research Institute, Fraser Road, Perivale, Greenford, Middlesex, England. Tin Research Institute, Inc., 492 West Sixth Avenue, Columbus 1, Ohio, U.S.A. Centre d'Information de l'Etain, 31, Rue du Marais, Brussels, Belgium. Technisch Informatie Centrum, N. V. Billiton Maatschappij, Louis Couperusplein 19, The Hague, Holland.

For laboratory workers in fields where complete spectrophotometric data is essential to accurate results, the Eastman Kodak Company has issued a revised Kodak Data Book, "Kodak Wratten Filters for Scientific and Technical Use." The booklet is priced at 75 cents per copy and is available from Kodak dealers. Also available is the Kodak Data Book on Chemical Preparations at 50 cents per copy.

Leeds & Northrup Company has published a newly revised, 20-page Catalog Section ED, "Galvanometers and Dynamometers." A copy of this Catalog will be sent upon request. Address Leeds & Northrup Company, 4934 Stenton Avenue, Philadelphia 44, Pennsylvania. Also obtainable is a new, 36-page catalog and buyer's guide, "Thermohms, Assemblies, Parts and Accessories."

Bausch & Lomb has issued a new catalog on three-dimensional microscopes entitled, "Bausch & Lomb Stereomicroscopes." The catalog is fully illustrated with photographs and sketches of various models and accessories.

Knapp Mills Inc. has published a new 22-page booklet, "The History and Development of Ferrolum Lead Clad Steel and Cupralum Lead Clad Copper." Interested readers may obtain copies by writing to: Research Department, Knapp Mills Inc., 23–15 Borden Avenue, Long Island City, New York.

A new 28-page, two-color booklet describing the basic characteristics and the applications of selenium rectifier stacks has been announced by the Lighting and Rectifier Department of the General Electric Company. Designated as GET-2350, the booklet is complete with charts, graphs, and tables illustrating the principles of rectification, and the characteristics, manufacture, circuit design, and application of selenium rectifiers.

Also, a new 80-page catalog summarizes for the first time under one cover all of the General Electric Company's testing and measuring equipment for laboratory and production line use. To be used primarily as a reference to the apparatus available for the complex measurements to be made in industry, the new catalog (GEC-1016) contains more than 150 photographs and diagrams and describes the uses, features, specifications, and prices of more than 130 G-E testing and measuring equipments.

Eberbach & Son Company, Ann Arbor, Michigan, has the following booklets available—free on request: Eberbach *Announcer* of Scientific Equipment, No. 51 10 44; No. 52 1 45; and No. 52 3 46.